University
of Catania

Ph.D. in
"Materials Science and Nanotechnologies"

XXXIV cycle

Self- assembly of soft matter under 2D nanoconfinement

Roberta Ruffino

Tutor: Prof. G. Marletta

Ph.D. Coordinator: Prof. G. Compagnini

TABLE OF CONTENTS

Abstract

The possibility of creating 2D confined nano and microstructures that can be integrated on a large scale, was for many years one of the central interests in nanotechnology and nanoscience. The main goal is to control and manipulate the assembly of building blocks in order to obtain structures with the desired characteristics and unique properties. However, there are still different unknowns about the interactions and forces that come into play at the nanoscale and how they can affect the final structure. With this in mind, in order to shed more light into the processes involved and the resulting structures, the self-assembly of soft matter at two different interfaces was investigated, i.e. solid/air and liquid/air.

In particular, a new approach was developed to prepare, at the solid/air interface, substrates with controlled nano-curvature and surface free energy (SFE), to be used to investigate how geometric and energetic factors affect self-assembly of polymeric thin films. The results obtained suggest that, for a semi-crystalline model polymer, namely poly-3-hexyltiphen (P3HT), polymeric crystals follow the curvature of surfaces only in the presence of an energy gain. The effects induced by the geometric and energetic conditions of the substrate on the crystalline structure were studied using grazing incidence X-ray diffraction (GIXRD) and atomic force microscopy (AFM). It has been revealed that the substrate curvature influences the process of nucleation and growth of polymeric lamellae and consequently, the resulting lamellar orientation, with differences in the resulting structures before and after thermal annealing of the film. In particular, a randomization that increases with the surface curvature is observed before the annealing, while, following the treatment, there is an increase of the crystalline quality which is a function of the surface curvature. It is then hypothesized a dual mechanism of nucleation and growth, assuming a favoured nucleation in the curved portions of the surface, resulting in the formation of shorter lamellae, while the growth is instead favoured in the interstices between the particles, thus obtaining the formation of longer lamellae. At the same time, in-situ GIXRD analysis during the annealing allow to observe how the curvature and the energy associated affect the crystallization temperature. In particular, we observed a reduction of the crystallization temperature under conditions of high SFE, diagnostics of the growth of distorted crystals, while the reduction of SFE is accompanied by an increase of the crystallization temperature, which appears identical to that recorded on flat surfaces. Therefore, a new and easy method is provided to modulate the structure of polymer films by exploiting geometric distortion and interfacial interactions with possible effects on the functional properties of the polymer film.

The self-assembly of soft matter at the water-air interface was investigated by studying the spontaneous adsorption of negatively charged silica nanoparticles, decorated with cationic surfactant, which allow the creation of nanostructures in which the particle interactions along the asymmetrical interfacial environment determine their structure and stability. The variation of the hydrophobic chain length of the surfactant and of the ionic strength, allows to shed more light into the energetic landscape of the nanoparticles confined in an 2D asymmetric environment. The compression isotherms carried out in a Langmuir trough allow to suppose a two - fold nature of the repulsive interfacial interactions, that is steric and electrostatic, given the dependence of the isotherm on both the surfactant chain length and the ionic strength. The structural characterization of the interface, by means of synchrotron radiation grazing incidence small-angle X-Ray scattering (GISAXS) measurement, allows to determine the interactions, by simply compressing the surface and by acquiring simultaneously the GISAXS patterns; this represents the main innovation of this study. In particular, given the homogeneity of the monolayer, compression can be considered as the work done by the system to approach the particles. Therefore, once the work is known and, from the recorded diffractograms, the interparticle distance is determined, by taking into account the hexagonal packing, for small variations of distances it is possible to determine the interparticle forces acting in a strongly confined environment. Thus, long-range forces are detected with a dependence on the inverse power law with lateral separation, which suggests an electrostatic nature, and short-range forces, in which the surfactant molecules decorating the NPs are in contact with each other and can interpenetrate. The short-range forces have a steric nature and they depend on the chain length and on the surfactant concentration, with a variation of the repulsions and slope probably related to the flexibility of the chains. It is therefore presented a new methodology that allows to determine simultaneously the average interparticle distance and the repulsive forces that come into play between the particles, by performing simple compression isotherms. In this way, by understanding the interactions involved, this approach provides the ability to design and synthesize NPs monolayers and functional membranes with customized structures and properties.

1) Introduction to nanostructure

The origins of nanostructures date back to very ancient times. Already in the thirteenth-fourteenth centuries BCE, working with glass, unconsciously, the Egyptians used copper nanoparticles that allowed to confer red colour to the glass.[1] However, the origins of these structures are even more ancient, comparable to the origin of the Earth and involved in important processes in the dynamic evolution of the Planet.[2]

The chemical identity related to the structure of natural materials, as shape and dimensions, give them unique characteristics which can be appreciated also at the macroscale, as a result of interaction with light, water and other materials.[2,3]

An example is the fine structure of the butterfly wings (Figure 1.1a), whose unique colours are due to the nanostructured multilayer that acts as a diffraction gratings and induces phenomena of interference and consequently iridescence.[1,4]

More generally, natural nanostructures confer to living tissues properties which are essential for the thriving of organisms in their living environment.

The patterned structure on the shark skin, shown in Figure 1.1b, allows it to move with agility in the water,[5] while the one on the gecko's feet (Figure 1.1c) allows it to walk upside down thanks to the strong adhesion due to Van der Waals interactions. The gecko feet structure is an outstanding example of the relationship between nanostructure and functions. In particular, such nanostructure, consisting of flexible spatulae, allows gecko's feet to adapt to any surface structures, thanks to the strong adhesion generated by weak force acting on high surface areas. Furthermore, these spatulae are capable to self-cleaning, as the adhesion of dirty particles on them is not energetically favoured.[1,3,4,6]

This self-cleaning ability is known as "Lotus Effect", resulting from the super-hydrophobicity that mainly characterizes lotus flowers. The hydrophobic nature of leaves, connected to the surface nanostructure (Figure 1.1d), leads the water to slip away into drops picking up dirt particles, given the greater adhesion with the water drops than with the leaf surface.[1,3,7,8] Moreover, the super-hydrophobicity and chemical composition protects the plant from fungi and germs, increases the resistance to climate changing and provide, at the same times, unique aspect like orchids surface, shown in Figure 1.1e, which appears glossy even to the naked eye.[4]

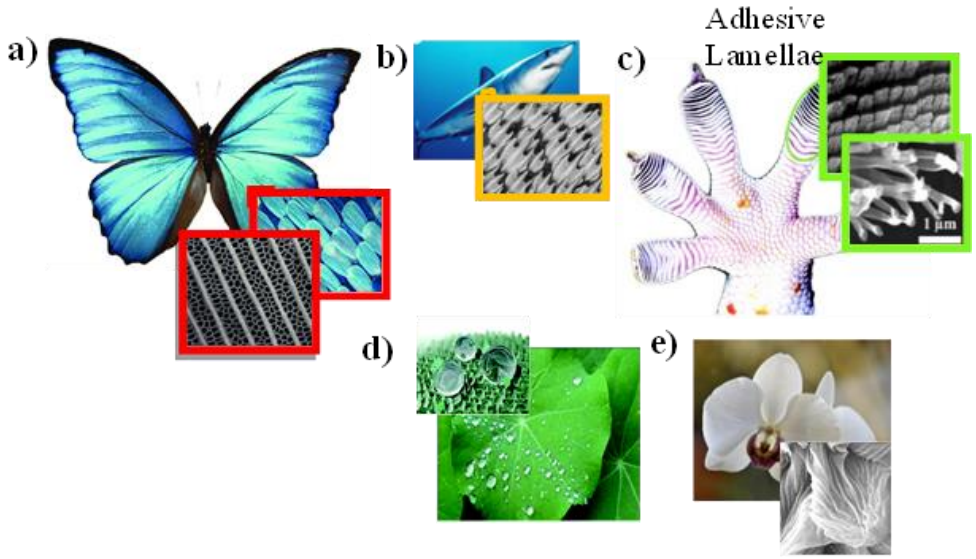

Figure 1.1. Nanostructure of butterfly wings[9] which, following interactions with light, provides unique colours at the macroscale (a); patterned shark skin[5] (b) and gecko feet[6] with their adhesive lamellae made by flexible spatulae. Superhydrophobic leaves[7] on lotus flower (d) and glossy petals of orchids[4] (e).

The charm of nature inspires scientists in engineering new materials with advanced properties, just by learning the secrets of nature at the nanoscale.[1]

Although nanomaterials have assisted the evolution of man, especially following the industrial revolution, the exploration of the nano-world begins only in the 900s. In 1925 the term "nanometre" was used for the first time to describe the size of colloidal gold particles observed at the microscope.[10] Since then, a new era begun, an era where small artificial devices meet atoms and molecules at the nanometre scale with the idea of carrying out manipulation at progressively smaller size ranges down to the atomic level (Feynman 1959, to which is attributed the concept of nanotechnology).[10,11,12] In 1974 Taniguchi hypothesized the potential exploitation of nanotechnology into the semiconductor technology in order to obtain with high precision ordered structures with sizes down to 1 nm.[1,10] Only in the 1980s, with the invention of Scanning Tunneling Microscope (STM) and atomic force microscope (AFM), the actual development on nanotechnology took place. These tools provide scientists the possibility to characterize structures and manipulate objects at the nanoscale, making real the Feynman prediction, i.e. to write at the nanometric scale (Figure 1.2a, b).[1,13] It was thus paved the way towards the nanoworld, enchanted by the idea of being able to control and reorganize matter at the atomic and molecular level, with dimensions from 1 to 100 nm.[14]

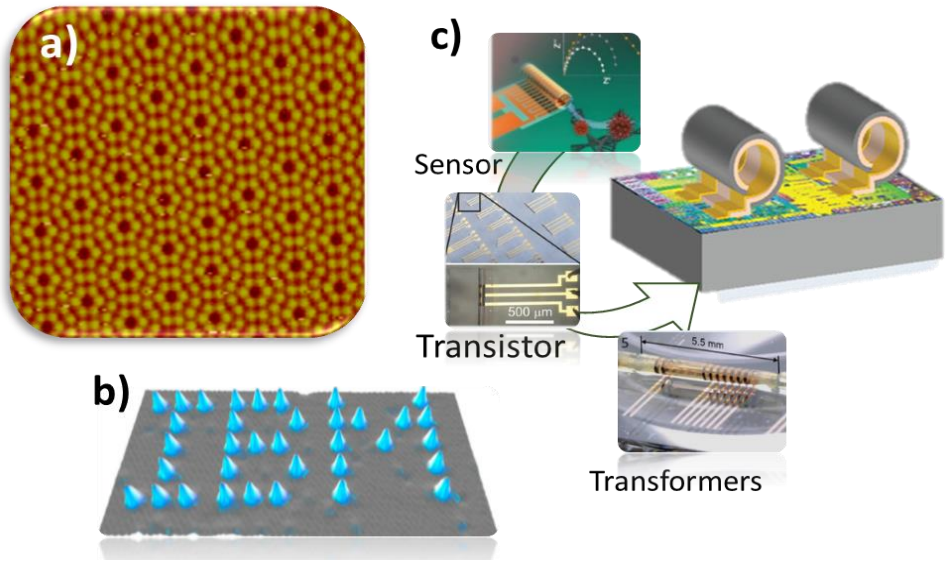

Figure 1.2. Atomic scale resolution of Si (111) surface (a) and creation of IBM logo with atoms positioned on substrates (b) by STM.[12] (c) Parallel self-assembly process of different component with a reduction of number of sequential steps and a high level of performance.[15]

Individual molecules are used to design functional structures where properties are related to structure, morphology and resulting interfacial interactions.[13] The possibility to create nano and microstructures that can then be integrated over a large area, was the central interest in electronics for many years.[1,16] Initially, the surface nanostructuring was performed via the deposition of thin films, followed by lithography and etching processes, achieving resolutions of the order of tens of nanometers.[16] Driven by the desire to obtain increasingly smaller devices, the attention of scientists moved to the self-assembly of nano-objects that, as a result of local weak interactions, allows the formation of ordered structure, with nanoscale resolutions, the so-called bottom-up approach was born (Figure 1.2.c).[16,17,18]

When focusing on the spontaneous self-assembly, soft-matter, whose constituents are sensitive to mechanical stress and self-organize under the influence of thermal energy, appears the most promising class of materials to generate controlled meso and nano-structures. Moreover, as soft matter self-assembly is driven by the system free energy minimization,[19] the so-obtained structures are stable.

The flexibility of soft matter, which is related to its ability to respond to external stimuli, allows to obtain structures with different conformations according to the interactions between its constituents and the enthalpic and entropic factors involved.

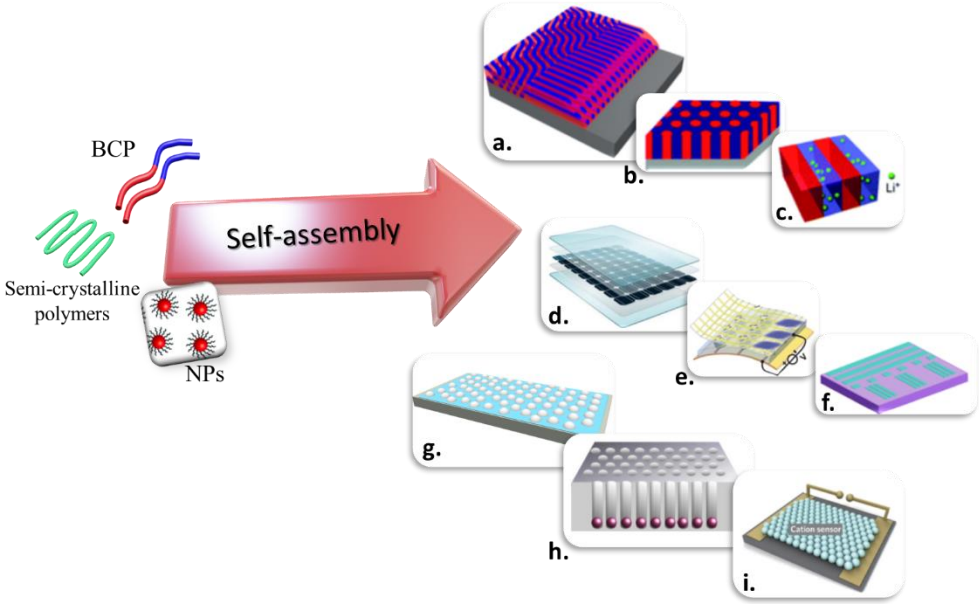

Figure 1.3. Schematic representation of functional structures as a results of self-assembly of soft materials like block co-polymers (BCP), semicrystalline polymers and nanoparticles[20] (NPs). Thermal annealing allows polymeric domains to reorganize into orderly structures useful in different nanotechnology applications. It becomes possible to align the morphology of BCPs to discontinuous films[21] (a), to generate cylinder patterns embedded in a matrix [22](b) and even to obtain ion conducting membranes[16] (c). In the same way, even the self-assembly of semi-crystalline polymers allows to obtain structures with applications in photovoltaics for the production of new semi-flexible modules[23](d), in fluidics for the creation of area lighting modules[24](e) as well as in electronics with the formation of patterned structures[25](f). Colloidal nanoparticles are also promising, their adsorption at the liquid interface creates nanostructures (g), they provide the possibility of making pores in polymer matrices[26] (h) and at the same time, their ordered arrays can be used to produce specific sensors for ions, gas or humidity[27] (i).

Therefore, it is possible to obtain different functional structures depending on size, shape, surface functionalization of the building blocks involved as well as on the adopted environmental conditions.[18,19,28] Soft matter includes a wide variety of systems, from polymers to colloids, from liquid crystals to surfactants.

Polymeric materials, in particular polymeric thin films, have attracted increasing interest due to their ability to assemble in different structures as a function of geometric constrains, interfacial interaction, as well as film thickness. [28,29] It is, therefore, possible to obtain the desired functional structures by tuning intermolecular and polymer-substrate interactions.[28,29] Conductive polymers have

attracted great interest, since they are characterized by electrical and optical properties close to the ones of metals and semiconductors but, at the same time, they show the mechanical properties and ease processability typical of polymers, which make them promising to achieve the desired functions by tuning their structures (Figure 1.3 d-f).[30] Also, the interfacial nature of the surface allows modulating the polymeric structure with more evident effects in block copolymers, where the morphology achieved is a function of individual blocks-surface interactions. This ability makes them promising for the production of models and scaffolds for the fabrication of nanostructured materials with nanoscopic periodic matrices to be used for applications with nanostructured networks, membranes with nanoscale pores and lithographic masks (Figure 1.3 a-c).[18,29,31]

With the marked development of organic and inorganic synthesis and the possibility to synthesize nanoscale objects, the interest of scientist raised toward colloidal particles and, in particular, nanoparticles which seem to bridge the gap between bulk materials and molecular structures. The uniqueness of nanoparticles is the possibility to tune their electrical, optical and magnetic properties by simply acting on their size and shape, with direct effects on interactions and collective behaviour that allow obtaining properties and functions never observed before. Therefore, they appear to be versatile building blocks for the production of ordered nanostructures with application ranging from medicine to electronics to water treatment processes[32] (Figure 1.3 g-i).[1,12,33,34,35,36, 37]

Given the wide variety of tools and systems available for the creation of nanostructures, the next step toward the development of nanotechnology is the integration of nanoscale in multi-functional platforms, by extending the unique effects that characterize the nano-world to the macroscale.[38]

The research focused on the design, from building blocks and interactions involved, the final structure having the required function, is increasingly growing.[39] The complex dependence of inter-molecular (or inter-particle) interactions on both distance and environmental conditions lead to nanostructures characterized by complex and delicate energy landscapes, sensitive to defects, which determine the conditions for each assembly process.[40,41] Obviously, the main scientific goal is to predict the energy path leading to the spontaneous assembly into a single, defect-free specific structure.[28] Several efforts were made to understand the factors that guide the creation of these superstructures. Among them, it is known that a significant role is played by surface and interfacial energetic factors however, the prediction of their effect is still beyond our capabilities. Indeed, although the final structure is in thermodynamic equilibrium, the simultaneous involvement of multiple factors into the self-assembly of soft matter does not allow to predict, through classical models based on the minimization of free energy, the behaviour arising from the contribution of individual constituents and the environmental conditions.[39]

Soft matter is organized into mesoscopic or nanoscopic structures according to the delicate balance between entropic and energetic contribution to free energy. The surface energy, as well as the morphology of the surface, are intimately related to the size of the system. Therefore the intrinsic reactivity of the surface, as well as the tendency of soft matter constituents to aggregate, are significantly influenced by composition and surface area.[11]

Thus in order to extend the soft matter meso-scale or nano-scale behaviour to the macroscale, it is important to understand how the interactions involved with different surfaces nature affects the soft matter assembly and the resulting properties.[42]

By taking inspiration from the flexibility of soft materials and from the unique structures they can generate, the purpose of this thesis is to study the self-assembly of soft matter thin films and monolayers as a function of energy factors and interfacial and surface interactions. The following chapter gives a brief overview of the main self-assembly mechanisms of soft matter and of the related driving forces and on the exploitation of these phenomena for the nanostructuring of surfaces and interfaces; by taking into account the different ways in which the interface nature affects the assembly.

Based on that, two different kinds of interfaces were investigated:

- *Solid/air interface*, assimilable to a static system in which the surface and interfacial energy are the driving force of self-assembly of soft matter

- *Liquid/air interface*, which acts as a dynamic system characterized by continuous interaction with bulk. The interface can act as a scaffold to colloidal self-assembly, affecting their structure and properties.

1.1) Self-assembly of soft matter at interface

Despite considerable progress in recent years, some issues still remain, including the effect of interfacial geometric factors on self-assembly processes. Indeed, spatial constraints, induced by such factors, are expected to strongly alter the processes of self-assembly of soft matter and, consequently, the nanostructures and properties related to them. As proof of this, there are already examples in the literature of self-assembly under nanometric confinement, where the presence of barriers along one or more directions leads to super-unique behaviours and structures, generally not obtainable in the absence of confinement.[43]

However, up to now these studies have focused almost exclusively on the simplest case, namely on monomolecular or ultrathin films, where the confinement can be modulated by varying the thickness of the film and the interface free energy plays a prominent role in determining the final super-structure.[44,45] This effect was particularly studied on ultra-thin or monomolecular polymer films,[46] given the wide variety of structures and behaviours that such systems offer and, consequently, the vastness of technologies in which polymer thin films are applied.[47,48,49] In particular, the two main investigated self-assembly phenomena are: crystallization, for semi-crystalline polymers, and micro-separation phase for block copolymers (BCPs).

The studies carried out on the self-assembly of polymer thin-films mainly concerned the phenomena of micro-phase separation of BCPs. They can be seen as amphiphilic macromolecular made by homo-polymeric blocks, chemically distinct and end-to-end linked to each other. Their assembly is driven by the separation of chemically different polymer segments forming different domains called microdomains or microphases, where the volume fraction of the constituent blocks ultimately determines the structure of the system. In particular, the increase of the volume fraction of one of the two blocks allows to obtain different structures ranging from cubes with spheres packed to hexagonally packed cylinders, to gyroids and lamellae, as is shown in Figure 1.4.[50,51] In order to obtain customized models from the BCP self-assembly it is important to know the interfacial interactions. Depending on the length ratio of the blocks, the Flory-Huggins parameter and the degree of polymerization, the BCPs are separated into arrays of different blocks, obtaining versatile structures at the nanoscale.[52] The interaction between the polymer and the substrate surface may also influence, in the case of BCP thin films, the morphology equilibrium nanostructure. Consideration should therefore be given to polymer wettability,[53,54] the orientation and uniformity of the nanopattern through thin film,[55,56,57,58,59] and the density of defects.[60,61]

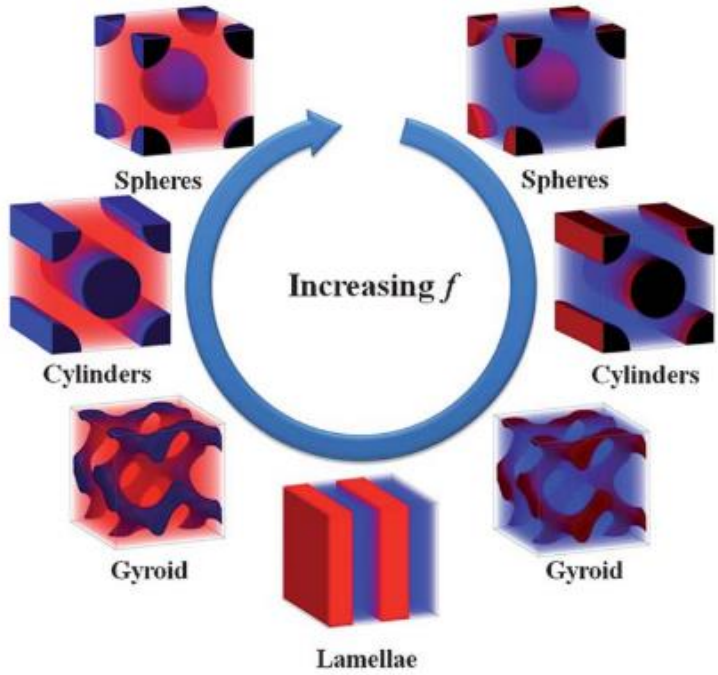

Figure 1.4. Various nanostructures that can be obtained from the self-assembly of BCPs, where "f" is the fractions in volume of a component of the two blocks.[31]

A crucial parameter is the understanding of the interactions between BCP thin films and the solid substrate. Furthermore, dewetting of the BCP film from the surface, which is crucial in the morphology and topography of the film at the microscale, and micro-phase separation of the BCP in ordered models, contribute to the formation of the pattern, driven by interfacial energy. The interdependence of the two mechanisms complicates the understanding of the interactions involved. In particular, dewetting leads to the formation of holes and islands, as well as the formation of drops that allow to shape the morphology (Figure 1.5).[52] In addition, the film thickness can also influence the nanostructure and, in particular, its orientation.

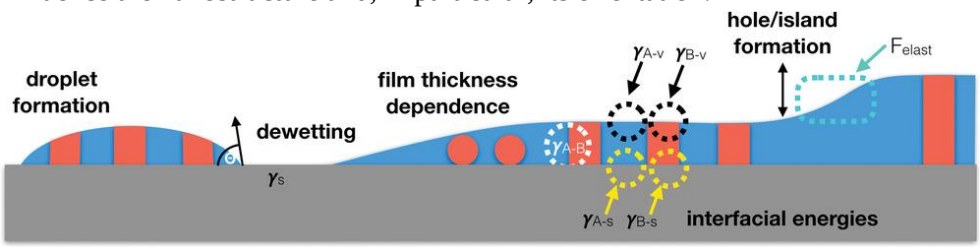

Figure 1.5. Micro and nanoscale events during dewetting and micro-phase separation of BCPs driven by interfacial energy.[52]

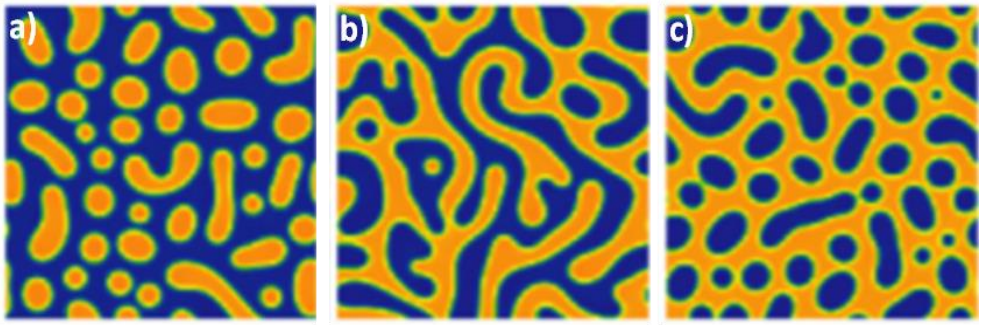

Figure 1.6. Phase separation pattern: spinodal decomposition, bicontinue structures (b). Nucleation and growth with Block A (a) and Block B (c) islands.[62]

The resulting morphology will be a function of the surface wettability, as one of the two blocks constituting the BCP may show a greater affinity towards the substrate, resulting in stable films even at low thicknesses.[16,63,64] The stability of the polymer film can be determined by the spreading parameter, S, which establishes a relationship between the surface tension of the substrate, γ_s, and the liquid, γ_l, and their interfacial energy $\gamma_{s\text{-}l}$.[65,66]

$$S = \gamma_s - (\gamma_{s-l} + \gamma_l) \qquad \textit{Equation 1.1}$$

The polymer film will be stable for S>0, otherwise dewetting will be observed, resulting in the formation of drops. The driving force of the process is energy minimization; therefore, polymer chains will try to assume the energy configurations that will correspond to minimum energies. A correlation between thickness stability and the intrinsic property of the structure was also observed. In particular, a local variation in thickness can be observed after annealing of the polymer film, suggesting the formation of superficial holes.[67,68] For thicknesses below a critical value, the annealing of the film leads to dewetting, depending on polymer-substrate interactions such as, long-range forces, polar interactions and molecular forces.[69,70,71] Dewetting occurs mainly by two mechanisms: spinodal decomposition and nucleation and growth (Figure 1.6). Spinodal decomposition occurs mainly in thin films and it is caused by fluctuations in the film's thickness forming capillary waves that can amplify spontaneously. [23] At greater thicknesses, dewetting follows the mechanism of nucleation and growth, with formation of holes in the points of defects to be nucleated. [23] The BCP micro-phase separation in the bulk is determined by the mixing energy F_{mix} of the copolymer blocks A and B; described by the mixing free energy of Gibbs ΔG_{mix}, mainly dependent on the Flory-Huggins parameter, χ_{AB}

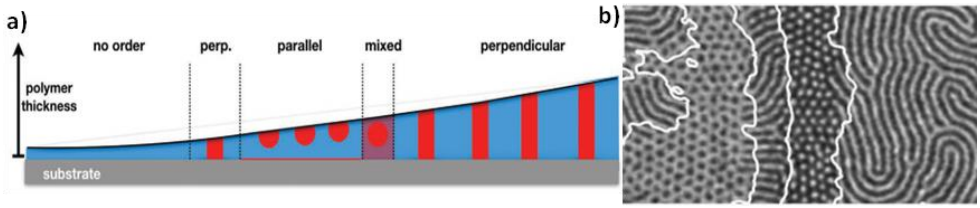

Figure 1.7. Cross-section of a BCP micro-phase separation, with increasing thickness gradient, on a planar substrate (a)[6] and scanning force microscope images in tapping mode (TM – SFM) (b)[69].

(consisting of an entropic and an enthalpic part) of the BCP species and the degree of polymerisation.[72,73]

$$\Delta G_{mix} = RT(n_A \ln(\varphi_A) + n_B \ln(\varphi_B) + n_A \varphi_B \chi_{AB}) \qquad \textit{Equation 1.2}$$

In addition, the interfaces that are formed during the micro-phase separation has a considerable extension. In particular, if the self-assembly of BCPs takes place in a thin film on a solid surface, it is necessary to consider also the interfacial energy, $F_{interface}$, and the elastic energy, $F_{elastic}$, connected to polymer deformation, where the surface is rough[58] or where the film thickness does not correspond to the periodicity, L_0. It follows that the surface free energy will be equal to:[74,58]

$$F = F_{mix} + F_{interface} + F_{elastic} \qquad \textit{Equation 1.3}$$

where the interfacial energy is given by the sum of the interfacial energies of the species involved. The balancing of interfacial energies, therefore, allows to guide the morphology on a nanometric scale. In order to minimise surface free energy, polymeric domains may assume different orientations to the substrate, i.e. parallel or perpendicular to the substrate (Figure 1.7) minimizing or maximizing the interface area, in order to achieve conformation with minimum total free energy. Due to the different geometries, the interface areas change depending on the thickness of the polymer film, therefore, the individual contributions of the different interfacial energy vary the total energy with the thickness of the polymer film.[58,53,75,76]

As is evident in Figure 1.7, the increase of polymer thickness leads to a change of the structure. The system can be driven towards the minimum energy acting, for example, on free surface energy at the polymer/substrate interface. Since the interfacial area changes greatly, depending on whether the domains orient parallel or perpendicular to the surface, controlling the interfacial energy between the polymeric species and the substrate allows to control the orientation. The correlation between interfacial energy and polymeric orientation is classified in terms of surface wettability, depending on the affinity of each polymeric species with the substrate.[68]

Different studies have reported that the modification of the substrate support, by reducing, for instance, the preferential wettability, can favour perpendicular orientation.[77,78,79] This orientation suffers from the parallel orientation induced by the preferential segregation of a block to the free surface.[80] Therefore, it was initially assumed that the perpendicular orientation propagated up to a certain distance from the substrate, subsequently a specific thickness range was identified, that is, $(n+\frac{1}{2})L_0$, with L_0 spacing of the domain of a given block and n integer number.[40,55] In proximity of commensurate thicknesses a parallel orientation is obtained; the substrate will be closer to a block. Moving from such thickness, it is possible to obtain perpendicular orientation; free energy, as well as surface area are increased. It follows that the formation of islands, holes and bicontinue structures takes place for thicknesses different from that commensurates.[81] Recently it was tried to understand and predict how substrates with different surface energy, by considering also the influence of surface roughness, may influence polymer assembly and crystallization phenomena.[82] However, these studies mainly concern BCP. It is therefore interesting to extend the study to thin films of semi-crystalline polymers, for which less is known about the distortive effects that can be induced on the film structure due to the substrate roughness, as well as how the energy effects associated with the substrate can affect the polymeric assembly.
It is in this perspective that the first section of my thesis, entitled "***Static interfaces***", develops. After a brief scientific report on superficial nanoconfinement and on conjugated crystalline polymers, it is shown how non-planar surfaces influence the process of self-assembly of semi-crystalline polymer thin films, in particular poly-3-hexyltophene thin film (P3HT) and how the modulation of the surface free energy (SFE) together with the geometric factors can affect the structure and morphology of the thin films.

Polymer systems, and BCPs in particular, were used for a long time to create nanostructures at the liquid interface. Using the Langmuir-Blodgett (LB) technique, polymeric films could be created at the liquid interface with different morphologies. Assembly of polymeric systems at fluid interfaces is more complex than in bulk or at solid interfaces, as the influence of dynamic factors as well as the soft interface of the water on which the film is formed must be considered; complex factor that influence the resulting morphology, highlighting the important role played by interfacial energies in determining the final structure[83,84,85] Of course the composition of blocks is a key factor in determining the morphology that is obtained.[86,87] In particular, with the variation of the percentage of the hydrophilic block, different morphologies can be obtained (Figure 1.8): planar aggregates are obtained at low percentage of the hydrophilic block; increasing the amount of hydrophilic block

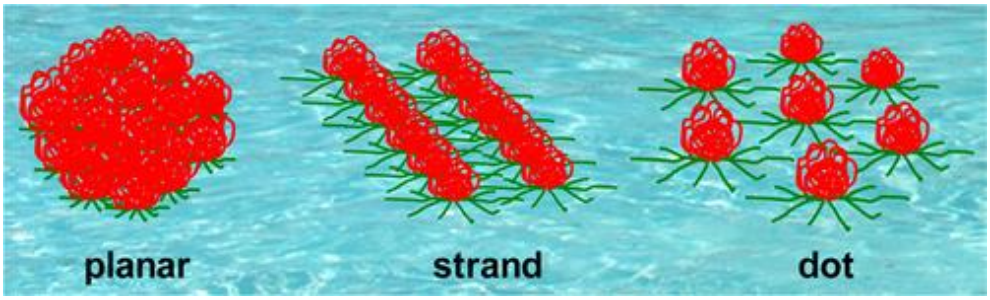

Figure 1.8. Schematic representation of the different morphology of the BCP obtained at the liquid interface, according to the % of hydrophilic block (green part in figure).[88]

leads to the formation of stripes, characterized by constant width but variable length, while further increase leads to the formation of uniform size dots, which tend to pack in 2D arrays.[86,87] Additionally, different morphologies of the same film were observed under different experimental conditions, such as nanofoams[89] nanoring[90], which can be attributed to kinetic effects. They affect the assembly of the film, with formation of frozen morphologies, resulting from a dewetting process of a film initially uniform in solution.[89,90,91,92] Moreover, it can also be the diffusion of the film, before dewetting, to develop particular structures that influence the final morphology.[93] It follows that understanding and underlining the factors that govern the morphology soft matter monolayers at liquid interfaces is complex.

Recently, the formation of nanostructures at the liquid interface involved the use of colloidal particles, whose assembly appears a versatile tool to prepare monolayers with custom structure and properties.[91,92,94] Typically, the assembly of nanoparticles on surfaces and liquid interfaces can take place through direct spreading of insoluble nanoparticles at the interface and formation of a diffuse monolayer,[91,92] or by spontaneous migration and adsorption of homogeneously dispersed nanoparticles in one of the two fluid phases, with formation of an adsorbed monolayer.[95,96,97] The interfacial density of the particles is controlled, in the first case, by the volume of nanoparticles that spreads to the interface, while in the second case by the affinity of the particles to the fluid interface.

Until now, the most used method in the preparation of functional monolayers was the spreading, as it allows to easily modulate the structure of the monolayer through an accurate control of the experimental parameters.[98,99] However, due to the intrinsic hydrophobicity of spread particles, spreading generally leads to the formation of islands rather than homogeneous monolayers on a macro-scale.[100] Conversely, the adsorption of amphiphilic particles from bulk dispersions, at the liquid interface, may lead to the formation of homogeneous monolayers where the equilibrium between the adsorption energy and the inter-particle interactions at the interface regulate the

interparticle distance.[95] In particular, if the particle size is greater than 10 nm, they are irreversibly adsorbed to the interface, since the desorption energy significantly exceeds the K_BT.[101] It follows that the functionalization of the particles with suitable dispersed molecules, leads to the formation of nanostructured monolayers in which particles can be treated as 2D colloids, whose structures and properties are determined by interparticle interactions in an asymmetrical environment.[102] Therefore, understanding interparticle interactions is of fundamental importance to modulate and adapt the structure of the nanoparticle monolayer, with a view to optimising properties.[103]

Hence, the second section of my thesis entitled "***Dynamic interfaces***", in which the nanostructuring at the water/air interface is investigated, after a brief theoretical background about the confinement to the interface between two different fluids, as well as the interactions involved and the formation of the corresponding nanostructures. Nanostructuring process occurs via adsorption at the interface of negatively charged silica nanoparticles, decorated with cationic surfactant. In particular, it is studied how the hydrophobic chain length of the surfactant and the ionic strength affect the interfacial interactions and the interparticle forces involved.

References

(1) Schaming, D.; Remita, H. Nanotechnology: From the Ancient Time to Nowadays. *Found. Chem.* **2015**, *17* (3), 187–205. https://doi.org/10.1007/s10698-015-9235-y.

(2) Hochella, M. F.; Mogk, D. W.; Ranville, J.; Allen, I. C.; Luther, G. W.; Marr, L. C.; McGrail, B. P.; Murayama, M.; Qafoku, N. P.; Rosso, K. M.; Sahai, N.; Schroeder, P. A.; Vikesland, P.; Westerhoff, P.; Yang, Y. Natural, Incidental, and Engineered Nanomaterials and Their Impacts on the Earth System. *Science (80-.).* **2019**, *363* (6434). https://doi.org/10.1126/science.aau8299.

(3) Jeevanandam, J.; Barhoum, A.; Chan, Y. S.; Dufresne, A.; Danquah, M. K. Review on Nanoparticles and Nanostructured Materials: History, Sources, Toxicity and Regulations. *Beilstein J. Nanotechnol.* **2018**, *9* (1), 1050–1074. https://doi.org/10.3762/bjnano.9.98.

(4) Kroisova, D. *Microstructures and Nanostructures in Nature*; Elsevier Inc., 2012; Vol. 57. https://doi.org/10.1016/B978-0-44-459422-8.00002-3.

(5) Perera, A. S.; Coppens, M. O. Re-Designing Materials for Biomedical Applications: From Biomimicry to Nature-Inspired Chemical Engineering. *Philos. Trans. R. Soc. A Math. Phys. Eng. Sci.* **2019**, *377* (2138). https://doi.org/10.1098/rsta.2018.0268.

(6) Xu, Q.; Zhang, W.; Dong, C. Biomimetic Self-Cleaning Surfaces : Synthesis , Mechanism and Applications. **2016**.

(7) Agarwal, S.; Gogoi, M.; Talukdar, S.; Bora, P.; Basumatary, T. K.; Devi, N. N. Green Synthesis of Silver Nanoplates Using the Special Category of Plant Leaves Showing the Lotus Effect. *RSC Adv.* **2020**, *10* (60), 36686–36694. https://doi.org/10.1039/d0ra06533a.

(8) Zhang, M.; Feng, S.; Wang, L.; Zheng, Y. Lotus Effect in Wetting and Self-Cleaning. *Biotribology* **2016**, *5*, 31–43. https://doi.org/10.1016/j.biotri.2015.08.002.

(9) Das, S.; Shanmugam, N.; Kumar, A.; Jose, S. Review: Potential of Biomimicry in the Field of Textile Technology. *Bioinspired, Biomim. Nanobiomaterials* **2017**, *6* (4), 224–235. https://doi.org/10.1680/jbibn.16.00048.

(10) Hulla, J. E.; Sahu, S. C.; Hayes, A. W. Nanotechnology: History and Future. *Hum. Exp. Toxicol.* **2015**, *34* (12), 1318–1321. https://doi.org/10.1177/0960327115603588.

(11) Subramani, K.; Elhissi, A.; Subbiah, U.; Ahmed, W. Introduction to Nanotechnology. *Nanobiomaterials Clin. Dent.* **2019**, *3*, 3–18. https://doi.org/10.1016/B978-0-12-815886-9.00001-2.

(12) Bayda, S.; Adeel, M.; Tuccinardi, T.; Cordani, M.; Rizzolio, F. The History of Nanoscience and Nanotechnology: From Chemical-Physical Applications to Nanomedicine. *Molecules* **2020**, *25* (1), 1–15. https://doi.org/10.3390/molecules25010112.

(13) Nasrollahzadeh, M.; Sajadi, S. M.; Sajjadi, M.; Issaabadi, Z. *An Introduction to Nanotechnology*, 1st ed.; Elsevier Ltd., 2019; Vol. 28. https://doi.org/10.1016/B978-0-12-813586-0.00001-8.

(14) Bhushan, B. *Introduction to Nanotechnology: History, Status, and Importance of Nanoscience and Nanotechnology Education*; 2016. https://doi.org/10.1007/978-3-319-31833-2_1.

(15) Karnaushenko, D.; Kang, T.; Schmidt, O. G. Shapeable Material Technologies for 3D

Self-Assembly of Mesoscale Electronics. *Adv. Mater. Technol.* **2019**, *4* (4), 1–29. https://doi.org/10.1002/admt.201800692.

(16) Hu, H.; Gopinadhan, M.; Osuji, C. O. Directed Self-Assembly of Block Copolymers: A Tutorial Review of Strategies for Enabling Nanotechnology with Soft Matter. *Soft Matter* **2014**, *10* (22), 3867–3889. https://doi.org/10.1039/c3sm52607k.

(17) Pisco, M.; Galeotti, F. Nano- and Micropatterning on Optical Fibers by Bottom-Up Approach: The Importance of Being Ordered. *Appl. Sci.* **2021**, *11* (7), 3254. https://doi.org/10.3390/app11073254.

(18) Talapin, D. V.; Engel, M.; Braun, P. V. Functional Materials and Devices by Self-Assembly. *MRS Bull.* **2020**, *45* (10), 799–806. https://doi.org/10.1557/mrs.2020.252.

(19) Furst, E. M. Directed Self-Assembly. *Soft Matter* **2013**, *9* (38), 9039–9045. https://doi.org/10.1039/c3sm90126b.

(20) Lu, Z.; Yin, Y. Colloidal Nanoparticle Clusters: Functional Materials by Design. *Chem. Soc. Rev.* **2012**, *41* (21), 6874–6887. https://doi.org/10.1039/c2cs35197h.

(21) Basutkar, M. N.; Majewski, P. W.; Doerk, G. S.; Toth, K.; Osuji, C. O.; Karim, A.; Yager, K. G. Aligned Morphologies in Near-Edge Regions of Block Copolymer Thin Films. *Macromolecules* **2019**, *52* (19), 7224–7233. https://doi.org/10.1021/acs.macromol.9b01703.

(22) Berman, D.; Shevchenko, E. Design of Functional Composite and All-Inorganic Nanostructured Materials: Via Infiltration of Polymer Templates with Inorganic Precursors. *J. Mater. Chem. C* **2020**, *8* (31), 10604–10627. https://doi.org/10.1039/d0tc00483a.

(23) Kumar, N. M.; Chopra, S. S.; de Oliveira, A. K. V.; Ahmed, H.; Vaezi, S.; Madukanya, U. E.; Castañón, J. M. Solar PV Module Technologies. *Photovolt. Sol. Energy Convers.* **2020**, 51–78. https://doi.org/10.1016/b978-0-12-819610-6.00003-x.

(24) Park, S. C.; Fang, J.; Biswas, S.; Mozafari, M.; Stauden, T.; Jacobs, H. O. A First Implementation of an Automated Reel-to-Reel Fluidic Self-Assembly Machine. *Adv. Mater.* **2014**, *26* (34), 5942–5949. https://doi.org/10.1002/adma.201401573.

(25) Pal, M.; Lee, G.; Giri, A.; Thiyagarajan, K.; Baek, K.; Kumar, M.; Jeong, U. High-Performance Transparent Conductive Pyrolyzed Carbon (Py-C) Ultrathin Film. *J. Mater. Chem. C* **2020**, *8* (27), 9243–9251. https://doi.org/10.1039/d0tc01936d.

(26) Scheeler, S. P.; Ullrich, S.; Kudera, S.; Pacholski, C. Fabrication of Porous Silicon by Metal-Assisted Etching Using Highly Ordered Gold Nanoparticle Arrays. *Nanoscale Res. Lett.* **2012**, *7*, 1–7. https://doi.org/10.1186/1556-276X-7-450.

(27) Yan, Y.; Warren, S. C.; Fuller, P.; Grzybowski, B. A. Chemoelectronic Circuits Based on Metal Nanoparticles. *Nat. Nanotechnol.* **2016**, *11* (7), 603–608. https://doi.org/10.1038/nnano.2016.39.

(28) Sherman, Z. M.; Howard, M. P.; Lindquist, B. A.; Jadrich, R. B.; Truskett, T. M. Inverse Methods for Design of Soft Materials. *J. Chem. Phys.* **2020**, *152* (14). https://doi.org/10.1063/1.5145177.

(29) Ramanathan, M.; Kilbey, S. M.; Ji, Q.; Hill, J. P.; Ariga, K. Materials Self-Assembly and Fabrication in Confined Spaces. *J. Mater. Chem.* **2012**, *22* (21), 10389–10405. https://doi.org/10.1039/c2jm16629a.

(30) Cataldo, S.; Pignataro, B. *Polymeric Thin Films for Organic Electronics: Properties and Adaptive Structures*; 2013; Vol. 6. https://doi.org/10.3390/ma6031159.

(31) Koo, K.; Ahn, H.; Kim, S. W.; Ryu, D. Y.; Russell, T. P. Directed Self-Assembly of Block Copolymers in the Extreme: Guiding Microdomains from the Small to the Large. *Soft Matter* **2013**, *9* (38), 9059–9071. https://doi.org/10.1039/c3sm51083b.

(32) Baruah, S.; Najam Khan, M.; Dutta, J. Perspectives and Applications of Nanotechnology in Water Treatment. *Environ. Chem. Lett.* **2016**, *14* (1), 1–14. https://doi.org/10.1007/s10311-015-0542-2.
(33) Laghrib, F.; Aghris, S.; Ajermoun, N.; Hrioua, A.; Bakasse, M.; Lahrich, S.; El Mhammedi, M. A. Recent Progress in Controlling the Synthesis and Assembly of Nanostructures: Application for Electrochemical Determination of p-Nitroaniline in Water. *Talanta* **2020**, *219* (June), 121234. https://doi.org/10.1016/j.talanta.2020.121234.
(34) van Dommelen, R.; Fanzio, P.; Sasso, L. Surface Self-Assembly of Colloidal Crystals for Micro- and Nano-Patterning. *Adv. Colloid Interface Sci.* **2018**, *251*, 97–114. https://doi.org/10.1016/j.cis.2017.10.007.
(35) Li, X.; Liu, X.; Liu, X. Self-Assembly of Colloidal Inorganic Nanocrystals: Nanoscale Forces, Emergent Properties and Applications. *Chem. Soc. Rev.* **2021**, *50* (3), 2074–2101. https://doi.org/10.1039/d0cs00436g.
(36) Chen, L.; Su, B.; Jiang, L. Recent Advances in One-Dimensional Assembly of Nanoparticles. *Chem. Soc. Rev.* **2019**, *48* (1), 8–21. https://doi.org/10.1039/c8cs00703a.
(37) Ghosh, S. K.; Böker, A. Self-Assembly of Nanoparticles in 2D and 3D: Recent Advances and Future Trends. *Macromol. Chem. Phys.* **2019**, *220* (17). https://doi.org/10.1002/macp.201900196.
(38) Israelachvili, J. N. *Intermolecular and Surface Forces*; 2010. https://doi.org/https://doi.org/10.1016/C2009-0-21560-1.
(39) van der Gucht, J. Grand Challenges in Soft Matter Physics. *Front. Phys.* **2018**, *6* (AUG), 6–8. https://doi.org/10.3389/fphy.2018.00087.
(40) Yager, K. G.; Berry, B. C.; Page, K.; Patton, D.; Karim, A.; Amis, E. J. Disordered Nanoparticle Interfaces for Directed Self-Assembly. *Soft Matter* **2009**, *5* (3), 622–628. https://doi.org/10.1039/b813970a.
(41) Packwood, D. M.; Han, P.; Hitosugi, T. Self-Assembly Process. *Nat. Publ. Gr.* **2017**, 1–8. https://doi.org/10.1038/ncomms14463.
(42) Eremeyev, V. A. On Effective Properties of Materials at the Nano- and Microscales Considering Surface Effects. *Acta Mech.* **2016**, *227* (1), 29–42. https://doi.org/10.1007/s00707-015-1427-y.
(43) Shi, A. C.; Li, B. Self-Assembly of Diblock Copolymers under Confinement. *Soft Matter* **2013**, *9* (5), 1398–1413. https://doi.org/10.1039/c2sm27031e.
(44) Napolitano, S.; Rotella, C.; Wübbenhorst, M. Can Thickness and Interfacial Interactions Univocally Determine the Behavior of Polymers Confined at the Nanoscale? *ACS Macro Lett.* **2012**, *1* (10), 1189–1193. https://doi.org/10.1021/mz300432d.
(45) Binder, K.; Horbach, J.; Vink, R.; De Virgiliis, A. Confinement Effects on Phase Behavior of Soft Matter Systems. *Soft Matter* **2008**, *4* (8), 1555–1568. https://doi.org/10.1039/b802207k.
(46) Liu, Y.; Chen, E. Polymer Crystallization of Ultrathin Films on Solid Substrates. *Coord. Chem. Rev.* **2010**, *254* (9–10), 1011–1037. https://doi.org/10.1016/j.ccr.2010.02.017.
(47) Gupta, S. K.; Jha, P.; Singh, A.; Chehimi, M. M.; Aswal, D. K. Flexible Organic Semiconductor Thin Films. *J. Mater. Chem. C* **2015**, *3* (33), 8468–8479. https://doi.org/10.1039/c5tc00901d.
(48) Yang, Y.; Mielczarek, K.; Aryal, M.; Zakhidov, A.; Hu, W. Effects of Nanostructure Geometry on Nanoimprinted Polymer Photovoltaics. *Nanoscale* **2014**, *6* (13), 7576–7584. https://doi.org/10.1039/c4nr01114g.

(49) Beckwith, K. S.; Cooil, S. P.; Wells, J. W.; Sikorski, P. Tunable High Aspect Ratio Polymer Nanostructures for Cell Interfaces. *Nanoscale* **2015**, *7* (18), 8438–8450. https://doi.org/10.1039/c5nr00674k.

(50) Khandpur, A. K.; Förster, S.; Bates, F. S.; Hamley, I. W.; Ryan, A. J.; Bras, W.; Almdal, K.; Mortensen, K. Polyisoprene-Polystyrene Diblock Copolymer Phase Diagram near the Order-Disorder Transition. *Macromolecules* **1995**, *28* (26), 8796–8806. https://doi.org/10.1021/ma00130a012.

(51) Matsen, M. W.; Bates, F. S. Unifying Weak- and Strong-Segregation Block Copolymer Theories - Macromolecules (ACS Publications). *Macromolecules* **1996**, *29* (4), 1091–1098.

(52) Brassat, K.; Lindner, J. K. N. Nanoscale Block Copolymer Self-Assembly and Microscale Polymer Film Dewetting: Progress in Understanding the Role of Interfacial Energies in the Formation of Hierarchical Nanostructures. *Adv. Mater. Interfaces* **2020**, *7* (5). https://doi.org/10.1002/admi.201901565.

(53) Brassat, K.; Kool, D.; Nallet, C. G. A.; Lindner, J. K. N. Understanding Film Thickness-Dependent Block Copolymer Self-Assembly by Controlled Polymer Dewetting on Prepatterned Surfaces. *Adv. Mater. Interfaces* **2020**, *7* (1), 1–10. https://doi.org/10.1002/admi.201901605.

(54) Albert, J. N. L.; Baney, M. J.; Stafford, C. M.; Kelly, J. Y.; Epps, T. H. Generation of Monolayer Gradients in Surface Energy and Surface Chemistry for Block Copolymer Thin Film Studies. *ACS Nano* **2009**, *3* (12), 3977–3986. https://doi.org/10.1021/nn900750w.

(55) Han, E.; Stuen, K. O.; La, Y. H.; Nealey, P. F.; Gopalan, P. Effect of Composition of Substrate-Modifying Random Copolymers on the Orientation of Symmetric and Asymmetric Diblock Copolymer Domains. *Macromolecules* **2008**, *41* (23), 9090–9097. https://doi.org/10.1021/ma8018393.

(56) Jaeger, H. M.; De Pablo, J. J. Perspective: Evolutionary Design of Granular Media and Block Copolymer Patterns. *APL Mater.* **2016**, *4* (5). https://doi.org/10.1063/1.4948270.

(57) Khaira, G. S.; Qin, J.; Garner, G. P.; Xiong, S.; Wan, L.; Ruiz, R.; Jaeger, H. M.; Nealey, P. F.; De Pablo, J. J. Evolutionary Optimization of Directed Self-Assembly of Triblock Copolymers on Chemically Patterned Substrates. *ACS Macro Lett.* **2014**, *3* (8), 747–752. https://doi.org/10.1021/mz5002349.

(58) Brassat, K.; Kool, D.; Bürger, J.; Lindner, J. K. N. Hierarchical Nanopores Formed by Block Copolymer Lithography on the Surfaces of Different Materials Pre-Patterned by Nanosphere Lithography. *Nanoscale* **2018**, *10* (21), 10005–10017. https://doi.org/10.1039/c8nr01397g.

(59) Xu, T.; Hawker, C. J.; Russell, T. P. Interfacial Interaction Dependence of Microdomain Orientation in Diblock Copolymer Thin Films. *Macromolecules* **2005**, *38* (7), 2802–2805. https://doi.org/10.1021/ma048005u.

(60) K. Brassat, D. Kool, J. K. N. L. Modification of Block Copolymer Lithography Masks by O2/Ar Plasma Treatment: Insights from Lift-off Experiments, Nanopore Etching and Free Membranes. *Nanotechnology* **2019**, 0–14.

(61) Welander, A. M.; Kang, H.; Stuen, K. O.; Solak, H. H.; Müller, M.; De Pablo, J. J.; Nealey, P. F. Rapid Directed Assembly of Block Copolymer Films at Elevated Temperatures. *Macromolecules* **2008**, *41* (8), 2759–2761. https://doi.org/10.1021/ma800056s.

(62) Li, Y. C.; Shi, R. P.; Wang, C. P.; Liu, X. J.; Wang, Y. Phase-Field Simulation of Thermally Induced Spinodal Decomposition in Polymer Blends. *Model. Simul. Mater.*

Sci. Eng. **2012**, *20* (7). https://doi.org/10.1088/0965-0393/20/7/075002.
(63) Choi, S. Y.; Lee, C.; Lee, J. W.; Park, C.; Kim, S. H. Dewetting-Induced Hierarchical Patterns in Block Copolymer Films. *Macromolecules* **2012**, *45* (3), 1492–1498. https://doi.org/10.1021/ma2019655.
(64) Müller-Buschbaum, P. Dewetting and Pattern Formation in Thin Polymer Films as Investigated in Real and Reciprocal Space. *J. Phys. Condens. Matter* **2003**, *15* (36). https://doi.org/10.1088/0953-8984/15/36/201.
(65) Butt, H. J. *The Physics and Chemistry of Interfaces R0.7*; 2013; Vol. 53.
(66) P. G. de Gennes, F. Brochard-Wyart, D. Q. Capillarity and Wetting Phenomena. *Springer, New York* **2004**, 1–2.
(67) Maher, M. J.; Self, J. L.; Stasiak, P.; Blachut, G.; Ellison, C. J.; Matsen, M. W.; Bates, C. M.; Willson, C. G. Structure, Stability, and Reorganization of 0.5 L0 Topography in Block Copolymer Thin Films. *ACS Nano* **2016**, *10* (11), 10152–10160. https://doi.org/10.1021/acsnano.6b05390.
(68) Shelton, C. K.; Epps, T. H. Decoupling Substrate Surface Interactions in Block Polymer Thin Film Self-Assembly. **2015**. https://doi.org/10.1021/acs.macromol.5b00833.
(69) Brassat, K.; Lindner, J. K. N. Nanoscale Block Copolymer Self-Assembly and Microscale Polymer Film Dewetting: Progress in Understanding the Role of Interfacial Energies in the Formation of Hierarchical Nanostructures. *Advanced Materials Interfaces*. 2020. https://doi.org/10.1002/admi.201901565.
(70) Lee, S. H.; Yoo, P. J.; Kwon, S. J.; Lee, H. H. Solvent-Driven Dewetting and Rim Instability. *J. Chem. Phys.* **2004**, *121* (9), 4346–4351. https://doi.org/10.1063/1.1770475.
(71) Green, P. F.; Limary, R. Block Copolymer Thin Films: Pattern Formation and Phase Behavior. *Adv. Colloid Interface Sci.* **2001**, *94* (1–3), 53–81. https://doi.org/10.1016/S0001-8686(01)00055-0.
(72) Huggins, M. L. Solutions of Long Chain Compounds. *J. Chem. Phys.* **1941**, *9* (5), 440. https://doi.org/10.1063/1.1750930.
(73) Kontogeorgis, G. M. Thermodynamics of Polymer Solutions. *Handb. Surf. Colloid Chem. Second Ed.* **2002**, 683–748. https://doi.org/10.1201/9781420040944.
(74) Andreozzi, A.; Poliani, E.; Seguini, G.; Perego, M. The Effect of Random Copolymer on the Characteristic Dimensions of Cylinder-Forming PS-b-PMMA Thin Films. *Nanotechnology* **2011**, *22* (18). https://doi.org/10.1088/0957-4484/22/18/185304.
(75) Albert, J. N. L.; Epps, T. H. Self-Assembly of Block Copolymer Thin Films. *Mater. Today* **2010**, *13* (6), 24–33. https://doi.org/10.1016/S1369-7021(10)70106-1.
(76) Doerk, G. S.; Li, R.; Fukuto, M.; Rodriguez, A.; Yager, K. G. Thickness-Dependent Ordering Kinetics in Cylindrical Block Copolymer/Homopolymer Ternary Blends. *Macromolecules* **2018**, *51* (24), 10259–10270. https://doi.org/10.1021/acs.macromol.8b01773.
(77) In, I.; La, Y. H.; Park, S. M.; Nealey, P. F.; Gopalan, P. Side-Chain-Grafted Random Copolymer Brushes as Neutral Surfaces for Controlling the Orientation of Block Copolymer Microdomains in Thin Films. *Langmuir* **2006**, *22* (18), 7855–7860. https://doi.org/10.1021/la060748g.
(78) Han, E.; In, I.; Park, S. M.; La, Y. H.; Wang, Y.; Nealey, P. F.; Gopalan, P. Photopatternable Imaging Layers for Controlling Block Copolymer Microdomain Orientation. *Adv. Mater.* **2007**, *19* (24), 4448–4452. https://doi.org/10.1002/adma.200602708.

(79) Kim, S.; Wang, H. S.; Choe, Y.; Choi, S. H.; Bang, J. Controlling the Microdomain Orientation in Block Copolymer Thin Films via Cross-Linkable Random Copolymer Neutral Layer. *Polym. J.* **2016**, *48* (4), 333–340. https://doi.org/10.1038/pj.2016.9.
(80) E. Huang, L. Rockford, T. P. R.; Hawker, C. J. Nanodomain Control in Copolymer Thin Films. *Macromolecules* **2000**.
(81) Suh, H. S.; Kang, H.; Nealey, P. F.; Char, K. Thickness Dependence of Neutral Parameter Windows for Perpendicularly Oriented Block Copolymer Thin Films. *Macromolecules* **2010**, *43* (10), 4744–4751. https://doi.org/10.1021/ma100150j.
(82) Modi, A.; Karim, A.; Tsige, M. Solvent and Substrate Induced Synergistic Ordering in Block Copolymer Thin Films. *Macromolecules* **2018**, *51* (18), 7186–7196. https://doi.org/10.1021/acs.macromol.8b00816.
(83) Hamley, I. W. Ordering in Thin Films of Block Copolymers: Fundamentals to Potential Applications. *Prog. Polym. Sci.* **2009**, *34* (11), 1161–1210. https://doi.org/10.1016/j.progpolymsci.2009.06.003.
(84) Van Zoelen, W.; Ten Brinke, G. Thin Films of Complexed Block Copolymers. *Soft Matter* **2009**, *5* (8), 1568–1582. https://doi.org/10.1039/b817093b.
(85) Aterials, M.; Ethods, M. BLOCK COPOLYMER THIN FILMS: Physics and Applications. **2010**, No. c, 1–25.
(86) Kumaki, J. Monolayer of Polystyrene Monomolecular Particles on a Water Surface Studied by Langmuir-Type Film Balance and Transmission Electron Microscopy. *Macromolecules* **1988**, *21* (3), 749–755. https://doi.org/10.1021/ma00181a033.
(87) Zhu, J.; Eisenberg, A.; Bruce Lennox, R. Interfacial Behavior of Block Polyelectrolytes. 1. Evidence for Novel Surface Micelle Formation. *J. Am. Chem. Soc.* **1991**, *113* (15), 5583–5588. https://doi.org/10.1021/ja00015a011.
(88) Perepichka, I. I.; Lu, Q.; Badia, A.; Bazuin, C. G. Understanding and Controlling Morphology Formation in Langmuir-Blodgett Block Copolymer Films Using PS-P4VP and PS-P4VP/PDP. *Langmuir* **2013**, *29* (14), 4502–4519. https://doi.org/10.1021/la3040962.
(89) Cheyne, R. B.; Moffitt, M. G. Self-Assembly of Polystyrene-Block-Poly(Ethylene Oxide) Copolymers at the Air-Water Interface: Is Dewetting the Genesis of Surface Aggregate Formation? *Langmuir* **2006**, *22* (20), 8387–8396. https://doi.org/10.1021/la061953z.
(90) Cheyne, R. B.; Moffitt, M. G. Novel Two-Dimensional "Ring and Chain" Morphologies in Langmuir-Blodgett Monolayers of PS-b-PEO Block Copolymers: Effect of Spreading Solution Concentration on Self-Assembly at the Air-Water Interface. *Langmuir* **2005**, *21* (12), 5453–5460. https://doi.org/10.1021/la0503707.
(91) Price, E. W.; Harirchian-Saei, S.; Moffitt, M. G. Strands, Networks, and Continents from Polystyrene Dewetting at the Air-Water Interface: Implications for Amphiphilic Block Copolymer Self-Assembly. *Langmuir* **2011**, *27* (4), 1364–1372. https://doi.org/10.1021/la1040618.
(92) Glagola, C. P.; Miceli, L. M.; Milchak, M. A.; Halle, E. H.; Logan, J. L. Polystyrene-Poly(Ethylene Oxide) Diblock Copolymer: The Effect of Polystyrene and Spreading Concentration at the Air/Water Interface. *Langmuir*. 2012, pp 5048–5058. https://doi.org/10.1021/la204100d.
(93) Perepichka, I. I.; Badia, A.; Bazuin, C. G. Nanostrand Formation of Block Copolymers at the Air/Water Interface. *ACS Nano* **2010**, *4* (11), 6825–6835. https://doi.org/10.1021/nn101318e.
(94) Tuccitto, N.; Amato, T.; Gangemi, C. M. A.; Trusso Sfrazzetto, G.; Puglisi, R.;

Pappalardo, A.; Ballistreri, F. P.; Messina, G. M. L.; Li-Destri, G.; Marletta, G. Driving Coordination Polymer Monolayer Formation by Competitive Reactions at the Air/Water Interface. *Langmuir* **2018**, *34* (39), 11706–11713. https://doi.org/10.1021/acs.langmuir.8b02607.

(95) Isa, L.; Amstad, E.; Schwenke, K.; Del Gado, E.; Ilg, P.; Kröger, M.; Reimhult, E. Adsorption of Core-Shell Nanoparticles at Liquid-Liquid Interfaces. *Soft Matter* **2011**, *7* (17), 7663–7675. https://doi.org/10.1039/c1sm05407d.

(96) Rauh, A.; Rey, M.; Barbera, L.; Zanini, M.; Karg, M.; Isa, L. Compression of Hard Core-Soft Shell Nanoparticles at Liquid-Liquid Interfaces: Influence of the Shell Thickness. *Soft Matter* **2017**, *13* (1), 158–169. https://doi.org/10.1039/C6SM01020B.

(97) Schwenke, K.; Isa, L.; Del Gado, E. Assembly of Nanoparticles at Liquid Interfaces: Crowding and Ordering. *Langmuir* **2014**, *30* (11), 3069–3074. https://doi.org/10.1021/la404254n.

(98) Geuchies, J. J.; Van Overbeek, C.; Evers, W. H.; Goris, B.; De Backer, A.; Gantapara, A. P.; Rabouw, F. T.; Hilhorst, J.; Peters, J. L.; Konovalov, O.; Petukhov, A. V.; Dijkstra, M.; Siebbeles, L. D. A.; Van Aert, S.; Bals, S.; Vanmaekelbergh, D. In Situ Study of the Formation Mechanism of Two-Dimensional Superlattices from PbSe Nanocrystals. *Nat. Mater.* **2016**, *15* (12), 1248–1254. https://doi.org/10.1038/nmat4746.

(99) Cho, K. S.; Talapin, D. V.; Gaschler, W.; Murray, C. B. Designing PbSe Nanowires and Nanorings through Oriented Attachment of Nanoparticles. *J. Am. Chem. Soc.* **2005**, *127* (19), 7140–7147. https://doi.org/10.1021/ja050107s.

(100) Pang, J.; Xiong, S.; Jaeckel, F.; Sun, Z.; Dunphy, D.; Brinker, C. J. Free-Standing, Patternable Nanoparticle/Polymer Monolayer Arrays Formed by Evaporation Induced Self-Assembly at a Fluid Interface. *J. Am. Chem. Soc.* **2008**, *130* (11), 3284–3285. https://doi.org/10.1021/ja710994m.

(101) Maestro, A.; Santini, E.; Guzmán, E. Physico-Chemical Foundations of Particle-Laden Fluid Interfaces. *Eur. Phys. J. E* **2018**, *41* (8). https://doi.org/10.1140/epje/i2018-11708-6.

(102) Forth, J.; Kim, P. Y.; Xie, G.; Liu, X.; Helms, B. A.; Russell, T. P. Building Reconfigurable Devices Using Complex Liquid–Fluid Interfaces. *Adv. Mater.* **2019**, *31* (18), 1–39. https://doi.org/10.1002/adma.201806370.

(103) Homede, E.; Zigelman, A.; Abezgauz, L.; Manor, O. Signatures of van Der Waals and Electrostatic Forces in the Deposition of Nanoparticle Assemblies. *J. Phys. Chem. Lett.* **2018**, *9* (18), 5226–5232. https://doi.org/10.1021/acs.jpclett.8b02052.

First Section:

Static Interfaces

Nanostructured surfaces - conjugated polymers: State of Art

2) Introduction to surface nano-confinement

The possibility to create self-assembled nanostructured thin films with potential application in technology, has attracted increasing interest.[1] Surface nano-structuring with typical dimensions of the order of one hundred nanometres and dimensional confinement provides materials with physical and chemical properties that are different from those they possess in bulk.[2,3] When the dimensions of the material approach those of the constituent elements, confinement effects emerge that can persist even on larger scales, with consequent effects in the kinetics and thermodynamics of assembly, due to geometric constraints and specific interactions with the host medium.[3] In this case, the simultaneous effect played by the interfacial interactions and the spatial confinement can act a key role in the design of materials with appropriate physical and chemical properties at the nanoscale.[3,4] Among the phenomena where interfacial interactions and nano-confinement can be simultaneously exploited to obtain tailored nanostructures, the self-assembly of soft matter under spatial confinement at the nanometre scale is one of the most sensitive. In particular, polymeric thin films are one of the more extensively investigated soft materials at both liquid and solid interface, as it is possible to finely modulate several key parameters such as composition, molecular weight and film thickness.[4,5,6,7] As a matter of fact, several reports have shown that the geometric constraints imposed by the nanometre thickness and the interfacial interactions affect the self-assembly process and the polymer films exhibit unique behaviours.[8,9,10,11,12,13] For instance, with the proper interactions between the polymer chains and the substrate, it is possible to induce anisotropic conformations and, in turn, the formation of super-structures which are not obtainable in the absence of confinement.[4,9] Among the parameters that affect the nano-structuring, the nature of the substrate on which the thin films are deposited must be considered. In fact, due to the high area/volume ratio, the polymer/substrate interactions play a fundamental role in self-organization processes.[14] Several studies were conducted on the polymer structures obtained by modulating the thickness of the film,[15] the polymer/substrate affinity[16] and the nature of the substrate.[17] Among the many polymer self-assembly processes, block-copolymer microphase separation and polymer crystallization were thoroughly investigated, showing a broad range of obtainable nanostructures with the proper control of confinement degree and interfacial interactions[1,18,19,20,21] More recently, another parameter affecting the self-assembly was investigated by preparing non-planar substrates able to induce nanoscale distortion to the polymer thin film.[22,23]

Experimental evidence has shown how nano-curved substrates, consisting of particle monolayers which, due to the nanoscale curvature of the particle involved, can induce periodic distortion on polymer films deposited on them, can influence the microphase separation of block copolymer thin films.[24,25] The effect of surface curvature on the distortion of the polymeric crystals, as well as on the crystallization and consequently on the assembly has not been studied yet. Moreover, the combination of the geometric effects, i.e. the surface curvature, with the SFE may give the possibility to observe more complex behaviours and, in turn, to more finely control the self-assembly. This is due to the fact that the coating of the substrate by the polymer and the eventual distorting effects induced by the curvature are influenced by the polymer/substrate interactions as well as by the wettability of the nanostructure. As a result, the combined effect of substrate nano-curvature and SFE need to be systematically investigated.
In order to investigate how these two important factors, affect the assembly of polymeric films, in this work soft lithography methods were used to create nanostructured surfaces composed of hexagonally packed silica particles, with a controlled periodic curvature determined by the diameter of the particles. The so-obtained nanostructured surfaces were subsequently chemically functionalized, in order to modulate the SFE. Given the complexity of the system, to better understand the role played by geometric and energetic factors in the self-assembly of thin films of semi-crystalline polymers, the first part of this study will only describe the effect of substrate curvature under constant SFE conditions. Then, the SFE effect under constant nano-curvature will be reported and, finally, results of the combination of the two effects will be discussed.

2.1) Conjugated polymer thin films

The low cost as well as the functionality, flexibility and ease of processing have made conjugated polymers a promising material for making electronic devices.[26,27]
It was observed that the performances of these devices are not only connected to the intrinsic materials properties, but they also depend on the process conditions, influenced by the conformational freedom of the polymer chains and by the weak interactions that govern the structure. Therefore, it is possible to improve the performance of devices based on conjugated polymers by acting on the design, interactions, as well as on the improvement of the process conditions.[28] This is due to the fact that the polymeric active layer of the electronic devices is a thin film with a thickness of the order of one hundred of the nanometre, in which the weak molecular interactions with the substrate affect its structure, while the morphology and the orientations of the polymeric crystals influence the charge transport properties.[29,30,31,32]

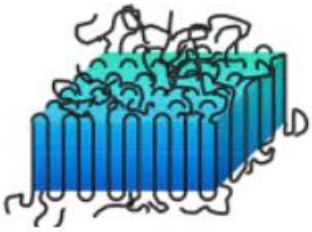

Figure 2.1. Schematic representation of the polymer lamellar structure.[36]

Therefore, the modulation of the polymer film thickness and of the resulting polymer/substrate interactions allow to obtain different structures, with a direct impact on the charge transport within the active layer of electronic devices.[33]

Many conjugated polymers are semi-crystalline. The crystallization involves a transition from a random coil to an ordered state; polymer chains fold, forming crystalline structures known as polymer lamellae (Figure 2.1), characterized by a period of constant folding and with dimensions of the order of tens of nanometres; the base unit of crystalline polymeric substances.[14] The lamellar thickness is a function of the molecular weight and the crystallization temperature.[34] It follows that the lamellar structure is not at the thermodynamic equilibrium that would be reached if the crystals were formed by chains completely extended and parallel to each other,[34] but has a kinetic origin. They are therefore non-equilibrium structures, trapped in metastable states with a high degree of disorder, characterized by the folding of the chain.[35] However, unlike other soft systems, polymer crystallization involves only a fraction of the polymer chains, resulting in the formation of small crystals immersed in an amorphous matrix; hence the term semi-crystalline.[34] The main reasons for this partial crystallinity are the slowness of the crystallization kinetics and the intrinsic disorder of the polymer chains.[34] Therefore, for crystallization temperatures below the melting temperature, lamellae characterized by a certain thickness will be created, while thicker lamellae will be kinetically disadvantaged, due to the slow growth, and thinner lamellae will be thermodynamically disadvantaged, due to the high interfacial free energy. The increase in the crystallization temperature leads to an increase in the lamellar thickness, following the increase in molecular mobility and the subsequent increase of growth velocity.[34] In the case the crystallization process involves a thin film, the interfacial interactions play an important role in controlling the crystallites orientation.[37] This, when dealing with conductive polymer films, allows to modify the conduction properties by acting on the confinement and interfaces.[38] It is known that the crystallization of polymer thin films leads to characteristic nanostructures.[14] In particular, the orientation and mobility of the chains, as well as the interface free energy become dominant factors. It should be also considered that the degree of

confinement is related to the thickness of the polymeric film; it follows that the substrate and film thickness are two important parameters in controlling the interaction strength of the substrate/polymer interface.[13] Although the dimensional effect associated with the thickness of the polymer film was studied extensively in the literature, less is known about the effect induced by the substrate, even if the importance of substrate-polymer interactions in crystallization is known.[14]

In addition, nanostructure substrate may induce structural distortion which should significantly vary the functional properties of the devices as the polymer assembly sees the formation of nanoscale crystals in which disordered and amorphous regions coexist, resulting in an anisotropic structure with a critical structure-electrical property relationship.[39,40,41] It was observed that the improvement in charge transport is not related to the increase in crystallinity, but to the extension of the conjugation and consequently, to the increase in interactions between the polymer chains. This happens because the deflection of the polymeric backbone allows the connection of the various crystalline domains, with a consequent overlap of the orbitals and an improvement in the efficiency of the charge conjugation.[27,39,41,42,43,44,45] Hence the hypothesis that charge transport is promoted by the ability to adapt to disorder,[26] underlining the importance of control the morphology.

Given the many studies conducted on the semi-crystalline behaviour, as well as on the structure/property relationship of P3HT, it appears, among the conjugated polymers, to be the ideal candidate for investigating how the different surface geometry associated with surface energy factors can induce distortions in the crystalline structure with effects on the charge transport properties.

The P3HT is a p-type semiconductor widely studied for its stability, high crystallinity and optoelectronic properties that favour its use in sensors, field effect transistors (FETs), memory and photovoltaic devices.[46,42,47,32] The interest in conducting polymers such as P3HT lies in their tendency to crystallize, with efficient charge transport pathways in the ordered crystalline domains.[44] Charge transport occurs mainly along the π-stacking direction and along the chain backbone, therefore, understanding the crystallization process and controlling crystal size and orientation could improve both the device performance and the design of new semiconductors with high charge mobility.[48] The rigidity of the polymeric backbone and the presence of side chains make crystallization complex; the side chains can increase steric hindrance or favour crystallization of the main chain or similarly, it can be the main chain that causes the crystallization of the side chains.[44,49] The fast kinetics of the processes involved make it difficult to fully understand the mechanism of nucleation and growth.[49] Despite the morphological differences, it was observed that the P3HT is characterizes by a crystallization process similar to polyethylene (PE),[40] a semi-crystalline polymer. Through crystals studies from polymer solution, it was found that PE crystallizes into single and lamellar crystals in solutions. Following the folding of the chain, lamellar crystals are formed, and the period of the chain folding

is function of the crystallization temperature. This leads to the formation of fundamental and complex crystalline structures in the presence of high polymer concentrations.[49] Through scanning tunnelling microscopy, STM, the folding of the individual chains of P3HT was observed, a typical feature of the semi-crystalline polymers such as polyolefins.[50] This should involve periodic alternation, of the order of tens of nanometres, in which the polymer chains are arranged in an order and disordered inter-lamellar regions, containing the folds and ends of the chains. [50] The thermal annealing of the polymer film, associated with slow cooling, could promote the fraction of micro-crystals having a conformation ordered which results in an increase in conjugation, as well as an increase in π interactions.[51] Morphological variations were also identified as a function of molecular weight (M_W), observing the presence of extended chains, nanoroads, at low M_W while the increase in M_W is accompanied by the folding of the chains, attributable to the increase in length with a consequent increase in interconnections.[44,48] At high M_W, P3HT film is made by heterogeneous microstructures in which the crystalline domains, characterized by high charge mobility, are immersed in an amorphous matrix.[52,53] It has been observed that if the distance between the crystalline domains is a few nanometres, the polymer chains are able to deflect; this allows the crystalline regions to be connected, bypassing the amorphous ones with a consequent increase in charge transport. Contrary to what is observed at low M_W, where the nanoroads are weakly interconnected and the grain boundaries between the nanocrystals trap the charge.[44,54] The distribution of the in-plane orientations of crystalline domains significantly influences the film properties. In particular, it is known that P3HT can assume two preferential orientations, edge-on and face-on (Figure 2.2) characterized by two opposite directions of the polymer chains folding. That is, while in the case of the edge-on the polymer chain folds perpendicularly to the surface, with the π-stacking parallel to the substrate plane, vice versa in the face-on the folding direction of the chain will be parallel to the substrate. In particular, while the edge-on orientation seems to be energetically favoured, as it is obtained in close to equilibrium conditions, the face-on is a kinetically trapped orientation.[44] The orientation of the crystalline domains influences the charge transport, since change the direction along which the charge mobility is greater.

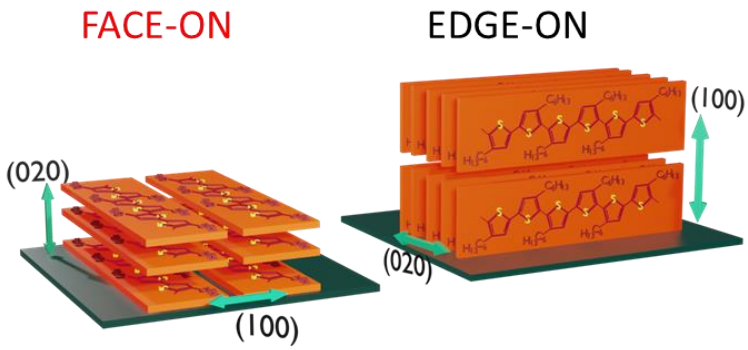

Figure 2.2. Schematic illustration of the two crystalline orientations: Face-on orientation with lamellar stacking (100) parallel to the substrate plane and π-stacking (020) perpendicular to the substrate plane. While in the edge-on orientation, the lamellar stacking is perpendicular to the substrate plane and π-stacking (020) parallel to the substrate plane.

Therefore, depending on whether you want to use the P3HT in OFETs or solar cells, you need to favour one orientation rather than another. In the case of OFETs, the charge transport occurs parallel to the surface, which favours the edge-on orientation, as the π-stacking lies along the substrate plane. Conversely, to increase the performance of solar cells, in which the direction of the charge transport must be maximized perpendicularly to the substrate plane, it is necessary to favour the face-on orientation, where the π-stacking is perpendicular to the plane.[44,48]
The thickness of the polymeric film and the nature of the substrate, i.e, of the involved interfacial interactions, also influence the orientations of the micro-crystals. In particular, it is possible to observe preferential orientations for polymeric films having thicknesses comparable to the dimensions of the crystals, < 25 nm, since it increases the affinity of the chains at the film-substrate interface.[44] Furthermore, it is possible to improve the performance of semiconductors with post-deposition process, thus improving the intra and inter-molecular orientation.[48] In particular, an increase of crystalline quality was observed by annealing the polymeric film near the melting point, followed by slow cooling.[48] This provides the possibility to explore the anisotropic crystallization behaviour, along the different crystallographic orientations, and to characterize the different structural orientations by X-ray diffraction based on synchrotron radiation. In this way it is possible to monitor the lamellar and π-stacking in real time even during the annealing of the polymeric film, thus providing the possibility of better understanding the crystallization behaviour of semiconductor conjugated polymers.[55] The need to use synchrotron sources lies in the fact that conventional X-rays cannot resolve the weak signals related to π-stacking.[55] In particular, in this work we used grazing incidence X-ray diffraction synchrotron radiation (GIXRD) to characterize the influence of both geometric factors induced by substrates with controlled nanometric curvature and energy

factors involved in the P3HT thin films self-assembly. In particular, the in situ structural characterization, carried out during the annealing of the film, allows to obtain information about the crystallization temperature as a function of the geometric and energetic surface conditions. To support the structural characterization, the morphology was analysed ex-situ by means of the atomic force microscopy (AFM) which allows to observe the crystal morphology and assembly.

2.2) Wettability of nanostructured surfaces

Wettability measurements represent one of the most popular methods for determining the surface free energy of a solid and, following the recent development of nanoscience and nanotechnologies, constitute a valuable tool for the surface characterization of nanomaterials.[56,57] In the case of flat solid surfaces the wettability can be studied by exploiting the concepts of capillarity and interface tension, $\sigma_{\alpha\beta}$, between two different phases α and β, i.e. the energy necessary to create a unitary surface area at the interface.[58]

In particular, from Young's equation (Equation 2.1) it is possible to determine if a liquid completely wets the surface, when σ_{SV}- (σ_{SL} + σ_{LV})> 0, or if a contact angle ϑ different from zero is recorded at the solid-liquid interface, indicating the partial wettability of the surface.[58]

$$\cos\vartheta = \frac{(\sigma_{SV} - \sigma_{SL})}{\sigma_{LV}} \qquad \textit{Equation 2.1}$$

where σ_{SV}, σ_{SL} and σ_{LV} are respectively the tension at the solid-vapor, solid-liquid and liquid-vapor interface. However, Young's equation is applicable only in the case of homogeneous flat surfaces, assuming the presence of a quasi-equilibrium in the range of observations, provided that the strain ratio of the solids is small.[58,59] This is due to the fact that Young equation does not consider the vertical component related to the surface tension along the contact line; therefore, in order to ensure equilibrium in the event that the capillary force is not balanced, an external force must be applied which can induce high deformations, destroying the assumption of co-planarity of the interfacial tensions.[58] Therefore, to the ideal condition proposed by Young, it is necessary to add the non-homogeneity of the surface and consequent correlation between the wetting liquid and the underlying surface roughness.[60,61]

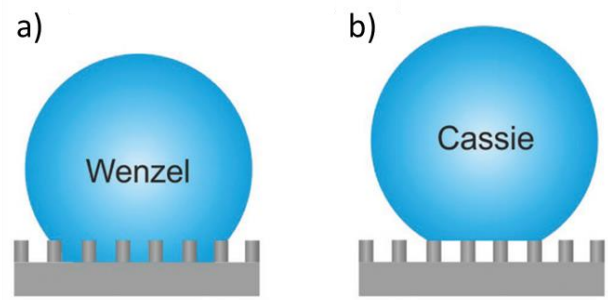

Figure 2.3. Complete wetting condition proposed by Wenzel (a).[67] Cassie-Baxter prediction with formation of the composite interface (b).[67]

In particular, it is possible to observe a condition of partial wetting, with a finite contact angle, in which the roughness and surface inhomogeneities cause the hysteresis of the contact angle and a condition of complete wetting, with a zero contact angle, in which the liquid is able to completely wet the surface.[60,62] The studies on non-homogeneity surface and consequently on the changing of wettability were implemented by Cassie-Baxter and Wenzel.[63] On the one hand, the Cassie-Baxter model supposes the formation of a composite contact angle in which air is trapped under the drop of the wetting liquid, which emphasises the concept of surface hydrophobicity. Conversely, Wenzel model assumes an increase of the solid surface with roughness, with changes in the hydrophobicity.[64] The surface roughness means that the drop of liquid that comes into contact with the surface may not penetrate the texture and generate a composite interface making the surface super-hydrophobic. This is because below the drop, the capillary forces maintain a layer of air; it follows that the liquid is in contact only with the upper part of the structure.[65,66] With the intention of correlating the composite interface with solid surface structures, Cassie and Baxter hypothesized that the droplet that wets the surface reaches an apparent equilibrium, described by the contact angle ϑ_E*, in order to reduce, as in the case of surfaces plane, the total free energy.[65] The Cassie-Baxter relationship (Equation 2.2) is then identified on the assumption that the surface structure is much smaller than the droplet size, indicating with Φ_s the area fraction of the air-liquid interface, r_Φ is the roughness of the wet surface, ϑ_1 and ϑ_2 are the contact angles on the solid and on the air. r_Φ, Φ_s and 1- Φ_s are the air ratios of the solid-liquid and liquid-air interface with respect to the total projected area.[65]

$$cos\vartheta_E^* = r_\Phi \Phi_s cos\vartheta_1 + (1 - \Phi_s) cos\vartheta_2 \qquad \textit{Equation 2.2}$$

However, the conditions under which this equation is applicable are not indicated; it describes only one contact angle ϑ_E*, consequently it is not able to explain the different contact angles observed. This opens the way for more rigorous equations

based on pure thermodynamic aspects.[60,65] The opposite condition in terms of surface wettability was proposed by Wenzel. He hypothesized the loss of the super-hydrophobic properties of the surface, therefore the liquid is able to wet the surface structure, identifying an apparent contact angle, ϑ_w:[60,66]

$$cos\vartheta_w = \bar{r}cos\vartheta_Y \qquad \textit{Equation 2.3}$$

where $\bar{r}$ is the average roughness ratio, i.e. the factor by which the roughness increases the solid-liquid interface area. The fact that the derivation of the equation is similar to that of Young suggests the possibility of determining a relationship between the apparent and intrinsic contact angle, in a completely wet surface in which superficial grooves can be ignored.[60,68] In summary, the surface wettability is described either by the Young equation or by Wenzel or Cassie-Baxter ones, although the conditions where each of them applies are not fully understood yet.[63,56] Therefore, it is necessary to identify the correlation between the intrinsic contact angle, associated with the interfacial properties of the material and the apparent contact angle, i.e. the measured one, in order to be able to deduce the intrinsic wettability of rough surfaces.[68] Wettability is extremely sensitive to surface geometric factors and therefore to roughness, as well as to surface chemistry. These effects make it difficult to understand the wettability by recording a hysteresis in the contact angle.[63,58] Different studies were conducted to correlate the different states of wettability with the surface morphology but, despite the various advances, the effects of nano-structured surfaces on the wetting states of the drops are not yet well understood.[57]

Therefore, fascinated by the combination of energetic and geometric factors in driving the self-assembly of thin films of soft matter at the interface, in this work, a novel approach was developed to prepare non-planar substrates with controlled SFE, in order to analyse how these two important factors, influence the assembly and, simultaneously, to determine how SFE affects the wettability of nanostructured surfaces characterized by a constant radius of curvature.

Results and Discussions

3) Polymer crystallization on nanostructured interfaces

3.1) Randomization of lamellar orientation

Nanostructured surfaces with controlled nanometric curvature were obtained by spin-coating silica particles with diameter ranging from 50 to 403 nm on (100) silica wafer. The spin coating conditions were adjusted for each particles size (See Appendix), to obtain a hexagonally packed particle monolayer[78] with local nanometric curvature, κ (nm^{-1}), spanning an order of magnitude, from 0.00492 to 0.04 nm^{-1}, expressed as $\kappa = \frac{1}{r}$, being r the particle radius and $\kappa = 0$ the reference for flat surfaces. Then, the substrates were made highly hydrophilic, by means of a basic piranha treatment, which guarantees a highly polar surface terminated by -OH groups[79], to ensure the best spreading of the spin coating P3HT, solutions and the consequent full coverage. Regardless of the curvature, the polymer film homogeneously covers the surface, with an average thickness of 67.5 ± 6.8 nm, as measured by profilometry.

The AFM height images shown in Figure 3.1 underline the homogeneous coverage of the surface, supporting the conformal adhesion of P3HT on any substrate. Furthermore, the AFM phase images (Figure 3.2) show that the as-deposited P3HT forms crystalline lamellae that perfectly follow the curvature of the substrate, except for the substrate with the highest curvature, for which the phase image is similar to the one obtained for the flat case. The lack of features characteristic of nano-curved substrates for the phase images recorded for P3HT films deposited on 0.0400 nm^{-1} curved substrates can be explained by considering that the contrast in the AFM phase images is generated by the variation of superficial viscoelastic properties[80]. Therefore, in Figure 3.2 f, the viscoelasticity P3HT lamellae does not depend on the curvature. This may be attributed to the thickness of the polymeric film, equal to 67.5 ± 6.8 nm, that exceeds the diameter of the smallest particles.

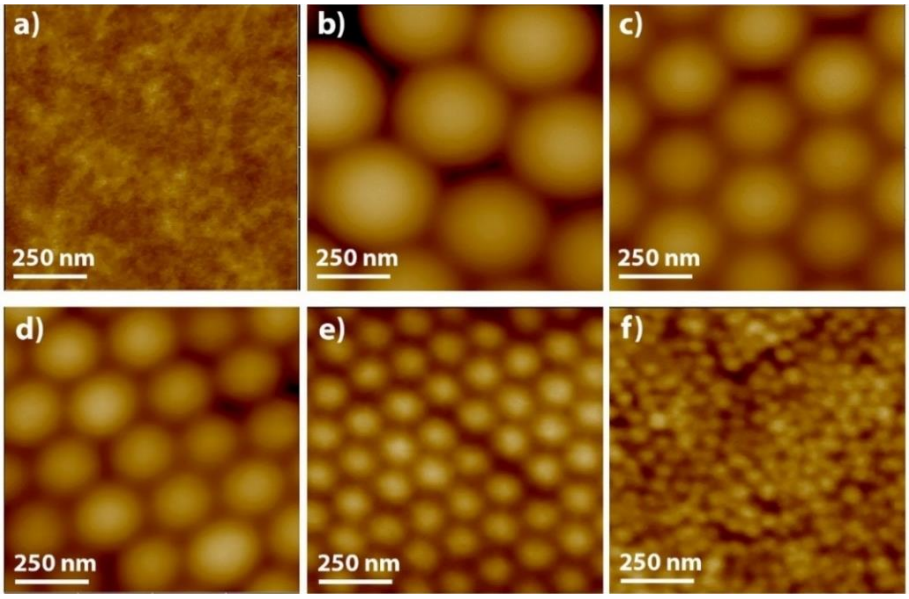

Figure 3.1. 1x1μm^2 AFM height images of P3HT films deposited on flat substrates (a) and on substrates with different curvatures: 0.00492 nm^{-1} (b), 0.00658 nm^{-1} (c), 0.00851 nm^{-1} (d), 0.0140 nm^{-1} (e) and 0.0400 nm^{-1} (f).

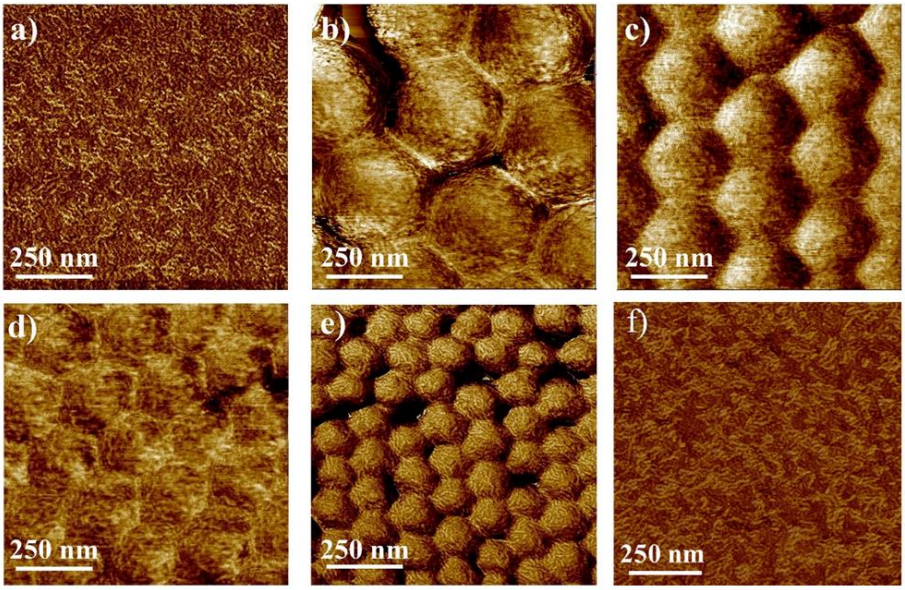

Figure 3.2. 1x1μm^2 AFM phase images of P3HT films crystallized on flat substrate (a) and on substrates with different curvature: 0.00492nm^{-1} (b), 0.00658 nm^{-1} (c), 0.00851 nm^{-1} (d), 0.0140 nm^{-1} (e) and 0.0400 nm^{-1} (f).

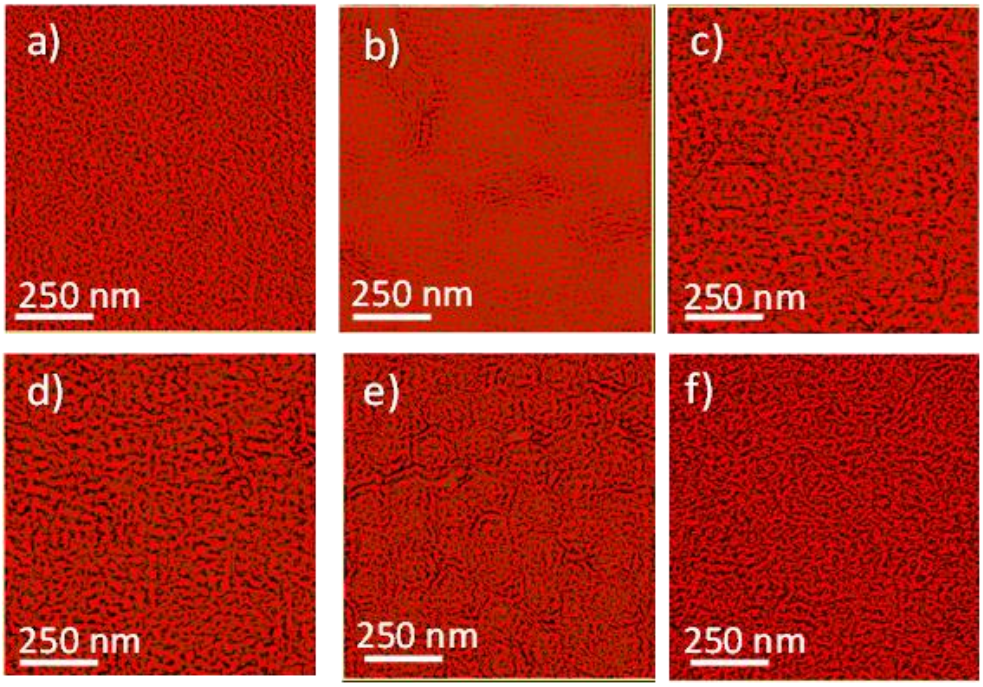

Figure 3.3. 1x1μm^2 AFM phase image. Lamellae coverage (%) of P3HT thin film on substrates having different curvature: 52.5 % of coverage on flat (a), 52.2% on 0.00492 nm^{-1} (b), 52.8% on 0.00658 nm^{-1} (c), 48.6% on 0.00851 nm^{-1} (d), 49.1% on 0.0140 nm^{-1} (e) and 50% on 0.0400 nm^{-1} (f).

Given the high contrast of the polymeric lamellae in the phase images, the surface fraction occupied by the lamellae was determined by means of the bearing analysis (Figure 3.3), recording a coverage of 51 ± 2% of the film area, regardless of the curvature of the substrate. This shows that nor the substrate coverage neither the P3HT film crystalline fraction are affected by the nano-curvature.

However, although the superficial density of P3HT crystals does not depend on the curvature of the substrate, the lamellar morphology can be influenced by the superficial nano-curvature and in particular the persistence length, i.e. the average length of the straight sections along the lamella. To this end, an open-source program coded with MATLAB, FiberApp, was used to trace the lamellae in AFM images (Figure 3.4) and determine their coordinates and persistence length from the mean-squared end-to-end distance (MSED) between contour segments.[81,82]

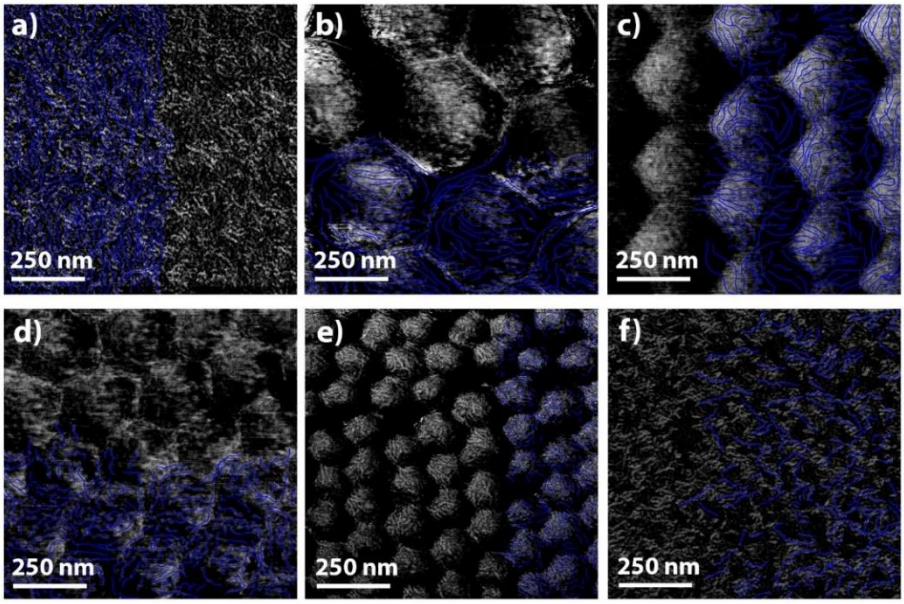

Figure 3.4. 1x1μm^2 AFM phase images of P3HT films on flat substrate (a) and on substrates having different curvatures: 0.00492 nm^{-1} (b), 0.00658 nm^{-1} (c), 0.00851 nm^{-1} (d), 0.0140 nm^{-1} (e) and 0.0400 nm^{-1} (f). The blue traces mark the exemplificative lamellar tracing for each image, used to determine the persistence length.

The projected length recorded (l_p) was then converted into the real one (l_{pr}) by taking into account the substrate curvature:

$$l_{pr} = \frac{\cos^{-1}\left(\frac{r-l_p}{r}\right)\cdot C}{2\pi} \qquad \textit{Equation 3.1}$$

where r is the particle radius and C is its circumference. It is not possible to determine the real persistence length for the polymer lamellae covering the substrate with the highest curvature (0.04 nm^{-1}), since, even before correction, the measured persistence length value was greater than the diameter of the nanoparticles.

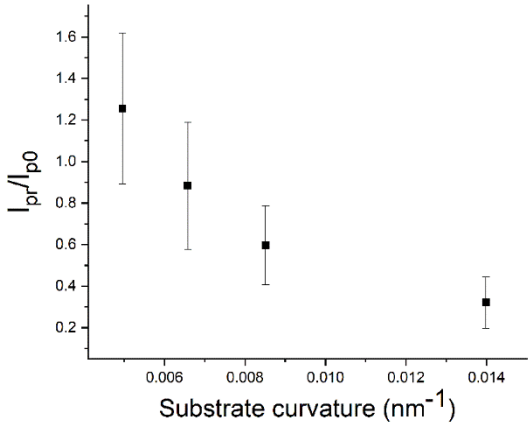

Figure 3.5. Real persistence lengths (l_{pr}) normalized to the persistence length measured on the flat substrate (l_{p0}). The data for 0.04 nm^{-1} are not reported (see text for explanation).

This suggests that the lamellae may lie on more than one particle, preventing an accurate curvature correction calculation. The so-obtained persistence length values, reported in Figure 3.5, show a systematic effect of the substrate nano-curvature, as the persistence length decreases with curvature. This progressive reduction may be due to the effective bending of the flexible polymeric lamellae that follow the surface nano-curvature. In order to shed more light into the influence of surface curvature on the polymer film structure, the P3HT films were characterized by GIXRD. It is known that P3HT lamellae, when confined in ultrathin films, adopt two orientations, edge-on and face-on (Figure 3.6), where the orientations are defined in terms of the lamellar stacking direction with respect to the substrate plane leading to two distinct diffraction patterns. In particular, the face-on orientation (Figure 3.6 a) is characterized by the lamellar stacking parallel to the surface plane, with a diffraction peak (100) along the q_{xy} direction and a (020) signal, associated to the π-stacking, along q_z direction. Conversely, in the edge-on orientation (Figure 3.6 b) the lamellar stacking direction is perpendicular to the substrate, leading to a (100) signal along the q_z direction while the π-stacking (020) signal is detected along the q_{xy} direction.

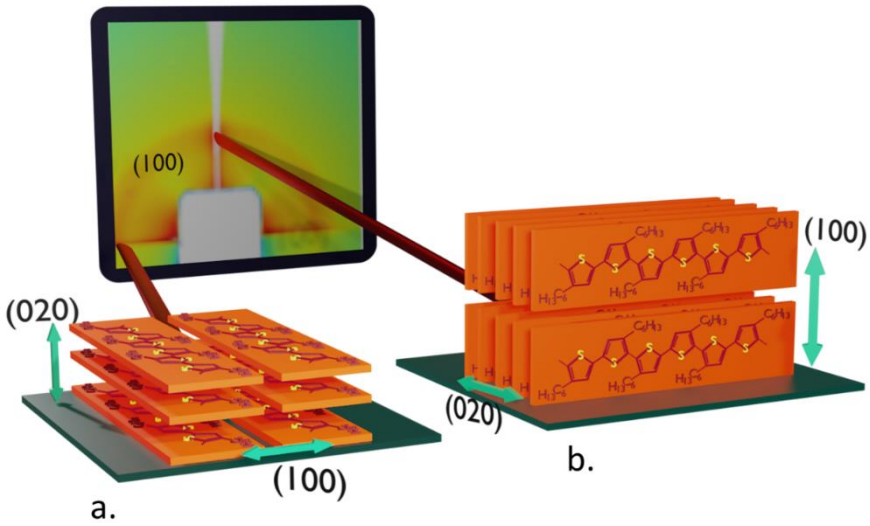

Figure 3.6. Schematic illustration of the two crystalline orientations and of the correspondent diffraction signals. Lamellar stacking parallel to the substrate plane, typical of the face-on orientation, generates the (100) diffraction signal in-plane (a). Edge-on orientation, characterized by the lamellar stacking perpendicular to the substrate plane, leads to a (100) diffraction signal out-of-plane (b).

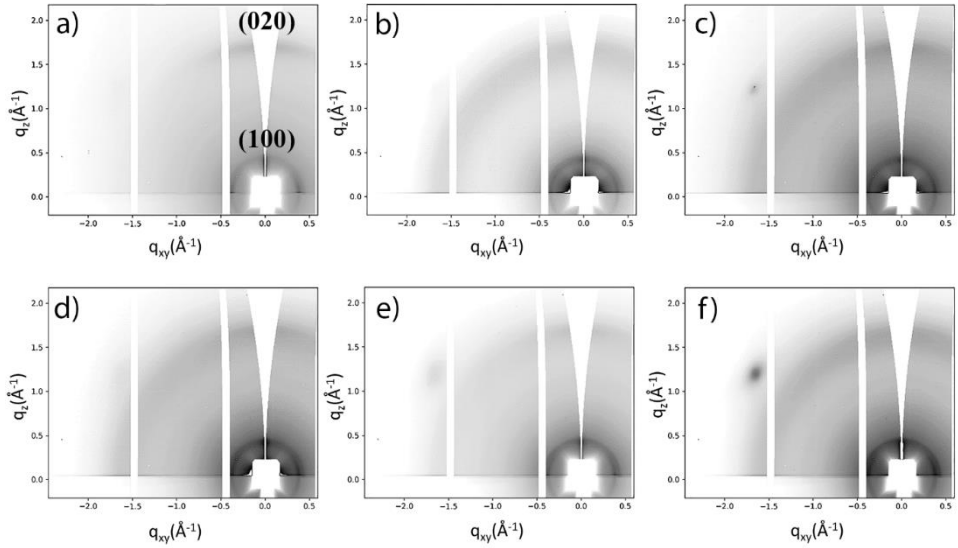

Figure 3.7. 2D GIXRD patterns of P3HT on flat substrates (a) and on substrates with different curvatures: 0.00492 nm^{-1} (b), 0.00658 nm^{-1} (c), 0.00851 nm^{-1} (d), 0.0140 nm^{-1} (e) and 0.0400 nm^{-1} (f).

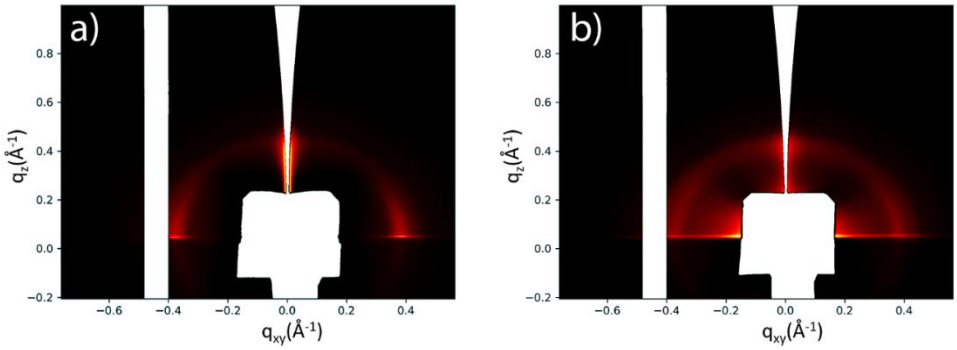

Figure 3.8. Contrast-enhanced 2D GIXRD pattern of P3HT on flat substrates (a) and on substrates having a nano-curvature of 0.00851 nm^{-1} (b). The intensity scale of the two patterns is identical.

Figure 3.7 shows the 2D GIXRD patterns recorded for flat and nano-curved substrates, with two prominent peaks or rings for all substrates, corresponding to (100) Bragg peak at approximately 0.45Å^{-1} and the (020) at approximately 1.70 Å^{-1}. As shown in Figure 3.7, differences appear in the diffractogram recorded from P3HT on nano-curved and flat substrates. In particular, while samples deposited on flat substrates exhibit higher intensity along the q_{xy} and q_z direction, rings of uniform intensity are observed on the nano-curved substrates for both (100) and (020) signals. This difference between flat and nano-curved substrates is even more evident in Figure 3.8, where the contrast between the (100) signal and the background is maximized, to enhance the difference between the peaks observed on flat substrates and the ring observed on substrates with a nano-curvature of 0.00851nm^{-1}. These results suggest that the rapid solvent evaporation leads to the formation of crystals that adhere with one of their crystallographic faces to the curved portion of the substrates. At the same time, with respect to the macroscopic silicon wafer substrate plane, this adhesion leads to a random orientational distribution for the nano-curved substrates and a predominant edge-on and face-on orientation for the flat ones. By extracting 1D profiles from 2D patterns[33] along q_{xy} direction at $\beta = 0°$ as well as along the q_z direction at $\beta \approx 90°$ (due to the Ewald sphere curvature, the determination of the intensity exactly along the normal to the substrate surface is not possible since the intensity at $\beta=90°$ is zero) and at $\beta = 45°$, reported respectively as blue, red and yellow lines in Figure 3.9 a, it is possible to obtain semi-quantitative information on the nano-curvature induced orientational randomization. In particular, the nano-curvature induced randomization was related to the variation of the ratio of the other than edge-on crystalline orientations with respect to the overall

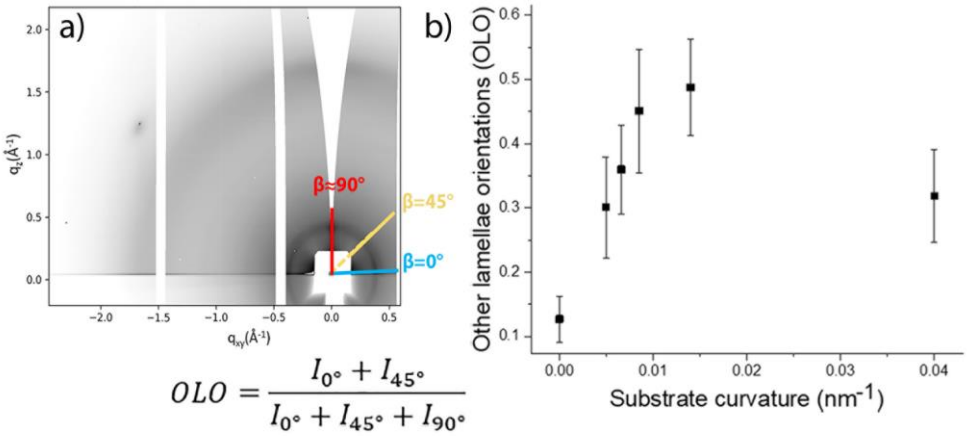

Figure 3.9. Schematic representation of the cut directions for the extraction of 1D profiles from the 2D GIXRD pattern (a). Other than edge-on lamellar orientation ratio as a function of surface curvature (b). The ratio was obtained using the equation under the diffraction pattern, where I is the intensity, determined by the fit area of the peak reported in the 1D profiles (see Appendix).

crystalline fraction (OLO) by employing the equation in Figure 3.9, where peak intensities were extracted from Lorentzian fit along the line cut directions.

As it is shown in Figure 3.9 b, while on flat substrates about 90% of the crystalline fraction adopts an edge-on orientation, the increase of surface curvature, due to the conformal adhesion of polymeric lamellae on nano-curved portions of the substrate, leads to a significant increase of the other than edge-on orientations.

This variation of the lamellae orientations has to be considered with respect to an ideal baseline of a flat substrate, in which the lamellae adhere to the particles on both edge-on and face-on, as schematized in Figure 3.10.

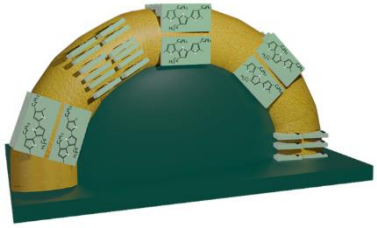

Figure 3.10. Schematic picture of the conformal adhesion of the polymeric lamellae on the nano-curved surface, leading to the progressively changing orientation of both face-on and edge-on lamellae with respect to the substrate baseline (The figure is not scaled, and it does not represent the actual arrangement of lamellae on nano-curved substrates).

Accordingly, the lamellae can be seen as a brick placed on a horizontal and on a sloped plane. In both cases, the brick longest axis may arrange parallel or perpendicular to the surface plane but, with respect to the baseline, its orientations will appear different. In particular, while the orientations assumed in the horizontal plane coincide with those observed along the baseline, in the case of the sloped plane, the angle between the plane and the baseline affects the brick orientation. As a sphere adopts any angles with respect to the horizontal plane where it lays, bricks placed on a spherical surface will adopt random orientation with respect to the baseline. It is worth noting that the decrease of the edge-on fraction is enhanced by the substrate nano-curvature up to 0.014 nm^{-1}, while it is less marked for the 0.04 nm^{-1} nano-curvature, where the thickness of the P3HT film exceeds the diameter of the particles, thus weakening the bending effect on the lamellae. Furthermore, the increasing randomization with curvature can be observed in a curvature range where the particle radii and lamellar lengths are comparable, leading to a degree of lamellar bending which is inversely proportional to the particle radius. In other words, if the curvature is not comparable to the lamellar length, the randomization becomes insensitive to the curvature, for substrates with low curvature, or negligible if the curvature is very high. Thus, it seems that, in order to prompt the control of the orientational randomization, it is necessary to correctly choose the curvature of the substrate. Since the correlation between the microstructure and the electrical properties of conjugated polymers thin films of is widely known, although not yet fully clarified, it is expected that the film conductivity is also affected by nano-curvature. In particular, a dark conductivity of about 10^{-6} S cm^{-1} is measured for the regio-regular P3HT on flat substrates, consistent with literature values for un-doped thin films.[83] The presence of surface curvature, on the other hand, involves an conductivity increase and consequently a ten-fold reduction in electrical resistance, proportionally to the surface curvature increase, as shown in Figure 3.11 a (red circles). In order to confirm that this conductivity variation is related to changes of lamellar orientation and persistence length, the same electrical characterization was performed on regio-random P3HT films deposited on nano-curved substrates.

Unlike regio-regular P3HT, regio-random conductivity does not depend on the substrate nano-curvature. As regio-random P3HT cannot assemble into crystals, these results unambiguously prove that the electrical properties of the undoped conjugated polymer are strongly affected by the lamellae orientation and the conductivity can be modulated by tuning the nano-curvature. Furthermore, a linear relationship between the fractions of other-than-edge-on crystal orientation and the electrical resistivity is shown in Figure 3.11 b, further underlining the extremely complex effect of 3D conjugated polymer structure on electrical properties.

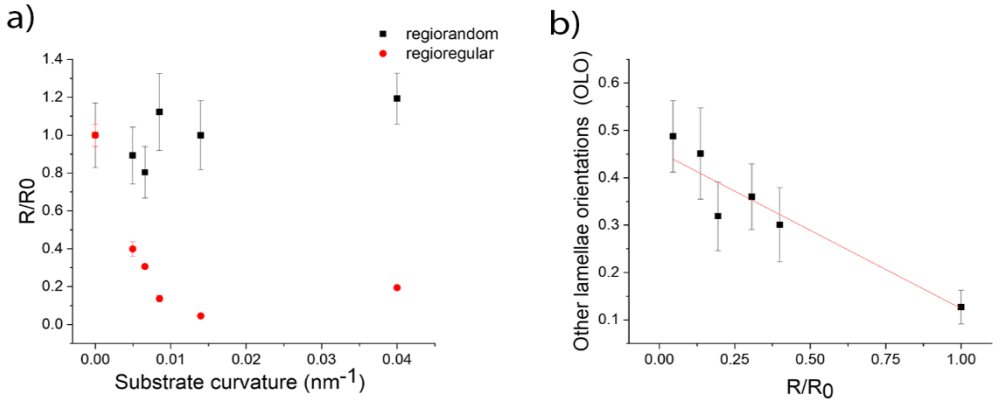

Figure 3.11. Relative resistance of regio-regular (red) and regio-random (black) P3HT thin films on flat and on nano-curved substrates (a). Correlation between P3HT crystal orientation and normalized conductivity (b).

The low conductivity of regio-random neutral P3HT films, about two orders of magnitude smaller than the regio-regular ones,[83] can be explained in terms of lack of of π-stacking interactions in amorphous P3HT assemblies, thus involving structural characteristics of the lamellae in the 3D arrangement. The so-obtained results show that the spatial orientation of the crystalline domains also plays a critical role with respect to dark conductivity.

The results obtained are consistent with literature. In particular, since the presence of grain boundaries constitutes high energy barriers for charge transport, several scientific results hypothesize transport across the grains is facilitated by the creation of percolation paths.[45,44,84] The results here presented support other literature reports in which higher conductivities are recorded for polymeric devices characterized by short-range intermolecular aggregates rather than by long-range crystallinity.[53] Hence the prevailing hypothesis is that it is the ability to adapt to the disorder rather than to attain the perfect order that promotes charge transport.[26]

Consequently, the dependence of the electrical properties on the lamellar orientation, as well as the conductivity increase with the surface nano-curvature, can be related to the higher probability of creating efficient percolation pathways between the randomly oriented domains, compared to the aligned but separated lamellae, as suggested by Zozoulenko et al.[85] The obtained results support this model, by hypothesizing that the substrate curvature facilitates efficient percolative pathways, thanks to the randomly oriented crystals, in which the loosely aligned chains act as bridges between adjacent lamellae. This effect varies with the curvature, underlining,

once more, the importance of controlling the film structure and morphology. Therefore, it could be used to finely modulate the polymer conductivity or even to pattern the film conductivity by spatially modulating the substrate curvature.

3.2) Distortion of P3HT lamellae

Although spin coated P3HT thin films of P3HT homogeneously cover the surface, the rapid evaporation of the solvent leads to the formation of out-of-equilibrium crystalline structure with low crystallinity.[86] Therefore, in order to improve the crystalline quality, polymer films are usually annealed. One of the most common annealing procedure implies the heating of P3HT films above its melting temperature, as upon exposure to a thermal gradient, the polymer chains acquire mobility and reorganize themselves to approach the most thermodynamically favoured crystalline state.[28,87] To this end, P3HT films on substrates with different curvature were subjected to thermal annealing and then characterized by GIXRD synchrotron radiation. 2D diffraction patterns recorded for films on flat substrates, before and after the thermal treatment, are reported in Figure 3.12. The appearance of higher order peaks, namely (200) and (300), confirms that thermal annealing increases the crystalline fraction of P3HT films. Moreover, although before the treatment signals originated by both face-on and edge-on lamellar orientations appear, Figure 3.12 a, in the annealed film the intensity of the lamellar stacking decreases along the q_{xy} direction and increases along q_z. This suggests a predominance of the edge-on lamellar orientation, as also confirmed by the presence of the (020) peak along the q_{xy} direction, due to in-plane π-stacking. The results are in agreement with literature, where several reports show a preference for the edge-on orientation after treatment, since annealing guides the system to reorganize itself in the lower free energy state.[88]

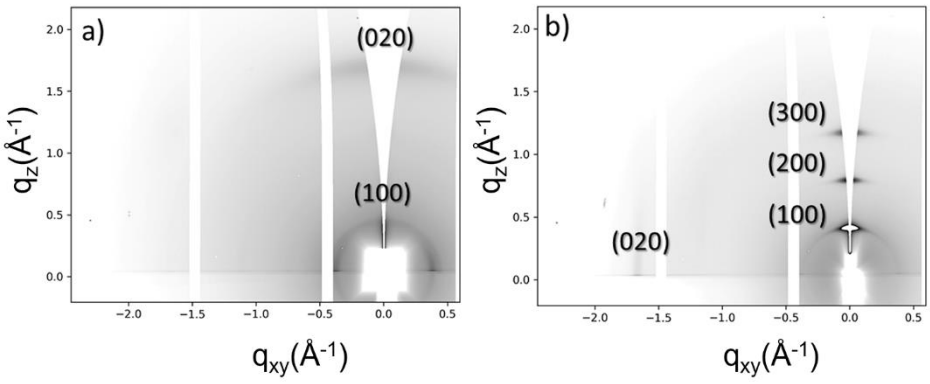

Figure 3.12. 2D GIXRD pattern of P3HT on flat substrates before(a) and after (b) thermal annealing.

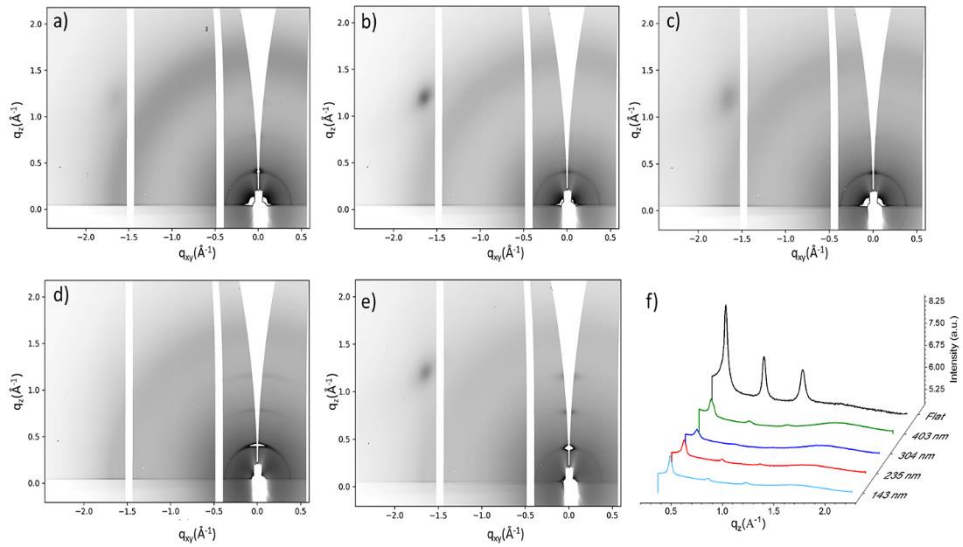

Figure 3.13. 2D GIXRD pattern of P3HT after thermal annealing, on substrates having different curvature: 0.00492 nm^{-1} (a), 0.00658 nm^{-1} (b), 0.00851 nm^{-1} (c), 0.0140 nm^{-1} (d) and 0.0400 nm^{-1} (e). 1D profiles, extracted from 2D patterns along q_z direction (f).

Unlike the flat substrate, on the nano-curved ones even after thermal annealing, a ring appears in the 2D diffraction patterns (Figure 3.13) corresponding to the Bragg peaks (100) at about 0.45 Å^{-1} and (020) at about 1.70 Å^{-1} with weak signals associated with the higher orders (200) and (300), as it can be seen from the 1D profile (Figure 3.13 f) extracted along the q_z direction of the 2D pattern. From the comparison of the out of plane 1D profiles for each curvature (Figure 3.14), before and after the treatment, the change of the polymeric film structure is evident: the peaks appear narrower and more intense. What observed indicates an increase of the crystalline quality since thermal annealing causes the lateral growth of crystallites with the incorporation of new chains.[28,89] By performing a Lorentzian fit after the annealing of the 1D profiles shown in Figure 3.14, it is possible to obtain semi-quantitative information regarding the crystalline quality and how it varies following heat treatment. From the width of the peak at half height (w) of the diffraction peak, it is possible to determine the out of plane correlation length, i.e. the average size of the ordered domains, $\frac{2\pi}{w}$.

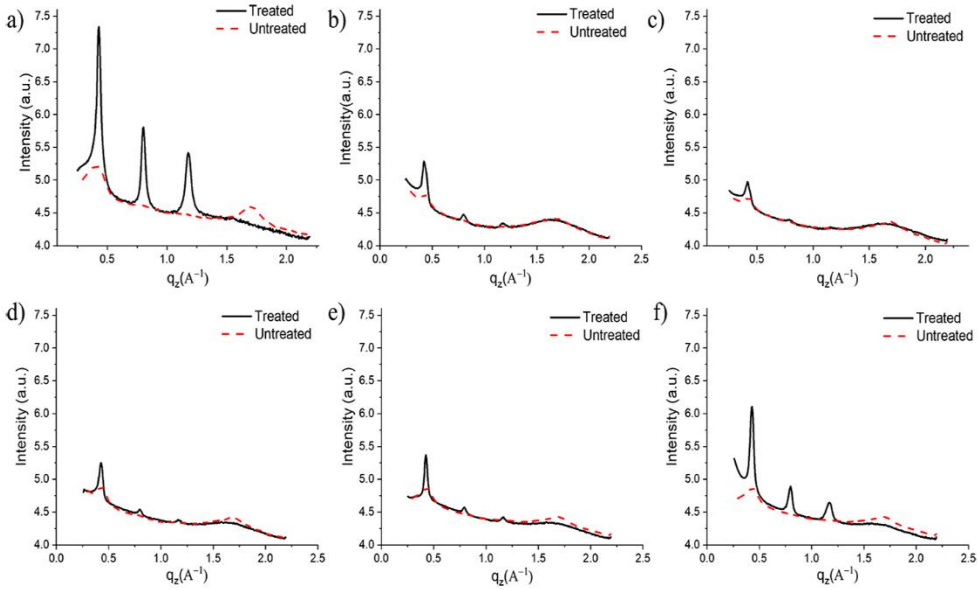

Figure 3.14. 1D profiles, extracted from 2D patterns along the q_z direction before thermal annealing (red dashed line) and after annealing (black line) on flat substrate (a) and on substrates having different curvature: 0.00492 nm^{-1} (b), 0.00658 nm^{-1} (c), 0.00851 nm^{-1} (d), 0.0140 nm^{-1} (e) and 0.0400 nm^{-1} (f).

The data obtained are reported in Figure 3.15 a showing, contrary to the as-deposited P3HT films, a dependence on the surface curvature. This difference is attributable to the fact that in the absence of post-deposition treatment, the morphology of the thin film is not in equilibrium; the crystalline nuclei present were formed during the rapid evaporation of the solvent and are in a kinetically trapped state that does not allow their growth.[55,90] This leads to the formation of small crystalline domains with random orientations, whose dimensions do not depend on the surface curvature. On the contrary, the thermal treatment provides enough energy for the polymer film to reorganize.[55] Therefore, the growth of crystalline nuclei is favoured, leading to the formation of crystalline domains whose size depends on the geometric strains induced by the surface curvature. In particular, from the results reported in Figure 3.15.a, the increase of surface curvature is accompanied by a reduction of the domains size, with a threshold curvature value of 0.0085 nm^{-1}. Further increase of the surface curvature leads to the formation of domains with dimensions comparable to the flat substrate case and, therefore, the dependence on the surface curvature is lost.

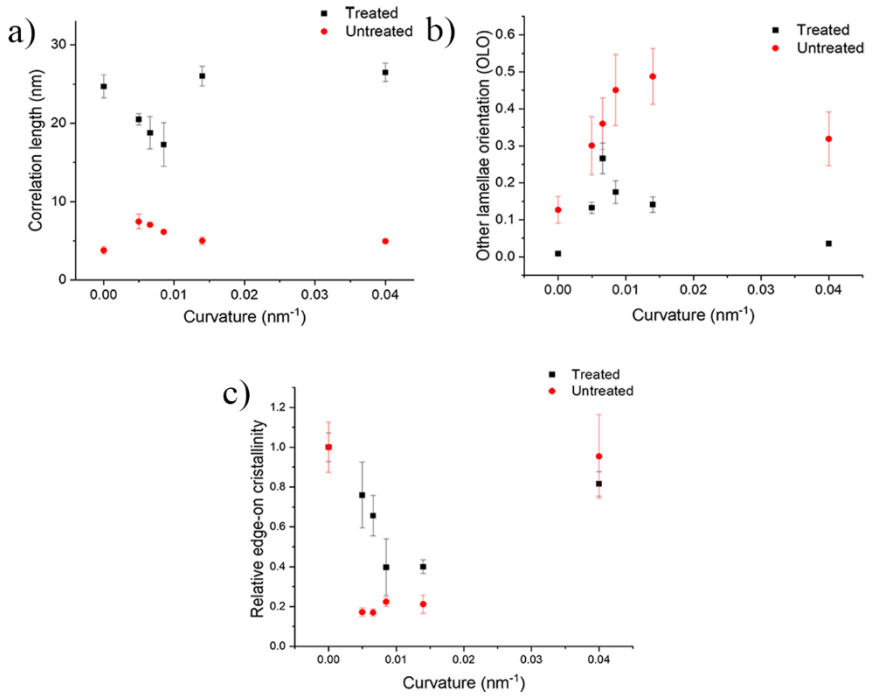

Figure 3.15. Comparison of correlation length (a), other than edge-on lamellar orientation ratio (b) and relative edge-on crystallinity (c) reported as a function of the surface curvature for unannealed (red) and annealed (back) P3HT films.

An overall view of the organization of the crystalline domains is shown in Figure 3.15 b, where the lamellar orientations different from the edge - on are reported. As for the unannealed films, the OLO was determined using the equation shown in Figure 3.9, i.e. by normalizing the intensity of the Bragg peak (100) at $\beta = 0°$ and $\beta = 45°$ with respect the total intensities i.e. the peak intensity at $\beta = 0°$, $\beta = 45°$ and $\beta \approx 90°$. The obtained results show how, while in the case of as-deposited P3HT films it is possible to observe a significant percentage of OLO as a function of the surface curvature, after annealing this dependence is lost. In particular, the percentage of OLO on nano-curved substrates after thermal treatment is only about 15% regardless of the substrate curvature. It is evident that the randomization dependence on the surface curvature which clearly characterizes unannealed P3HT films is lost upon thermal treatment. Despite this, a ring is recorded in the 2D diffraction pattern, probably due to this 15% of lamellar orientations that differ from the preferred edge-on one. In order to better understand the effect induced by geometric strains following annealing in the polymer structure, the out-of-plane diffraction signals were further investigated, since, given the low percentage of OLO, the intensity of

Bragg peak is predominantly originated by edge-on lamellae. From the intensity of the out of the plane (100) Bragg peak recorded for curved substrates and normalized with respect to the flat one, it was possible to determine the relative variation of the edge-on crystallinity with the curvature. The results, reported in Figure 3.15 c, show a reduction of the crystallinity with the increase in surface curvature, with a threshold value at for 0.0085 nm^{-1} and a higher crystallinity at the highest substrate curvature. Interestingly, on untreated samples, on the other hand, the same significant reduction of relative crystallinity is observed regardless of the substrate curvature value. Therefore, the surface curvature influences the growth of the polymeric lamellae. The presence of larger domains and more abundant edge-on fractions at smaller curvatures could be caused by surfaces which are more similar to the flat ones, given both the lower curvature and the larger size of interstices between adjacent particles. This suggests that the growth of P3HT lamellae is preferred in the interstices between the particles, where they can adopt a preferential edge-on orientation. The increase in surface curvature, instead, causes the reduction of the interstice size with the consequent formation of smaller crystalline domains and the reduction of the crystalline fraction. In support of the above, the morphological analysis of P3HT annealed films deposited on substrates with different curvatures is reported in Figure 3.16.

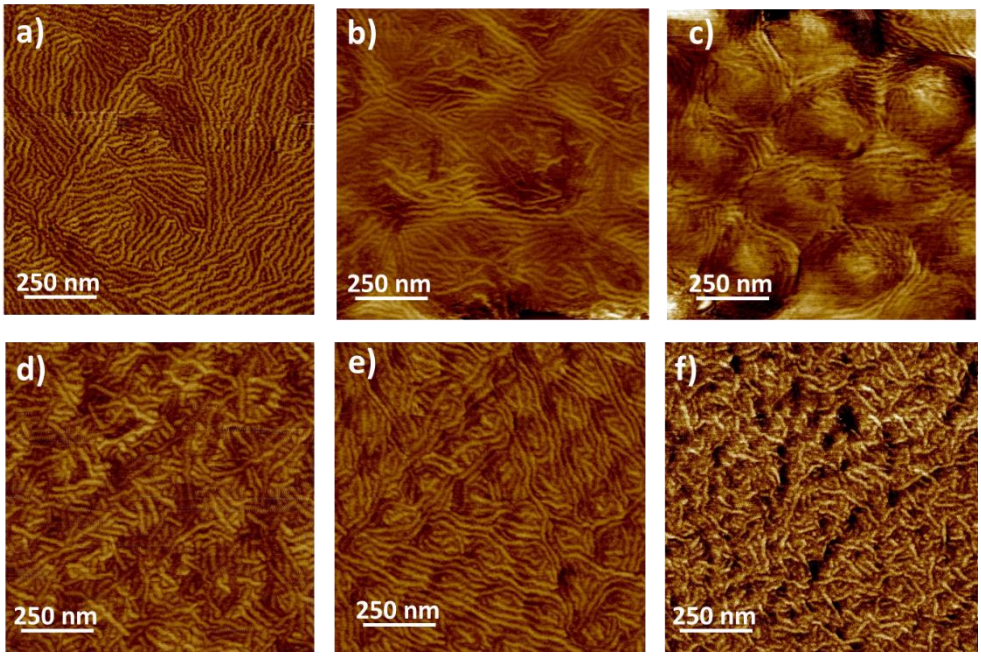

Figure 3.16. 1x1µm2 AFM phase images of annealed P3HT films deposited on flat substrates (a) and on substrates with different curvatures: 0.00492 nm^{-1} (b), 0.00658 nm^{-1} (c), 0.00851nm^{-1} (d), 0.0140 nm^{-1} (e) and 0.0400 nm^{-1} (f).

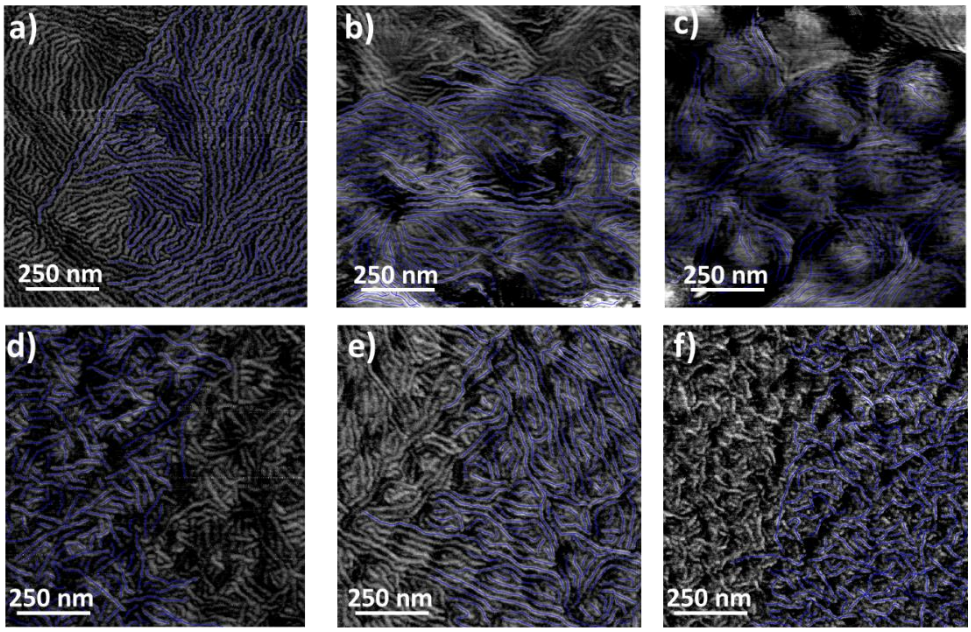

Figure 3.17. 1x1μm^2 AFM phase images of annealed P3HT films on flat substrate (a) and on substrates with different curvatures: 0.00492 nm^{-1} (b), 0.00658 nm^{-1} (c), 0.00851 nm^{-1} (d), 0.0140 nm^{-1} (e) and 0.0400 nm^{-1} (f). The blue traces mark the exemplificative lamellar tracing for each image, used to determine the persistence length.

The phase AFM images reported in Figure 3.16, show a variation of the length distribution of the polymeric lamellae, which seem to grow longer in the interstices between the particles and shorter in the curved portions. This effect varies with the surface curvature and in particular, at 0.00851 nm^{-1} (Figure 3.16 d) shorter lamellae that homogeneously cover the surface are observed, while at greater curvatures the covering is given by longer lamellae, with a behaviour similar to flat substrates.

Tracing the lamellae (Figure 3.17) observed on the phase images, by means FiberApp, allows to determine the length distribution by recording, as shown in Figure 3.18, the variation of tail distribution as the surface curvature increases.

Figure 3.18 shows the lamellae length distribution as a function of the surface curvature where the contour length represents the lengths of the lamellae traced in the AFM phase image, while the number of traced lamellae with that given length is shown on the y axis.

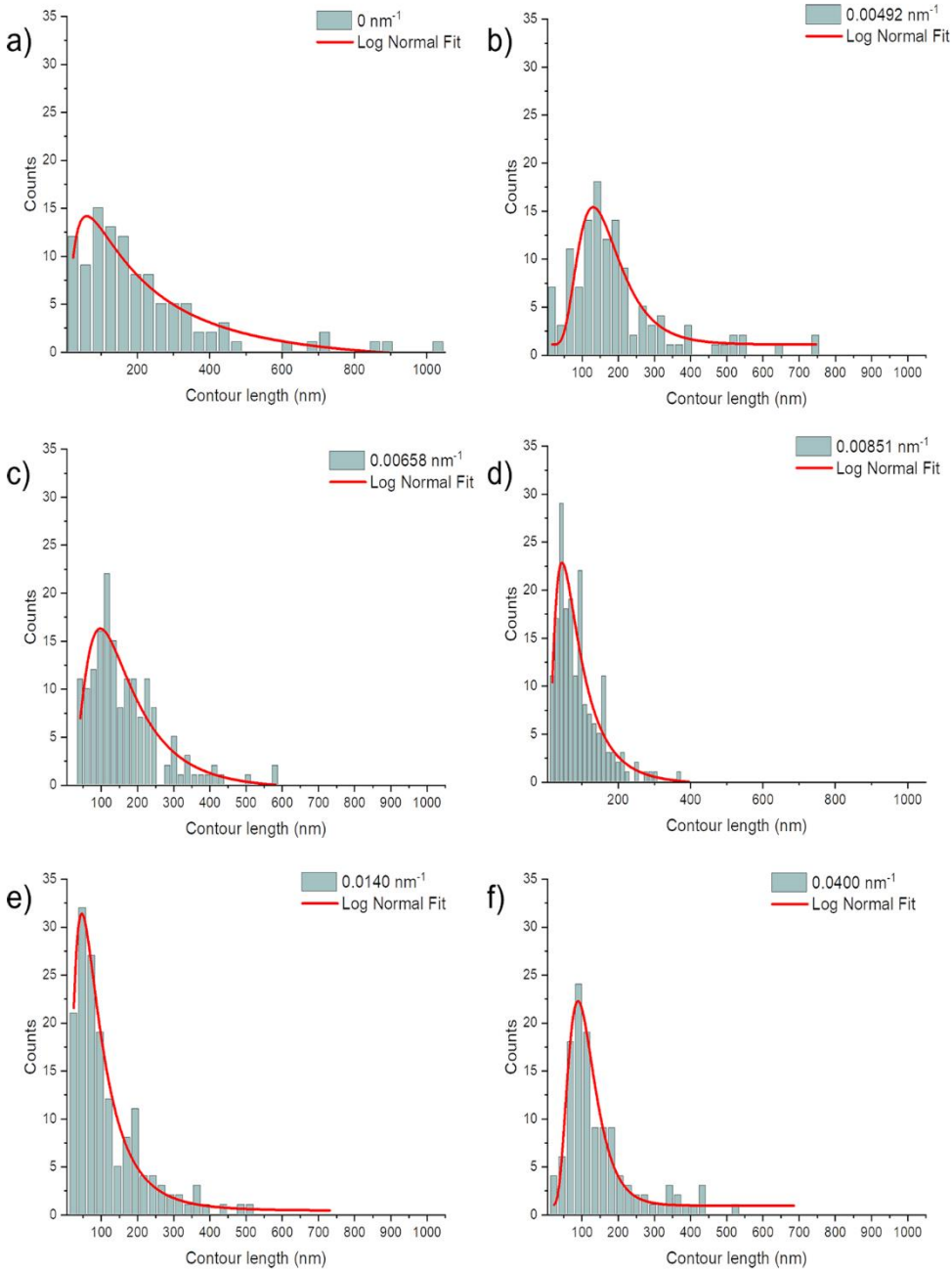

Figure 3.18. Lamellae length distribution, after annealing, on flat substrate (a) and on substrates with different curvatures: 0.00492 nm^{-1} (b), 0.00658 nm^{-1} (c), 0.00851 nm^{-1} (d), 0.0140 nm^{-1} (e) and 0.0400 nm^{-1} (f). The red lines represent the log-normal fit of the distributions.

From the length distribution it is possible to obtain information about the nucleation and growth of polymeric lamellae. The trends shown in Figure 3.18 for the different surface curvatures present a log-normal distribution of the length density function; therefore, from the log-normal fit of the histograms shown in Figure 3.18, additional information can be obtained on the distribution of polymer lengths as a function of surface curvature:

$$y = \frac{A}{\sqrt{2\pi}\sigma L} e^{\frac{-(\ln L-\mu)^2}{2\sigma^2}} \qquad \textit{Equation 3.5}$$

where L is the total length, μ and σ are the mean value and the standard deviation of the length natural logarithm, respectively, and A is a normalizing constant. From the trends obtained (Figure 3.18, red lines), it is evident how the surface curvature influences the distribution of the lamellar lengths. The curvature increases results in a shift of the maximum distribution to smaller lengths, with a threshold value for substrates with curvatures of 0.00851 nm^{-1}. At the same time, it is possible to observe a variation in the width of the distribution, which appears much narrower at higher curvatures. The above could indicate a variation of the nucleation and growth process induced by surface curvature, assuming a dual nucleation and growth mechanism. That is, while the curved portion of the surface could favour the nucleation process at the expense of the growth, thus leading to the formation of shorter lamellae, the flat portions of the surface, i.e. the interstices between the particles, could favour the growth of crystalline nuclei, causing, consequently, the formation of longer polymeric lamellae. In support of the above, the AFM phase images, shown in Figure 3.16, evidence the presence of long polymeric lamellae in the interstices between the particles while shorter lamellae are observed at the top of the particles. Given that the geometry of the substrate influences the growth of polymeric crystals, we may expect a variation of the length distribution with the increase of surface curvature. In particular, the increase of curvature favours the nucleation process at the expense of growth. This is attributable to the reduction of the flat portions of the surface in which crystalline growth is favoured. In fact, as is evident in Figure 3.18, the increase of curvature is accompanied by an increase of the fraction of shorter lamellae while the length of the distribution tail is reduced, with a curvature threshold value equal to 0.00851 nm^{-1}. On the other hand, further increases of the surface curvature result in an increase in the distribution tail (Figure 3.18 e-f), with the consequent formation of long polymeric lamellae, as it appears evident in Figure 3.16 e-f. At the same time, a narrower distribution of the polymeric crystal length is recorded, with a shift of the maximum towards longer contour lengths.

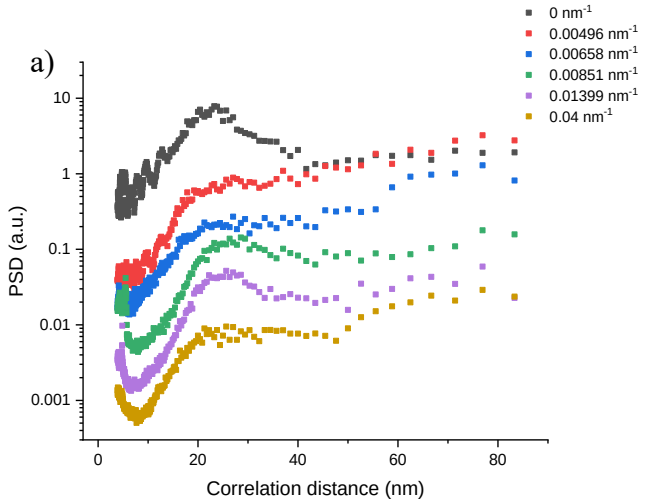

Curvature (nm^{-1})	Lamellar Thickness
0	23 ± 0.1
0.00496	28 ± 0.9
0.00658	27 ± 0.7
0.00851	27 ± 0.3
0.01399	26 ± 0.2
0.04	26 ± 0.6

Table 3.1

Figure 3.19. Power spectral density (PSD) distributions of lamellar thickness of P3HT thin film on substrates having different curvature (a). By carrying out a Gaussian fit of the peak that appears in Figure a, the lamellar thicknesses were determined as a function of the various surface curvatures, the values of which are reported in Table 3.1.

Despite the distribution shift and the presence of longer polymeric lamellae observed for the threshold curvature, the lamellar morphology differs from the flat case, indicating that the geometry of the substrate influences, albeit in part, the polymeric growth. Given that the surface curvature affects the lamellar growth, as well as their orientation, it is reasonable to expect the effects of the curvature also in the folding of the chain and, therefore, in the lamellar thickness. To this end, the analysis of the power spectral density (PSD) was conducted on the AFM phase images. This analysis allows to convert the AFM images in the frequency domain, through a Fourier transform, and to identify the characteristic wavelengths corresponding to the most frequent morphological features.[91] In particular, PSD allows to determine the correlation length associated to the lateral distribution of the surface peaks, thus identifying the periodic surface characteristics at which, for the present case, correspond to the apparent lamellar width which is given by the folding period of the chain.[91,92] From the results reported in Figure 3.19 semiquantitative information was obtained by carrying out a Gaussian fit of the curves, and the peak position was interpreted as the most probable lamellar thickness (Table 3.1 in Figure 3.19). Contrary to what expected, no significant variations in lamellar thickness with curvature were observed. Although a shift is identified in terms of the peak position between the flat and nano-curved substrate (Figure 3.19), the different degree of curvature does not allow to appreciate any variations of the lamellar thickness.

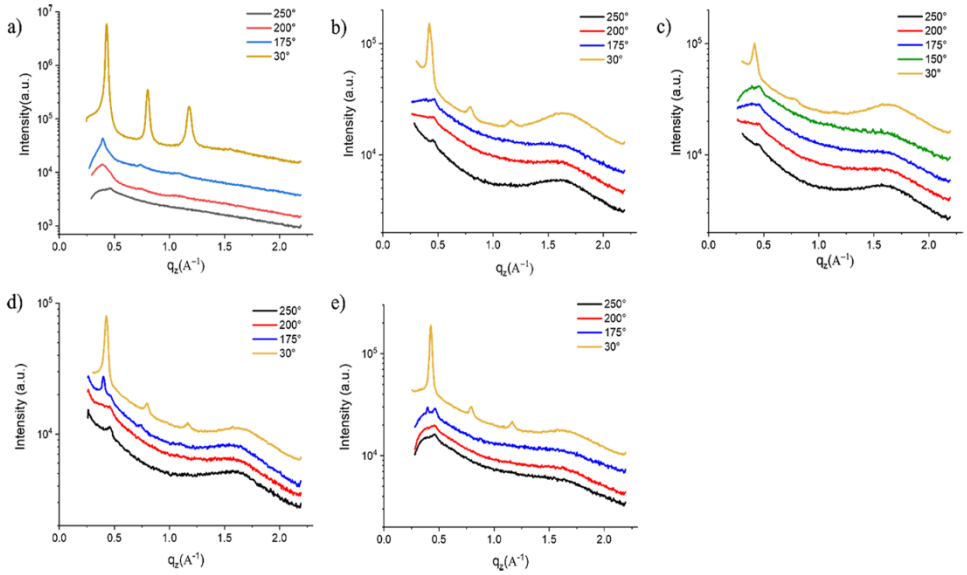

Figure 3.20. Comparison between out of plane diffractograms of P3HT in-situ thermal annealing on flat substrate (a) and on substrates with different curvatures: 0.00492 nm^{-1} (b), 0.00658 nm^{-1} (c), 0.00851 nm^{-1} (d), 0.0140 nm^{-1} (e).

To shed more light on how surface curvature affects the growth of polymer lamellae, an in-situ GIXRD structural characterization was conducted during thermal annealing. In particular, the crystallization of the polymer film was investigated after melting at 250°C for 30 minutes in vacuum, monitoring the temperature at which the Bragg peak appears. Figure 3.20 shows the out of plane diffractograms of P3HT recorded during cooling on substrates with a curvature ranging from 0.0049 to 0.0139 nm^{-1}. In-situ structural characterization was not conducted for substrates with a curvature of 0.04 nm^{-1}, since the influence of surface geometry on the polymer assembly is less marked than in the cases of substrates with lower curvatures. By comparing the evolution of the diffractograms shown in Figure 3.20, it is evident how the curvature affects the crystallization temperature. In particular, while for flat surfaces the peak appears at 200°C (Figure 3.20 a), in agreement with previous reports,[93] on curved substrates the onset of crystallization occurs at lower temperatures. This result reveals that curvature does not only influence the overall crystalline fraction and orientation, but it also affects the lamellar structure itself. As a matter of fact, the other structural parameters which may justify a decrease of the melting temperature is lamellar thickness;[94] as it is known that thinner lamellae are

characterized by lower melting temperatures. However, PSD analysis does not show any thickness reduction with curvature therefore, the lowering of melting temperature must be related to the strain induced by the curvature on the lamellar structure. In particular, the conformal surface coverage implies the adhesion of lamellae on the curved portions of the substrate. As the curvature is comparable to the lamellar size, it forces the growth of distorted crystals, with a consequent reduction of the enthalpy of crystallization and of the melting temperature. The reduction in melting temperature in the presence of distorted crystals was already observed by Ahmed et al. who hypothesized a softer nature of the distorted portions, which favours the onset of melting and, as a consequence, the reduction of the melting temperature.[95] They correlated the reduction of the melting point to the structure of the film, by associating the crystalline distortion to a variation of the defect concentration, with both an increase of Gibbs free energy and molar entropy, due to the variations induced by the lattice parameters, and an increase of grain boundary effects, also considered sort of defects.[95] The reduction of particle size and, therefore, the increase of surface curvature should lead to an increase of defects concentration, such as grain boundaries, with effects that should have repercussions on the crystalline structure and in particular on the distortion of the polymer lamellae. However, from the analyses conducted, it is not possible to extract quantitative information that allows us to appreciate variations of the degree of distortion as a function of surface curvature. Additional information could be obtained by combining the structural effects induced by surface curvature with SFE. The introduction of energetic factors involves a further study of thermodynamic factors, and, in particular, of the interface free energy, in the molecular assembly as they influence the molecular mobility of the polymer chains and, consequently, the polymer crystallization.[92]

The possibility of correlating the different mobility of the polymer chains, as a function of the energetic effects, with the lamellar distortion induced by the curvature, could provide the possibility to shed more light on how the substrate geometry can influence the crystallization of the polymer film. A greater understanding of these factors could pave the way towards obtaining the desired crystalline structures by simply controlling the morphology and energy associated to the substrates.

4) SFE Modulation

It has been observed, both theoretically[96] and experimentally,[97,98] that the nature of the substrate strongly influences the mobility of the chains and, consequently, the crystals orientation. In the presence of repulsive interactions with the substrate, the mobility of the chains increases and favours the formation of edge-on crystals,[96] vice versa, flat-on growth is favoured.[96] This phenomenon can be interpreted in terms of interface free energy between the substrate and the polymer. In particular, on low-interface energy, the high molecular mobility leads to the formation of polymeric crystals parallel to the substrate plane and well packed together.[92,29] Conversely, at high interface free energy, the molecular mobility is reduced, the crystallization process is less efficient and leads to the formation of poorly oriented crystals both with respect to the substrate plane and reciprocally. [29,92] The experiments carried out so far have concerned only flat substrates, however interesting information could be obtained by studying the combined effect of substrate nano-curvature and SFE. While the characterization of wettability as a function of nanostructure was extensively studied for substrates with constant SFE and curvature,[65,66] very little is known about nanostructured substrates with different SFE and curvature.[24,99] In this perspective, substrates with different curvature investigated in previous chapters were used and their interfacial properties were modulated by means of suitable surface functionalization processes. The systematic variation of the SFE makes it possible to understand the combined role of interfacial interactions and substrate nano-curvature on the self-assembly of polymeric thin films. In fact, for flat substrates, the efficient spreading of the polymer on the substrate increases the mobility of the chains and leads to the formation of crystals parallel to the substrate plane and better ordered.[92] For curved surfaces, it is necessary to understand how the mobility of the chains and the diffusion of the polymer are affected by the morphology and surface energy. In particular, it is hypothesized that to follow the surface morphology, the polymeric lamellae have to be an energetic gain as a function of substrate curvature, allowing an effective adhesion of the lamellae to the surface with consequent deformation in the structure.

4.1) SFE modulation with constant curvature

The morphological and structural study in the previous chapter identified a curvature threshold value of 0.008 nm^{-1}, where the geometric effects induced by the surface appear most marked. Therefore, this curvature value was used to study the modulation of the SFE and see how it affects the assembly and crystallization of P3HT.

4.1.1) Study of surface wettability

Curved substrates were made highly hydrophobic by means octadecyltrichlorosilane (OTS)-functionalization (See Appendix), as the self-assembly monolayer of OTS gives very apolar surfaces.[100] Wettability modulation was then obtained as a consequence of surfaces oxidation of the OTS layer by exposition of the hydrophobic substrate to Ar/O_2 radio frequency (RF) plasma. By varying the plasma treatment time, substrates with different SFE values were obtained.[101] Unlike flat surfaces, where it is possible to determine the SFE by means of contact angle measurements and by using the three-liquid model,[102] on nanostructured surfaces the liquid may undergo different wetting regimes, with the possible inclusion of air nanobubble. This may generate an apparent contact angle higher or lower than the corresponding flat case. As the wetting regime is not known a priori, it is not possible to determine the SFE with the three liquid model. In the assumption that the OTS coverage and the plasma oxidation are not affected by the substrate curvature, the SFE determination was carried out, via the three-liquid model (See Appendix), on flat substrates, simultaneously functionalized and treated with the nano-curved ones. From the results reported in Table 4.1, it was possible to modulate SFE within a range of 40 mN/m. Once the SFE is known, the wettability for curved and flat substrates can be compared as a function of the three different wetting liquids (Figure 4.1). It is evident that the apparent contact angle, that is, the contact angle measured on the nano-curved substrates, depends on both the SFE and the wetting liquid.

Treatment time (sec.)	*SFE (mN/m)*	γ^{LW} *(mN/m)*	γ^{+} *(mN/m)*	γ^{-} *(mN/m)*
0	21.95 ± 0.52	21.77 ± 0.36	0.04 ± 0.05	0.22 ± 0.1
1	24.79 ± 1.67	23.23 ± 0.77	0.59 ± 0.4	1.04 ± 0.46
2	37.41 ± 1.37	34.19 ± 0.31	0.18 ± 0.11	14.29 ± 0.6
3	41.61 ± 1.35	36.05 ± 0.26	0.42 ± 0.15	18.51 ± 0.78
5	51.34 ± 1.47	38.72 ± 0.12	1.32 ± 0.24	30.08 ± 1.09
10	58.7 ±2.05	38.89 ± 0.21	2.85 ± 0.48	34.41 ± 0.62
15	63.98 ± 0.94	39.33 ± 0.23	3.32 ± 0.15	45.67 ± 0.53

Table 4.1. SFE and the corresponding apolar (γ^{LW}), acid (γ^{+}) and basic (γ^{-}) components measured with the three liquids method on flat piranha-treated substrate (last row), on OTS-functionalized substrate (first row) and on plasma-treated OTS-functionalized substrates.

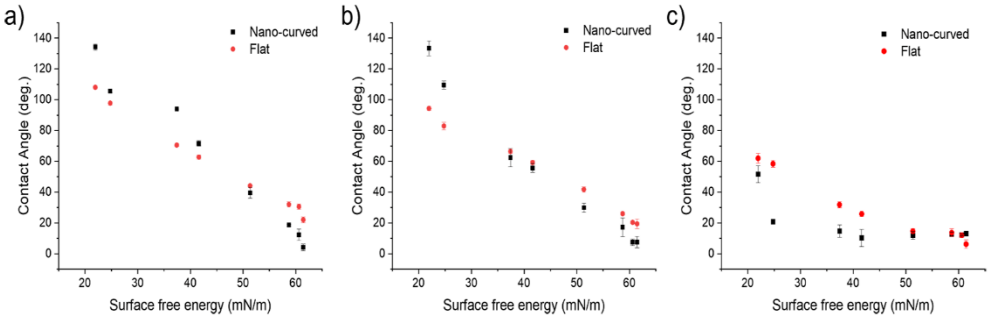

Figure 4.1. Contact angle of water (a), glycerol (b) and TCP (c) on nano-curved (black symbols) and flat (red symbols) substrates at various SFE. Water and glycerol display a wetting transition with contact angles on nano-curved substrates passing from higher to lower than the ones on the corresponding flat substrates.

If the wetting liquid is water or glycerol (Figure 4.1 a-b), the difference between the apparent contact angle and the corresponding contact angle measured on flat subtrates markedly varies with SFE. In particular, at low SFE nanostructured surfaces show apparent contact angles higher than the ones recorded on flat substrates with the same SFE. Vice versa, at high SFEs, contact angles on flat substrates are higher than apparent contact angles on nanostructured substrates. The TCP behaviour is different, as the apparent angles are always greater or at most equal to those recorded on flat substrates. The recorded wettability behaviour can be explained by considering two limit regimes that may occur on rough surfaces. In particular, the low surface wettability observed at low SFE resembles the Cassie-Baxter model, which assumes the formation of a composite interface where the liquid is in contact with both the structured substrate and the air bubbles trapped between the nanostructures. If ϑ is the ideal contact angle between the wetting liquid and the flat surface and f ($1 \leq f \leq 0$) is the fraction of the nanostructured surface where the solid and the liquid are in contact,[103,65] the apparent contact angle, ϑ_{CB}, is given by:

$$cos\vartheta_{CB} = f\ cos\vartheta - (1 - f) \qquad \textit{Equation 4.1}$$

On the contrary, the increased surface wettability recorded at high SFE agrees with the Wenzel model,[104] which considers a homogeneous wetting regime, with an apparent contact angle, ϑ_w, given by:

$$cos\vartheta_w = r\ cos\vartheta \qquad \textit{Equation 4.2}$$

where ϑ is the ideal contact angle formed by a liquid wetting a perfectly flat surface and r is the roughness ratio, defined as the ratio of the real area of the solid surface and the nominal area (r = 1 for purely flat surfaces and r >1 for rough surfaces).[104] Therefore, the increased wettability, that is, the lower contact angle, recorded at high SFE, indicates the increased contact area between the wetting liquid and the surface by a factor r. Usually, especially if $\theta < 90°$, $\theta_{CB} > \theta_W$[105] , with Wenzel apparent contact angles lower than those measured on flat substrates, due to increased contact surface. On the other hand, if the liquid conforms to the Cassie-Baxter model, the apparent recorded contact angles will be higher than the ones measured on the corresponding flat substrate.[105] Based on this evidence, the inversion of the wettability behaviour shown in Figure 4.1, i.e. a higher apparent contact angle at low SFEs and lower one at high SFEs with respect to the flat case, can be interpreted as a transition from Cassie-Baxter to Wenzel behaviour. This transition is not observed in Figure 4.1c, as the TCP always wets the surface homogeneously. However, at high SFEs higher contact angles are recorded for curved substrates than for flat ones, suggesting some not negligible repulsive components which may result from the interaction between a non-polar liquid and a strongly polar substrate. The observed transition from the Cassie-Baxter regime to Wenzel one can also be rationalized by taking into account, in addition to the substrate SFE, the interfacial free energy (IFE or γ_{LS}) between the wetting liquid and the substrate. IFE was experimentally determined, from flat surfaces, by using the combination rule Good-Girifalco-Fowkes[106] (See Appendix).

Treatment time (sec.)	*SFE (mN/m)*	$\gamma_{SL\ (H2O)}$ *(mN/m)*	$\gamma_{SL\ (Gly)}$ *(mN/m)*	$\gamma_{SL(TCP)}$ *(mN/m)*	S_{P3HT}
0	21.95 ± 0.52	51.31 ± 1.37	31.17 ± 1.45	2.94 ± 1.33	0.33 ± 4.46
1	24.79 ± 1.67	49.96 ± 1.38	29.46 ± 1.28	3.83 ± 1.28	3.11 ± 6.07
2	37.41 ± 1.37	49.68 ± 0.77	26.79 ± 0.50	3.43 ± 0.73	12.68 ± 4.00
3	41.61 ± 1.35	47.71 ± 0.69	24.45 ± 0.42	5.68 ± 0.65	14.72 ± 3.91
5	51.34 ± 1.47	41.31 ± 0.56	17.55 ± 0.28	12.61 ± 0.51	18.18 ± 3.89
10	58.7 ± 2.05	34.15 ± 0.55	10.36 ± 0.26	19.81 ± 0.51	19.55 ± 4.15
15	63.98 ± 1.17	32.49 ± 0.44	8.54 ± 0.14	21.68 ± 0.42	20.43 ± 2.82

Table 4.2. Interface free energy (γ_{SL}) calculated for the three different wetting liquids and P3HT spreading coefficient as a function of the substrate SFE.

The observed trend, reported in Table 4.2, allows us to relate the observed variations of the apparent contact angles to the interfacial free energy and it strengthens the hypothesis of a transition from Cassie-Baxter to Wenzel behaviour. In particular, a Cassie-Baxter regime is identified when SFE < IFE, as the wetting of the solid surface by the air is favoured with respect to the wetting by the liquid. Therefore, air bubbles are trapped. On the other hand, the increase of SFE makes the contact between liquid and solid more favourable than the one between the solid and air, in particular when SFE > IFE [105], this implies the transition to the Wenzel behaviour. These results represent the first report of a Cassie-Baxter to Wenzel transition induced by SFE modulation on nanostructured substrates.

4.1.2) P3HT crystallization on substrates with controlled nano-curvature and SFE

It is known that surface wettability and IFE affect the molecular mobility of polymeric thin films and consequently their crystallization on surfaces.[17,107,108,109] In this perspective, substrates with a curvature of $0.008 nm^{-1}$ were used to study how SFE modulation, combined with a geometric distortion induced by the substrate, affects the crystallization behaviour of P3HT thin films. Regardless of surface wettability, the P3HT film covers the substrate with a constant thickness, without altering the hexagonal packing of the silica nanoparticles, as confirmed by the AFM topographic images (Figure 4.2). While P3HT crystallization is not significantly affected by substrate SFE on flat substrates,[92] on nano-curved substrates the energetic factors affect the polymer assembly, leading to a non-homogeneous lamellar distribution with a strong dependence on the SFE.

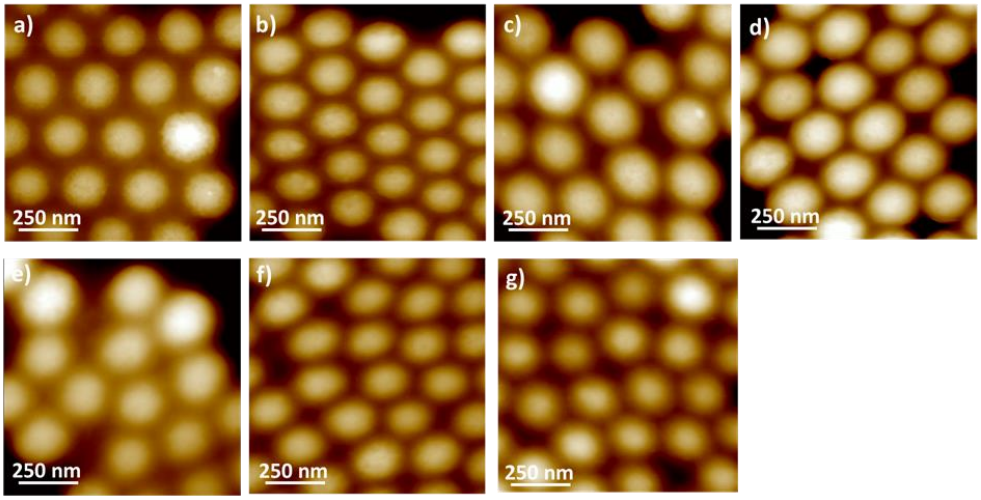

Figure 4.2. 1x1 μm^2 AFM height image of P3HT spin coated on nano-curved substrates with different SFE: 22 mN/m (a), 25 mN/m (b), 37mN/m (c), 42 mN/m (d), 51 mN/m (e), 58 mN/m (f), 64 mN/m (g).

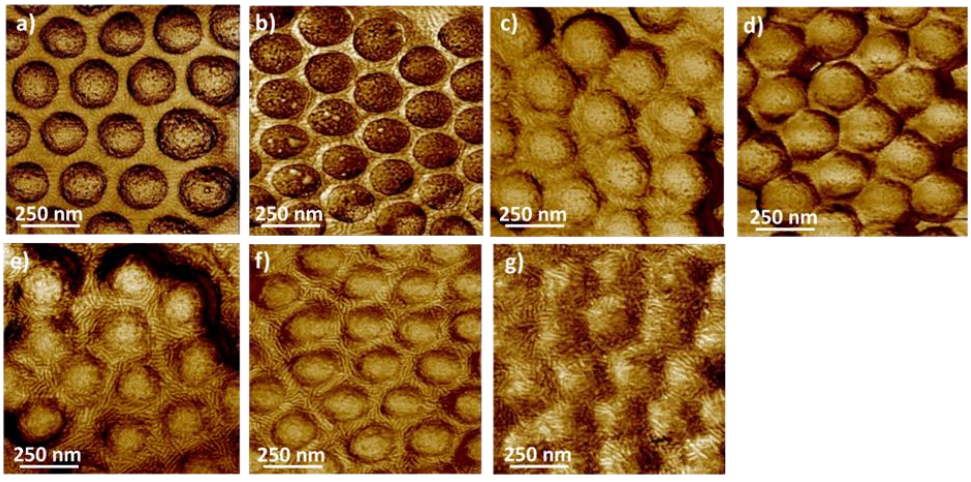

Figure 4.3. 1x1 μm^2 AFM phase image of P3HT films crystallized on 21.95 mN/m (a), 24.79 mN/m (b), 37.41 mN/m (c), 41.61 mN/m (d), 51.34 mN/m (e), 58.7 mN/m (f) and 63.98 mN/m (g) nano-curved substrates. By increasing SFE lamellae progressively cover the nano-curved portions of substrates.

As shown in figure 4.3, at low SFE P3HT crystallizes only in the interstices between the particles, (Figure 4.3a,b) forming short and straight lamellae. As the SFE increases, the lamellae begin to cover the curved portions of the substrates (Figure 4.3 c−f), to achieve an effective wetting with a homogeneous coverage of the

substrates with high SFE values (Figure 4.3 g). To better understand this behaviour, the spreading coefficient, S, was calculated:

$$S = SFE - \gamma_{SubP3HT} - \gamma_{P3HT} \qquad \textit{Equation 4.3}$$

where γ_{P3HT} is the P3HT SFE (21,7 mN/m with SFE components of γ^{LW} 21.4 ± 0.6 mN/m, γ^{+} 0.1 ± 0.1 mN/m, γ^{-} 1.1 ± 0.2 mN/m determined by contact angle measurements) and $\gamma_{SubP3HT}$ is the IFE between P3HT and solid substrates. Regardless of the SFE value, the spreading coefficient is always zero or positive, indicating the spontaneous wetting of P3HT of any substrates. Therefore, the spontaneous retraction of P3HT from the curved portion at low SFE can not be explained in terms of dewetting, nor in thickness variations induced by different crystallization degrees on nanostructured substrates, as the mass density difference between fully crystalline and fully amorphous P3HT is only 4%.[110] On the contrary, it is possible to attribute the observed behaviour to two driving forces that govern the crystallization process: SFE minimization and crystallization enthalpy maximization. These driving forces act toward two opposite directions and, if one of the two is markedly predominant with respect to the second one, the limit behaviours observed at on 21.95 mN/m and 63.98 mN/m occur. In particular, given the curvature induced lamellar distortion, the crystallization on the nano-curved portion of substrates occurs only in the presence of energetic gain that counterbalances the loss of crystallization enthalpy derived from the growth of distorted lamellae. Indeed, for substrates having high SFE full surface coverage is observed (Figure 4.3 g), since the SFE reduction occurring upon the full substrate coverage by P3HT compensates the lower enthalpy gain due to the growth of distorted lamellae on nano-curved surfaces. This allows the P3HT to crystallize on any part of the substrate. On the contrary, there are no energy gains for the crystallization of P3HT on the nano-curved portions of low SFE substrates, as P3HT SFE is no longer lower than the substrate one, therefore, straight lamellae, characterized by higher crystallization enthalpy, form exclusively in the interstices between the particles. To support this hypothesis, GIXRD measurements were performed (Figure 4.4). No difference is shown by the diffraction patterns of P3HT crystals on flat and on nano-curved low SFE substrates, as in both case, the (100) peak and two higher orders are observed. As the GIXRD scan is performed out-of plane, these peaks are diagnostic of preferential edge-on orientation.[92] In contrast, on high-SFE substrates, the diffractogram is characterized by lower intensity (100) peak and by the absence of higher orders, indicating a poorer crystalline order and orientational randomization[111,112] due to the curved crystals growing on the curved portions of the substrate.

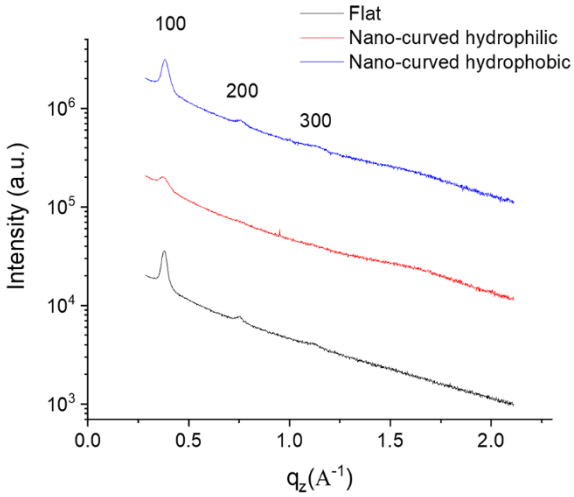

Figure 4.4. Grazing incidence diffractograms of P3HT films crystallized on flat, 63.98 mN/m and 21.95 mN/m nano-curved substrates.

These results clearly indicate that the nucleation is a key parameter for lamellar growth, since crystallization only occurs when the free nucleation energy exceeds the energy loss caused by the creation of new interfaces.

4.2) Combined effect: SFE and curvature modulation

The combined effect induced by surface curvature and free energy on P3HT crystallization was investigated by performing an in-situ GIXRD structural characterization during thermal annealing. In particular, the growth of P3HT crystals was studied as a function of both the substrate curvature and the SFE, by modulating the SFE for each curvature. By applying the procedure illustrated in the previous paragraph, substrates with intermediate hydrophobicity and different curvatures were selected, as we expect that the P3HT crystallization at intermediate SFE conditions, that is, where nor the crystallization enthalpy maximization nor the SFE minimization are prevalent, may be more sensitive to changes in substrate curvature. Therefore, we employed substrates with curvature of 0.00851 nm^{-1}, 0.00496 nm^{-1}, and 0.01399 nm^{-1} and SFE values of 43.56 and 55.49 mN/m. On the other hand, it was not possible to investigate crystallization on highly hydrophobic substrates since, even in the flat case, the dewetting of the polymer film was observed during the annealing. We believe this is due to the sample stage employed for in-situ structural analysis, which is characterized by a non-homogeneous heat flow, as the heating unit lays below the substrate, which may facilitate dewetting processes when the substrate is warmer than the rest of the environment.

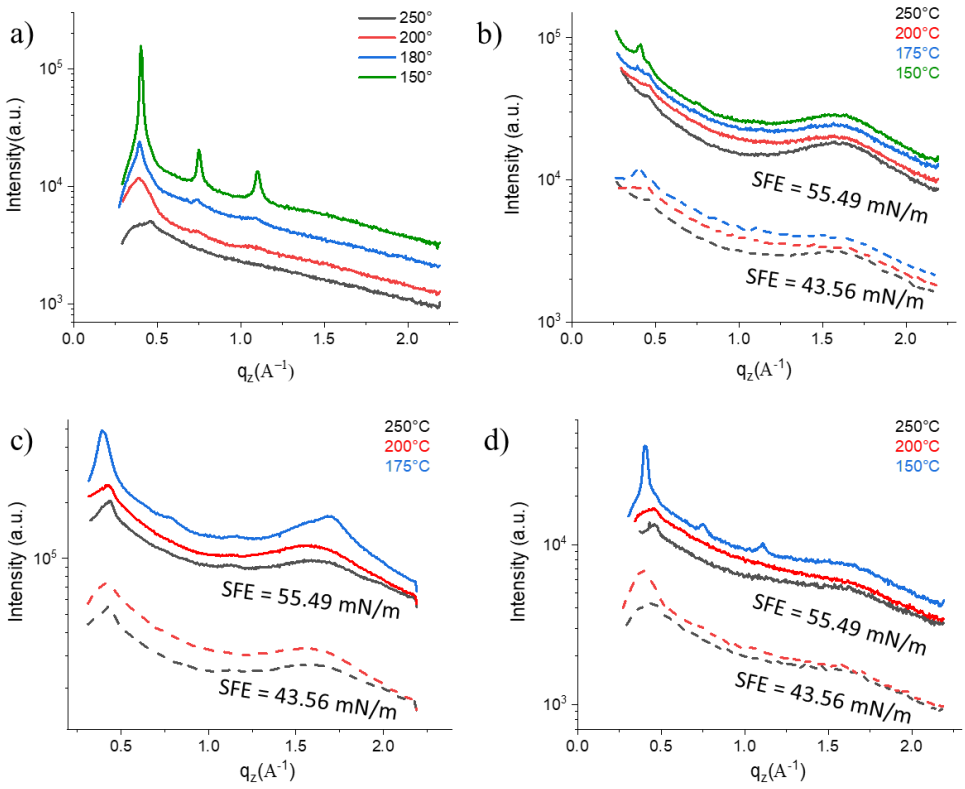

Figure 4.5. Comparison between out of plane diffractogram of P3HT in-situ thermal annealing on hydrophilic flat substrate (a) and on substrates with modulated SFE and different curvatures: 0.00492 nm^{-1} (b), 0.00851 nm^{-1} (c), 0.0140 nm^{-1} (d).

Figure 4.5 shows the out of plane diffractograms of P3HT thin films recorded under controlled curvature and SFE. In particular, attention is paid to cooling, in order to monitor the appearance of Bragg peaks and, in turn, to have an estimate of P3HT crystallization temperature as a function of substrate SFE and curvature. Figure 4.5 a resumes the diffractograms obtained during thermal cooling, for flat substrate with high SFE, showing a crystallization temperature of 200 °C, in agreement with what observed previously in literature.[93] The variation of the surface curvature, as well as of the SFE, leads to changes of the crystallization temperature, which seems to be influenced by both effects, i.e. geometric and energetic factors. In particular, at low SFE and for surface curvature equal to 0.00851 nm^{-1} and 0.01399 nm^{-1} (Figure 4.5 c-d, dashed line) the crystallization temperature is equal to that observed on the flat substrate, suggesting the growth of straight lamellae in the interstices between particles as already observed by AFM in the previous paragraph. On the contrary,

when the substrate curvature is lower (0.00492 nm^{-1}, Figure 4.5 b, dashed line) the crystallization temperature is lower than the flat case, that is, distorted crystals growth on the curved portion of the substrate. When increasing SFE, we observe, for all substrate curvatures, lower crystallization temperatures than the one observed on flat substrates (Figure 4.5 b-d, continuous line). The observed results fully agree with the hypothesis reported in the previous paragraph, as the variation observed in the crystallization temperature with SFE and substrate curvature can be explained in terms of crystallization enthalpy maximization and SFE reduction. In particular, when SFE is the lowest, only the substrate with the lowest curvature allows the growth of distorted crystals, as the lower distortion induced by this substrate implies a lower crystallization enthalpy loss which can be counterbalanced by the coverage of substrates with relatively low surface energy. On the contrary, on substrates with higher curvatures, that is, on substrates which induces higher distortion, the growth of distorted crystals requires higher SFEs, as the higher enthalpy loss must be counterbalanced by a higher SFE reduction upon P3HT coverage. Therefore, we observe a significant reduction of the crystallization temperature, which is diagnostic of the growth of distorted crystals, only at high SFE while at lower ones crystal growth predominantly in the flat interstices between the curved portion of the substrates and the crystallization temperature is unaltered with respect to the flat case. These results highlight the interplay between substrate nano-curvature and SFE opening the way to a new method to finely modulate the crystal distortion and substrate coverage and, in turn, to modulate both film morphology and 3D structure.

5) Summary and outlook

The results reported in this section showed how the 3D structure of the thin films of P3HT can be modulated as a function of the nano-curvature of the substrate, as well as the associated energetics. It must be considered that in covering non-flat surfaces, the mobility of the chains and the efficient spreading act in different directions. Therefore, if, on the one hand, the high molecular mobility favours the formation of straight lamellae, on the other hand the efficient spreading will favour the formation of curved lamellae that will better adhere to the substrate. In particular, it was observed that for substrates with high SFE, the polymeric lamellae are able to completely cover the surface. The formation of polymeric lamellae was already observed on the as-deposited out of equilibrium P3HT films, with a reduction of the persistence length as the surface curvature increases and a random orientation of the crystals induced by surface geometric factors. This suggests that the crystals formed during the rapid evaporation of the solvent adhere to the substrate with one of the two crystallographic faces, corresponding to the two preferential edge-on and face–on orientations in the case of the flat substrate and to an isotropic orientation of the polymeric backbone with respect to the macroscopic plane on nano-curved substrates. The annealing of the polymeric films leads to a variation of the crystalline fraction as a function of the surface geometries. A marked effect played by the surface curvature is observed. In particular, the increase of curvature leads to the formation of smaller crystalline domains, with a reduction of the edge-on fraction.
However, the curvature does not induce a significant variation of the lamellar orientations with respect to the edge-on, in fact, only 15% of OLO is recorded regardless of the surface geometry. Therefore, unlike the as-deposited P3HT thin films, for which the increase of curvature leads to an increase of lamellae randomization on the surface, the heat treatment involves a reduction of the crystalline fractions. At the same time, lower crystallization temperature are observed. Therefore, since this reduction is not attributable to the presence of smaller lamellar thicknesses, it is related to the crystalline structure, which appears more distorted with the increase in surface curvature. In particular, when adhering to the curved portions of the surface, the P3HT lamellae undergo distortions in their structure, with consequent effects in the crystallization temperature. It was also observed that the modulation of the SFE also influences the crystallization process of the polymer lamellae on the curved surfaces. P3HT crystallization appears to be governed by two driving forces: SFE minimization and crystallization enthalpy maximization, which act in opposite directions, with significant variations of morphology and nanostructure as a function of the substrate properties. In particular, crystallization on curved substrates only occurs if the SFE gain counterbalances the

loss of crystallization enthalpy resulting from the growth of distorted crystals. The in situ structural characterization carried out during the thermal cooling allowed to highlight how the crystalline distortion increases with the curvature. As the growth of distorted lamellae on substrates with higher curvatures requires higher SFEs to occur, since the increase in enthalpy loss must be counterbalanced by a higher SFE gain. The reported work provides a novel and easy method to modulate the structure of polymer films by exploiting geometric distortion and interfacial interactions with possible effects on the functional properties of the polymer film. Overall, the reported results could pave the way for subtle management of the morphology and structure control of thin films and to a deeper understanding on the self-assembly behaviour of confined soft matter by enabling the quantitative determination of fundamental parameters such as the crystallization enthalpy and its related loss when nanometric strain is applied. This would allow a greater control of the system and the design of advanced devices in which it is possible to control the individual building blocks, model the polymeric assembly finely, thus allowing to create devices based on a local control of the properties of the system, where the interactions with the substrate are the key parameters for the realization of unique devices having the desired characteristics. At the same time, it is possible to exploit the unique effects and properties associated with surface nano-confinement, which provides the possibility of obtaining devices with properties not previously observed, thanks to the intrinsic properties of the building blocks involved.

References

(1) Krausch, B. G.; Magerle, R. Nanostructured Thin Films via Self-Assembly of Block Copolymers **. **2002**, No. 21, 1579–1583.

(2) Rosei, F. Nanostructured Surfaces : Challenges and Frontiers in Nanotechnology. **2004**, *1373*. https://doi.org/10.1088/0953-8984/16/17/001.

(3) Verstraete, L. 2D Self-Assembled Molecular Networks and on-Surface Reactivity under Nanoscale Lateral Confinement. **2021**. https://doi.org/10.1039/d0cs01338b.

(4) Carmen, A.; Rebeca, M.; Martin, J. A review on the progress of polymer nanostructures with modulated morphologies and properties, using nanoporous aao templates. *Prog. Polym. Sci.* **2015**. https://doi.org/10.1016/j.progpolymsci.2015.10.003.

(5) Kim, D. H.; Kim, S. Y. E Ff Ective Morphology Control of Block Copolymers and Spreading Area-Dependent Phase Diagram at the Air/Water Interface. **2017**. https://doi.org/10.1021/acs.jpclett.7b00471.

(6) Yu, C.; Xie, Q.; Bao, Y.; Shan, G.; Pan, P. Crystalline and Spherulitic Morphology of Polymers Crystallized in Confined Systems. **2017**. https://doi.org/10.3390/cryst7050147.

(7) Pdp, P. V. P.; Perepichka, I. I.; Lu, Q.; Badia, A.; Bazuin, C. G. Understanding and Controlling Morphology Formation in Langmuir − Blodgett Block Copolymer Films Using PS-P4VP and PS- P4VP/PDP. **2013**.

(8) Ellison, C. J.; Torkelson, J. M. The Distribution of Glass-Transition Temperatures in Nanoscopically Confined Glass Formers. **2003**, *2* (October), 695–700. https://doi.org/10.1038/nmat980.

(9) Shi, A. C.; Li, B. Self-Assembly of Diblock Copolymers under Confinement. *Soft Matter* **2013**, *9* (5), 1398–1413. https://doi.org/10.1039/c2sm27031e.

(10) Binder, K.; Horbach, J.; Vink, R.; De Virgiliis, A. Confinement Effects on Phase Behavior of Soft Matter Systems. *Soft Matter* **2008**, *4* (8), 1555–1568.

(11) McKenna, M. A. and G. B. Effects of Confinement on Material Behaviour at the Nanometre Size Scale Effects of Confinement on Material Behaviour at The. *J. Phys. Condens. Matter* **2005**, *17*. https://doi.org/10.1088/0953-8984/17/15/R01.

(12) Kim, S.; Ju, M.; Lee, J.; Hwang, J.; Lee, J. Polymer Interfacial Self – Assembly Guided Two – Dimensional Engineering of Hierarchically Porous Carbon Nanosheets. **2020**.

(13) Verduzco, R.; Li, X.; Pesek, L.; Stein, G. E. Structure, Function, Self-Assembly, and Applications of Bottlebrush Copolymers. *Chem. Soc. Rev.* **2015**.

(14) Liu, Y.; Chen, E. Polymer Crystallization of Ultrathin Films on Solid Substrates. *Coord. Chem. Rev.* **2010**, *254* (9–10), 1011–1037. https://doi.org/10.1016/j.ccr.2010.02.017.

(15) Zhang, C.; Fukuto, M. Thickness Limit for Alignment of Block Copolymer Films Using Solvent Vapor Annealing with Shear. **2018**.

(16) Shelton, C. K.; Epps, T. H. Decoupling Substrate Surface Interactions in Block Polymer Thin Film Self-Assembly. **2015**. https://doi.org/10.1021/acs.macromol.5b00833.

(17) Li Destri, G.; Keller, T. F.; Catellani, M.; Punzo, F.; Jandt, K. D.; Marletta, G. Interfacial Free Energy Driven Nanophase Separation in Poly(3- Hexylthiophene)/[6,6]-Phenyl-C61-Butyric Acid Methyl Ester Thin Films. *Langmuir* **2012**, *28* (11), 5257–5266. https://doi.org/10.1021/la300229u.

(18) Wu, H.; Higaki, Y.; Takahara, A. Molecular Self-Assembly of One-Dimensional Polymer Nanostructures in Nanopores of Anodic Alumina Oxide Templates. *Prog. Polym. Sci.* **2018**, *77*, 95–117. https://doi.org/10.1016/j.progpolymsci.2017.10.004.

(19) Mijangos, C.; Hernández, R.; Martín, J. A Review on the Progress of Polymer

Nanostructures with Modulated Morphologies and Properties, Using Nanoporous AAO Templates. *Prog. Polym. Sci.* **2016**, *54–55*, 148–182.
(20) Tran, H. D.; Li, D.; Kaner, R. B. One-Dimensional Conducting Polymer Nanostructures: Bulk Synthesis and Applications. *Adv. Mater.* **2009**, *21* (14–15), 1487–1499. https://doi.org/10.1002/adma.200802289.
(21) Steinhart, M. Supramolecular Organization of Polymeric Materials in Nanoporous Hard Templates. *Adv. Polym. Sci.* **2008**, *220* (1), 123–127.
(22) Higuchi, T.; Tajima, A.; Motoyoshi, K.; Yabu, H. Frustrated Phases of Block Copolymers in Nanoparticles. **2008**, 8044–8046.
(23) Ma, M.; Titievsky, K.; Thomas, E. L.; Rutledge, G. C. Continuous Concentric Lamellar Block Copolymer Nanofibers with Long Range Order 2009. **2009**.
(24) Karim, A. Disordered Nanoparticle Interfaces for Directed Selfassembly. **2009**, *5* (3). https://doi.org/10.1039/b813970a.
(25) Page, K. A.; Patton, D. L.; Douglas, J. F.; Jones, L.; Karim, A. Thermally-Induced Transition of Lamellae Orientation in Block-Copolymer Films on 'Neutral' Nanoparticle-Coated Substrates. *Soft Matter* **2015**. https://doi.org/10.1039/C5SM00896D.
(26) Noriega, R. Efficient Charge Transport in Disordered Conjugated Polymer Microstructures. *Macromol. Rapid Commun.* **2018**, *39* (14), 1–9.
(27) Gu, K.; Loo, Y. L. The Polymer Physics of Multiscale Charge Transport in Conjugated Systems. *J. Polym. Sci. Part B Polym. Phys.* **2019**, *57* (23), 1559–1571.
(28) Gu, K.; Wang, Y.; Li, R.; Tsai, E.; Onorato, J. W.; Luscombe, C. K.; Priestley, R. D.; Loo, Y. Role of Postdeposition Thermal Annealing on Intracrystallite and Intercrystallite Structuring and Charge Transport in Poly(3- Hexylthiophene). **2021**.
(29) Li Destri, G.; Keller, T. F.; Catellani, M.; Punzo, F.; Jandt, K. D.; Marletta, G. Interfacial Free Energy Driven Nanophase Separation in Poly(3- Hexylthiophene)/[6,6]-Phenyl-C61-Butyric Acid Methyl Ester Thin Films. *Langmuir* **2012**, *28* (11), 5257–5266.
(30) Ham, S.; Shin, C.; Kim, E.; Ryu, D. Y.; Jeong, U.; Russell, T. P.; Hawker, C. J. Microdomain Orientation of PS-b-PMMA by Controlled Interfacial Interactions. *Macromolecules* **2008**, *41* (17), 6431–6437. https://doi.org/10.1021/ma8007338.
(31) Schulze, R.; Arras, M. M. L.; Li Destri, G.; Gottschaldt, M.; Bossert, J.; Schubert, U. S.; Marletta, G.; Jandt, K. D.; Keller, T. F. Extended-Chain Induced Bulk Morphologies Occur at Surfaces of Thin Co-Oligomer Films. *Macromolecules* **2012**, *45* (11), 4740–4748. https://doi.org/10.1021/ma300643m.
(32) Dolynchuk, O.; Schmode, P.; Fischer, M.; Thelakkat, M.; Thurn-Albrecht, T. Elucidating the Effect of Interfacial Interactions on Crystal Orientations in Thin Films of Polythiophenes. *Macromolecules* **2021**, *54* (12), 5429–5439.
(33) Boulanger, N.; Yu, V.; Hilke, M.; Toney, M. F.; Barbero, D. R. In Situ Probing of the Crystallization Kinetics of Rr-P3HT on Single Layer Graphene as a Function of Temperature. *Phys. Chem. Chem. Phys.* **2017**, *19* (12), 8496–8503.
(34)Lechner, M. D. Polymers. *Springer Handbooks*. 2018, pp 485–536.
(35) Cheng, S. Z. D. Phase Transitions in Polymers: The Role of Metastable States. *Elsevier* **2008**.
(36) Yang, S. G.; Lei, J.; Zhong, G. J.; Xu, J. Z.; Li, Z. M. Role of Lamellar Thickening in Thick Lamellae Formation in Isotactic Polypropylene When Crystallizing under Flow and Pressure. *Polymer (Guildf).* **2019**, *179* (February), 121641.
(37) Busch, P.; Krishnan, S.; Paik, M.; Toombes, G. E. S.; Smilgies, D. M.; Gruner, S. M.; Ober, C. K. Surface Induced Tilt Propagation in Thin Films of Semifluorinated Liquid Crystalline Side Chain Block Copolymers. *Macromolecules* **2007**, *40* (1), 81–89.

(38) Frank, C. W.; Rao, V.; Despotopoulou, M. M.; Pease, R. F. W.; Hinsberg, W. D.; Miller, R. D.; Rabolt, J. F. Structure in Thin and Ultrathin Spin-Cast Polymer Films. *Science (80-.).* **1996**, *273* (5277), 912–915. https://doi.org/10.1126/science.273.5277.912.
(39) Pan, G.; Hu, L.; Zhang, F.; Chen, Q. Out-of-Plane Alignment of Conjugated Semiconducting Polymers by Horizontal Rotation in a High Magnetic Field. **2021**. https://doi.org/10.1021/acs.jpclett.1c00385.
(40) Liu, J.; Arif, M.; Zou, J.; Khondaker, S. I.; Zhai, L. Controlling Poly(3-Hexylthiophene) Crystal Dimension: Nanowhiskers and Nanoribbons. *Macromolecules* **2009**, *42* (24), 9390–9393. https://doi.org/10.1021/ma901955c.
(41) Yao, Y.; Dong, H.; Hu, W. Charge Transport in Organic and Polymeric Semiconductors for Flexible and Stretchable Devices. *Adv. Mater.* **2016**, *28* (22), 4513–4523. https://doi.org/10.1002/adma.201503007.
(42) Wang, B.; Chen, J.; Shen, C.; Reiter, G.; Zhang, B. Relation between Charge Transport and the Number of Interconnected Lamellar Poly(3-Hexylthiophene) Crystals. *Macromolecules* **2019**, *52* (16), 6088–6096.
(43) Steyrleuthner, R.; Di Pietro, R.; Collins, B. A.; Polzer, F.; Himmelberger, S.; Schubert, M.; Chen, Z.; Zhang, S.; Salleo, A.; Ade, H.; Facchetti, A.; Neher, D. The Role of Regioregularity, Crystallinity, and Chain Orientation on Electron Transport in a High-Mobility n-Type Copolymer. *J. Am. Chem. Soc.* **2014**, *136* (11), 4245–4256. https://doi.org/10.1021/ja4118736.
(44) Tremel, K.; Ludwigs, S. Morphology of P3HT in Thin Films in Relation to Optical and Electrical Properties. **2014**, No. September, 39–82. https://doi.org/10.1007/12.
(45) Qu, S.; Ming, C.; Yao, Q.; Lu, W.; Zeng, K.; Shi, W.; Shi, X.; Uher, C.; Chen, L. Understanding the Intrinsic Carrier Transport in Highly Oriented Poly(3-Hexylthiophene): Effect of Side Chain Regioregularity. *Polymers (Basel).* **2018**, *10* (8), 1–14. https://doi.org/10.3390/polym10080815.
(46) Chaudhary, V.; Pandey, R. K.; Prakash, R.; Singh, A. K. Self-Assembled H-Aggregation Induced High Performance Poly (3-Hexylthiophene) Schottky Diode. *J. Appl. Phys.* **2017**, *122* (22). https://doi.org/10.1063/1.4997554.
(47) Kim, D. H.; Jang, Y.; Park, Y. D.; Cho, K. Surface-Induced Conformational Changes in Poly(S-Hexylthiophene) Monolayer Films. *Langmuir* **2005**, *21* (8), 3203–3206.
(48) Agbolaghi, S.; Zenoozi, S. A Comprehensive Review on Poly(3-Alkylthiophene)-Based Crystalline Structures, Protocols and Electronic Applications. *Org. Electron.* **2017**, *51* (August), 362–403. https://doi.org/10.1016/j.orgel.2017.09.038.
(49) Malik, S.; Nandi, A. K. Crystallization Mechanism of Regioregular Poly (3-Alkyl Thiophene) S. **2002**, No. June, 2073–2085. https://doi.org/10.1002/polb.10272.
(50) Brinkmann, M.; Wittmann, J. C. Orientation of Regioregular Poly(3-Hexylthiophene) by Directional Solidification: A Simple Method to Reveal the Semicrystalline Structure of a Conjugated Polymer. *Adv. Mater.* **2006**, *18* (7), 860–863.
(51) A New Method to Improve P3HT Crystalline Behavior Decreasing Chains Entanglement to Promote Order− Disorder Transformation in.Pdf.
(52) Brown, P. J.; Thomas, D. S.; Köhler, A.; Wilson, J. S.; Kim, J. S.; Ramsdale, C. M.; Sirringhaus, H.; Friend, R. H. Effect of Interchain Interactions on the Absorption and Emission of Poly(3-Hexylthiophene). *Phys. Rev. B - Condens. Matter Mater. Phys.* **2003**, *67* (6), 1–16. https://doi.org/10.1103/PhysRevB.67.064203.
(53) Noriega, R.; Rivnay, J.; Vandewal, K.; Koch, F. P. V.; Stingelin, N.; Smith, P.; Toney, M. F.; Salleo, A. A General Relationship between Disorder, Aggregation and Charge

Transport in Conjugated Polymers. *Nat. Mater.* **2013**, *12* (11), 1038–1044. https://doi.org/10.1038/nmat3722.
(54) Printz, A. D.; Lipomi, D. J. Competition between Deformability and Charge Transport in Semiconducting Polymers for Flexible and Stretchable Electronics. *Appl. Phys. Rev.* **2016**, *3* (2). https://doi.org/10.1063/1.4947428.
(55) Jiao, X.; Statz, M.; Lai, L.; Schott, S.; Jellett, C.; Mcculloch, I.; Sirringhaus, H.; Mcneill, C. R. Resolving Different Physical Origins Toward Crystallite Imperfection in Semiconducting Polymers : Crystallite Size vs Paracrystallinity.
(56) Whyman, G.; Bormashenko, E.; Stein, T. The Rigorous Derivation of Young , Cassie – Baxter and Wenzel Equations and the Analysis of the Contact Angle Hysteresis Phenomenon. **2008**, *450*, 355–359. https://doi.org/10.1016/j.cplett.2007.11.033.
(57) Xiao, K.; Zhao, Y.; Ouyang, G.; Li, X. Modeling the Effects of Nanopatterned Surfaces on Wetting States of Droplets. **2017**. https://doi.org/10.1186/s11671-017-2086-9.
(58) Marmur, A. Wetting on Hydrophobic Rough Surfaces: To Be Heterogeneous or Not to Be? *Langmuir* **2003**, *19* (20), 8343–8348. https://doi.org/10.1021/la0344682.
(59) Kim, J.; Kim, C. J. Nanostructured Surfaces for Dramatic Reduction of Flow Resistance in Droplet-Based Microfluidics. *Proc. IEEE Micro Electro Mech. Syst.* **2002**, 479–482.
(60) Raphael, E.; Joanny, J. F.; Robbins, M. O.; Joanny, J. F.; Tan, A. W.; Torkelson, J. M.; Distance, H.; Films, T. W. Complete Wetting on Rough Surfaces : Statics. **1988**.
(61) Wetting Transition from the Cassie−Baxter State to the Wenzel.Pdf.
(62) Palasantzas, G. WETTING ON ROUGH SURFACES. **2001**, *49*, 3533–3538.
(63) Patankar, N. A. On the Modeling of Hydrophobic Contact Angles on Rough Surfaces. **2003**, 1249–1253.
(64) Bormashenko, E.; Pogreb, R.; Whyman, G.; Bormashenko, Y.; Erlich, M.; Bormashenko, E.; Pogreb, R.; Whyman, G.; Bormashenko, Y.; Erlich, M. Vibration-Induced Cassie-Wenzel Wetting Transition on Rough Surfaces Vibration-Induced Cassie-Wenzel Wetting Transition on Rough Surfaces. **2015**, *201917* (2007), 1–3.
(65) Choi, W.; Tuteja, A.; Mabry, J. M.; Cohen, R. E.; McKinley, G. H. A Modified Cassie-Baxter Relationship to Explain Contact Angle Hysteresis and Anisotropy on Non-Wetting Textured Surfaces. *J. Colloid Interface Sci.* **2009**, *339* (1), 208–216.
(66) Amabili, M.; Meloni, S.; Giacomello, A.; Casciola, C. M. Activated Wetting of Nanostructured Surfaces : Reaction Coordinates , Finite Size E Ff Ects , and Simulation Pitfalls. **2018**. https://doi.org/10.1021/acs.jpcb.7b07429.
(67) Jayaramulu, K.; Geyer, F.; Schneemann, A.; Kment, Š.; Otyepka, M.; Zboril, R.; Vollmer, D.; Fischer, R. A. Hydrophobic Metal–Organic Frameworks. *Adv. Mater.* **2019**, *31* (32), 1–31. https://doi.org/10.1002/adma.201900820.
(68) Wolansky, G.; Marmur, A. Apparent Contact Angles on Rough Surfaces : The Wenzel Equation Revisited. **1999**, *156*, 381–388.
(69) Bonn, D.; Ross, D. Reports on Progress in Physics Related Content Wetting Transitions Wetting Transitions. **2001**.
(70) Peters, A. M.; Pirat, C.; Sbragaglia, M.; Borkent, B. M.; Wessling, M.; Lohse, D. Cassie-Baxter to Wenzel State Wetting Transition : Scaling of The. **2009**, *397*, 391–397.
(71) Marmur, A. The Lotus Effect: Superhydrophobicity and Metastability. *Langmuir* **2004**, *20* (9), 3517–3519. https://doi.org/10.1021/la036369u.
(72) Patankar, N. A. On the Modeling of Hydrophobic Contact Angles on Rough Surfaces. *Langmuir* **2003**, *19* (4), 1249–1253. https://doi.org/10.1021/la026612+.
(73) Patankar, N. A. Transition between Superhydrophobic States on Rough Surfaces. *Langmuir* **2004**, *20* (17), 7097–7102. https://doi.org/10.1021/la049329e.

(74) Moulinet, S.; Bartolo, D. Life and Death of a Fakir Droplet: Impalement Transitions on Superhydrophobic Surfaces. *Eur. Phys. J. E* **2007**, *24* (3), 251–260.
(75) Drelich, J.; Chibowski, E.; Meng, D. D.; Terpilowski, K. Hydrophilic and Superhydrophilic Surfaces and Materials. *Soft Matter* **2011**, *7* (21), 9804–9828.
(76) Li, W.; Amirfazli, A. Microtextured Superhydrophobic Surfaces: A Thermodynamic Analysis. *Adv. Colloid Interface Sci.* **2007**, *132* (2), 51–68.
(77) Zhang, Y.; Chen, Y.; Shi, L.; Li, J.; Guo, Z. Recent Progress of Double-Structural and Functional Materials with Special Wettability. *J. Mater. Chem.* **2012**, *22* (3), 799–815.
(78) Messina, G. M. L.; Bocchinfuso, G.; Giamblanco, N.; Mazzuca, C.; Palleschi, A.; Marletta, G. Orienting Proteins by Nanostructured Surfaces: Evidence of a Curvature-Driven Geometrical Resonance. *Nanoscale* **2018**, *10* (16), 7544–7554.
(79) Donose, B. C.; Taran, E.; Vakarelski, I. U.; Shinto, H.; Higashitani, K. Effects of Cleaning Procedures of Silica Wafers on Their Friction Characteristics. *J. Colloid Interface Sci.* **2006**, *299* (1), 233–237. https://doi.org/10.1016/j.jcis.2006.01.044.
(80) Scott, W. W.; Bhushan, B. Use of Phase Imaging in Atomic Force Microscopy for Measurement of Viscoelastic Contrast in Polymer Nanocomposites and Molecularly Thick Lubricant Films. *Ultramicroscopy* **2003**, *97* (1–4), 151–169. https://doi.org/10.1016/S0304-3991(03)00040-8.
(81) Usov, I.; Mezzenga, R. FiberApp: An Open-Source Software for Tracking and Analyzing Polymers, Filaments, Biomacromolecules, and Fibrous Objects. *Macromolecules* **2015**, *48* (5), 1269–1280. https://doi.org/10.1021/ma502264c.
(82) Rivetti, C.; Guthold, M.; Bustamante, C. Scanning Force Microscopy of DNA Deposited onto Mica: Equilibration versus Kinetic Trapping Studied by Statistical Polymer Chain Analysis. *J. Mol. Biol.* **1996**, *264* (5), 919–932. https://doi.org/10.1006/jmbi.1996.0687.
(83) Neusser, D.; Malacrida, C.; Kern, M.; M. Gross, Y.; van Slageren, J.; Ludwigs, S. High Conductivities of Disordered P3HT Films by an Electrochemical Doping Strategy. *Chem. Mater.* **2020**, *32* (14), 6003–6013. https://doi.org/10.1021/acs.chemmater.0c01293.
(84) Rivnay, J.; Jimison, L. H.; Northrup, J. E.; Toney, M. F.; Noriega, R.; Lu, S.; Marks, T. J.; Facchetti, A.; Salleo, A. Large Modulation of Carrier Transport by Grain-Boundary Molecular Packing and Microstructure in Organic Thin Films. *Nat. Mater.* **2009**, *8* (12), 952–958. https://doi.org/10.1038/nmat2570.
(85) Rolland, N.; Franco-Gonzalez, J. F.; Volpi, R.; Linares, M.; Zozoulenko, I. V. Understanding Morphology-Mobility Dependence in PEDOT:Tos. *Phys. Rev. Mater.* **2018**, *2* (4), 1–9. https://doi.org/10.1103/PhysRevMaterials.2.045605.
(86) An, L.; Duan, Y.; Yuan, Y.; Zhou, L.; Zhang, J. Effect of Thermal Annealing on the Microstructure of P3HT Thin Film Investigated by RAIR Spectroscopy. *Vib. Spectrosc.* **2013**, *68*, 40–44. https://doi.org/10.1016/j.vibspec.2013.05.002.
(87) Peng, R.; Zhu, J.; Pang, W.; Cui, Q.; Wu, F. Journal of Macromolecular Science , Part B : Physics Thermal Annealing Effects on the Absorption and Structural Properties of Regioregular Poly (3-Hexylthiophene) Films. **2011**, No. February 2013, 37–41.
(88) Oyewole, D. O.; Oyewole, O. K.; Kushnir, K.; Shi, T.; Oyelade, O. V.; Adeniji, S. A.; Agyei-Tuffour, B.; Evans-Lutterodt, K.; Titova, L. V.; Soboyejo, W. O. Pressure and Thermal Annealing Effects on the Photoconversion Efficiency of Polymer Solar Cells. *AIP Adv.* **2021**, *11* (4). https://doi.org/10.1063/5.0045694.
(89) Salammal, S. T.; Mikayelyan, E.; Grigorian, S.; Pietsch, U.; Koenen, N.; Scherf, U.; Kayunkid, N.; Brinkmann, M. Impact of Thermal Annealing on the Semicrystalline Nanomorphology of Spin-Coated Thin Films of Regioregular Poly (3- Alkylthiophene)

s as Observed by High-Resolution Transmission Electron Microscopy and Grazing Incidence X-Ray Di Ff Raction. **2012**.
(90) Brinkmann, M. Structure and Morphology Control in Thin Films of Regioregular Poly (3-Hexylthiophene). **2011**, 1218–1233. https://doi.org/10.1002/polb.22310.
(91) Mwema, F. M.; Akinlabi, E. T. The Use of Power Spectrum Density for Surface Characterization of Thin Films. 379–411.
(92) Li Destri, G.; Keller, T. F.; Catellani, M.; Punzo, F.; Jandt, K. D.; Marletta, G. Crystalline Monolayer Ordering at Substrate/Polymer Interfaces in Poly(3-Hexylthiophene) Ultrathin Films. *Macromol. Chem. Phys.* **2011**, *212* (9), 905–914. https://doi.org/10.1002/macp.201000753.
(93) Verploegen, E.; Mondal, R.; Bettinger, C. J.; Sok, S.; Toney, M. F.; Bao, Z. Effects of Thermal Annealing upon the Morphology of Polymer-Fullerene Blends. *Adv. Funct. Mater.* **2010**, *20* (20), 3519–3529. https://doi.org/10.1002/adfm.201000975.
(94) Weeks, J. J. Melting Temperature and Change of Lamellar Thickness with Time for Bulk Polyethylene. **1963**, *67* (5), 441–451.
(95) Commins, P.; Hu, Q.; Ahmed, E.; Karothu, D. P. From Mechanical E Ff Ects to Mechanochemistry : Softening and Depression of the Melting Point of Deformed Plastic Crystals. **2020**. https://doi.org/10.1021/jacs.0c03990.
(96) Ma, Y.; Hu, W.; Chimie, I. De; Starcky, J.; April, R. V; Re, V.; Recei, M.; May, V. Lamellar Crystal Orientations Biased by Crystallization Kinetics in Polymer Thin Films. **2006**, 5159–5164.
(97) Jin, Y.; Rogunova, M.; Hiltner, A.; Baer, E.; Nowacki, R.; Galeski, A.; Piorkowska, E. Structure of Polypropylene Crystallized in Confined. **2004**, 3380–3396. https://doi.org/10.1002/polb.20211.
(98) In-Situ Hot Stage Atomic Force Microscopy Study of Poly(ε-Caprolactone) Crystal Growth in Ultrathin Films.Pdf.
(99) Manuscript, A. Controlling States of Water Droplets on Nanostructured Surfaces by Design. **2017**. https://doi.org/10.1039/C7NR06896D.
(100) Konovalov, O.; Destri, G. L.; Seeck, O. H.; Mezger, M.; Haddad, J.; Deutsch, M.; Checco, A.; Ocko, B. M. Nanoscale Structure of Si / SiO 2 / Organics. *ACS Nano* **2014**, *8* (12), 12676–12681.
(101) Kondo, T.; Watanabe, R.; Shimoyama, Y.; Shinohe, K.; Kulinich, S. A.; Iwamori, S. Effect of Reactive Oxygen Species Generated with Ultraviolet Lamp and Plasma on Polyimide Surface Modification. *Surf. Interface Anal.* **2017**, *49* (11), 1069–1077.
(102) van Oss, C. J.; Chaudhury, M. K.; Good, R. J. Interfacial Lifshitz—van Der Waals and Polar Interactions in Macroscopic Systems. *Chem. Rev.* **1988**, *88* (6), 927–941.
(103) Cassie, B. D. Of Porous Surfaces,. **1944**, No. 5, 546–551.
(104) Wenzel, R. N. Resistance of Solid Surfaces to Wetting by Water. *Ind. Eng. Chem.* **1936**, *28* (8), 988–994. https://doi.org/10.1021/ie50320a024.
(105) Murakami, D.; Jinnai, H.; Takahara, A. Wetting Transition from the Cassie-Baxter State to the Wenzel State on Textured Polymer Surfaces. *Langmuir*. 2014, pp 2061–2067. https://doi.org/10.1021/la4049067.
(106) Good, R. J.; Girifalco, L. A. A Theory for Estimation of Surface and Interfacial Energies. III. Estimation of Surface Energies of Solids from Contact Angle Data. *J. Phys. Chem.* **1960**, *64* (5), 561–565. https://doi.org/10.1021/j100834a012.
(107) Li, B.; Zhang, S.; Andre, J. S.; Chen, Z. Relaxation Behavior of Polymer Thin Films: Effects of Free Surface, Buried Interface, and Geometrical Confinement. *Prog. Polym. Sci.* **2021**, 101431. https://doi.org/10.1016/j.progpolymsci.2021.101431.

(108) Fondren, Z. T.; Fondren, N. S.; McKenna, G. B.; Weeks, B. L. Crystallization Kinetics of Pentaerythritol Tetranitrate (PETN) Thin Films on Various Materials. *Appl. Surf. Sci.* **2020**, *522* (April), 146350. https://doi.org/10.1016/j.apsusc.2020.146350.

(109) Roth, C. B. Polymers under Nanoconfinement: Where Are We Now in Understanding Local Property Changes? *Chem. Soc. Rev.* **2021**. https://doi.org/10.1039/d1cs00054c.

(110) Shen, X.; Hu, W.; Russell, T. P. Measuring the Degree of Crystallinity in Semicrystalline Regioregular Poly(3-Hexylthiophene). *Macromolecules* **2016**, *49* (12), 4501–4509. https://doi.org/10.1021/acs.macromol.6b00799.

(111) Li-Destri, G.; Tuccitto, N.; Livio, P. A.; Messina, G. M. L.; Pithan, L.; Marletta, G. Energy-Sustained Reversible Nanoscale Order and Conductivity Increase in Polymer Thin Films. *Polymer (Guildf).* **2018**, *153* (August), 344–353.

(112) Na, J. Y.; Kang, B.; Sin, D. H.; Cho, K.; Park, Y. D. Understanding Solidification of Polythiophene Thin Films during Spin-Coating: Effects of Spin-Coating Time and Processing Additives. *Sci. Rep.* **2015**, *5* (August), 1–14. https://doi.org/10.1038/srep13288.

Second Section:

Dynamic Interfaces

Nanostructured liquid interfaces: State of Art

6) The charm of liquid interfaces

The properties of liquid surfaces have always fascinated scientists. It was 1774 when Benjamin Franklin, fascinated by the behaviour of a drop of oil spread on the water surface, said: "*It seems as if a mutual repulsion between its particles took place as soon as it touched the water, and a repulsion as strong as that air on other bodies swimming on the surface, forcing them to recede every way from the drop. The quantity of this force, and the distance at which it will operate, I have not yet ascertained, but I think it is a curious investigation and I wish to understand whence it arrives*".[1]
It began to be understood that the theory of Newton about the gravity was unable to explain the interactions involved. The study of capillarity, on the other hand, appeared promising although the first theories considered the liquid surface to be devoid of any structure, also because of its involvement in the transition to the vapor phase.[2] Considerable progress was made at the end of the nineteenth century, when the theory of surface tension was introduced; the interface was no longer considered as a clear boundary between two phases but the concept of diffuse interface appeared.[2,3,4] It was thus possible to fix the size of a molecule of olive oil in water, increasingly assuming the existence of attractive intermolecular forces between water and oil. The first experiments on molecular films were introduced, allowing to hypothesize the shapes and sizes of molecules, subsequently confirmed by modern methods of investigation.[2] The studies on liquid interfaces increased; in the twentieth century, colloidal particles trapped at interfaces began to be studied.[5] Pickering and Ramsden studied paraffin-water emulsions with solid particles which inhibited the coalescence of the emulsion droplets as they formed a film at the interface between the two phases.[6] Later, it was discovered that the assembly of spherical particles at the liquid interface involves a reduction of the interfacial free energy, as well as surface tension, γ, defined as the energy cost, G_γ, associated with the formation of a unit of contact area, A, between two fluids, and that this reduction is the actual driving force of the interfacial colloidal assembly:[5,6,7]

$$\gamma = \left(\frac{\delta G_\gamma}{\delta A}\right)_{T,p} \qquad \textit{Equation 6.1}$$

Therefore, it is the minimization of Gibbs free energy, due to the reduction of the contact area between two liquids, that drives the adsorption of colloidal particles at

the interface despite the entropic penalty connected to the confinement of the molecules at the interface.[7,8] The interaction of colloidal systems with fluid interfaces is of particular importance, for example in the biomedical field, in the transport of colloidal particles through the respiratory tract and appear also promising in industrial processes and in the manufacture of miniature light sources.[9,10,11] The presence of the interface is responsible for dimensional confinement, as well as symmetry breaking, making it versatile for the production of nanomaterials where the interface acts as a template for the colloidal assembly and guides their organization into soft and reconfigurable structures.[7,12] The simplicity with which the assembly takes place makes it an excellent process for coating the surface; the colloidal particles self-assemble spontaneously, guided by the interface free energy reduction.[8,13] They are active at the surface and act as building blocks for the production and stabilization of foams and emulsions.[14,15] The small size associated to colloidal particles at the nanoscale confers unique properties to monolayers that they spontaneously form at liquid interfaces, probably deriving from collective effects, due to the interactions between the first neighbours, and fascinating structural characteristics thanks to their hierarchical organization.[12,15]

The remarkable developments in nanoscience has provided the possibility of synthesizing nanoparticles (NPs) of different materials, with tuneable shapes and sizes and with properly designed chemical and physical properties.[12,13] The possibility of engineering complex geometries by exploiting the interfacial assembly is a simple and precise method for the preparation of nanostructured functional monolayers.[12,16] The lateral mobility associated to the particles at the interface allows them to reorganize following the application of external stimuli. Therefore, it becomes possible to produce materials whose structure and functionality can be reconfigured on demand, a long-sought objective in material science.[12] The geometric restrictions and the prospect of controlling the assembly of nano-objects paves the way for the construction of functional materials with sophisticated and mechanically stable structures, in which the nanoparticles impart specific functions to the nanostructures.[5,6,7] To be able to fully control the resulting structure, a good understanding of the physical chemistry of complex interfaces is required, as well as the dynamic and equilibrium properties of assembled systems.[9,17,18,19] Classic thermodynamics models, which consider systems to be continuous, have limitations when dealing with nano-sized objects. At the nanoscale, metastable systems can be observed, with very slow relaxation at equilibrium or single particles trapped in a state of non-equilibrium.[20] Therefore, it is necessary to deepen our better understanding of the dynamic effects involved, deriving from the nanoscale and surface heterogeneity, which could allow the development of new applications where the control of motions associated to particles can be relevant.[16] As a matter of fact, nano-colloidal systems become a central topic in the science of liquid interfaces, given the need to identify and measure the forces determining the physical behaviour

of colloids at the interfaces in order to create and control the formation of complex two-dimensional structures with many potential applications.[21,22] For a long time, the only physical quantity that could be experimentally measured was the surface tension, this allowed to explain the energy effects involved but it ignored the entropic component associated with it.[2] Although the surface tension has a significant effect in many heats transfer processes, providing also information about the wettability of fluids, it is not sufficient to describe the adsorption of colloidal systems at the interface.[23,24] The use of standard thermodynamic quantities for the bulk and some parameters of the materials, could allow a deeper understanding of the adsorption at the interface. These models do not take into account the molecular nature of the solvent, or the other species involved. Therefore, although they are valid methods for micrometric dimensions, they are not satisfactory enough at the nanoscale, where it is no longer possible to neglect the thickness of the interfacial layer, as it is comparable, if not greater, to the size of the colloidal nuclei.[7,13,15,25,26,27,28,29] Although interfaces may appear as abrupt borders, they are characterized by a finite thickness of the order of a few nanometres, where the materials appear inhomogeneous, with properties that differ from the bulk. Therefore, nanoscale particles are affected by the irregularities of the surrounding medium or molecules.[30] The reduction in the size of the particles involved means that negligible interactions at the macroscale can no longer be neglected. In addition, the corpuscular nature of matter must be considered, given the reduction of kinetic units and the importance of thermal energy.[30] In the mid-1970s, the development of synchrotron X-ray sources, characterized by a high incident flux and a small beam, made it possible to structurally characterize liquid surfaces with unprecedented resolution.[31,32] The possibility of working at grazing angle of incidence (GID) allows to reduce the dispersion of the background of the material, making the intensity diffracted by the surface measurable.[2] This allows the precise determination of the positions of the particles with respect to the interface and the inter-particle distance.[11] This structural information allows us significantly broaden the methods to investigate the organization of colloidal monolayers at liquid interfaces, so far mainly limited to Langmuir trough approach based on the measurement of surface pressure variations recorded by compressing the interface at a constant speed.[2]

Despite the considerable progress achieved in the characterization of fluid interfaces, many questions still remain about the processes that are involved in the adsorption of colloidal particles at the interface and therefore in its nano-structuring.

6.1) Energy factors and interactions involved

The adsorption of nanoparticles at interface is thermodynamically favoured since it is accompanied by a reduction of surface tension; a lateral pressure is generated opposing the contraction of the interface to minimize its area following the adsorption of particles.[7,13] The stability of the adsorbed particles is mainly related to the complex interactions that arise between the particles and the properties of the liquids that form the interface and it also depends on the size of the particles.[13] In particular, irreversible adsorption occurs, in non-equilibrium conditions, for particles with micrometric dimensions; as the adsorption energy exceeds the thermal bath. In the case of nanometric particles, the adsorption energy may be comparable to the K_BT, where K_B is the Boltzmann constant and T is the temperature. Therefore, the displacement towards the interface occurs with a speed that is a function of the size of the particles thus, allowing the system to reach interfacial equilibrium.[5,6,12,33] Although irreversible adsorption is to be attributed to microparticles, even at the nanoscale it is possible to have high trapping energies of nanoparticles at the interface.[6] If we consider that the adsorption of the particle at the interface involves the loss of the fluid interface, the surface energy will be equal to the difference in the tension of the new interfaces formed as a result of the adsorption compared to the initial tension.[6,13] It follows that the free energy variation will be proportional to the fluid interface area replaced by the particle, to the radius of the particle (r) and to the angle it forms at the interface (ϑ), namely:[34]

$$\Delta E = -\pi r^2 \gamma_{\alpha\beta}(1 \pm cos\vartheta)^2 \qquad \textit{Equation 6.2}$$

Therefore, the variation of the free energy will always be negative. It follows that the positioning of a particle at the interface is thermodynamically favoured. The energy reduction can be expressed as a function of surface tension, wettability and interparticle interactions.[5,6,7,13,33,35] On this basis, it appears that the driving force of the interfacial assembly is enthalpically driven.[6,13] Similarly, ΔE is the amount of energy required to remove the adsorbed particle at the fluid interface and scales quadratically with the radius of the particle. It follows that the desorption energy is often much higher than the thermal bath, allowing to affirm that the particle is strongly attached to the interface, such that it can be considered irreversibly adsorbed.[7,15,13] Although thermodynamics allows us to explain why particles are strongly adsorbed at the interface, the description of the adsorption process is more complex.[12] Once the particles are transported to the interface, in order to be adsorbed at the interface, the particles must overcome an energy barrier, originating from the potential particle-interface interaction.[36] The presence of an attractive interaction and a favourable adsorption energy means that the particles remain immobilized at the interface. Once adsorbed, the particles will reorganize according to the different

forces acting on the system and the tension is seen as an energetic barrier to be overcome so that the particle can escape from the interface.[6,12] Therefore, the interaction potential that derives and that determines the assembly of the particles at the interface is generated by many different factors.[15,37] This means that the interfacial assembly cannot be easily predicted. It is necessary to consider the different forces, attractive and repulsive that act on the system in addition to the complexity of the interface with respect to the bulk.[12] Furthermore, once adsorbed at the interface, the particles do not remain fixed but diffuse in a limited random walk, along the plane of the interface.[5] Hence it is of importance to consider the fluctuations around the equilibrium position, which perturb the contact line due to the roughness at the nanoscale and generate deformations.[5] Therefore, the necessity to develop thermodynamic models that allow to correctly describe the mechanisms involved, and in particular the inter-particle interactions and their wettability, is evident.[7] In the 40s of the twentieth century Derjaguin and Landau[38] and subsequently, Verwey and Overbeek[39] studied the interactions that are established between particles and their interactions with the medium in which they are dispersed. They developed a quantitative theoretical analysis of the problems related to the stability of colloids, known as the DLVO theory, from the initials of their names. The theory is based on the electrical properties at the particle-water interface and on the interaction energies that come into play when two charged particles approach each other.[40] It assumes that the stability of colloids depends on long-range forces and in particular on the balance between the attractive interactions of Van der Waals, $V_A(h)$, and the repulsions of the bilayer, $V_R(h)$, which are formed at a charged interface and increase exponentially with decreasing distance, h. Therefore, the total interaction potential and the corresponding strength will be equal to: [26]

$$V(h) = V_A(h) + V_R(h) \qquad F = -\frac{dV}{dh} = -\frac{dV_A}{dh} - \frac{dV_R}{dh} \qquad \textit{Equation 6.3 and 6.4}$$

where the attractive term is inversely proportional to the distance, h, while in the repulsive term the dependence on the distance is given by the Debye screening in solution.[26] It follows that at very large or very small distances, the attractive term prevails while at intermediate distances the strength of the double layer prevails, if the surface is sufficiently charged, giving rise to an energy barrier.[26] The height of this barrier represents the stability of the system since, in order to aggregate, the particles must overcome the energy barrier.[26] While the theory is correct, other types of forces have emerged from several studies. Moreover, the theory simplifies the properties of colloids as it does not consider either the irregularity in size or the surface roughness of particles and its influence on acting forces.[40,41] A uniform distribution of the charge and potential is also assumed while the solvent is considered as a homogeneous medium, with a single dielectric constant.

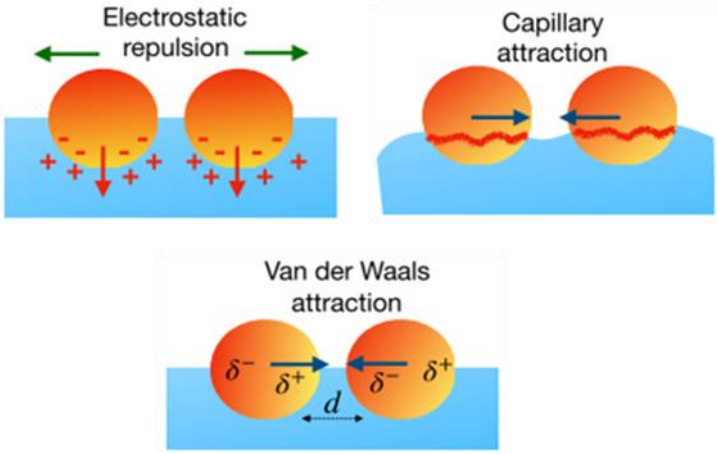

Figure 6.1. Different interactions that can arise between the colloidal particles trapped at the water/air interface. In particular, electrostatic repulsions resulting from the dipolar and Coulomb interaction can occur, which are counterbalanced by the attractive Van der Waals and capillary forces.[5]

Furthermore, the dimensions of the ions of the diffuse layer are ignored, considering them like point charges. These hypothesis are no longer valid at small distances and high surface potentials.[40,42] Further limitations of the theory are observed at the nanoscale, where the nanoscale dimensions of colloidal particles complicate the system.[25] The dimensions of the nanoparticles are comparable to those of the solvent molecules, ions and other components of the solution. It is therefore not possible to consider the uniformity of the medium nor the additivity of the potential involved; therefore, it is necessary to consider the structure of the surrounding medium and the interactions with the other groups present.[25] It should also be considered that, due to the discontinuity of the interface, the strength of the interactions between the particles and the dependence on the parameters will be altered with respect to the bulk, which makes the quantitative analysis of the interactions involved more difficult.[12] New forces, in addition to bulk ones, emerge at the interface, such as dipolar repulsive forces, capillarity attraction and hydrophobic interactions.[7,13] In particular, it has been observed that, depending on the degree of hydrophobicity, the particles assemble at the interface forming isolated or close packed systems (respectively at low and high hydrophobicity), with consequent variation in surface tension and interfacial concentration.[7] Surface confinement, therefore, gives to particles physico-chemical properties that differ from the bulk.[7] Several models were developed in order to understand and obtain a description of the interactions involved. Martinez-López et al. developed a simplified model for understanding the involved potentials.[43] In particular, they considered that at the interface it is possible to identify a part of the particles immersed in the aqueous medium and an emerging

part in the apolar medium, this leads to interactions that are established only between the parts that are in the same phase.[43] It is assumed that the total energy will depend on the electrostatic and hydrophobic interactions between the immersed parts but also on the electrostatic and capillary interactions between the emerging parts.[44]
In particular, we can consider a dependence of the electrostatic interactions on the properties of the two phases where the particles are found while, additionally, the partial immersion of the particles generates forces, attributable to the deformation of the interface.[8,15] Therefore, while at the microscale the interfacial deformation can be attributed to gravity, at the nanoscale it is the immersion forces (capillary forces) that induce the interfacial perturbation. In particular, even in the case of nanometric particles, their adsorption to the interface leads to the formation of a finite contact angle, able to deform the surrounding fluid, with consequent attractive lateral capillary interactions. These forces derive from the partial immersion of the particles and, therefore, they depend on the wettability of the particles and not on the gravity, as it happens for larger particles. This creates a meniscus at the interface, with consequent interactions between the colloids, either attractive or repulsive, depending on whether the formed menisci are the same or not,[7,15,45] in order to minimize the area. The shape of the formed menisci may also be irregular, due to the surface roughness of the particles, responsible for non-uniform wetting and irregular contact lines.[46] It follows that the particles will regulate their orientation and their distance, in order to optimize the deformation with the interactions, which will be anisotropic.[47] If the distance between the NPs centres, L, is less than the capillary length (q^{-1}, which for the water/air interface is equal to 2.7 mm)[48], easily achievable at the nanoscale and if L is greater than the radii of the contact lines, r_k, i.e. $r_k \ll L \ll q^{-1}$, then the capillary energy will be proportional to $F \propto \gamma R^2 qL$ where R is the particle radius and γ the surface tension. Therefore, it is possible to affirm a linear increase of the immersion force with the surface tension.[49] Moreover, adsorption at the interface therefore involves a reduction in surface tension and an increase in the stiffness of the interface, whose position is affected by thermal fluctuations.[50,51] Colloids are not fixed at the interface but are affected by interactions with their first neighbours, generating a motion similar to the Brownian harmonic oscillator.[52] In order to create a model that fully describes the behaviour of the nanoparticles at the interface, it would be necessary to consider the movement of the particles also in the third dimension.[53] Finally, the full understanding of interfacial inter-particle forces require to consider the presence of dissociable charged groups on the surface of the colloids,[15] whose modulation can significantly influence the particle assembly.[54] It is in this perspective that the silica nanoparticles have been studied, as they are cheap, easy to chemically modify and with controllable surface topography.[55]

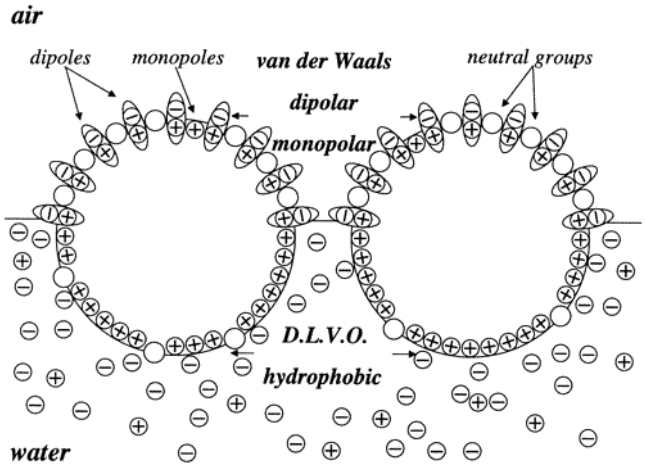

Figure 6.2. Schematic representation of the particles at the water/air interface. In the emerging parts, the particles interact according to classical theories while in the immersed parts, in addition to the Van der Waals and dipolar interactions, hydrophobic interactions should also be considered.[44]

They are characterized by dissociable silanol groups on the surface, therefore, their assembly will depend on the attractive Van der Waals forces, on the electrostatic double-layer repulsive forces between the particles and it is also necessary to consider the contribution of the dipolar interactions.[8,15]

The origin of these dipoles was explained by Robinson and Earnshaw[56] who assumed that the dissociated groups on the surface of the particles can interact with counterions present in solution, trapping them and forming a dipole that can also be exposed to the interface with air.

The groups that do not interact with the counterions remain in solution in the form of monopoles. Therefore, the dipolar interactions affect the aggregation while the Coulomb monopole ones affect the stability.[13] A further description of the interactions involved at the water/air interface was given by Stillinger and Hurd[57,58] who considered colloids as point charges at the interface in the framework of the linearized theory of Poisson-Boltzmann (description of electrostatic potentials in the normal direction with respect to the charged surface, assuming that the potential is much smaller than the K_BT[59]). The linearity approximation is valid at high interparticle distances, where the interaction potential is lower than the thermal bath. At short distances, however, it is necessary to consider the charge density on the surfaces and the particle-water interaction exerts a non-negligible contribution. Therefore, the approximation of linearity is no longer valid and the corpuscular nature of the water molecules must be considered.[57,58] The electrostatic interactions between particles and charged interfaces are not always precisely known and the

charging effects become increasingly important as the difference between the dielectric constants increases.[12] It is certain that the particles interact both attractively, causing their mutual approach, and repulsively due to electric charges and the presence of molecules adsorbed on surfaces.[30] The presence of dipoles also determines a power-law repulsion between the particles that drives the formation of compact 2D lattices at the interface, with a greater range of action than that observed in the bulk.[22]

6.2) Additives in solution: surfactants and salts

Additives, such as surfactants and salts, are generally added to colloidal dispersions to provide stability to the suspensions by interfering with the inter-particle and particle-interface interactions. Therefore, they also contribute in determining the structure of monolayers eventually formed by adsorption of particles.[12] In particular, additives mediate the interactions between the particles and the interface and this may result in a reduction of the adsorption energy barrier.[60] A good additive must therefore be able to facilitate the adsorption of particles at the interface and control the assembly.[12] They have an effect on the interactions of particles both in bulk and at the interface thus, they must tune the short range attractive and repulsive forces.[12] The repulsive interactions are attributed to the presence of surface dipoles and residual charges in addition to the repulsive forces of the electric double layer, while the attractive interactions can be attributed to capillary forces. It follows that, since additives influence the strength and range of the interactions involved, they can balance these interactions and control the interfacial assembly.[61,62,63] The use of surfactants to facilitate adsorption has ancient origins, they are also used in the mining industry to recover precious materials.[60] Understanding the particle-surfactant interactions at the liquid / air interface is also important for applications. In particular, in the presence of particles and surfactants with opposite charges, the interactions that arise promote the adsorption of the surfactant on the surface of the particles, making them more hydrophobic.[24] The variation of the particle wettability of the particles generates a reduction of the dispersion surface tension, which is significant in many hydraulic processes.[64]

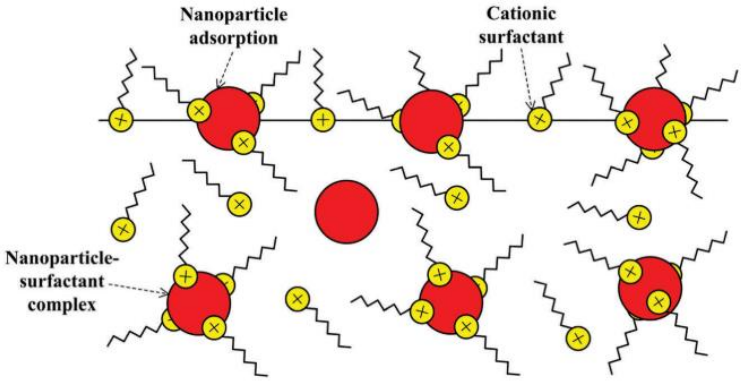

Figure 6.3. Schematic representation to explain the effect of cationic surfactants on hydrophilic nanoparticles and consequently on the surface tension at the interface.[24]

Harikrishnan et al. considered the combined surfactant-particle effect and proposed that the first phase of the assembly involves the adsorption of the surfactant molecules on the surface of the particles in bulk, such surfactant-decorated particles will then diffuse towards the interface, where they will adsorb.[65]
Therefore, the surface energy will be affected by the surfactant molecules. Through surface tension measurements, it is possible to study the effect of particles on equilibrium, as a function of both surfactant and particle concentrations while the measurement of the tension during the achievement of equilibrium allows to obtain kinetic information.[35] In some cases, it was also observed that in the presence of particle/surfactant complexes, the surface activity is greater than that recorded in the presence of surfactants alone as opposed to the absorption dynamics which appear slower.[66] The adsorption at the interface is governed by the Gibbs adsorption equation:

$$\Gamma = -(\frac{\delta\gamma}{\delta\mu})_T \qquad \textit{Equation 6.5}$$

where γ is the surface concentration of the moles adsorbed, μ is the chemical potential at absolute temperature and γ is surface tension.[67] As a result, the adsorption leads to the formation of a monolayer at the liquid/air interface with consequent reduction of the tension, which is a function of bulk concentration.[68] The addition of the surfactant modifies the wettability and the charge of particles, this makes the particle surface hydrophobic and it allows their adsorption at the interface. The surface modification is due to the electrostatic particle-surfactant interactions which favour the physisorption. Therefore, the degree of particle hydrophilization and the resultant interfacial assembly are dependent on the concentration of the surfactant.[69] In the case of anionic particles, like silica particles, the surface charge prevents the

particles from adsorbing at the interface. In the absence of surfactant, the hydrophilicity associated with the particles does not make them akin to the interface.[8,12] Their interaction with surfactants of opposite charge increases the hydrophobicity and consequently the adsorption at the interface, while the surface tension decreases.[8] Therefore, the balance between the lipophilic and hydrophilic character of the nanoparticles is responsible for their affinity for fluid interfaces.[69] At the interface the particles generate a surface pressure equal to $\Pi = \gamma_w - \gamma$ where γ_w is the surface tension of the water, 72.8 mN/m at 20°C, while γ is the tension of the adsorbed monolayer. Moreover, as the increase of the surfactant concentration determines an increase of the fractions of active species adsorbed to the interface, the surface pressure depends on the surfactant concentration.[8] It follows that the surfactant has a dual function, on the one hand it promotes the adsorption of particles at the interface, by decreasing the adsorption barrier.[70] This phenomenon, which is believed to dominate the adsorption processes at low surfactant concentrations, leaves the surface properties unchanged, i.e. it does not involve the decoration of the particle surface by surfactants, thus allowing the formation of 2D assemblies. Above a threshold surfactant concentration, whose value depends on the hydrophobicity of the surfactant and on the extent of its adsorption on the particles, the surfactants are believed to behave as modifiers, as they adsorb significantly on the particle surface in order to neutralize the charge and induce aggregation, hindering the formation of ordered structures.[70,71] Silica particles (anionic) and cationic surfactants such as cetyltrimethylammonium bromide (C_{16}TAB) have been widely used for interfacial coating. The electrostatic interactions between the amino terminal groups of the surfactant and the negative charges of the nanoparticles determine the formation of C_{16}TAB /NPs complexes.[69] An explanation of what is happening is not yet possible. Ravera et al.[35] formulated considerations in order to explain the processes involved in the formation of the complexes and in the interfacial assembly. They assumed that initially the surfactant is present only on the particle surface, in the bulk, making the particles surface active. The greater hydrophobic character of the particles, due to the adsorption of the surfactant on their surface and the consequent migration of the resultant complexes towards the interface, involves a reorganization of the composite layer; different balances are established, and the surfactant is redistributed to the solid/liquid and liquid/air interface. This is accompanied by a reduction of surface tension, in proportion to the increase of the C_{16}TAB concentration; since the increase of concentration involves an increase of the surface portion covered by the surfactant and, consequently, an increase of the particle hydrophobicity.[35] The adsorption of C_{16}TAB on the silica particles is confirmed by measurements of the zeta potential, as a changes of the charge, from negative to positive, are recorded by following the addition of the cationic surfactant.[24] Further increases of the surfactant concentration

are accompanied by the formation of a double layer of surfactant molecules on the surface of the particles, with a consequent increase of the particle hydrophilicity due to the exposure of the polar heads to the aqueous phase.[72,73] This is confirmed by the inversion of the zeta potential, from negative to positive.[72] In most of the works in the literature, the salt, typically NaCl, promotes the particle-surfactant interaction, which improves the adsorption of the surfactant on the particles and it increases their adsorption at the liquid interface, thanks to the screening of the electrostatic repulsions.[23] Therefore, the addition of electrolytes in solution leads to a reduction of the adsorption barrier and facilitates their adsorption to the fluid interface.[74,75] The effect of ionic strength was studied with polystyrene (PS) particles by observing a variation of the interactions as a function of the concentration of the salt present.[76] It was observed that at low salt concentrations the accessibility of the particles to the interface was limited by the presence of a finite adsorption energy barrier. The increase of the salt concentration, on the other hand, leads to a reduction of the height of the barrier, which facilitates the particle adsorption; while further addition of salt facilitates bulk aggregation, leading to a reduction of the number of particles at the interface. This is possible because the increase of ionic strength reduces the electrostatic repulsion between the particles and, in combination with the Van der Waals attraction, the particles can assemble at an equilibrium interparticle distance. Thus, it becomes possible to quantify the probability of particle adsorption with ionic strength.[76,77] It follows that, although the increase of ionic strength screens the electrostatic repulsions, it induces the flocculation of the particles, i.e. the formation of a loosely packed network of aggregate particles, which results in an increase of the Gibbs modulus for smaller surface coverage.[74,78] The salts, therefore, allow to control the particle distance through the screening of electrostatic repulsions. This must be done in a controlled way so that the short-range repulsions are greater than the attractive interactions, in order to avoid aggregation.[79] Therefore, although the electrostatic attractions between particles and surfactant are responsible for the adsorption at the interface, the interparticle electrostatic repulsions in the aqueous phase controls the number of particles that reach the interface.[74] In conclusion, salt and surfactant act in a similar manner, as they both mediate the adsorption of particles at the fluid interface. Although surfactants promote adsorption at much lower concentrations than those required to obtain the same amount of particles at the interface in the presence of salt.[61]

6.3) Model system: in situ structural and morphological characterization at liquid/air interface

Costa et al.[80] studied the assembly of SiO_2 nanoparticles decorated by cationic surfactant at the water-oil interface. In particular, they combined nanoscale imaging obtained by in situ AFM with GISAXS synchrotron radiation, in order to correlate real and reciprocal space structural data. By modulating the concentration of C_{16}TAB, the authors showed the possibility of controlling the density of the monolayer at the interface, and then determining the interparticle distance. In particular, AFM imaging allows to characterize the interfacial forces and the morphology of the monolayers in real space, and these results were consistent with the reciprocal space ones. Using the configuration shown in Figure 6.4.a, the authors were able to in situ visualize the nanoparticle monolayers locally, with nanometric resolution. This allowed to observe single local defects not detectable with reciprocal space techniques. From the AFM images, the authors were able to measure the surface coverage of NPs, showing an increase with the concentration of surfactant, and to determine, from the coverage values obtained, the interparticle distance, in the assumption of hexagonal packing of the particles. The impact of the surfactant concentration on the surface coverage and interparticle distance was confirmed by the diffraction analyses performed on the same systems.

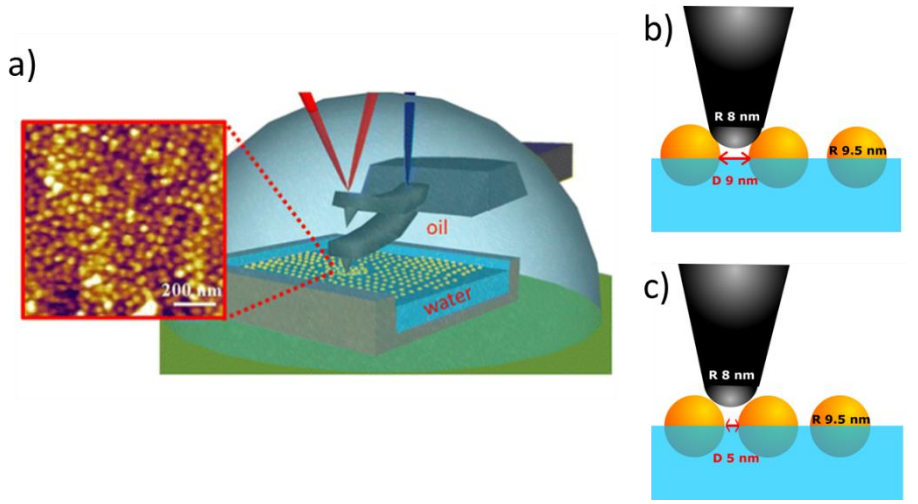

Figure 6.4. Schematic representation of the AFM and typical images of NPs monolayers containing local defects (a). If the distance between the particles is comparable to the radius of curvature of the tip, the probe can penetrate between the particles (b), contrary to what is observed in (c), where the probe cannot penetrate between the particles.[80]

Given the possibility of modulating the interparticle distance by varying the bulk ratio SiO_2/surfactant, the second section of this thesis will focus on the nanostructuring of liquid interfaces by modulating not only the concentration of the surfactant but also the length of its hydrophobic chain. Surface tension measurements and compression isotherms, accompanied by GISAXS, were conducted to characterize the monolayer formed at the interface. Furthermore, it is reasonable to assume that similarly to the role played by the surfactant concentration, the ionic strength will be equally decisive in affecting the final structure, thus allowing us to observe how the presence of ions in solution, in different quantities, can influence the interfacial nano-structuring. Finally, it will be shown how, by simultaneously recording the isotherm compression of a nanoparticle monolayer and the compression-induced structural variation, it is possible to understand and quantify the inter-particle repulsive forces acting at the liquid interface.

Results and discussion

7) Interfacial nano-structuring by NPs/surfactant complexes

The spontaneous adsorption of colloidal dispersion at the liquid/air interface allows the creation of nano-structures whose structure and stability are dictated by the interactions between the particles acting along an asymmetrical environment. To understand and control the interfacial and intermolecular interactions that occur on soft liquid interfaces, a model amphiphilic nanoparticle, which consists of an aqueous dispersion of negatively charged SiO_2 nanoparticles decorated with cationic surfactant, was used (Figure 7.1). It is known that the surfactant structure controls the surface tension of the system.[23] In order to understand how the different nature of the surfactant affects the assembly and interfacial properties, we used different cationic surfactants, characterized by the same polar head, trimethylammonium, and different chain length, such as dodecyltrimethylammonium bromide (C_{12}TAB), myristyltrimethylammonium bromide (C_{14}TAB), hexadecyltrimethylammonium bromide (C_{16}TAB) and octadecyltrimethylammonium (C_{18}TAB). (See appendix). It is known that the SiO_2 NPs alone do not appreciably adsorbate the water/air interface,[35] contrary to the cationic surfactants C_nTAB, which are highly surface active.[81] In order to shed more light on how the different nature of the surfactant can change the interface properties, surface tension measurements were carried out for all four different chain lengths, in the presence of NaCl 1mM. Figure 7.2 shows the trend of the equilibrium surface tension, γ, as a function of the bulk concentration of C_nTAB surfactants. At low concentrations in bulk, the surfactant does not significantly affect the system, recording a surface tension close to that of pure water, regardless of the length of the chain. This is due, given the low concentration of surfactant molecules in solution, to the low number of molecules adsorbed at the surface. The increase of concentration is accompanied by an increase of C_nTAB molecules adsorbed at the interface and a consequent reduction in surface tension.

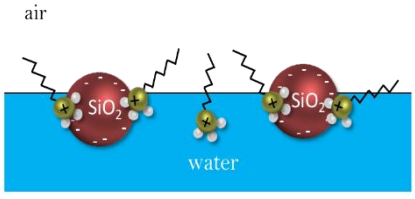

Figure 7.1. Model hydrophilic nanoparticles when decorated with cationic surfactants spontaneously adsorb at the liquid interface.

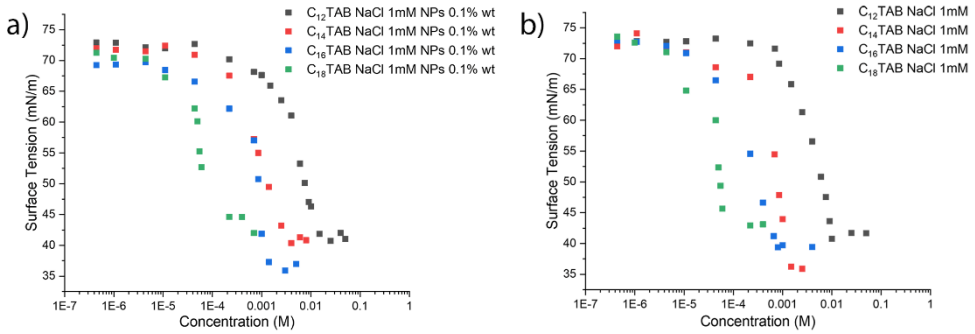

Figure 7.2. Variation of surface tension as a function of the different nature and concentration of surfactants. By increasing the length of the hydrophobic chain, the surface tension decreases with a lower surfactant concentration. While in (a) the monolayer is made up of the surfactant molecules adsorbed at the interface, in (b) the monolayer at the interface is made up of the NPs decorated with surfactants of different lengths. In both cases, the NaCl concentration is 1 mM.

The surface tension reduction is gradual and is related to the length of the surfactant; the effect occurs at lower concentrations for C_{18}TAB and the surfactant concentration required to appreciate surface tension variations increases with shortening the chain length. This effect is consistent with the adsorption of the pure surfactant C_nTAB at air/water interfaces.[23] Further increase in the surfactant concentration in bulk determine the achievement of a second plateau, as the critical micellar concentration (CMC) is reached. From the values shown in Figure 7.2, CMC are estimated at about $2 \cdot 10^{-2}$M for C_{12}TAB, about $3 \cdot 10^{-3}$M for C_{14}TAB, about $8 \cdot 10^{-4}$M for C_{16}TAB and about $2 \cdot 10^{-4}$M for C_{18}TAB, in agreement with literature.[82,83,84] This shows how, the increase of the chain length is accompanied by a reduction of its solubility. Above the CMC, the concentration of free surfactant molecules is constant and the increase of concentration leads to the increase of the number of micelles in solution. Since the micelles show no tendency to adsorb at the surface, only free molecules, whose concentration above CMC is constant, contribute to the reduction of surface tension, which, consequently, remains constant. The same study was conducted in the presence of NPs, in particular, mixed dispersions C_nTAB/NPs/NaCl were prepared to monitor the adsorption of complexes at the interface via surface tension measurements. As can be seen in Figure S2.2, in the appendices, the equilibrium is reached after one hour. However, the presence of NPs does not result in significant changes of the surface tension compared to what is obtained in the presence of pure surfactant (Figure 7.2 a and b). Therefore, it can be said that the variation of surface tension is connected to the adsorption of the surfactant at the interface and does not depend on the presence of NPs. A similar behaviour was found by Kirby et al.[23] who assumed that while surfactants alone are

responsible for reducing surface tension, NPs alone contribute to the diffusion time scale for adsorption at the interface. In order to shed more light on the role of the surfactant on the reduction of surface tension and on the adsorption of the C_nTAB/NPs complexes at the water/air interface, compression isotherms were conducted in a Langmuir trough at low concentrations of surfactants. Moreover, it is known that, under suitable ionic strength conditions, the C_nTAB/NPs complexes are trapped at the water/air interface with consequent effects on the surface tension and stiffness of the interface, since the complexes provide resistance to compression.[20,85] To this end, compression isotherms were carried out for surfactant concentrations equal to $1.1*10^{-6}$ M and $4.4*10^{-6}$ M, for all four lengths, in the presence of 1mM NaCl and NPs0.1% wt. Despite the surface tension measurements shown in Figure 7.2, at these concentrations, do not show significant variations of the tension compared to that of pure water (72.8 mN/m), the compression isotherms shown in Figure 7.3 and 7.4 show variations of surface pressure following monolayer compression. Moreover, such variations are observed only in the presence of NPs (black curves in the figure); the surfactant alone (red curves) shows no variations of surface pressure with compression.

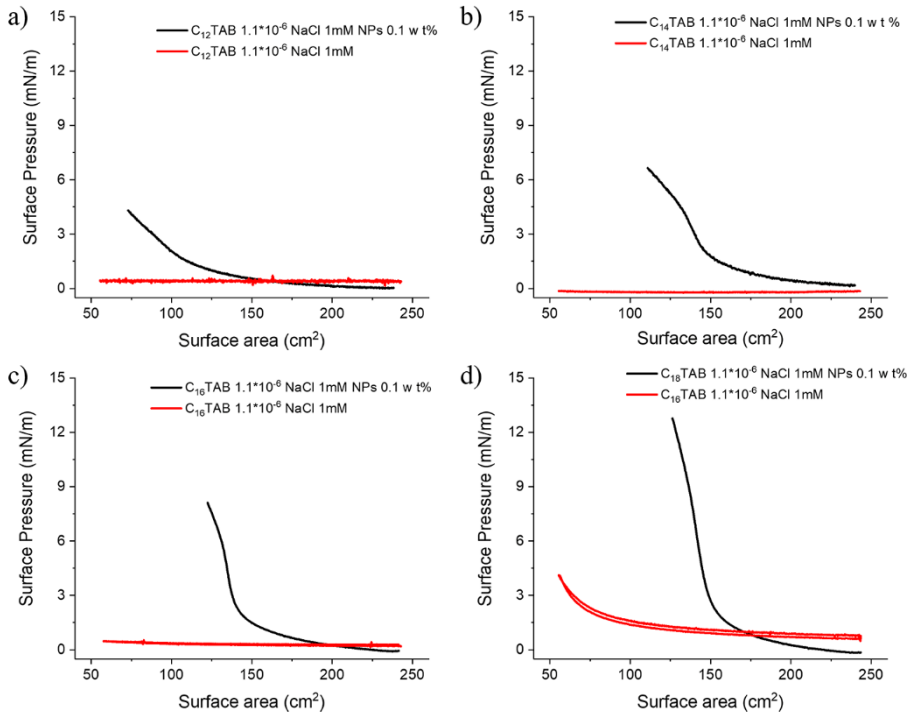

Figure 7.3. Compression isotherms of monolayer of C_nTAB $1.1*10^{-6}$ M, NaCl 1 mM and NPs 0.1% wt (black curves) and of the corresponding surfactant monolayer in the absence of NPs (red curves).

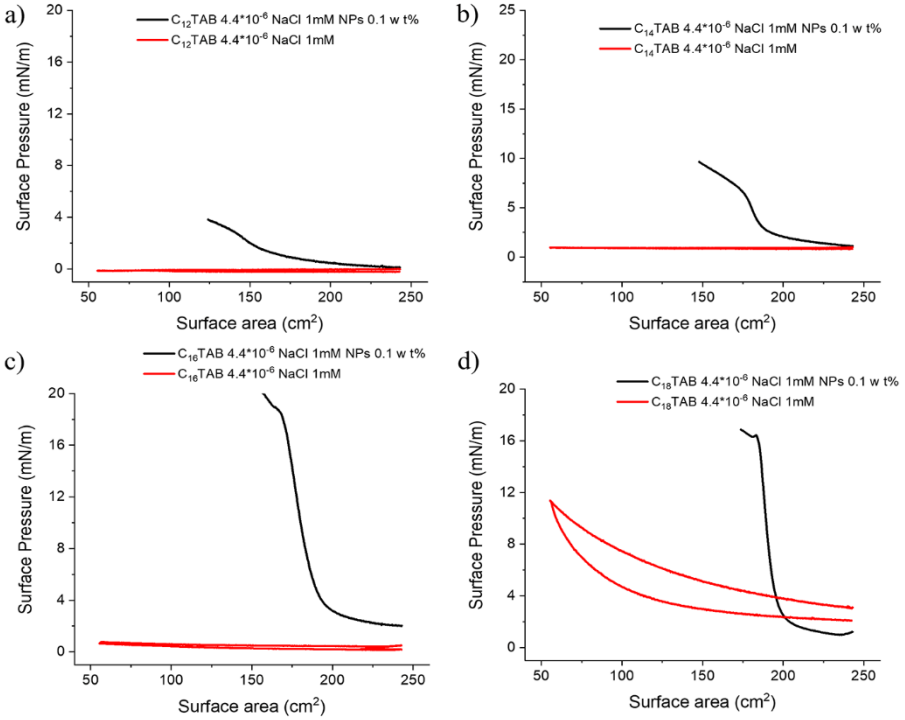

Figure 7.4. Compression isotherms of C_nTAB 4.4*10-6 M monolayer, 1 mM NaCl and 0.1% wt NPs (black curves) and of the corresponding surfactant monolayer in the absence of NPs (red curves).

The main differences between the two systems shown in Figure 7 and Figure 8, in the presence or not of NPs, is attributable to the desorption energy of the species involved. The adsorption of the surfactant molecules at the interface is reversible, since the adsorption energy of the surfactant is lower than the K_BT. This causes the surfactant molecules to desorb from the interface, following the perturbation of the equilibrium induced by compression; the resulting surface pressure will remain constant. On the contrary, the adsorption of the NPs/C_nTAB complexes at the interface is irreversible, since the desorption energy is greater than the K_BT.[86] By comparing the compression isotherms obtained for the different surfactants with the same concentration (Figure 9), the surface area at which the surface pressure begins to increase, does not depend on the surfactant chain length, except for C_{12}TAB, for which the pressure increase occurs at smaller areas. As surface pressure increase with compression is related to the formation of a relatively dense monolayer and that the same increase is not observed in the absence of NPs, it can be assumed that the surface pressure starts increasing when C_nTAB/NPs complexes are sufficiently close to significantly reduce area exposed by the water to air.

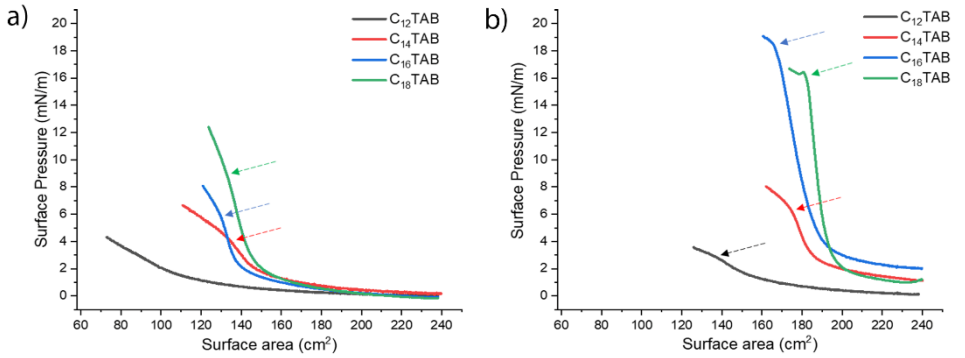

Figure 7.5. Compression isotherms recorded for solution having NaCl 1mM, NPs 0.1% wt and surfactant concentrations of $1.1*10^{-6}$M in (a), while $4.4*10^{-6}$M in (b). As the tail length and the concentration of surfactant increase, the monolayer becomes less compressible, showing a rapid increase in surface pressure at larger surface areas.

Therefore, the number of particles adsorbed at the interface, at a given surfactant concentration, is the same for the three longest surfactants, as the compression needed to induce the increase of the surface pressure does not depend on the surfactant chemical composition. This leads, in addition, to similar collapse areas, indicated by the arrows in Figure 7.5, for the three systems. The collapse area indicates the highest compression degree of the monolayer, as further compression are not possible because of the strong repulsive interactions between particles leading to expulsion of particles toward air or water[87] and a decrease of the isotherm slope. Remarkably, the collapse can not be observed for C_{12}TAB / NPs complexes at $1.1*10^{-6}$M surfactant concentration, probably because of the lower monolayer density. When increasing the surfactant concentration, all the monolayers reach the collapse (see Figure 7.5 b) and the corresponding area is still similar for the surfactants with the longest chains. These results suggest that the monolayer density, that is the number of adsorbed particles is mainly affected by the surfactant concentration, by increasing the surfactant concentration the number of adsorbed nanoparticles increases, and it depends on the surfactant nature only for C_{12}TAB. In particular, when C_{12}TAB fewer particles adsorb at the interface, presumably because of the lower surface activity caused by the shorter hydrophobic chain length. On the other hand, the steepness of the isotherm, which is diagnostic of the monolayer stiffness, is sensitive to both surfactant chain length and concentration (see Figure 7.5). In particular, monolayers formed by surfactants having longer chain length show higher steepness and higher sensitivity to the surfactant concentration.

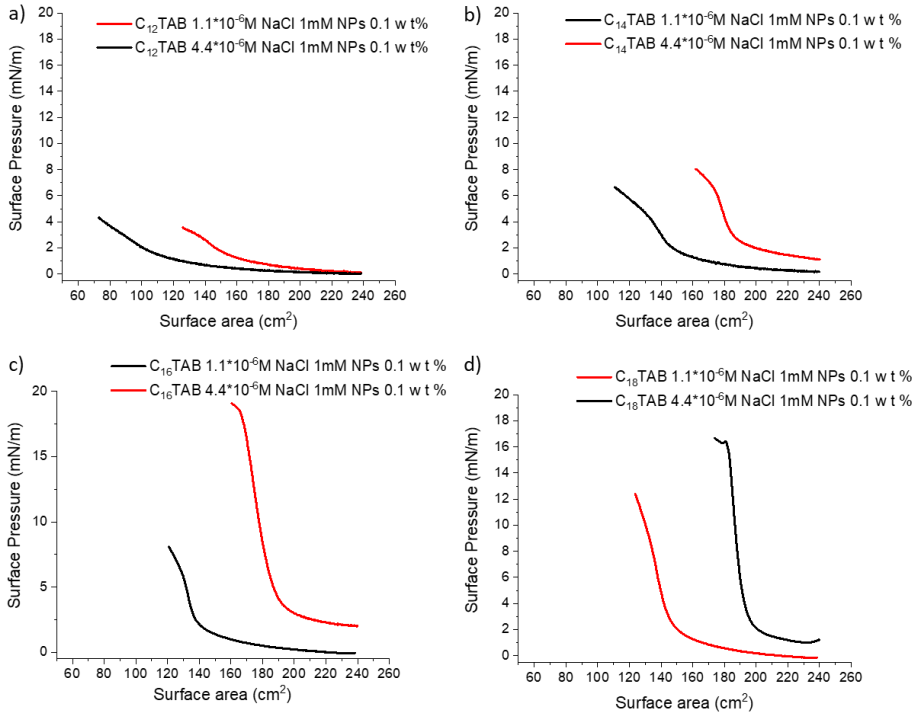

Figure 7.6. Compression isotherms of monolayer of C_nTAB 1.1 * 10^{-6} M, NaCl 1 mM and NPs 0.1% wt (black curves) and of CnTAB 4.4 * 10^{-6} M, NaCl 1 mM and NPs 0.1% wt (red curves) for the different chain lengths of surfactants: C_{12}TAB (a), C_{14}TAB (b), C_{16}TAB (c), C_{18}TAB (d).

As a matter of fact, while in Figures 7.6 a and 7.6 b, i.e. C_{12}TAB and C_{14}TAB, the slopes of the curves do not significantly change with concentration, Figure 7.6 c and 7.6 d shows steeper compression isotherms at higher concentrations. As we demonstrated that the monolayer density is not significantly influenced by the surfactant composition, the higher steepness measured for surfactants having longer hydrophobic chains, suggest that the repulsive interactions acting during the monolayer compression are also influenced by the surfactant nature and that they presumably consist of a steric contribution. This effect is clearly evident by plotting the highest isotherm slope, i.e. the slope of the section before the collapse, where the monolayer stiffness is highest, as a function of the surfactant chain length (Figure 7.7). It is possible to observe how the increase of the surfactant chain length leads to a variation in the slope, which becomes increasingly negative. This effect appears more evident for higher surfactant concentrations, where it is possible to observe an increase, in absolute value, of an order of magnitude.

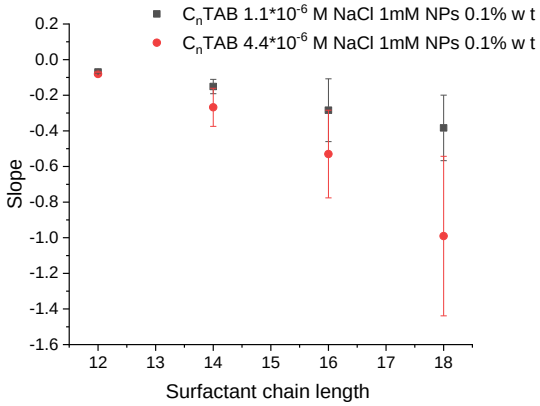

Figure 7.7. Slope variation of the isotherm compression as a function of the length of the surfactant and for concentrations of CnTAB of 1.1*10^{-6}M, black spots, and 4.4*10^{-6} M, red spots**.**

The origin of these interactions could be both electrostatic and steric. In particular, the occurrence of steric repulsions would explain why, at a given surfactant concentration, the highest slope is observed in the case of the surfactant with the longest chain length (C_{18}TAB). This effect becomes more marked at higher concentration. On the other hand, the weaker dependence of the monolayer stiffness at the lower concentration may indicate that the major contribution to inter-particle repulsions is given by electrostatic interactions. If this is the case, it would be possible to tune these interactions and, in turn, the monolayer stiffness, by modulating the ionic strength. On the other hand, the modulation of the ionic strength could also lead to variations in the surface coverage density with effects that affect the compressibility of the monolayer. This is possible because the dissolved ions shield the repulsive electrostatic interactions[88] and, therefore, they influence the number of particles adsorbed at the interface. In order to investigate the effect of ionic strength on both monolayer density and stiffness, surface tension and compression studies for the four surfactants with different chain lengths were conducted at different salt concentrations, i.e. 0.1mM and 10mM NaCl. Figure 7.8 shows the trend of the surface tension as a function of the ionic strength for the four different surfactants respectively. The results obtained show that, in the presence of higher ionic strength, the reduction of surface tension occurs at lower surfactant concentrations. This behaviour is accentuated by longer chain lengths, since in the case of C_{12}TAB and C_{14}TAB, no significant variation with ionic strength is observed. Therefore, the role of the surfactant in inducing variations of surface tension is influenced by saline concentration only for longer chains.

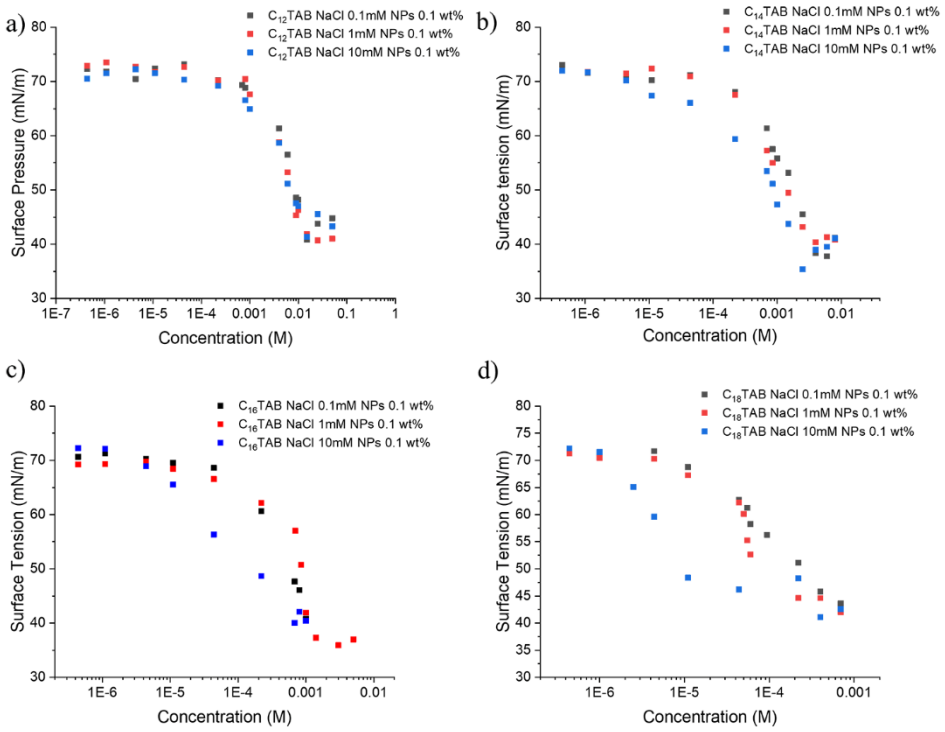

Figure 7.8. Role of the ionic strength for each surfactant chain length. In particular, it is reported in (a) C_{12}TAB, in (b) C_{14}TAB, in (c) C_{16}TAB and in (d) C_{18}TAB.

To better understand the observed effects, we need to consider the electrostatic interactions involved. In addition to the surface charge associated with particles, fluid interfaces can also carry electric charges.[89] Therefore, electrostatic interactions are generated between the interface and the particle. Several studies hypothesize that the interaction of the particle at the water/air interface may induce the formation of an "image charge" and, consequently, repulsive interactions.[76,90,91] Therefore, especially at low surfactant concentrations, where the surface tension does not change significantly with respect to the value of pure water, it is possible to hypothesize that the adsorption of the complexes at the interface sees, at least initially, the neutralization of the image charge by the few adsorbed surfactant molecules. This reduces the adsorption barrier of particles at the interface, resulting in the formation of a 2D assembly, reflecting the promoter character of the surfactant, proposed by Xu et al.[92] and then taken up in other studies.[93,94,70] However, the variation of surface tension, at the same surfactant concentration but with different ionic strength, suggests that the role of the surfactant, even at low concentrations, is not only to promote particle adsorption and screen repulsions of image charge. Since all four surfactants have the same charge, the effect of the ionic strength should not

result in any variation with the hydrophobic chain length. Therefore, it is reasonable to hypothesize that surfactant molecules, even at very low bulk concentrations, adsorb on the nanoparticles making them amphiphilic. Moreover, assuming the formation of a dense layer of surfactants on the NP surface, the steric repulsions, higher for longer chains, would lead to a lower adsorption of molecules on NPs and the effect on surface tension would be opposite to that shown in Figure 7.8. It follows that the number of surfactant molecules adsorbed on NPs is very low and that leads to a high sensitivity to the surfactant chain length, with a greater effect on the surface tension of surfactants with longer chain, as they are more active at the interface. Therefore, even the presence of a few more molecules on each NPs determines a greater effect. However, this remains only a hypothesis, the data obtained and the tools available, as well as the difficulty of the system, make it difficult to fully understand the effects involved. In order to study how the ionic strength affects the compressibility of the monolayer, compression isotherms were carried out at surfactant concentrations equal to $1.1*10^{-6}$M and $4.4*10^{-6}$M and NPs 0.1% wt. The variations of compressibility are attributable, once again, to the presence of NPs, since in the absence of NPs no variations of surface pressure are observed during compression (Figures S6-S9 appendices). From the curves shown in Figure 7.9 and Figure 7.10 it is evident how, with the same surfactant concentration, the ionic strength affects the density of the monolayer and, therefore, its compressibility. In particular, with increasing the ionic strength the monolayer compressibility decreases. This effect can be explained by considering that at higher salt concentrations more nanoparticles adsorb therefore, the increase of surface pressure, which is diagnostic of interacting particles, occurs at higher areas because it is necessary to compress less to approach nanoparticles. Moreover, as already suggested by the surface tension measurements, the effect of the ionic strength on the monolayer density is more marked for surfactants with longer chains, especially at the lowest surfactant concentration.

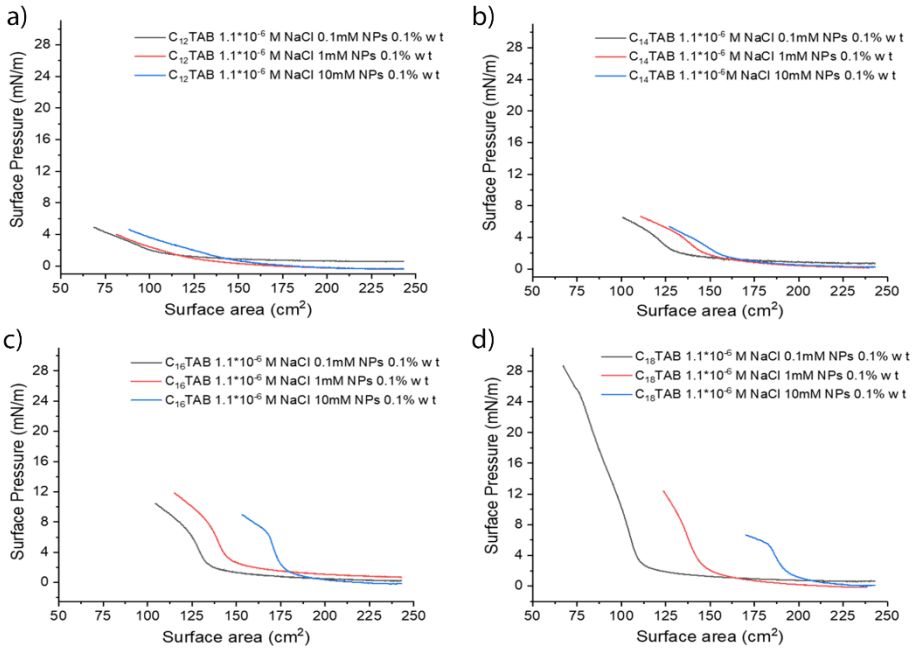

Figure 7.9. Compression isotherms of monolayer of C_nTAB 1.1*10^{-6} M, NPs 0.1% wt and increasing ionic strength: 0.1mM (black curves), 1mM (red curves) and 10mM (blue curves), for the different lengths of surfactant chain: $C_{12}TAB$ (a), $C_{14}TAB$ (b), $C_{16}TAB$ (c), $C_{18}TAB$ (d).

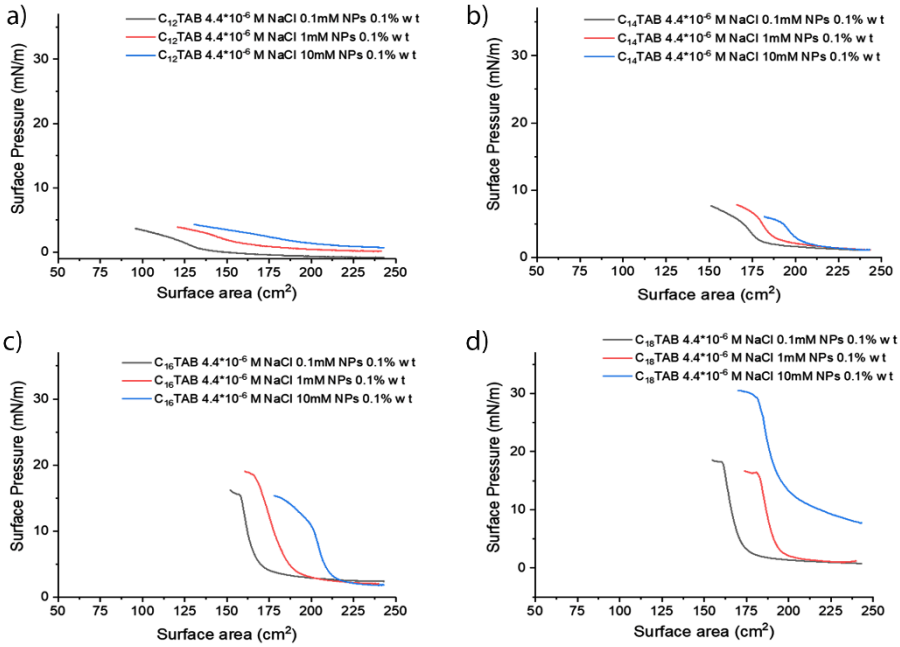

Figure 7.10. Compression isotherms of monolayer of C_nTAB 4.4*10^{-6} M, NPs 0.1% wt and increasing ionic strength: 0.1mM (black curves), 1mM (red curves) and 10mM (blue curves), for the different lengths of surfactant chain: $C_{12}TAB$ (a), $C_{14}TAB$ (b), $C_{16}TAB$ (c), $C_{18}TAB$ (d).

From the results obtained, it is evident that the increase in ionic strength is accompanied by a shift of the curves towards larger areas and a collapse of the monolayer due to minor compressions. This once again suggests that the ionic strength acts on the adsorption of the C_nTAB/NPs complexes at the interface, making the monolayer denser and less compressible. In addition, it shows more clearly what already suggested by the surface tension measurements. The increasingly pronounced effect on the monolayer compressibility with increasing the surfactant chain length, at the lowest concentration (Figure 7.9), confirms that the ionic strength contributes in determining the number of adsorbed nanoparticles but its contribution is intimately linked to the surfactant chain length. This confirms that the surfactant does not promote the nanoparticle adsorption by merely shielding the interfacial surface charges, but it decorates nanoparticles making them amphiphilic. As a matter of fact, its effect is enhanced by the ionic strength, which promotes its adsorption on silica surface[95] and, given the higher surface activity of surfactants with longer chains, the observed increase scales with the surfactant chain length. On the other hand, the less pronounced effect observed at the higher surfactant concentration may suggest that the number of surfactant molecules decorating each nanoparticle is already high enough and its variation with the ionic strength is not as marked as at the lower surfactant concentration. Interestingly, the combined effect of ionic strength and surfactant chain lengths also acts on the stiffness of the monolayer, as can be seen from the graphs reporting the slopes of the various isotherms (Figures 7.9 and 7.10), obtained from the linear best fit of the steepest sections. Figure 7.11 shows how the effect of the ionic strength at the lowest surfactant concentration is almost negligible for all the surfactant but C_{18}TAB while, at the higher concentration the effect less marked.

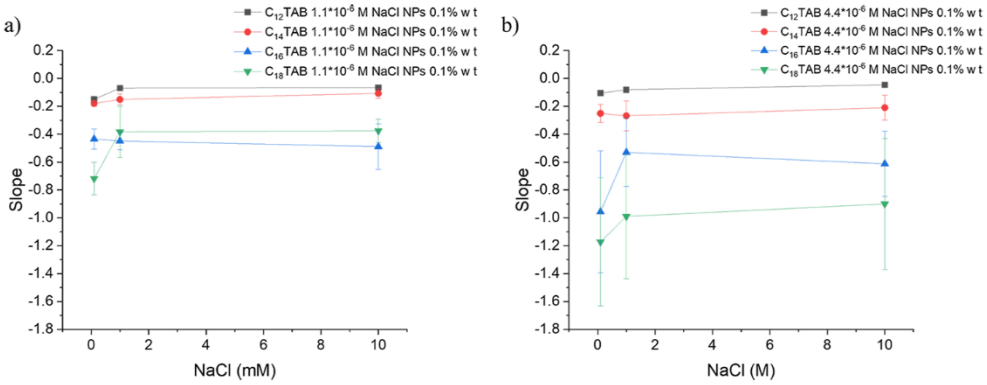

Figure 7.11. Slope variation of the compression isotherms as a function of the ionic strength, for CnTAB concentrations equal to $1.1*10^{-6}$M (a) and $4.4*10^{-6}$ M (b).

When considering the trends shown in Figure 7.11, the reported slopes only refer to the steepest part of the isotherms, that is to dense monolayers where particle are close to each other. Remarkably, the clear trend observed for C_{18}TAB shows that the main effect played by ionic strength on short-range interactions is on the electrostatic contribution, as the slope decrease, i.e. the inter-particle repulsions are stronger, with decreasing the ionic strength. This effect can be explained by considering that with decreasing the ionic strength electrostatic repulsions between adjacent nanoparticles are less screened and, thus, stronger. On the other hand, with increasing the ionic strength more surfactant molecules decorate each nanoparticle[95] therefore, stronger steric repulsions are expected giving rise to more negative slopes. The steric contribution to inter-particle repulsions increases with surfactant concentration and this may explain the weaker effect of the ionic strength at the $4.4*10^{-6}$ M surfactant concentration as well as, as shown by Figure 16, the more pronounced effect on stiffness played by surfactants having longer chain, whose concentration increase leads to systematically higher increase of the slope.

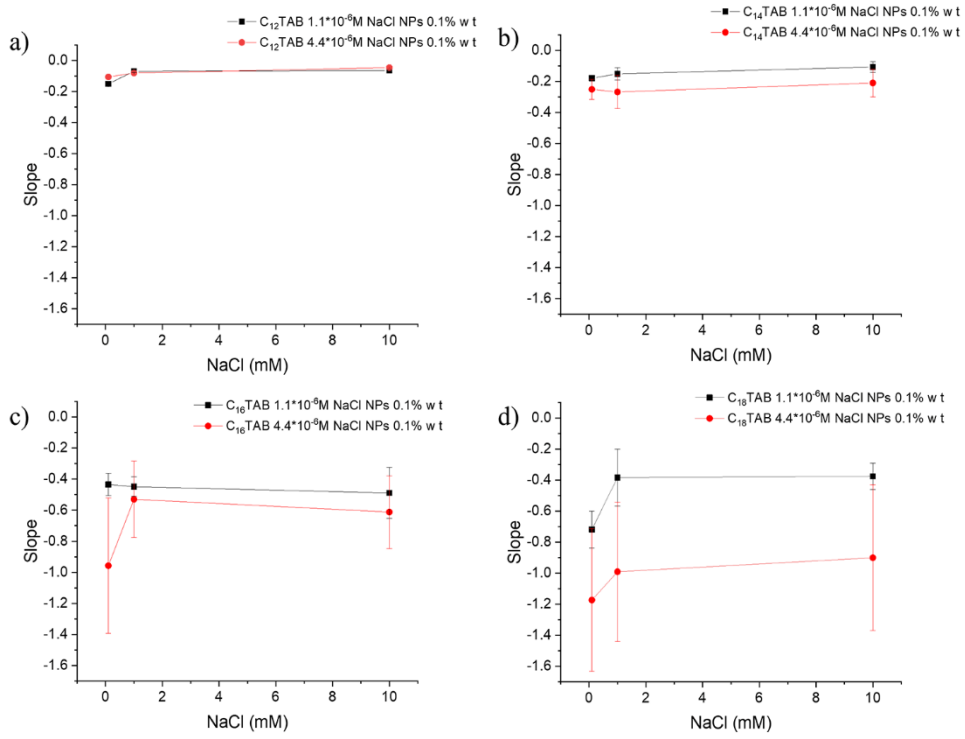

Figure 7.12. Slope variation of the compression isotherms as a function of the ionic strength, for C_nTAB concentrations equal to $1.1*10^{-6}$M (black spots) and $4.4*10^{-6}$ M (red spots), for each length of the hydrophobic chain: C_{12}TAB (a), C_{14}TAB (b), C_{16}TAB (c), C_{18}TAB (d).

Finally, the weakening of the steric contribution to repulsions between nanoparticles when shortening the surfactant chain length is confirmed by the higher stiffness recorded for C_{12}TAB-decorated nanoparticles at NaCl 0.1 mM and C_{12}TAB $1.1*10^{-6}$ M (Figure 7.12a). As the cationic surfactant decrease the negative charge of the nanoparticles, the electrostatic repulsions decrease with increasing the surfactant concentration. However, given the short surfactant chain this effect, unlike longer surfactants, is not counterbalanced by an increase of the steric repulsions leading to a less negative slope at C_{12}TAB $4.4*10^{-6}$M. Further insights into the nature of the inter-particle forces acting during the monolayer compression will be obtained by the structural characterization reported in the next chapter.

8) In situ structural characterization

The structure and stability of the interfacial monolayer depend on interparticle interactions along the asymmetrical environment.[96] Therefore, a greater understanding of such interactions would provide the possibility to modulate and adapt the structure of the monolayer and to optimize the resulting properties accordingly.[97] It was demonstrated that the structural characterization of monolayers and their responses to the induced deformations, provide valuable information on ongoing interface interactions.[98,99,100,101] These approaches are also valid for liquid interfaces where monolayers are made by NPs.[102,103] Previous studies have shown that in monolayers made by surfactant-decorated NPs, the variation of surfactant concentration changes the inter-particle distance.[80] It is therefore interesting to study how the interparticle distance can be modulated, as well as with the concentration of the surfactant, also as a function of the length of the hydrophobic chain. To this end, synchrotron radiation grazing incidence small angle X-ray scattering (GISAXS) was employed to characterize the structure of the monolayers in the presence of NPs 0.1% wt., NaCl 1mM and C_nTAB. Mixed dispersions of C_nTAB/NPs/NaCl at different surfactant concentrations were poured into a Teflon trough, allowed to equilibrate for 30 minutes (since the graph in figure S2.2 of the appendices shows that, after 30 minutes, the solution had already reached the equilibrium, as no more variations of the surface pressure are observed for longer times), and then illuminated by a monochromatic 8 keV X-ray beam with an incident angle of 0.113°, leading to a characteristic diffraction pattern (schematic representation in Figure 8.1). As it is evident in the diffraction pattern shown in Figure 8.1, the NPs scatter the radiation generating two intense symmetrical Bragg rods. These signals are obtained only in the presence of the C_nTAB/NPs complexes since, as shown in Figure S2.10 in the appendices, the absence of surfactant or NPs does not allow to record any signal. This confirms the hypothesis that the adsorption of NPs at the interface requires the

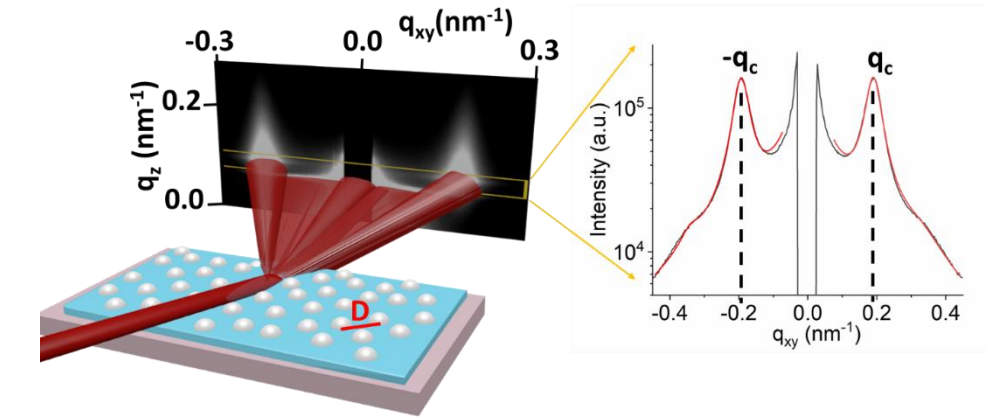

Figure 8.1. Schematic representation of the GISAXS experiment. The NPs adsorbed at the interface, scatter the radiation, generating two white Bragg rods detected by the 2D detector (black). Considering the intensity recorded inside the yellow box in the figure and by integrating the signals, it is possible to obtain the peaks shown in the figure. These peaks are then fitted to trace the position of the peak q_c, which provides useful information for determining the inter-particle distance.

decoration of their surface by the surfactant molecules, resulting in the formation of the C_nTAB/NPs complexes[35] or enabling the absorption by image charge screening.[91] In addition, the recorded diffraction patterns confirm that interfacial adsorption leads to the formation of a monolayer. If multilayers were formed, the NPs would be correlated also out of the plane, resulting in modulation of the signal along q_z and diffraction spots for $q_z > 0$.[104] Furthermore, quantitative information can be obtained from the diffraction patterns, making horizontal cuts (yellow box in Figure 8.1) to then integrate the signals and convert them into reciprocal space, using script 1 in the appendices. Thus, 1D intensity graphs are obtained as a function of the scattering vector in the xy plane, as reported in Figure 8.1, showing, in addition to the main Bragg peak positioned at q_c, a weak peak between $\sqrt{3}q_c$ and $2q_c$, i.e. at the positions of the hexagonal assembly (11) and (20) peaks.[105] GISAXS patterns suggest the formation of amorphous monolayers, in which each NPs has an average local coordination of six.[80,106] Based on the above, it is possible to determine the inter-particle distance and how it evolves with surfactant concentration, using the following equation:

$$D = \frac{4\pi}{q_c\sqrt{3}} \qquad \textit{Equation 8.1}$$

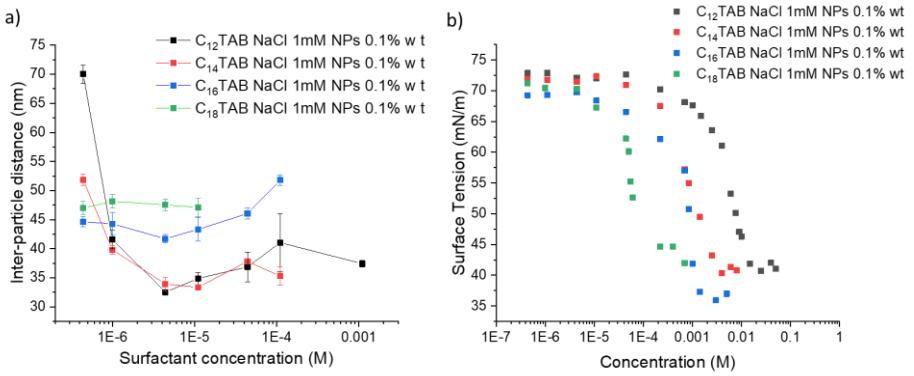

Figure 8.2 *(a)* Interparticle distance measured as a function of C_nTAB concentration with NPs 0.1%wt and NaCl 1mM. The gradual increase in the C_nTAB concentration involves a reduction in the interparticle distance. (b) Trend of the surface tension as the surfactant concentration varies.

where q_c is the position of the (10) peak obtained by performing a Lorentzian fit on the 1D graphs, (see appendix, Figures S2.11-S2.14) using script 2 in the appendices, extracted from the diffraction patterns, as the concentration and chain length of the surfactant vary. The results shown in Figure 8.2, allow to highlight the surprising role of the surfactant in the interfacial nanostructuring. Although at low concentrations of surfactant Figure 8.2 b shows no variations of the surface tension compared to pure water, in the sub-micromolar regime significant variations of the monolayer density already occur, as demonstrated by the marked dependence of the interfacial inter-particle distance on both surfactant chain length and concentration (Figure 8.2 a). In particular, the surfactant thus facilitates the adsorption of NPs at the interface, with a greater modulation with concentration of the monolayer density for shorter chains. In particular, the interparticle distance is adjustable over a range of 40nm is recorded for $C_{12}TAB$ at concentrations between $4.4*10^{-7}$ and $4.4*10^{-6}$M (Figure 8.3 a). This modulation appears reduced for surfactant with two more carbon atoms in the hydrocarbon chain while, for surfactants having longer chains the inter-particle distance at low surfactant bulk concentrations is mostly unaffected by the concentration. The herein reported effect of the surfactant nature of the monolayer density, which is fully consistent with the one hypothesized from the compression isotherms reported in the previous chapter, may be due either to the lower surface activity of surfactants with shorter chain lengths, which requires higher concentrations to make nanoparticles surface active enough to form dense monolayers, or to the lower steric interactions which allow, with increasing the surfactant concentration, the adsorption of more surfactant molecules on each nanoparticles thus, leading to a broader range of attainable inter-particle distance.

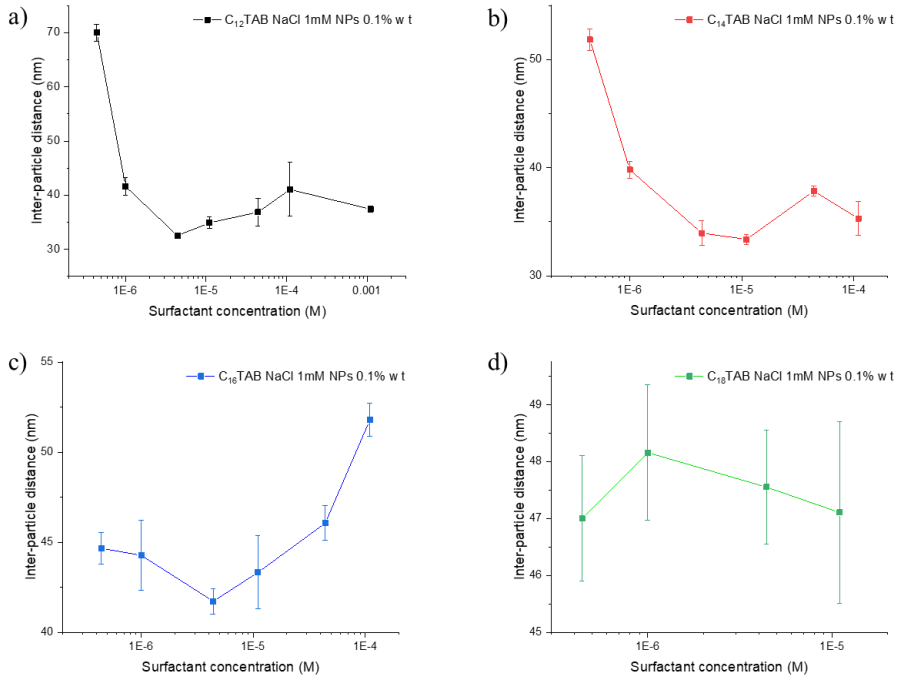

Figure 8.3. Interparticle distance variation as a function of the surfactant concentration, for the different chain lengths: C_{12}TAB (a), C_{14}TAB (b), C_{16}TAB (c), C_{18}TAB (d).

Interestingly, further increases of the surfactant concentration do not change the inter-particle distance or they even lead to its increase. It follows that, at high concentrations, free surfactant molecules adsorb massively at the interface leading to higher interparticle distances. Moreover, Maestro et al. studying C_{16}TAB/NPs complexes showed that, above a certain threshold concentration, the surfactant forms double layers on the aqueous side of the NPs,[69], which may lead to an increase in the interparticle distance. However, in our systems, the minimum lateral separations between the NPs as a function of the surfactant length, are between ~8 and ~20 nm (Figure 8.3, by subtracting to the inter-particle distance the 25 nm NP diameter), well above the average surfactants length, between ~2.3 and 3 nm.[107] Therefore, it is likely that the adsorption of free surfactant molecules at the surface is the main contribution to the increase of the interparticle distance with surfactant concentration. Therefore, at low C_nTAB/NPs ratios, the adsorption at the interface mainly involves NPs decorated by surfactants, with a coverage density that is a function of the lengths of the hydrophobic chains and, especially for the shortest chains, of the surfactant concentration. Above a threshold concentration, the increase of the surfactant concentration is instead accompanied by an increase of the free surfactant molecules adsorbed at the interface.

Quantitative information about interparticle interactions as a function of the chain length and their dependence on distance can be obtained by carrying out compression isotherms in a Langmuir trough and by simultaneously recording the structural modification by means of GISAXS. In particular, the compressions were carried out at low C_nTAB/NPs ratios in order to exclude the adsorption of free surfactant at the interface and to be able to attribute the effects obtained to the complexes at the interface. The compression isotherms shown in Figures 8.4 and 8.5 for the different lengths and concentrations of the surfactants confirm the trends shown in Figure 7.5 in the previous chapter. In particular, it is possible to observe a dependence of the collapse pressure on the nature of the surfactant, which increases as a function of the chain length.

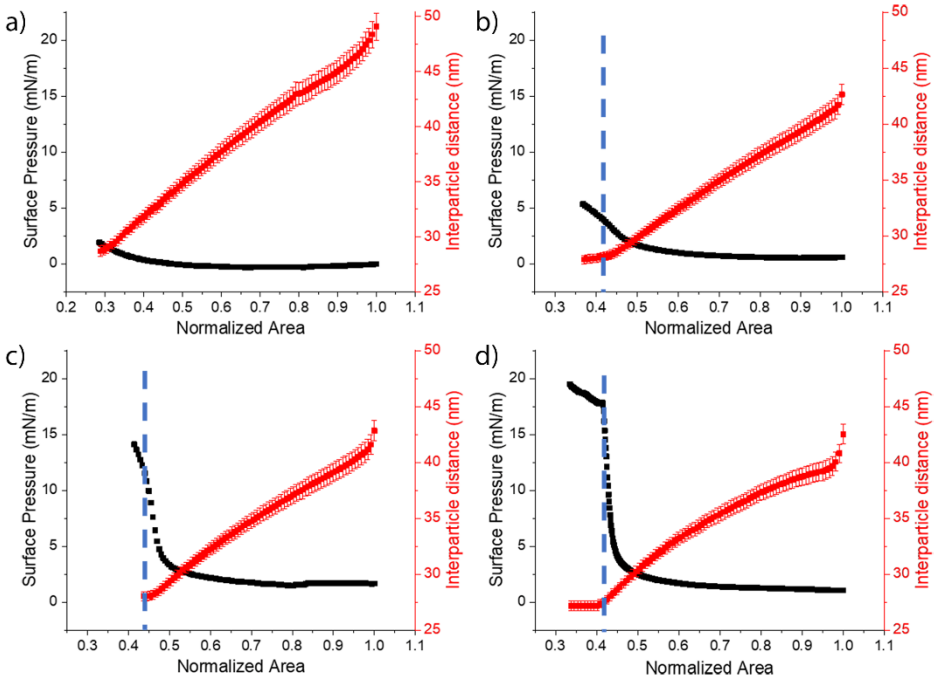

Figure 8.4. Interparticle distance variation during compression for CnTAB $1.1*10^{-6}$ M NaCl 1 mM NPs 0,1%wt, for the different chain lengths: C_{12}TAB (a), C_{14}TAB (b), C_{16}TAB (c), C_{18}TAB (d). The change of distance (red symbols) is correlated to the corresponding compression isotherms (black symbols). The compression leads to the gradual approach of the interfacial NPs up to the collapse of the monolayer (dashed light blue lines), after which the interparticle distance is constant, regardless of the degree of compression.

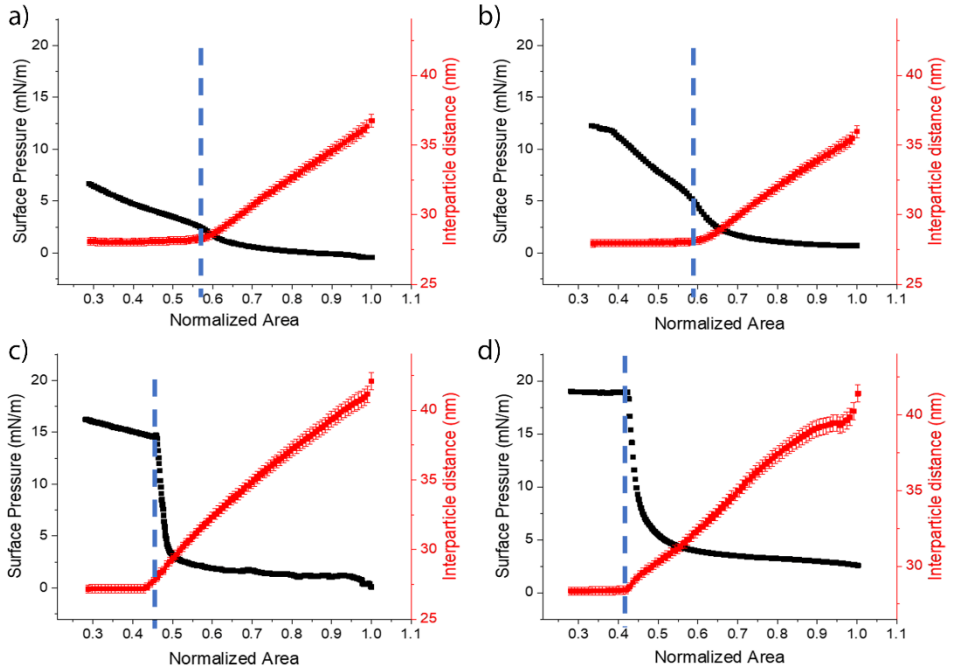

Figure 8.5. Variation of the interparticle distance during compression for C_nTAB 4.4*10^{-6} M NaCl 1 mM NPs 0,1%wt, for the different chain lengths: $C_{12}TAB$ (a), $C_{14}TAB$ (b), $C_{16}TAB$ (c), $C_{18}TAB$ (d). The change of distance (red symbols) is correlated to the corresponding compression isotherms (black symbols). The compression leads to the gradual approach of the interfacial NPs up to the collapse of the monolayer (dashed light blue lines), after which the interparticle distance is constant, regardless of the degree of compression.

In addition, the Figures 8.4 – 8.5 show a linear reduction of the interparticle distance with compression, which indicates a homogeneity of the monolayer. Since, in the presence of surface heterogeneity, such as aggregates or voids, discontinuities would be observed in the interparticle distance variation as a function of the compression. Furthermore, the trends obtained show that the interparticle distance at which the collapse occurs does not to depend either on the concentration or the nature of the surfactant. With the exception of $C_{12}TAB$ 1.1*10^{-6}M, which does not seem to reach collapse, as also observed in the previous chapter (Figure 7.5 a), in the other cases, a distance of about 28 nm is observed at the collapse point. Therefore, the complexes adsorbed at interface tend to approach each other with the compression, as confirmed by the reduction of the distance reported in Figure 8.4 and 8.5, until the collapse point, beyond which no variation in distance is observed, for further compressions. In addition, even after the collapse, the recorded GISAXS patterns continue to show Bragg rods, characteristic of a 2D monolayer (Figures S2.15-2.16). Therefore, contrary to what is observed in the literature for other systems,[108,109] the desorption of NPs occurs by redispersion in water rather than by expulsion in air.

This may be attributed to the highly hydrophilic nature of the NPs employed.[87] In addition, it is possible to obtain information on the arrangement of the surfactant that decorates the NPs at the interface, known the particle diameter, i.e. about 24.55 nm, and the interparticle distance at the collapse. In particular, a lateral separation between the particles equal to 3.45 nm is obtained. Since, the maximum extension of the headgroup of surfactants is equal to 0.6nm[110] while the maximum extension for a chain made by n carbon atoms is equal to $0{,}15 + 0.1265 * n$ nm[107], the lateral separation at the point of collapse is well below the length of two fully stretched surfactant molecules since the C_{12}TAB is 2.27nm length, C_{14}TAB 2.52nm, C_{16}TAB 2.77nm and C_{18}TAB 3.03nm. Therefore, it is reasonable to think that there is interpenetration between chains that adhere to adjacent particles and this confirms that, at the short range, steric forces play a considerable role. Additional information may be determined about the nanostructure of the monolayer and the extent of repulsive interactions as a function of the surfactant nature. As the GISAXS characterization allows to accurately measure the interparticle distance during compression, it is possible to evaluate the number of NPs present at the interface during compression, knowing the surface area and the interparticle distance.

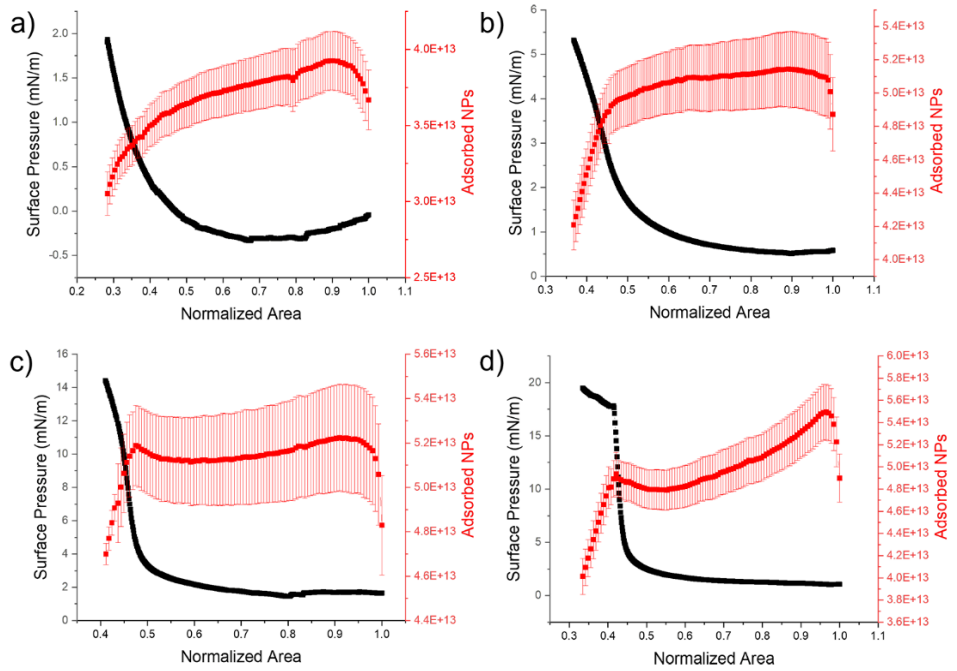

Figure 8.6. Adsorbed NPs (red curves) calculated from the average distance between particles as a function of compression for C_nTAB 1.1*10^{-6}M NaCl 1mM NPs 0.1%wt. shown together with the corresponding compression isotherms (black curves) for the different chain lengths: C_{12}TAB (a), C_{14}TAB (b), C_{16}TAB (c), C_{18}TAB (d). Given the high desorption energy, the number of adsorbed NPs decreases with compression only after the collapse of the monolayer.

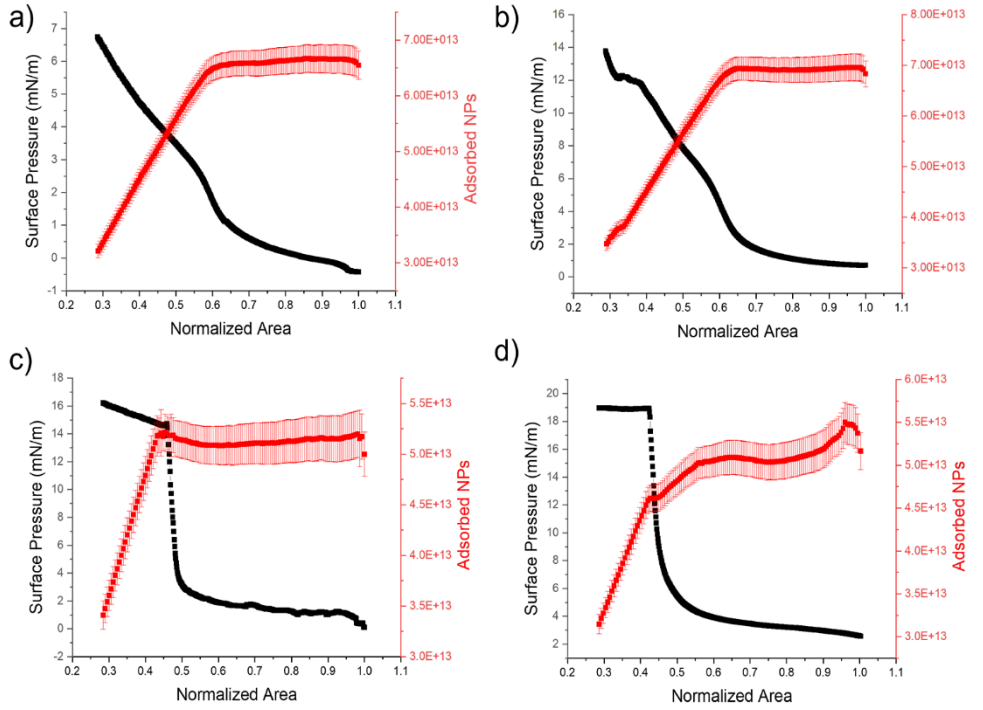

Figure 8.7. Adsorbed NPs (red curves) calculated from the average distance between particles as a function of compression for CnTAB 4.4*10^{-6}M NaCl 1mM NPs 0.1% wt. shown together with the corresponding compression isotherms (black curves) for the various chain lengths: C_{12}TAB (a), C_{14}TAB (b), C_{16}TAB (c), C_{18}TAB (d). Given the high desorption energy, the number of adsorbed NPs decreases with compression only after the collapse of the monolayer.

The results reported in Figures 8.6 and 8.7 show that the number of adsorbed NPs is approximately constant during compression. This is due to the high desorption energy,[96] which allows the NPs desorption only after the collapse of the monolayer. Given the constant number of NPs at the interface before the collapse, the compression of the monolayer can be seen as the work to exert to approach particles.[103,111] Moreover, the work of compression (W) before collapse will be equal to:

$$W = \Delta\Pi \cdot \Delta A \qquad \textit{Equation 8.2}$$

where $\Delta\Pi$ is the increase of surface pressure and ΔA is the area reduction during compression. Since the number of adsorbed particles is known, the compression work per single particle, W_{NP}, can be calculated. Once this compression work is determined by taking into account the hexagonal assembly,[80] for small variations on

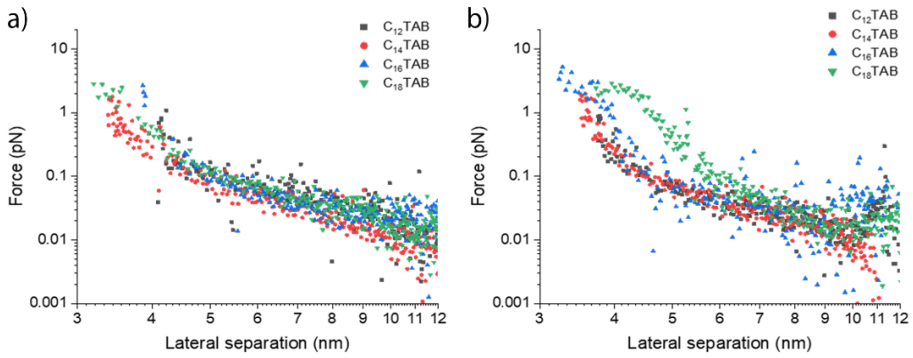

Figure 8.8. Interfacial inter-particle forces calculated from GISAXS data for the different surfactants C_nTAB 1.1* 10^{-6} M NaCl 1 mM NP 0.1% wt (a) and C_nTAB 4.4*10^{-6} M NaCl 1 mM NP 0.1 % wt (b) as a function of the distance between the particles.

the interparticle distance, dD, it is possible to determine the interparticle repulsive interactions that oppose the approach:

$$F(D) = \frac{W_{NP}}{6 \cdot dD} \qquad \textit{Equation 8.3}$$

where F(D) is the interparticle repulsion dependent on interparticle distance. Figure 8.8 shows the trend of the so-obtained forces as a function of the lateral separation. The results show that the interparticle repulsions extend for about two orders of magnitude and depend on the interparticle distance. Two distinct regimes can be identified, according to what is reported in the literature,[90] in which the interparticle forces act respectively at long range, for lateral separations between 10 and about 4 nm, so that surfactant-decorated NPs are not in direct contact, and short-range forces, for lateral separations lower than 4 nm, where it can be assumed that surfactant molecules decorating the NPs are in contact with each other and can interpenetrate. Furthermore, the trends shown in the Figure 8.8 show a dependence on the inverse power law with lateral separation, which suggests an electrostatic nature of the interactions, given the highly charged surface of the NPs.[90] Conversely, the notable increase in short-range repulsive forces, suggests the predominance of the steric contribution, which can reach values up to a few pN.[112] Furthermore, as can be seen in Figure 8.8, the slope and extent of the long-range forces are constant. Therefore, assuming that the density of functionalization is not affected by the chain length and considering that the polar head of all surfactants has the same charge, it can be assumed that in this range the predominant repulsive force have electrostatic nature. On the other hand, the observed behaviour is different for short-range interactions, which seem to depend on the concentration and nature of the surfactant. In particular, for lower surfactant concentrations, Figure 8.8a, the onset of short-range forces

occurs at about 4 nm, regardless of the chain length. This suggests a low adhesion density of the surfactant on the NPs, consequently giving the chains a coiled conformation. For higher surfactant concentrations, Figures 8.8b, there is a shift in the onset of steric interactions towards higher lateral separations for longer chains, which indicates a greater surface coverage density of the NPs. The result supports the hypothesis of the modifier nature of the surfactant[70,92], as the decoration of the NPs by surfactants directly influences the collapse distance, which increases with increasing the chain length. Furthermore, the chain length significantly influences the slope of the curve, which decreases with increasing the chain length. This slower increase of forces can be related to the higher entropic gains, in the case of longer chains, associated with conformational variation from extended to coiled chains. Therefore, it becomes possible to assume that the mechanism can be driven by entropic factors and, in particular, by the flexibility of the chains.

8.1) Interfacial nanostructuring: effect of NP size

A further study of the interfacial nanostructure was conducted using NPs with different diameters. In particular, we employed silica nanoparticles (Sicastar) with a diameter of 19nm ± 1.4nm[80], decorated with C_{16}TAB. Also in this case, surface tension measurements were conducted as a function of surfactant concentration, in the presence of NaCl 1mm and NPs 0.1%wt, to then characterize the structure by GISAXS synchrotron radiation and determine the interparticle distance, using Equation 8.1. The results obtained are shown in Figure 8.9, where it is possible to observe, once again, the surprising role of the surfactant on the adsorption process of NPs at the interface. The trend of the first part of the curve shown in Figure 8.9a suggests that for surfactant concentrations between $4.4*10^{-7}$ M and $4.4*10^{-6}$ M, the surface activity of surfactant-decorated NPs increases. It follows an increase of the density of NPs adsorbed and the formation of monolayers with an interparticle distance adjustable in a range of 20 nm. By further increasing the concentration of C_{16}TAB, the interparticle distance increases again and the surface tension decreases dramatically (Figure 8.9b). In Figure 8.9c it is reported how, as the size of the NPs varies, the ability to modulate the interparticle distance and consequently the interfacial nanostructuring varies. It would seem that in the presence of smaller NPs, with the same surfactant concentration, the interparticle distance is much more modulable than that observed for larger ones. Although the difference in particle size is about 6 nm, the variation in the resulting behaviour is very high.

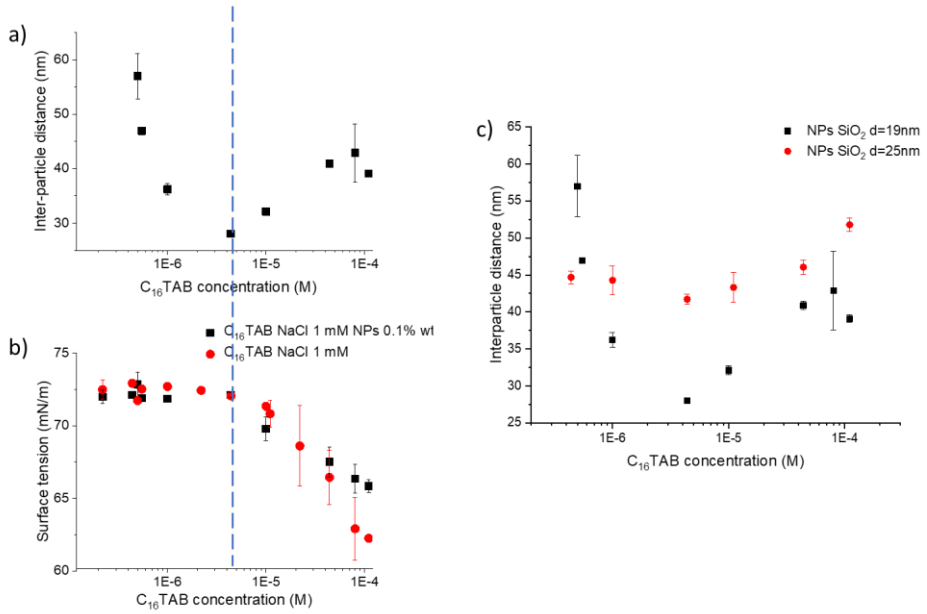

Figure 8.9. (a) Interparticle distance measured as a function of the bulk concentration of C_{16}TAB for the dispersion of silica NP 0.1% wt in the presence of NaCl 1mM. The increase in the surfactant concentration leads to an increase in the amount of NPs adsorbed at the interface, with a consequent reduction in the interparticle distance. The lowest particle distance is achieved at the same C_{16}TAB concentration required to start the surface tension reduction (b, dashed line). (c) Variation of the interparticle distance with the same surfactant concentration but with NPs having different diameters. More marked shift for smaller particles.

Also in this case, as observed in Figure 8.2a, the minimum interparticle distance value shown in Figure 8.9a corresponds to a lateral separation significantly greater than the thickness of two double layers of C_{16}TAB adsorbed on the SiO_2 surface. It follows that, at higher concentrations, free surfactant molecules adsorb at the interface, with a consequent increase of the interparticle distance and a reduction in surface tension (Figure 8.9a, b). Compression isotherms were performed at low C_{16}TAB/NPs ratios, by acquiring GISAXS diffraction patterns during compression, in order to characterize their structure. The increase of the surfactant concentration once again leads to a reduction of the monolayer compressibility, since the increase of the interfacial density of NPs requires smaller compressions to induce the surface pressure increase (Figure 8.10 red lines).

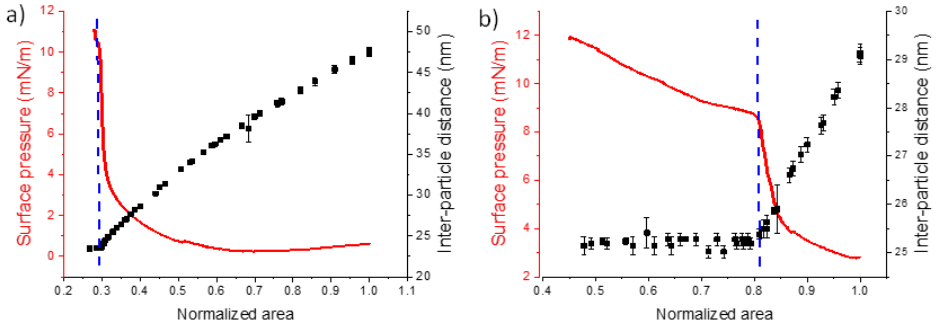

Figure 8.10. Interparticle distance variation during compression for CTAB 4.4 *10^{-7} M NaCl 1 mM NP 0.1% wt (a) and CTAB 4.4*10^{-6}M NaCl 1mM NP 0.1%wt(b) monolayers (black symbols) with respect to the corresponding compression isotherms (red curves). The dashed lines in blue indicate the collapse of the monolayer, beyond which, the interparticle distance, regardless of the degree of compression, remains constant.

From the interparticle distance reported in Figure 8.10, it is possible to observe how the compression induces a gradual approach of the NPs, with a strong increase of the surface pressure for distances of about 25 nm. Furthermore, the initial surface pressure increase occurs for relatively large areas and distances of about 30-35nm, suggesting long-range interactions that act when the NPs are not in direct contact. It is also evident that the interparticle distance at which the surface pressure begins to increase dramatically, as well as the threshold distance at which the monolayers collapse, are related to the concentration of the surfactant. For lower surfactant concentrations, the increase of surface pressure, as well as the collapse of the monolayer, occur at shorter interparticle distances. What was observed is attributable to the fact that the NPs are less screened (greater electrostatic repulsions)[69] and this underlines the important role of surfactant in the interactions involved. Furthermore, for 4.4*10^{-7} M, a lateral separation of 4.5 nm is recorded at the threshold distance, comparable to the length of two partially interpenetrated surfactant molecules, having the C_{16}TAB completely extended at a length of 2.8 nm.[107,110] For higher concentrations, on the other hand, a lateral separation of 6 nm is recorded, close to the thickness of two double layers adsorbed at the NPs/water interface.[22] Compression induces a phase transition, regardless of the surfactant concentration leading to the formation of a solid glass phase.[113,114,115] This can be revealed both by reducing the intensity of the GISAXS peak with compression (Figure 8.11 a, b) and by measuring the average correlation length, i.e. the average size of the ordered domains. To determine the average number of NPs, the correlation length must be normalized with respect to the interparticle distance, D, since, due to the significant variation of the distance with compression, the lengths to the various stages of compression are not comparable.

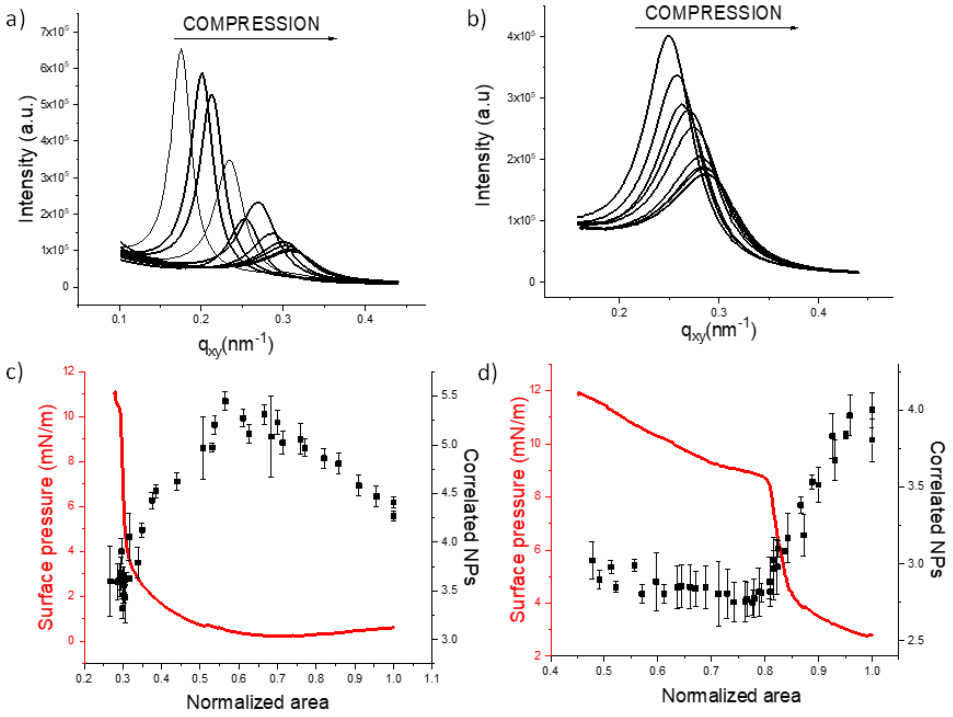

Figure 8.11. Evolution of the horizontal cut of the GISAXS Bragg rod with compression for the NP 0.1% wt NaCl 1 mM CTAB 4.4 * 10^{-7} M (a) and CTAB 4.4 * 10^{-6}M (b). The shift of the peak towards higher q_{xy} indicates the approach of the NPs induced by the compressions, while the reduction in intensity and the increase of amplitude are attributed to the further amorphization induced by compression to the monolayers. (c) Evolution of correlated NPs during compression for CTAB 4.4 * 10^{-7} M (c) and CTAB 4.4 * 10^{-6}M (d) (black symbols) with respect to the corresponding compression isotherms (red lines).

It follows that the correlation length will be equal to:

$$\frac{2\pi/w}{D} \qquad \textit{Equation 8.4}$$

where w is the FWHM of the diffraction peak determined by GISAXS. Figure 8.11c and d shows the evolution of the number of correlated NPs with compression. The trends obtained show a reduction in the domain size normalized with compression, confirming that compression, rather than leading to an increase in the 2D order, leads to the formation of an amorphous glassy layer. Furthermore, also in this case, it is possible to determine the compression work, using Equation 8.2, in order to determine the repulsions between the particles, using Equation 8.3.

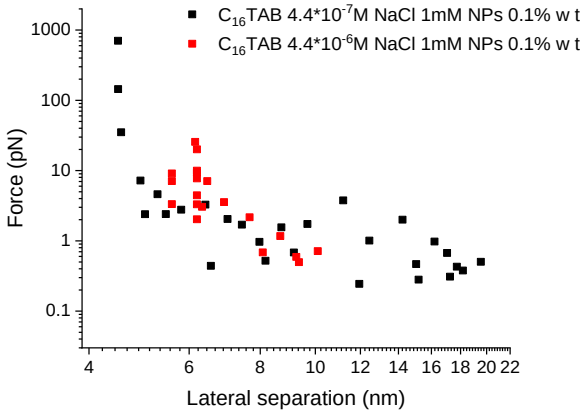

Figure 8.12. Interparticle interfacial forces for C_{16}TAB 4.4*10^{-7} M NaCl 1 mM NP 0.1% wt (black) and C_{16}TAB 4.4*10^{-6} M NaCl 1mM NP 0.1% wt (red) as a function of distance between the particles.

The trend obtained is shown in Figure 8.12, where it is evident how the interparticle repulsions extend over three orders of magnitude and depend on the bulk concentration of C_{16}TAB and the interparticle distance. At lower surfactant concentrations, black spots in Figure 8.12, it is possible to identify, also in this case, as obtained in the previous chapter, two different regimes: long range, for lateral separation between 20 and 6 nm, attributable to electrostatic interactions and short range below 6 nm, when the NPs are close enough to consider the surfactant molecules in contact. The order of magnitude of the forces in question is comparable to what is reported in the literature.[116] Contrary to what is observed in Figure 8.8b, in the case of smaller NPs, the repulsive interactions of C_{16}TAB at a concentration equal to 4.4*10^{-6} M are restricted to a smaller interval. This suggests that the aqueous sides of the adsorbed NPs are surrounded by double layers of C_{16}TAB that generate electrostatic interactions.

The reason why the double layer forms on Sicastar nanoparticles and it doesn't on Ludox ones is not known yet, as the different interfacial charge, the different size and possible differences of the interfacial smoothness may all concur in affecting the surfactant adsorption and self-assembly.

9) Summary and outlook

Surfactants having the same polar head but different hydrophobic chain length, guide the interfacial assembly of the NPs in a different way. Each surfactant leads to the formation of ordered 2D interfacial assemblies but the lateral separation between the adsorbed particles is modulated in a different way. The results obtained show that the shorter is the chain, the greater is the modulation of the interfacial structure. With the same concentration, the interface occupied by the NPs decorated with C_nTAB is a function of the chain length. At low surfactant/NPs ratios a greater reduction of surface tension is observed for surfactants having longer chains, while the corresponding interparticle distance will be smaller than that recorded, at the same concentration, for shorter chains. The full understanding of this behaviour requires further investigation, as it may be caused either by the lower surface activity of surfactants with shorter chains or by the hydrophobic and steric interactions between the chains of molecules adsorbed on each nanoparticle. However, a general trend with concentration can be rationalized in terms of two distinct regimes. In particular, at low ratios, the adsorption should mainly involve the NPs decorated by surfactants, at higher ratios, the simultaneous adsorption of the C_nTAB/NPs complexes and free surfactant should occur. Therefore, additional studies were carried out at low C_nTAB/NPs ratios in order to avoid the presence of free surfactant adsorbed at the interface and to be able to ascribe the effects on the compression of the monolayers of the surfactant chain length. The compression isotherms at low C_nTAB/NPs ratios allow further modulation of the interparticle distance, where a small influence is observed from the composition of the surfactant. In particular, variations of the compressibility of the monolayer are observed as a function of the length and concentration of the surfactant under examination; as monolayers are less compressible with increasing chain length and concentration of C_nTAB. On the other hand, the structural characterization shows that the interparticle distance at which the collapse of the monolayer occurs does not depend, for Ludox particles, on either the concentration or the chain length. As a consequence, the compression-induced interpenetration of the chains attached to the adjacent particles is hypothesized and the compression behaviour is then dominated by steric repulsions. The structural characterization during compression allows to identify and to quantify the interparticle forces involved, identifying, in particular, two regimes of interparticle forces involved. Long-range forces, characterized by a predominant electrostatic contribution, are independent from the concentration and length of the C_nTAB while short-range forces have steric nature and depend on the nature and concentration of C_nTAB. Further modulation of the interfacial structure was obtained by changing the ionic strength of the system, since the ions in the solution help to screen the

electrostatic repulsions, favouring the decoration of nanoparticles by the surfactant. This leads to the adsorption of more nanoparticles at the interface and, as a result, to the decrease of the monolayer compressibility with increasing the ionic strength. This effect is more pronounced for longer chains and lower concentrations, making the effect of ionic strength intimately related to the nature of the surfactant. The ionic strength then enhances the modifier character of the surfactant, as it decorates the nanoparticles making them amphiphilic. The combined effect of the ionic strength and the length of the surfactant also acts on the rigidity of the monolayer. In particular, the increase of the monolayer density, obtained with the increase of the ionic strength, involves an increase of the steric repulsions, which are connected to the nature and the concentration of the surfactant, with increased slope for higher chain concentrations and lengths. The decrease of chain length, conversely, leads to a weakening of the steric contribution, which are not able to counterbalance the reduction of electrostatic interactions related to the increase of the surfactant concentration, recording, as a result, less negative slope. However, it was not possible to carry out structural characterizations on the systems under examination as a function of the ionic strength, due to the unavailability of the time machine at the synchrotron structures. The results obtained provide a contribution to the full understanding the assembly and forces between particles in asymmetrical environments. A new methodology, allowing to simultaneously determine the average interparticle distance and to trace the repulsive forces that come into play, is presented. In this way, it seeks to aid the design and synthesis of functional NPs monolayers and membranes with customized structures and properties. The fluid interfaces can therefore act as scaffolds for the manufacture of soft materials, whose mechanical stability is based on the interfacial assembly of colloidal particles. The control of the adsorption and organization of colloids at the fluid interface is therefore receiving increasing interest, in order to manufacture 2D materials with precise order and composition. The full understanding of the chemical and physical processes is still a challenge due to the multiple parameters that influence the interfacial morphology. A greater understanding of the interactions involved could provide the possibility to properly design the material in order to obtain the desired functions. This knowledge will therefore allow these systems to be applied also in the industrial field, where reliability, speed as well as ease and the ability to use economic strategies are fundamental.

References

(1) Iv, X. L.; Franklin, B.; Brownrigg, F. R. S. W.; Farifti, M. Of the Stilling of Waves by Means of Oil. Extracted from Sundry Letters between Benjamin Franklin.

(2) Pershan, P. S.; Schlossman, M. *Liquid Surfaces and Interfaces: Synchrotron X-Ray Methods*; 2012; Vol. 9780521814. https://doi.org/10.1017/CBO9781139045872.

(3) Physics, S.; September, R. Translation of J . D . van Der Waals ' " The Thermodynamic Theory of Capillarity Under the Hypothesis of a Continuous Variation of Density ' ' 1. **1979**, *20* (2), 1975–1978.

(4) Young, T. An Essay on the Cohesion of Fluids. *Phil. Trans. Roy. Soc.* **1804**, *95*, 65–87.

(5) Maestro, A. Tailoring the Interfacial Assembly of Colloidal Particles by Engineering the Mechanical Properties of the Interface. *Curr. Opin. Colloid Interface Sci.* **2019**, *39*, 232–250. https://doi.org/10.1016/j.cocis.2019.02.013.

(6) Böker, A.; He, J.; Emrick, T.; Russell, T. P. Self-Assembly of Nanoparticles at Interfaces. *Soft Matter* **2007**, *3* (10), 1231–1248. https://doi.org/10.1039/b706609k.

(7) Maestro, A.; Guzmán, E. Colloids at Fluid Interfaces. *Processes* **2019**, *7* (12), 1–19. https://doi.org/10.3390/PR7120942.

(8) Maestro, A.; Deshmukh, O. S.; Mugele, F.; Langevin, D. Interfacial Assembly of Surfactant-Decorated Nanoparticles: On the Rheological Description of a Colloidal 2D Glass. *Langmuir* **2015**, *31* (23), 6289–6297. https://doi.org/10.1021/acs.langmuir.5b00632.

(9) Guzmán, E.; Santini, E. Lung Surfactant Models and Particles at Fluid Interfaces:Making Preliminary Toxicity Assessments of Inhaled Particles. *Curr. Opin. Colloid Interface Sci.* **2019**. https://doi.org/10.1016/j.cocis.2019.01.003.

(10) Sulin Zhang, H. G. and G. B. Physical Principles of Nanoparticle Cellular Endocytosis. *ACS Nano* **2015**, 8655–8671.

(11) Narayanan, T.; Konovalov, O. Synchrotron Scattering Methods for Nanomaterials and Soft Matter Research. *Materials (Basel).* **2020**, *13* (3). https://doi.org/10.3390/ma13030752.

(12) Vialetto, J.; Anyfantakis, M. Exploiting Additives for Directing the Adsorption and Organization of Colloid Particles at Fluid Interfaces. *Langmuir* **2021**, *37* (31), 9302–9335. https://doi.org/10.1021/acs.langmuir.1c01029.

(13) Liu, D.; Cai, W.; Marin, M.; Yin, Y.; Li, Y. Air-Liquid Interfacial Self-Assembly of Two-Dimensional Periodic Nanostructured Arrays. *ChemNanoMat* **2019**, *5* (11), 1338–1360. https://doi.org/10.1002/cnma.201900322.

(14) Santini, E.; Ravera, F.; Ferrari, M.; Alfè, M.; Ciajolo, A.; Liggieri, L. Colloids and Surfaces A : Physicochemical and Engineering Aspects Interfacial Properties of Carbon Particulate-Laden Liquid Interfaces and Stability of Related Foams and Emulsions. **2010**, *365*, 189–198. https://doi.org/10.1016/j.colsurfa.2010.01.041.

(15) Bresme, F.; Oettel, M. Nanoparticles at Fluid Interfaces. *J. Phys. Condens. Matter* **2007**, *19* (41). https://doi.org/10.1088/0953-8984/19/41/413101.

(16) Razavi, S.; Kretzschmar, I.; Koplik, J.; Colosqui, C. E.; Razavi, S.; Kretzschmar, I.; Koplik, J.; Colosqui, C. E. Nanoparticles at Liquid Interfaces : Rotational Dynamics and Angular Locking Nanoparticles at Liquid Interfaces : Rotational Dynamics and Angular Locking. **2014**, *014904*. https://doi.org/10.1063/1.4849135.

(17) Varga, I.; Campbell, R. A. General Physical Description of the Behavior of Oppositely

Charged Polyelectrolyte/Surfactant Mixtures at the Air/Water Interface. **2017**. https://doi.org/10.1021/acs.langmuir.7b01288.
(18) Ballauff, B. M. Self-Assembly Creates 2D Materials. *Science (80-.).* **2016**, 2–4.
(19) Garbin, V.; Garbin, V. Colloidal Particles: Surfactants with a Difference. **2013**, *66* (10), 1–3. https://doi.org/10.1063/PT.3.2158.
(20) Yazhgur, P. A.; Noskov, B. A.; Liggieri, L.; Lin, S. Y.; Loglio, G.; Miller, R.; Ravera, F. Dynamic Properties of Mixed Nanoparticle/Surfactant Adsorption Layers. *Soft Matter* **2013**, *9* (12), 3305–3314. https://doi.org/10.1039/c3sm27304k.
(21) Terao, T.; Nakayama, T. Crystallization in Quasi-Two-Dimensional Colloidal Systems at an Air-Water Interface. **1999**, *60* (6), 7157–7162.
(22) Pieranski, P. Two-Dimensional Interfacial Colloidal Crystals. *Phys. Rev. Lett.* **1980**, *45* (7), 569–572. https://doi.org/10.1103/PhysRevLett.45.569.
(23) Kirby, S. M.; Anna, S. L.; Walker, L. M. Effect of Surfactant Tail Length and Ionic Strength on the Interfacial Properties of Nanoparticle-Surfactant Complexes. *Soft Matter* **2017**, *14* (1), 112–123. https://doi.org/10.1039/c7sm01806a.
(24) Jin, J.; Li, X.; Geng, J.; Jing, D. Insights into the Complex Interaction between Hydrophilic Nanoparticles and Ionic Surfactants at the Liquid / Air Interface. **2018**, 15223–15235. https://doi.org/10.1039/c8cp01838c.
(25) Batista, C. A. S.; Larson, R. G.; Kotov, N. A. Nonadditivity of Nanoparticle Interactions. *Science (80-.).* **2015**, *350* (6257). https://doi.org/10.1126/science.1242477.
(26) D. Fennell Evans, H. W. *The Colloidal Domain – Where Physics, Chemistry, Biology and Technology Meet*.
(27) Matter, S. On the Long-Term Stability of Foams Stabilised by Mixtures of Nano-Particles and Oppositely Charged Short Chain Surfactants. **2012**, 11085–11097. https://doi.org/10.1039/c2sm26461g.
(28) Santini, E.; Guzmán, E.; Ravera, F.; Ciajolo, A.; Alfè, M.; Liggieri, L.; Ferrari, M. Colloids and Surfaces A : Physicochemical and Engineering Aspects Soot Particles at the Aqueous Interface and Effects on Foams Stability. *Colloids Surfaces A Physicochem. Eng. Asp.* **2012**, *413*, 216–223. https://doi.org/10.1016/j.colsurfa.2012.02.028.
(29) Maestro, A.; Rio, E.; Drenckhan, W.; Langevin, D.; Salonen, A. Soft Matter Foams Stabilised by Mixtures of Nanoparticles and Oppositely Charged Surfactants : Relationship between Bubble Shrinkage and Foam Coarsening †. *Soft Matter* **2014**, *10*, 6975–6983. https://doi.org/10.1039/C4SM00047A.
(30) John C Berg. *Introduction To Interfaces And Colloids, An: The Bridge To Nanoscience*; 2009.
(31) Marra, W. C.; Eisenberger, P.; Cho, A. Y.; Marra, W. C.; Eisenberger, P.; Cho, A. Y. Xray Totalexternalreflection – Bragg Diffraction : A Structural Study of the GaAsAl Interface X-Ray Total-External-Reflection-Bragg Diffraction : A Structural Study of the GaAs-AI Interface. **1979**, *6927*. https://doi.org/10.1063/1.325845.
(32) Dosch, H. Critical Phenomena at Surfaces and Interfaces : Evanescent X-Ray and Neutron Scattering Fivefold Symmetry. **1993**, *58*. https://doi.org/10.1063/1.2809011.
(33) Ro, S.; Hohl, L.; Kempin, M.; Enders, F.; Jurtz, N.; Kraume, M. Influence of Different Silica Nanoparticles on Drop Size Distributions in Agitated Liquid-Liquid Systems. **2019**, No. 11, 1640–1655. https://doi.org/10.1002/cite.201900049.
(34) Ikem, V. O.; Menner, A.; Bismarck, A.; Norman, L. R. Liquid Screen: A Novel Method to Produce an in-Situ Gravel Pack. *SPE J.* **2014**, *19* (3), 437–442. https://doi.org/10.2118/141256-PA.
(35) Ravera, F.; Santini, E.; Loglio, G.; Ferrari, M.; Liggieri, L. Effect of Nanoparticles on

the Interfacial Properties of Liquid / Liquid and Liquid / Air Surface Layers. **2006**, 19543–19551.
(36) Garbin, V.; Crocker, J. C.; Stebe, K. J. Nanoparticles at Fluid Interfaces: Exploiting Capping Ligands to Control Adsorption, Stability and Dynamics. *J. Colloid Interface Sci.* **2012**, *387* (1), 1–11. https://doi.org/10.1016/j.jcis.2012.07.047.
(37) Mcgorty, R.; Fung, J.; Kaz, D.; Manoharan, V. N. Colloidal Self-Assembly at an Interface. *Mater. Today* **2010**, *13* (6), 34–42. https://doi.org/10.1016/S1369-7021(10)70107-3.
(38) Derjaguin, B.; Landau, L. Theory of the Stability of Strongly Charged Lyophobic Sols and of the Adhesion of Strongly Charged Particles in Solutions of Electrolytes. *Prog. Surf. Sci.* **1993**, *43* (1–4), 30–59. https://doi.org/10.1016/0079-6816(93)90013-L.
(39) Verwey, E. J. W. and J. T. G. O. Theory of the Stability of Lyophobic Colloids. *Journal of Physical and Colloid Chemistry*. 1947, pp 631–636. https://doi.org/10.1021/j150453a001.
(40) Apted, M. J., Arthur, R., Bennett, D., Savage, D., Sällfors, G., & Wennerström, H. Buffer Erosion: An Overview of Concepts and Potential Safety Consequences. **2010**.
(41) V, E. S. B.; Swanton, W. M o d e l l i n g colloid t r a n s p o r t in groundwater ; the p r e d i c t i o n of colloid stability a n d retention behaviour a e a Technology , 429 Harwell , Didcot , Oxfordshire O X l l ORA , UK. **1995**, *54*, 129–208.
(42) Smith, A. M.; Borkovec, M.; Trefalt, G. Forces between Solid Surfaces in Aqueous Electrolyte Solutions. *Adv. Colloid Interface Sci.* **2020**, *275*, 102078. https://doi.org/10.1016/j.cis.2019.102078.
(43) Martínez-López, F.; Cabrerizo-Vílchez, M. A.; Hidalgo-Álvarez, R. Colloidal Interaction at the Air-Liquid Interface. *J. Colloid Interface Sci.* **2000**, *232* (2), 303–310. https://doi.org/10.1006/jcis.2000.7172.
(44) Moncho-Jordá, A.; Martínez-López, F.; González, A. E.; Hidalgo-Álvarez, R. Role of Long-Range Repulsive Interactions in Two-Dimensional Colloidal Aggregation: Experiments and Simulations. *Langmuir* **2002**, *18* (24), 9183–9191. https://doi.org/10.1021/la0258805.
(45) Loudet, J. C.; Alsayed, A. M.; Zhang, J.; Yodh, A. G. Capillary Interactions Between Anisotropic Colloidal Particles. **2005**, *018301* (January), 2–5. https://doi.org/10.1103/PhysRevLett.94.018301.
(46) Stamou, D.; Duschl, C.; Johannsmann, D. Long-Range Attraction between Colloidal Spheres at the Air-Water Interface: The Consequence of an Irregular Meniscus. *Phys. Rev. E - Stat. Physics, Plasmas, Fluids, Relat. Interdiscip. Top.* **2000**, *62* (4 B), 5263–5272. https://doi.org/10.1103/PhysRevE.62.5263.
(47) Reynaert, S.; Moldenaers, P.; Vermant, J. Control over Colloidal Aggregation in Monolayers of Latex Particles at the Oil - Water Interface. **2006**, No. 23, 4936–4945.
(48) Kralchevsky, P. A.; Nagayama, K. Capillary Forces between Colloidal Particles. *Langmuir* **1994**, *10* (1), 23–36. https://doi.org/10.1021/la00013a004.
(49) Kralchevsky, P. A.; Nagayama, K. Capillary Interactions between Particles Bound to Interfaces, Liquid Films and Biomembranes. *Adv. Colloid Interface Sci.* **2000**, *85* (2), 145–192. https://doi.org/10.1016/S0001-8686(99)00016-0.
(50) Lehle, H.; Oettel, M.; Dietrich, S. Effective Forces between Colloids at Interfaces Induced by Capillary Wave–like Fluctuations.
(51) Lehle, H.; Oettel, M. Importance of Boundary Conditions for Fluctuation-Induced Forces between Colloids at Interfaces. **2007**, 1–18.

https://doi.org/10.1103/PhysRevE.75.011602.
(52) Pusey, P. N. Dynamic Light Scattering by Non-Ergodic Media p.n. Pusey. **1989**, *157*, 705–741.
(53) Fenwick, N. I. D.; Bresme, F.; Quirke, N. Computer Simulation of a Langmuir Trough Experiment Carried out on a Nanoparticulate Array Computer Simulation of a Langmuir Trough Experiment Carried out on a Nanoparticulate Array. **2011**, *7274* (2001). https://doi.org/10.1063/1.1357795.
(54) Reincke, F.; Kegel, W. K.; Zhang, H.; Nolte, M.; Wang, D.; Vanmaekelbergh, D.; Möhwald, H. Understanding the Self-Assembly of Charged Nanoparticles at the Water/Oil Interface. *Phys. Chem. Chem. Phys.* **2006**, *8* (33), 3828–3835. https://doi.org/10.1039/b604535a.
(55) Andersson, M.; Olsson, C.; Bengtsson, J.; Hedlund, A.; Bordes, R. Journal of Colloid and Interface Science Directed Self-Assembly of Silica Nanoparticles in Ionic Liquid-Spun Cellulose Fibers Dope Solution. *J. Colloid Interface Sci.* **2019**, *553*, 167–176. https://doi.org/10.1016/j.jcis.2019.05.084.
(56) Robinson, D. J.; Earnshaw, J. C. Initiation of Aggregation in Colloidal Particle Monolayers. *Langmuir* **1993**, *9* (5), 1436–1438. https://doi.org/10.1021/la00029a045.
(57) Stillinger, F. H. Interfacial Solutions of the Poisson-Boltzmann Equation. *J. Chem. Phys.* **1961**, *35* (5), 1584–1589. https://doi.org/10.1063/1.1732113.
(58) Hurd, A. J. The Electrostatic Interaction between Interfacial Colloidal Particles. *J. Phys. A. Math. Gen.* **1985**, *18* (16), L1055–L1060. https://doi.org/10.1088/0305-4470/18/16/011.
(59) Butt, H. J. *The Physics and Chemistry of Interfaces R0.7*; 2013; Vol. 53.
(60) Tran, L.; Haase, M. F. Interface Components : Nanoparticles , Colloids , Emulsions , Surfactants , Proteins , Polymers Templating Interfacial Nanoparticle Assemblies via in-Situ Techniques. **2019**. https://doi.org/10.1021/acs.langmuir.9b00130.
(61) Anyfantakis, M.; Vialetto, J.; Best, A.; Auernhammer, G. K.; Butt, H.-J. J.; Binks, B. P.; Baigl, D. Adsorption and Crystallization of Particles at the Air−Water Interface Induced by Minute Amounts of Surfactant. 2018.
(62) Velikov, K. P.; Durst, F.; Velev, O. D. Direct Observation of the Dynamics of Latex Particles Confined inside Thinning Water-Air Films. *Langmuir* **1998**, *14* (5), 1148–1155. https://doi.org/10.1021/la970338f.
(63) Vogel, N.; Retsch, M.; Fustin, C. A.; Del Campo, A.; Jonas, U. Advances in Colloidal Assembly: The Design of Structure and Hierarchy in Two and Three Dimensions. *Chem. Rev.* **2015**, *115* (13), 6265–6311. https://doi.org/10.1021/cr400081d.
(64) Chinnam, J.; Das, D. K.; Vajjha, R. S.; Satti, J. R. International Journal of Thermal Sciences Measurements of the Surface Tension of Nano Fl Uids and Development of a New Correlation. *Int. J. Therm. Sci.* **2015**, *98*, 68–80. https://doi.org/10.1016/j.ijthermalsci.2015.07.008.
(65) Harikrishnan, A. R.; Dhar, P.; Gedupudi, S.; Das, S. K. Effect of Interaction of Nano-Particles and Surfactants on the Spreading Dynamics of Sessile Droplets Effect of Interaction of Nano-Particles and Surfactants on the Spreading Dynamics of Sessile Droplets. **2017**. https://doi.org/10.1021/acs.langmuir.7b02123.
(66) Vatanparast, H.; Javadi, A.; Bahramian, A. Silica Nanoparticles Cationic Surfactants Interaction in Water-Oil System. *Colloids Surfaces A Physicochem. Eng. Asp.* **2017**, *521*, 221–230. https://doi.org/10.1016/j.colsurfa.2016.10.004.
(67) Equation, G. A. Gibbs Adsorption Equation and Ad- Sorption on Solids. **1937**.
(68) Vatanparast, H.; Samiee, A.; Bahramian, A.; Javadi, A. Surface Behavior of Hydrophilic

Silica Nanoparticle-SDS Surfactant Solutions: I. Effect of Nanoparticle Concentration on Foamability and Foam Stability. *Colloids Surfaces A Physicochem. Eng. Asp.* **2017**, *513*, 430–441. https://doi.org/10.1016/j.colsurfa.2016.11.012.

(69) Matter, S.; Maestro, A.; Guzm, E.; Santini, E.; Ravera, F.; Liggieri, L.; Ortega, F. Wettability of Silica Nanoparticle–Surfactant Nanocomposite Interfacial Layers. **2012**, 837–843. https://doi.org/10.1039/c1sm06421e.

(70) Li, C.; Xu, Y.; Li, X.; Ye, Z.; Yao, C.; Chen, Q.; Zhang, Y.; Bell, S. E. J. Unexpected Dual Action of Cetyltrimethylammonium Bromide (CTAB) in the Self-Assembly of Colloidal Nanoparticles at Liquid–Liquid Interfaces. *Adv. Mater. Interfaces* **2020**, *7* (14). https://doi.org/10.1002/admi.202000391.

(71) Vialetto, J.; Rudiuk, S.; Morel, M.; Baigl, D. From Bulk Crystallization of Inorganic Nanoparticles at the Air/Water Interface: Tunable Organization and Intense Structural Colors. *Nanoscale* **2020**, *12* (11), 6279–6284. https://doi.org/10.1039/c9nr10965j.

(72) Binks, B. P.; Rodrigues, J. A. Double Inversion of Emulsions by Using Nanoparticles and a Di-Chain Surfactant. *Angew. Chemie - Int. Ed.* **2007**, *46* (28), 5389–5392. https://doi.org/10.1002/anie.200700880.

(73) Guzmán, E.; Ritacco, H.; Rubio, J. E. F.; Rubio, R. G.; Ortega, F. Salt-Induced Changes in the Growth of Polyelectrolyte Layers of Poly(Diallyl-Dimethylammonium Chloride) and Poly(4-Styrene Sulfonate of Sodium). *Soft Matter* **2009**, *5* (10), 2130–2142. https://doi.org/10.1039/b901193e.

(74) Chai, Y.; Lukito, A.; Jiang, Y.; Ashby, P. D.; Russell, T. P. Fine-Tuning Nanoparticle Packing at Water−Oil Interfaces Using.Pdf. Nano Lett. 2017. https://doi.org/10.1021/acs.langmuir.8b03535.

(75) Nayak, S.; Fieg, M.; Wang, W.; Bu, W.; Mallapragada, S.; Vaknin, D. Effect of (Poly)Electrolytes on the Interfacial Assembly of Poly(Ethylene Glycol)-Functionalized Gold Nanoparticles. *Langmuir* **2019**, *35* (6), 2251–2260. https://doi.org/10.1021/acs.langmuir.8b03535.

(76) Williams, D. F. Aggregation of Colloidal Particles at the Air-Water Interface. J. Colloid Interface Sci. 1991, pp 152 (1), 218− 229.

(77) Abdel-Fattah, A. I.; El-Genk, M. S. Sorption of Hydrophobic, Negatively Charged Microspheres onto a Stagnant Air/Water Interface. *J. Colloid Interface Sci.* **1998**, *202* (2), 417–429. https://doi.org/10.1006/jcis.1998.5442.

(78) Pham, H.; Nguyen, Q. P. Effect of Silica Nanoparticles on Clay Swelling and Aqueous Stability of Nanoparticle Dispersions. *J. Nanoparticle Res.* **2014**, *16* (1). https://doi.org/10.1007/s11051-013-2137-9.

(79) Turek, V. A.; Cecchini, M. P.; Paget, J.; Kucernak, A. R.; Kornyshev, A. A.; Edel, J. B. Plasmonic Ruler at the Liquid-Liquid Interface. *ACS Nano* **2012**, *6* (9), 7789–7799. https://doi.org/10.1021/nn302941k.

(80) Costa, L.; Li-Destri, G.; Thomson, N. H.; Konovalov, O.; Pontoni, D. Real Space Imaging of Nanoparticle Assembly at Liquid-Liquid Interfaces with Nanoscale Resolution. *Nano Lett.* **2016**, *16* (9), 5463–5468. https://doi.org/10.1021/acs.nanolett.6b01877.

(81) Seymour, K. G. *Surfactants and Interfacial Phenomena*; 1979; Vol. 62. https://doi.org/10.1093/jaoac/62.3.700.

(82) Simister, E. A.; Thomas, R. K.; Penfold, J.; Aveyard, R.; Binks, B. P.; Cooper, P.; Fletcher, P. D. I.; Lu, J. R.; Sokolowski, A. Comparison of Neutron Reflection and Surface Tension Measurements of the Surface Excess of Tetradecyltrimethylammonium

Bromide Layers at the Air/Water Interface. *J. Phys. Chem.* **1992**, *96* (3), 1383–1388. https://doi.org/10.1021/j100182a066.

(83) Lu, J. R.; Simister, E. A.; Thomas, R. K.; Penfold, J. Structure of an Octadecyltrimethylammonium Bromide Layer at the Air/Water Interface Determined. *J. Phys. Chem.* **1993**, No. 97, 6024–6033.

(84) Szymczyk, K.; Jańczuk, B. A Study of the Interactions of Ternary Surfactant Systems at the Water-Air Interface. *Langmuir* **2010**, *26* (4), 2491–2496. https://doi.org/10.1021/la9027173.

(85) Liggieri, L.; Santini, E.; Guzmán, E.; Maestro, A.; Ravera, F. Wide-Frequency Dilational Rheology Investigation of Mixed Silica Nanoparticle-CTAB Interfacial Layers. *Soft Matter* **2011**, *7* (17), 7699–7709. https://doi.org/10.1039/c1sm05257h.

(86) B. P. Binks, T. S. H. *Colloidal Particles at Liquid Interfaces*; 2006.

(87) Razavi, S.; Cao, K. D.; Lin, B.; Lee, K. Y. C.; Tu, R. S.; Kretzschmar, I. Collapse of Particle-Laden Interfaces under Compression: Buckling vs Particle Expulsion. **2015**. https://doi.org/10.1021/acs.langmuir.5b01652.

(88) Aveyard, R.; Clint, J. H.; Nees, D.; Paunov, V. N. Compression and Structure of Monolayers of Charged Latex Particles at Air/Water and Octane/Water Interfaces. *Langmuir* **2000**, *16* (4), 1969–1979. https://doi.org/10.1021/la990887g.

(89) Chaplin, M. Theory vs Experiment : What Is the Surface Charge of Water ? *Water* **2009**, *1* (July), 1–28.

(90) Israelachvili, J. N. *Intermolecular and Surface Forces*; 2010.

(91) Wang, H.; Singh, V.; Behrens, S. H. Image Charge Effects on the Formation of Pickering Emulsions. *J. Phys. Chem. Lett.* **2012**, *3* (20), 2986–2990. https://doi.org/10.1021/jz300909z.

(92)Xu, Y.; Konrad, M. P.; Lee, W. W. Y.; Ye, Z.; Bell, S. E. J. A Method for Promoting Assembly of Metallic and Nonmetallic Nanoparticles into Interfacial Monolayer Films. *Nano Lett.* **2016**, *16* (8), 5255–5260. https://doi.org/10.1021/acs.nanolett.6b02418.

(93) From-bulk Crystallization of Inorganic Nanoparticles at the.Pdf.

(94) Anyfantakis, M.; Vialetto, J.; Best, A.; Auernhammer, G. K.; Butt, H. J.; Binks, B. P.; Baigl, D. Adsorption and Crystallization of Particles at the Air-Water Interface Induced by Minute Amounts of Surfactant. *Langmuir* **2018**, *34* (50), 15526–15536. https://doi.org/10.1021/acs.langmuir.8b03233.

(95) Metin, C. O.; Lake, L. W. Stability of Aqueous Silica Nanoparticle Dispersions. **2011**, 839–850. https://doi.org/10.1007/s11051-010-0085-1.

(96)W. Russel, D. S. and W. S. *Colloidal Dispersions*; 1989. https://doi.org/10.1201/9780429497131-7.

(97) Goloub, T. P.; Koopal, L. K. Adsorption of Cationic Surfactants on Silica . Comparison of Experiment and Theory. **1997**, *7463* (8), 673–681.

(98) Forth, J.; Kim, P. Y.; Xie, G.; Liu, X.; Helms, B. A.; Russell, T. P. Building Reconfigurable Devices Using Complex Liquid–Fluid Interfaces. *Adv. Mater.* **2019**, *31* (18), 1–39. https://doi.org/10.1002/adma.201806370.

(99) Homede, E.; Zigelman, A.; Abezgauz, L.; Manor, O. Signatures of van Der Waals and Electrostatic Forces in the Deposition of Nanoparticle Assemblies. *J. Phys. Chem. Lett.* **2018**, *9* (18), 5226–5232. https://doi.org/10.1021/acs.jpclett.8b02052.

(100) Tuccitto, N.; Amato, T.; Gangemi, C. M. A.; Trusso Sfrazzetto, G.; Puglisi, R.; Pappalardo, A.; Ballistreri, F. P.; Messina, G. M. L.; Li-Destri, G.; Marletta, G. Driving Coordination Polymer Monolayer Formation by Competitive Reactions at the Air/Water Interface. *Langmuir* **2018**, *34* (39), 11706–11713.

https://doi.org/10.1021/acs.langmuir.8b02607.
(101) Geisel, K.; Isa, L.; Richtering, W. The Compressibility of Ph-Sensitive Microgels at the Oil-Water Interface: Higher Charge Leads to Less Repulsion. *Angew. Chemie - Int. Ed.* **2014**, *53* (19), 4905–4909. https://doi.org/10.1002/anie.201402254.
(102) Zhang, H.; Wang, W.; Mallapragada, S.; Travesset, A.; Vaknin, D. Macroscopic and Tunable Nanoparticle Superlattices. *Nanoscale* **2017**, *9* (1), 164–171. https://doi.org/10.1039/c6nr07136h.
(103) Li Destri, G.; Gasperini, A. A. M.; Konovalov, O. The Link Between Self-Assembly and Molecular Conformation of Amphiphilic Block Copolymers Monolayers at the Air/Water Interface: The Spreading Parameter. *Langmuir* **2015**, *31* (32), 8856–8864. https://doi.org/10.1021/acs.langmuir.5b02054.
(104) Rauh, A.; Rey, M.; Barbera, L.; Zanini, M.; Karg, M.; Isa, L. Compression of Hard Core-Soft Shell Nanoparticles at Liquid-Liquid Interfaces: Influence of the Shell Thickness. *Soft Matter* **2017**, *13* (1), 158–169. https://doi.org/10.1039/C6SM01020B.
(105) Garbin, V.; Jenkins, I.; Sinno, T.; Crocker, J. C.; Stebe, K. J. Erratum: Interactions and Stress Relaxation in Monolayers of Soft Nanoparticles at Fluid-Fluid Interfaces (Physical Review Letters (2015) 114:108301). *Phys. Rev. Lett.* **2015**, *115* (2), 1–6. https://doi.org/10.1103/PhysRevLett.115.029902.
(106) Vegso, K.; Siffalovic, P.; Jergel, M.; Weis, M.; Benkovicova, M.; Majkova, E.; Luby, S.; Kocsis, T.; Capek, I. Silver Nanoparticle Monolayer-to-Bilayer Transition at the Air/Water Interface as Studied by the GISAXS Technique: Application of a New Paracrystal Model. *Langmuir* **2012**, *28* (25), 9395–9404. https://doi.org/10.1021/la301577a.
(107) Heitsch, A. T.; Patel, R. N.; Goodfellow, B. W.; Smilgies, D. M.; Korgel, B. A. GISAXS Characterization of Order in Hexagonal Monolayers of FePt Nanocrystals. *J. Phys. Chem. C* **2010**, *114* (34), 14427–14432. https://doi.org/10.1021/jp1047979.
(108) Bera, M. K.; Chan, H.; Moyano, D. F.; Yu, H.; Tatur, S.; Amoanu, D.; Bu, W.; Rotello, V. M.; Meron, M.; Král, P.; Lin, B.; Schlossman, M. L. Interfacial Localization and Voltage-Tunable Arrays of Charged Nanoparticles. *Nano Lett.* **2014**, *14* (12), 6816–6822. https://doi.org/10.1021/nl502450j.
(109) Rennie, A. R.; Lee, E. M.; Simister, E. A.; Thomas, R. K. Structure of a Cationic Surfactant Layer at the Silica-Water Interface. *Langmuir* **1990**, *6* (5), 1031–1034. https://doi.org/10.1021/la00095a025.
(110) Manuscript, A. Tuneable 2D Self-Assembly of Plasmonic Nanoparticles at Liquid | Liquid Interfaces. **2016**. https://doi.org/10.1039/C6NR05081F.
(111) Garbin, V.; Crocker, J. C.; Stebe, K. J. Forced Desorption of Nanoparticles from an Oil À Water Interface. **2012**, 1663–1667.
(112) Tanford, C. Micelle Shape and Size. *J. Phys. Chem.* **1972**, *76* (21), 3020–3024. https://doi.org/10.1021/j100665a018.
(113) Santini, E.; Krägel, J.; Ravera, F.; Liggieri, L.; Miller, R. Colloids and Surfaces A : Physicochemical and Engineering Aspects Study of the Monolayer Structure and Wettability Properties of Silica Nanoparticles and CTAB Using the Langmuir Trough Technique. *Colloids Surfaces A Physicochem. Eng. Asp.* **2011**, *382* (1–3), 186–191. https://doi.org/10.1016/j.colsurfa.2010.11.042.
(114) Meyer, W. Steric Forces Measured with the Atomic Force Microscope. **1999**, No. 6, 2559–2565.
(115) Orsi, D.; Guzmán, E.; Liggieri, L.; Ravera, F.; Ruta, B.; Chushkin, Y.; Rimoldi, T.;

Cristofolini, L. 2D Dynamical Arrest Transition in a Mixed Nanoparticle-Phospholipid Layer Studied in Real and Momentum Spaces. *Sci. Rep.* **2015**, *5* (November), 1–14. https://doi.org/10.1038/srep17930.

(116) Maestro, A.; Santini, E.; Zabiegaj, D.; Llamas, S.; Ravera, F.; Liggieri, L.; Ortega, F.; Rubio, R. G.; Guzman, E. Particle and Particle-Surfactant Mixtures at Fluid Interfaces: Assembly, Morphology, and Rheological Description. *Adv. Condens. Matter Phys.* **2015**, *2015*. https://doi.org/10.1155/2015/917516.

(117) Maestro, A.; Zaccone, A. Nonaffine Deformation and Tunable Yielding of Colloidal Assemblies at the Air-Water Interface. *Nanoscale* **2017**, *9* (46), 18343–18351. https://doi.org/10.1039/c7nr06014a.

(118)Israelachvili, J. N. *Intermolecular and Surface Forces*; 2010. https://doi.org/https://doi.org/10.1016/C2009-0-21560-1.

Appendix:

First Section

Materials and Methods

Planar and non-substrates preparation. The substrates consist of silicon wafers (100) made hydrophilic with a basic piranha solution (15 ml of H_2O, 3 ml of NH_4OH and 3 ml of H_2O_2) at 60 ° C for 10 minutes. In this way, the native oxide layer is removed while a new one is formed, characterized by homogeneous terminations of silanol groups.[1] On the so-obtained hydrophilic flat substrates, an homogeneous surface nano-curvature was created by depositing, via spin coating, an aqueous suspensions at 5%w/v of silica particles having a diameter of 50 ± 10, 143 ± 4, 235±10, 304 ± 20 and 403 ± 10 nm (purchased from Microparticles GmbH, Berlin, Germany, and used as received). Hexagonally packed arrays[2] of particles were obtained with the proper spin-coating recipe (Table 1). Therefore, it is possible to obtain non-planar substrates where the individual particles contribute to the formation of the surface curvature (κ), defined as the inverse of the radius of the particles. In particular, substrates with surface curvature ranging from 0.0049 and 0.04 nm^{-1} are obtained while flat surfaces are considered as reference, with $\kappa = 0$. The various monolayers were then annealed at 90° C for 10 min in air to remove residual water and then underwent again to basic piranha treatment to ensure surface hydrophilicity. Hydrophobic substrates were prepared by dipping the flat and nano-curved hydrophilic substrates in a 4:1 solution of hexadecane - chloroform with one millimole of octadecyltrichlorosilane (OTS) and then left in solution for 1 hour at 40 °C. In this way, the substrates are covered with a monolayer of OTS, which makes the surface highly hydrophobic.[3] The so-obtained highly hydrophobic substrates were subsequently subjected to gradual oxidation of the OTS layer, by means of a radio frequency plasma of Ar/O_2 at 100W, with a volume ratio of 97/3. In this way, by controlling the plasma exposure time it is possible to modulate the surface wettability.[4]

Particle diameter (nm)	***50***	***143***	***235***	***304***	***403***
Volume (µl)	45	40	30	30	15
Spin speed -time	200 rpm-1s 400 rpm-10s 2000 rpm-30s	400 rpm-1s 800 rpm-10s 2200 rpm-30s	400 rpm-1s 750 rpm-40s 2000 rpm-30s	400 rpm-1s 750 rpm-100s 2000 rpm-30s	400 rpm-1s 600 rpm-200s 2000 rpm-30s

Table 1. Spin-coating recipe for the deposition of hexagonally packed silica particle monolayers. Each recipe was optimized for the specific particle size.

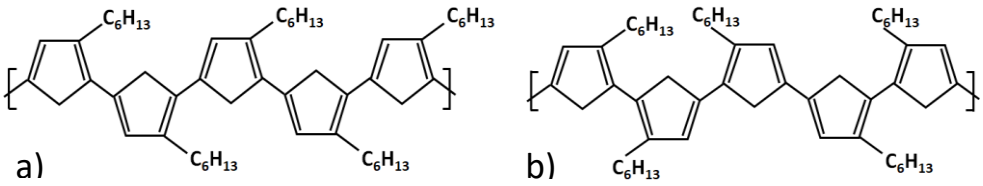

Figure S1.1. Regio-regular (a) and regio-random (b) orders of P3HT polymer chains.

Given the aggressiveness of the plasma, a few seconds of exposure are enough for the oxidation of the OTS. In particular, the substrates were subjected to different exposure times, between 1 and 15 sec, obtaining a SFE modulation between ~ 20 and ~ 60 mN/m.

Film preparation. Thin films of Regio-regular P3HT (Figure S1.a), having Mw: 54000 g/mol and polydispersity: 2.3, and regio-random P3HT (Figure S1.b), with Mw: 1109.32 g/mol and polydispersity: 17.28, both purchased from Sigma-Aldrich, Milan, Italy, and used as received, were obtained by deposition on planar and non-planar substrates, immediately after the treatments described above for the proper modulation of their surface free energy. The spin-coating parameters and the concentration of the solution were adjusted to ensure an equal polymer film thickness of 67.5 ± 6.8 nm for both P3HTs, regardless of the surface curvature. In particular, the following conditions were adopted: a chloroform solution of 5 mg/mL of regio-regular P3HT, with a spin speed of 2000 rpm for 1 sec and 4000 rpm for 59 sec, and a 10 mg/mL chloroform solution of regio-random P3HT, with a spin speed of 4000 rpm for 30 sec. Then, for the investigation of equilibrated films, the regio-regular P3HT thin films were thermally annealed in vacuum at 240 °C (P3HT melting temperature[5]) for 30 minutes and then slowly cooled at 3 °C/min until room temperature, in order to increase the crystalline fraction of the thin films.

Determination of the Surface Energetics. Contact angle measurements were performed using an OCA 20 apparatus (DataPhysics Instru- ments GmbH, Filderstadt, Germany). With the help of contact angle measurements, the surface free energy (SFE) or surface tension (γ) of the different substrates prepared can be described as a combination of attractive Lifshitz–van der Waals and Lewis acid–base polar contributions,[6] as shown by equation 1:

$$\gamma = \gamma^{LW} + 2\sqrt{\gamma^{+}\gamma^{-}} \qquad \textit{Equation 1}$$

where γ^{LW} is the Lifshitz–van der Waals component, γ^+ and γ^- are the acid and basic components respectively. By measuring the contact angles of three different liquids (water, glycerol, and tricresyl phosphate,TCP, whose surface tensions and the three related components are reported in the instrument database), it is possible, to determine the SFE, its Lifshitz–van der Waals and acid and base components of a solid by simply solving the three equations that describe the spreading of the three liquids on the solid surface[6]

$$(1 + cos\vartheta)\gamma_L = 2(\sqrt{\gamma_S^{LW}\gamma_L^{LW}} + \sqrt{\gamma_S^+\gamma_L^-} + \sqrt{\gamma_S^-\gamma_L^+}) \quad \textit{Equation 2}$$

where γ_L and γ_S refer to liquid surface tension component and to the solid SFE component respectively. The interfacial free energy (IFE), γ_{LS}, was determined by using the combination rule from Good - Girifalco - Fowkes[7] and the expression for the interactions Lewis acid-base through interface,[6] using the following equation, once that the SFE and the related components for solid substrates are known:

$$\gamma_{LS} = (\sqrt{\gamma_S^{LW}} - \sqrt{\gamma_L^{LW}})^2 + 2(\sqrt{\gamma_S^-\gamma_S^+} + \sqrt{\gamma_L^+\gamma_L^-} - \sqrt{\gamma_S^+\gamma_L^-} - \sqrt{\gamma_S^-\gamma_L^+}) \quad \textit{Equation 3}$$

However, when using water or glycerol as the spreading liquid, the calculation of the IFE was performed with the approximated equation 4,[6] as the high acid/base asymmetry of hydrophilic substrates causes negative values of IFE between the liquid and the high acid/base asymmetry of hydrophilic substrates.

$$\gamma_{SL} = (\sqrt{\gamma_S^{LW}} - \sqrt{\gamma_L^{LW}})^2 + \gamma_L^+\gamma_L^- - 2(\sqrt{\gamma_S^-\gamma_L^+}) \quad \textit{Equation 4}$$

Morphological characterization. Atomic Force Microscopy (AFM) measurements were carried out in tapping mode, in air, using a Nanoscope IIIA-MultiMode AFM (Digital Instruments, Santa Barbara, CA, USA. Images, having with 512 × 512 pixels, were recorded using Tap 300 G silicon probes (Budget sensors) mounted on cantilevers with a nominal force constant of 40 N m^{-1} and a resonant frequency of 300 kHz.

Determination of the Persistence Length. From the AFM phase images of P3HT thin films on flat and nano-curved substrates, the lamellar persistence length was determined by means of Fiber-App, an open-source software written in MATLAB programming languages. The lamellar persistence length is defined as the average length of straight sections along the lamella. This software allows to trace the lamellae on the AFM images, by acquiring the coordinates and then determining the

mean-squared end-to-end distance (MSED) between contour segments with the following equation:[8]

$$< R_e^2 >= \frac{2}{3} l_p \{\pi L - 2l_p [1 - \exp(-\pi L / 2l_p)]\} \qquad \textit{Equation 5}$$

where l_p is the persistence length and R_e is the direct distance between any pair of segments along a contour separated by an arc having length L. In particular, the software allows marking the points at which the polymeric lamellae are folded through the elements of a mask. In this way, the tracing algorithm, with the aid of the pathfinding algorithm A*, is able to correctly follow the lamellae and to obtain the statistical information necessary for determining the mean square distance.[8]

Structural characterization. The structural characterization of polymeric thin films was performed at the ID10 beamline of the European Synchrotron Radiation Facility (ESRF), Grenoble (France), by means of Grazing incidence X-ray diffraction measurements (GIXRD). A 22 keV X-ray beam, with an incident angle of 0.064, i.e. 80% of the critical angle and a Pilatus 300k 2D detector positioned at a distance of 389.7 mm from the sample were employed to record the GIXRD pattern. Samples were placed inside a sample holder covered by a Kapton dome and filled with helium (Figure S2). Then, for the in-situ characterization of thermally annealed films, the samples were subjected to thermal annealing at 240 °C for 30 minutes, in a controlled atmosphere chamber, since P3HT oxidizes in air at high temperatures, to monitor crystallization, in real time, during their slow cooling. Therefore, it becomes possible to detect any deviation from the observed "standard" behaviour for films on flat substrates, in terms of either nucleation or growth.

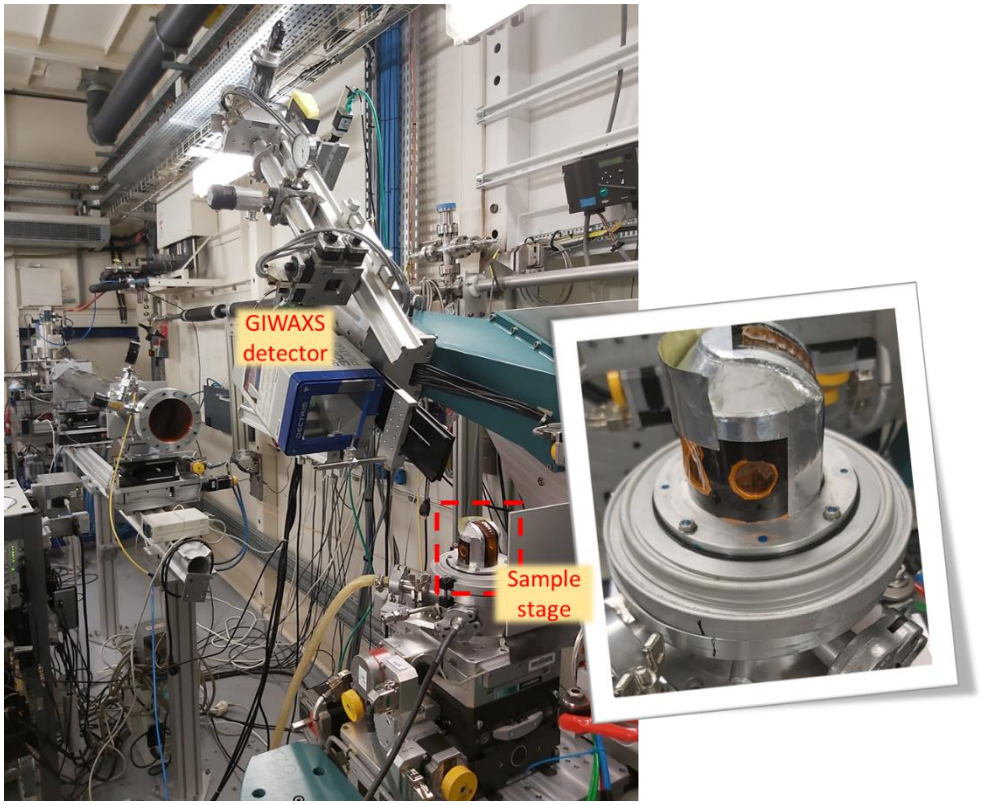

Figure S1.2. Photo of the experimental set-up at ID10, ESRF. The diffraction patterns were recorded by means of a Pilatus 300k 2D detector placed at a distance from the sample equal to 389.7 mm. The samples were placed inside a Kapton dome (whose high mechanical and thermal stability make it suitable for X-ray windows[9]) shown in the enlarged image, and filled with helium.

By taking into account the position of the direct beam, the sample-detector distance and the pixel size, we performed on each diffraction pattern geometrical correction followed by the conversion from the pixel matrix to scattering vector, q (Script_1). Then, 1D profiles were extracted from 2D corrected patterns by line cutting along the desired directions. (Script_2).
Lorentzian fitting of the obtained peaks was performed using the following equation:

$$y = B * e^{-\frac{x}{C}} + D + \frac{2A}{\pi} * \frac{w}{4(q-q_c)^2+w^2} + \frac{2E}{\pi} * \frac{w_1}{4(q-q_{c_1})^2+{w_1}^2} \qquad \textit{Equation 6}$$

where the first and the second terms takes into account the background and the third term represent the main Lorentzian peak originated by the integration of the Bragg

peak centred at q_c, characterized by an area A and a full width at half maximum (FWHM) w, while the fourth term takes into account the scattering originated by the Kapton dome. (Script_3)

Resistance measurements. Electric measurements of regio-regular and regio-random P3HT on nano-curved substrates were performed with prefabricated chips based on low-density silicon oxide substrates and an electric test board, both purchased from Ossila Ltd., Sheffield, UK. The chips are made by five individual source-drain connections and a common gate contact with channel length and width of 30 µm and 1mm respectively and gold electrodes in the active area. Silica particles with different diameters were deposited into the channels, by using the same spin-coating recipe previously described and covered, after proper hydrophilization of the surface, by P3HT thin films. Then, a cotton bud was used to remove the polymer film and silica particles from the unwanted areas, in order to avoid gate leakage and cross-talk. In particular, the polymer films covered only three of the five channels present in the chip. (Figure S3). Current – Voltage measurements were performed using Keithley 2611-B Source-Measure Unit. I-V curves were recorded by using linear voltage swept from -3V to 3V at 0.5 Vs^{-1}, to obtain the corresponding measured output current.

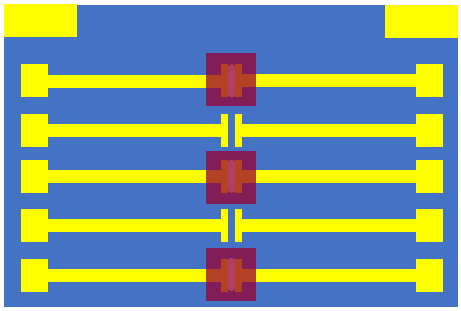

Figure S1.3. Schematic representation, top view, of the three active channels, of the five present in Ossila chips, covered by silica particle monolayers and P3HT thin films.

Script 1

```
# import libraries
import h5py
import numpy as np
import nexusformat.nexus as nx
import matplotlib.pyplot as plt
import matplotlib.colors as colors
from mpl_toolkits import mplot3d
from matplotlib import ticker, cm

#GIWAXS detector correction
## set parameters

Wavelength = 0.56 #A-1
distance = 389.7 #mm
pixel_size = 172/1000 #mm
mu = 5.06 # degree
mu_i = 0.064 # degree
```

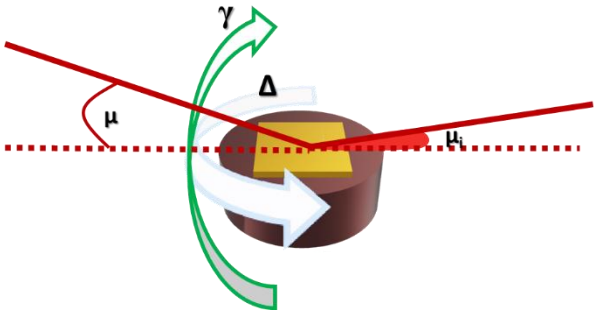


```
pixels_x = 619
pixels_y = 487
x = np.arange(0,pixels_x)

y = np.arange(0,pixels_y)
zero_x = 504
zero_y = 245

##angles in plane and out of plane: curvature correction

pixel_g = np.arange(0,zero_y)
gamma_0 = mu-((np.arctan(((zero_y-pixel_0)*pixel_size)/distance))*(180/np.pi))

pixel_s = np.arange(0,pixels_y-zero_y)
gamma_1 = mu+(np.arctan(((pixel_g*pixel_size)/distance))*(180/np.pi))
gamma =np.hstack((gamma_0,gamma_1))

pixel_s = np.arange(0,zero_x)
delta_0 = 0-((np.arctan(((zero_x-pixel_s)*pixel_size)/distance))*(180/np.pi))

pixel_d = np.arange(0,pixels_x-zero_x)
delta_1 = 0+((np.arctan((pixel_d*pixel_size)/distance))*(180/np.pi))
delta =np.hstack((delta_0,delta_1))
```

```
## from angle to scattering vector (q) by considering the curvature correction

gamma, delta = np.meshgrid(gamma,delta)
qx = (2*np.pi/Wavelength)*(np.cos((gamma)*(np.pi/180)))*(np.sin((delta)*
      *(np.pi/180)))
qy = (2*np.pi/Wavelength)*(((np.cos((gamma)*(np.pi/180)))*(np.cos((delta)*
      * (np.pi/180))))-(np.cos((0.064)*(np.pi/180))))
qz = (2*np.pi/Wavelength)*((np.sin((gamma)*(np.pi/180)))+(np.sin((mu_i)*
      * (np.pi/180))))
qxy_negative = - (np.sqrt((qx[:505,])**2 + (qy[:505, ])**2))
qxy_positive = (np.sqrt((qx[505:,])**2 + (qy[505:,])**2))
qxy = np.vstack((qxy_negative,qxy_positive))

## load data

fname = nx.nxload('file_name.h5')
scan_name = 'file_name'
scan = fname['5.1/measurement/pilatus300k'] # select Pilatus (2D detector) image
print(scan.shape)
data_sum = np.zeros((619,487)) # where (619,487) is the  image pixels size
for j in range (2):
   data = (scan[j,:,:])
   data_sum = data_sum+data #integration of the acquired images
line = np.abs(np.array(data_sum))

## correction of scans and transition from pixel to q space
### identify zero intensity values
first_part= line[:505,88:]
first_Intensity_max = np.amax(first_part)
first_part[first_part<= first_Intensity_max]=0

second_part = line[505:,88:]
second_Intensity_max = np.amax(second_part)
second_part[second_part<=second_part]=0

## Reshape Intensity matrix
Intensity1 = np.vstack((first_part, second_part))
Intensity = np.hstack((line[:,:88],Intensity1))
```

```
## Create 2D GIXRD pattern
fig = plt.figure()
colors_levels = np.linspace(5000, 50000,5000) # with values of minimum, maximum and
                                                number of points respectively
plt.contourf(qxy, qz, Intensity, locator=ticker.LogLocator(), cmap='Greys', levels
=colors_levels) #jet
Xflat, Yflat, lineflat = qxy.flatten(), qz.flatten(), line.flatten()
def fmt(x,y):
    dist = np.linalg.norm(np.vstack([Xflat - x, Yflat - y]), axis=0)
    idx = np.argmin(dist)
    z = lineflat[idx]
    return 'x={x:.5f}  y={y:.5f}  z={z:.5f}'.format(x=x, y=y, z=z)
plt.gca().format_coord = fmt
plt.xlabel(r'$q_{xy}$ ($\mathrm{\AA^{-1}}$)')
plt.ylabel(r'$q_{z}$ ($\mathrm{\AA^{-1}}$)')
plt.savefig(f'director /{scan_name}.png', dpi=300)
plt.show()
plt.close(fig)
```

Script 2

```
# import libraries

import numpy as np
import matplotlib.pyplot as plt
import matplotlib.colors as colors
from mpl_toolkits import mplot3d
from matplotlib import ticker, cm

##Line-cut from correct 2D patterns along desired directions
## Line-cut out of crystallographic plane and 1D plot
#Select range of cut in 2D pattern
cut_qxy = qxy[480:520,:]
cut_qz = qz[480:520,:]
Q = np.sqrt((cut_xy)**2+(cut_qz)**2)
y_data = ((Intenisty))[480:520,:]  #select intensity value

#Choose opportunity line cut
## define a function that allows you to delete unwanted cutting lines with a click
fig, ax = plt.subplots()
lines =[]
for l in range (np.shape(y_data)[0]):
```

```
    line, = ax.plot(Q[1],y_data[l,:],label = '%s data' % l )
    lines.append(line)
leg = fig.legend(loc='upper right', prop={'size': 7}, fancybox=True, shadow=True)
leg.get_frame().set_alpha(1)
lined = dict()
for legline, origline in zip(leg.get_lines(), lines):
  legline.set_picker(5)  # 5 points tolerance
  lined[legline] = origline
def onpick(event, figu=fig):
    legline = event.artist
    orig = lined[legline]
    vis = not orig.get_visible()
    orig.set_visible(vis)
    if vis:
        legline.set_alpha(1.)
    else:
        legline.set_alpha(.1)
    figu.canvas.draw()
fig.canvas.mpl_connect('pick_event',onpick)
plt.yscale('log')
plt.show()
plt.close(fig)
## select the desired line
scan = plt.figure()
slicing = int(input('select line to slice: '))
y = y_data[slicing]
plt.plot(Q[1], y)
plt.yscale('log')
plt.xlabel(r'$Q$ ($\mathrm{\AA^{-1}}$)')
plt.ylabel(r'$Intensity (a.u.)$')
plt.savefig(f'director/{scan_name}_{slicing}cut_ out of crystallographic plane.png',
dpi=300)
np.savetxt(f'director/scan_name}_{slicing}cut_ out of crystallographic plane.txt',
(np.vstack((Q[1],y))).T)
plt.show()
plt.close(scan)
## Line-cut at 45° and 1D plot
#Select range of cut in 2D pattern
x2 = qxy[505:, :433]
y2 = qz[505:, :433]
Q_diag = np.sqrt((x2)**2+(y2)**2)
```

```
diag = np.diag(Q_diag)
z = np.diag((Intenisty)[ 505:, :433])  #select intensity value
scan = plt.figure()
plt.plot(diag, z)
plt.yscale('log')
plt.xlabel(r'$Q$ ($\mathrm{\AA^{-1}}$)')
plt.ylabel(r'$Intensity (a.u.)$')
plt.savefig(f'director/{scan_name}_{slicing}cut_ 45_degree.png', dpi=300)
np.savetxt(f'director/scan_name}_{slicing}cut_ 45_degree.txt', (np.vstack((diag,z))).T)
plt.show()
plt.close(scan)
## Line-cut in crystallographic plane and 1D plot
#Select range of cut in 2D pattern
cut = qxy[:600,50:70]
Intensity_cut = Intensity [:600,50:70] #select intensity value

#Choose opportunity line cut
## define a function that allows you to delete unwanted cutting lines with a click
fig, ax = plt.subplots()
lines =[]
for l in range (np.shape(Intensity_cut)[1]):
    line, = ax.plot(cut[:,0],Intensity_cut[:,l],label = '%s data' % l )
    lines.append(line)
leg = fig.legend(loc='upper right', prop={'size': 7}, fancybox=True, shadow=True)
leg.get_frame().set_alpha(1)
lined = dict()
for legline, origline in zip(leg.get_lines(), lines):
   legline.set_picker(5)  # 5 points tolerance
   lined[legline] = origline
def onpick(event, figu=fig):
    legline = event.artist
    orig = lined[legline]
    vis = not orig.get_visible()
    orig.set_visible(vis)
    if vis:
        legline.set_alpha(1.)
    else:
        legline.set_alpha(.1)
    figu.canvas.draw()
fig.canvas.mpl_connect('pick_event',onpick)
plt.yscale('log')
plt.show()
plt.close(fig)
```

```
## select the desired line
scan = plt.figure()
slicing = int(input('select line to slice: '))
y = Intensity_cut[:,slicing]
plt.plot(cut[:,1], y)
plt.yscale('log')
plt.xlabel(r'$Q$ ($\mathrm{\AA^{-1}}$)')
plt.ylabel(r'$Intensity (a.u.)$')
plt.savefig(f'director/{scan_name}_{slicing}cut_ in crystallographic plane.png', dpi=300)
np.savetxt(f'director/scan_name}_{slicing}cut_ in crystallographic plane.txt',
(np.vstack((cut[:,1],y))).T)
plt.show()
plt.close(scan)
```

Script 3

```
# import libraries
Import glob
import numpy as np
from scipy.optimize import curve_fit
import matplotlib.pyplot as plt

# Define functions for fit
def func_correct (x, A, B, C, D, w, xc):
    return  A*np.exp(-x/B)+ C +(2*D/np.pi)*(w/(4*(x-xc)**2+w**2))

#Load scan
out_of_plane = [file for file in glob.glob('* out of crystallographic plane.txt')]
in_plane = [file for file in glob.glob('*in crystallographic plane.txt')]
degree_45 = [file for file in glob.glob('*45_degree.txt')]
# select scan
scan = ‘number_scan’
##Fit out_of_plane
#take scan name
Out_of_plane_name =[]
Out_of_plane_value =[]

for name in out_of_plane:
    fname = name
    Out_of_plane_name.append(fname)
```

```
    out_of_plane = np.loadtxt(fname)
    Out_of_plane_value.append((out_of_plane[:,1]))

# Select peak range
x_value = out_of_plane[90:150,0]
y = np.array(Out_of_plane_value).T
name = np.array(Out_of_plane_name)
fname = name[scan]
y_value = y[90:150,scan]

p0= (10, 2, 48480, 1000, 0.01, 0.4) #give values to the variables A, B, C, D, w, xc
respectively
popt, pcov = curve_fit(func_correct, x_value, y_value, p0, bounds = ((-np.inf, -np.inf, -
np.inf,0.1, 0.001, 0.3), (np.inf, 2.5, np.inf, np.inf, 0.9, 0.5)))
y_opt = func_correct(x_value, popt [0], popt [1], popt [2], popt [3], popt [4], popt [5]) #
          where 'popt' indicates  the values obtained from the fit
popt = [np.round (popt [i],5) for i in range (np.size (popt))]
error = np.sqrt(np.diag(pcov))
error = [np.round (error[i],5) for i in range (np.size (error))]
value_error = (np.vstack((popt_1,error))).T

plt.yscale('log')
plt.plot(x_value, y_value, 'k')
plt.plot(x_value, y_opt, label=f'D={popt [3]} ± {error[3]}\nw = {popt [4]} ±
{error[4]}\nxc={popt [5]} ± {error[5]}')
plt.xlabel(r'$Q$ ($\mathrm{\AA^{-1}}$)')
plt.ylabel(r'$Intensity (a.u.)$')
plt.legend()
plt.savefig(f'director/Fit_'+fname+'.png')
np.savetxt(f'director/Fit_'+fname+'.txt', (np.vstack((x_value, y_value, y1_opt))).T)
plt.show()

##Fit in_plane
#take scan name
in_plane_name =[]
in_plane_value =[]

for name in in_plane:
    fname = name
    in_plane_name.append(fname)
    in_plane = np.loadtxt(fname)
    in_plane_value.append((in_plane[:,1]))
```

```
# Select peak range
x_value = in_plane[565:585,0]
y = np.array(in_plane_value).T
name = np.array(in_plane_name)
fname = name[scan]
y_value = y[565:585,scan]

p0= (1000, 1, 48480, 100, 0.01, 0.37) #give values to the variables A, B, C, D, w, xc
respectively
popt, pcov = curve_fit(func_correct, x_value, y_value, p0, bounds = ((-np.inf, 0.1, -np.inf,
0.1, 0.0001, 0.34),  (np.inf, np.inf, np.inf, np.inf, 0.9, 0.38)))
y_opt = func_correct(x_value, popt [0], popt [1], popt [2], popt [3], popt [4], popt [5]) #
where 'popt' indicates the values obtained from the fit
popt = [np.round (popt [i],5) for i in range (np.size (popt))]
error = np.sqrt(np.diag(pcov))
error = [np.round (error[i],5) for i in range (np.size (error))]
value_error = (np.vstack((popt_1,error))).T

plt.yscale('log')
plt.plot(x_value, y_value, 'k')
plt.plot(x_value, y_opt, label=f'D={popt [3]} ± {error[3]}\nw = {popt [4]} ±
{error[4]}\nxc={popt [5]} ± {error[5]}')
plt.xlabel(r'$Q$ ($\mathrm{\AA^{-1}}$)')
plt.ylabel(r'$Intensity (a.u.)$')
plt.legend()
plt.savefig(f'director/Fit_'+fname+'.png')
np.savetxt(f'director/Fit_'+fname+'.txt', (np.vstack((x_value, y_value, y1_opt))).T)
plt.show()

##Fit 45 degree
#take scan name
degree_45_name =[]
degree_45_value =[]

for name in degree_45:
    fname = name
    degree_45_name.append(fname)
    degree_45 = np.loadtxt(fname)
    degree_45_value.append((degree_45[:,1]))

# Select peak range
```

```
x_value = degree_45[61:80,0]
y = np.array(degree_45_value).T
name = np.array(degree_45_name)
fname = name[scan]
y_value = y[61:80,scan]

p0= (1000, 1, 48480, 100, 0.01, 0.38) #give values to the variables A, B, C, D, w,   xc
                                                    respectively
popt, pcov = curve_fit(func_correct, x_value, y_value, p0, bounds = ((-np.inf, 0.1, -np.inf,
0.1, 0.001, 0.35), (np.inf, np.inf, np.inf, np.inf, 0.7, 0.4)))
y_opt = func_correct(x_value, popt [0], popt [1], popt [2], popt [3], popt [4], popt [5]) #
where 'popt' indicates  the values obtained from the fit
popt = [np.round (popt [i],5) for i in range (np.size (popt))]
error = np.sqrt(np.diag(pcov))
error = [np.round (error[i],5) for i in range (np.size (error))]
value_error = (np.vstack((popt_1,error))).T

plt.yscale('log')
plt.plot(x_value, y_value, 'k')
plt.plot(x_value, y_opt, label=f'D={popt [3]} ± {error[3]}\nw = {popt [4]} ±
{error[4]}\nxc={popt [5]} ± {error[5]}')
plt.xlabel(r'$Q$ ($\mathrm{\AA^{-1}}$)')
plt.ylabel(r'$Intensity (a.u.)$')
plt.legend()
plt.savefig(f'director/Fit_'+fname+'.png')
np.savetxt(f'director/Fit_'+fname+'.txt', (np.vstack((x_value, y_value, y1_opt))).T)
plt.show()

## for annealed samples the fit function described above was modified taking into account
the signal from Kapton; in particular two fits have been made, namely:

def kapton (x, A, B, C, D, w, xc):
   return A*np.exp(-x/B)+C + (2*D/np.pi)*(w/(4*(x-xc)**2+w**2))

def func_correct (x, A, B, C,  D, w, xc):
   return (2*area/np.pi)*(width/(4*(x-(peak_position))**2+(width)**2))+
            +A*np.exp(-x/B)+C +(2*D/np.pi)*(w/(4*(x-xc)**2+w**2))
## load Kapton scan

fname = np.loadtxt('Kapton_scan.txt')
x_data = fname[115:140,0]
y_data = fname[115:140,1]
```

```
## load all scan
scan = np.loadtxt('scan_name.txt')
y = scan[115:140,1]

## Fit Kapton

p0= (100, 0.1, 50000, 1, 0.001, 0.47)
popt, pcov = curve_fit(kapton, x_data, y_data, p0, bounds = (( 0.1, 0.01, 0.1, 0.1, 0.0001,
0.46), (np.inf, 2.5, np.inf, np.inf, 0.5, 0.48)))
y_opt = kapton(x_data, popt[0], popt[1], popt[2], popt[3], popt[4], popt[5])
z = np.sqrt(np.diag(pcov))
area= popt[3]
width= popt[4]
peak_position = popt[5]

## Fit scan, by considering the area, width and peak position associated to the Kapton

p0= (220028, 0.8, 48480, 80036, 0.053, 0.436)
popt_1, pcov = curve_fit(func_correct, x_data, y, p0, bounds = ((-np.inf, -np.inf, -np.inf, -
np.inf, 0.001, 0.3), (np.inf, 5, np.inf, np.inf, 0.1,  0.5)))
y1_opt = func_correct(x_data, popt_1[0], popt_1[1], popt_1[2], popt_1[3], popt_1[4],
popt_1[5])
popt_1 = [np.round (popt_1[i],5) for i in range (np.size (popt_1))]
error = np.sqrt(np.diag(pcov))
error = [np.round (error[i],5) for i in range (np.size (error))]
value_error = (np.vstack((popt_1,error))).T
plt.yscale('log')
plt.plot(x_data, y, 'k')
plt.plot(x_data, y1_opt, label=f'D={popt_1[3]} ± {error[3]}\nw = {popt_1[4]} ±
{error[4]}\nxc={popt_1[5]} ± {error[5]}')
plt.xlabel(r'$Q$ ($\mathrm{\AA^{-1}}$)')
plt.ylabel(r'$Intensity (a.u.)$')
plt.legend()
plt.savefig(f'director /Fit_'+scan_name+'.png')
np.savetxt(f'director /Fit_'+scan_name+'.txt', (np.vstack((x_data, y, y1_opt))).T)
np.savetxt(f'director /Fit_value_'+scan_name+'.par', value_error)
plt.show()
```

1D Profiles Extracted from the 2D Diffraction Pattern and Lorentzian Fit

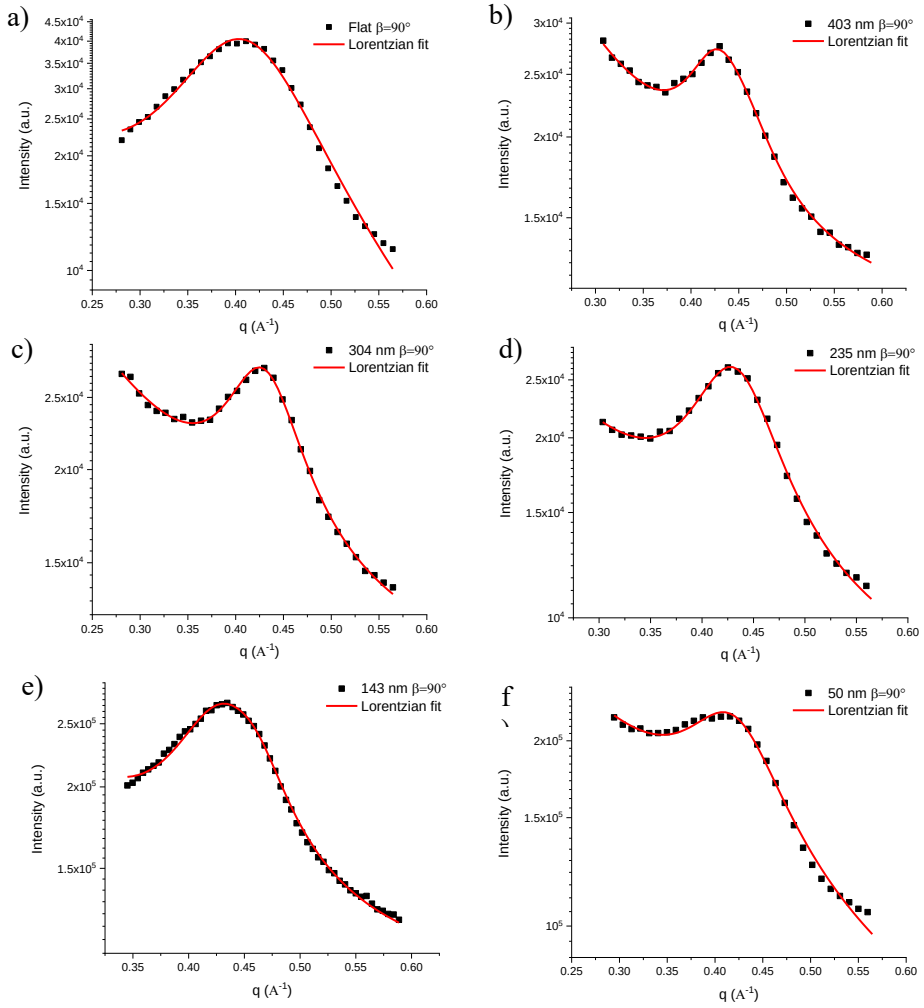

Figure S1.4. Experimental peak of untreated substrates and Lorentzian fit, black symbols and red line respectively, of 1D profiles, extracted from 2D patterns along the q_z direction at $\beta \approx 90°$.

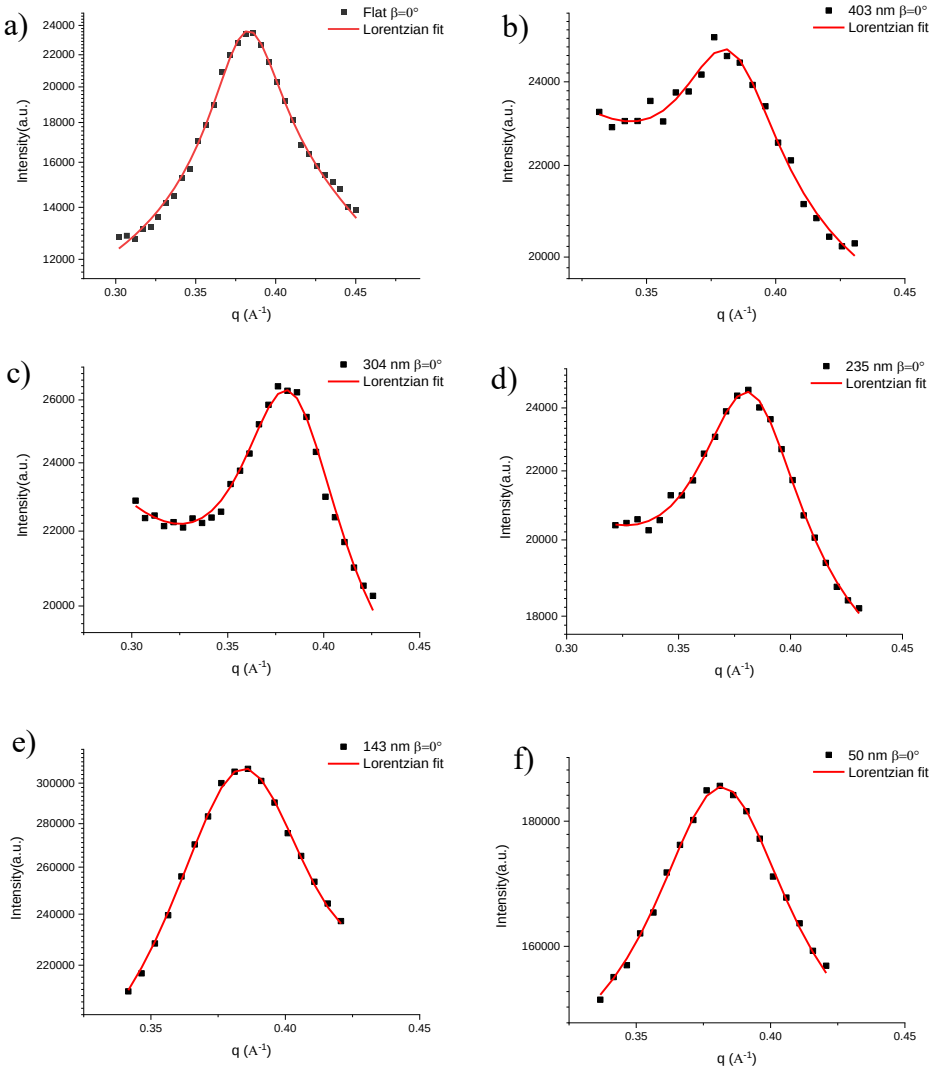

Figure S1.5. Experimental peak of untreated substrates and Lorentzian fit, black symbols and red line respectively, of 1D profiles, extracted from 2D patterns along the q_{xy} direction at $\beta = 0°$.

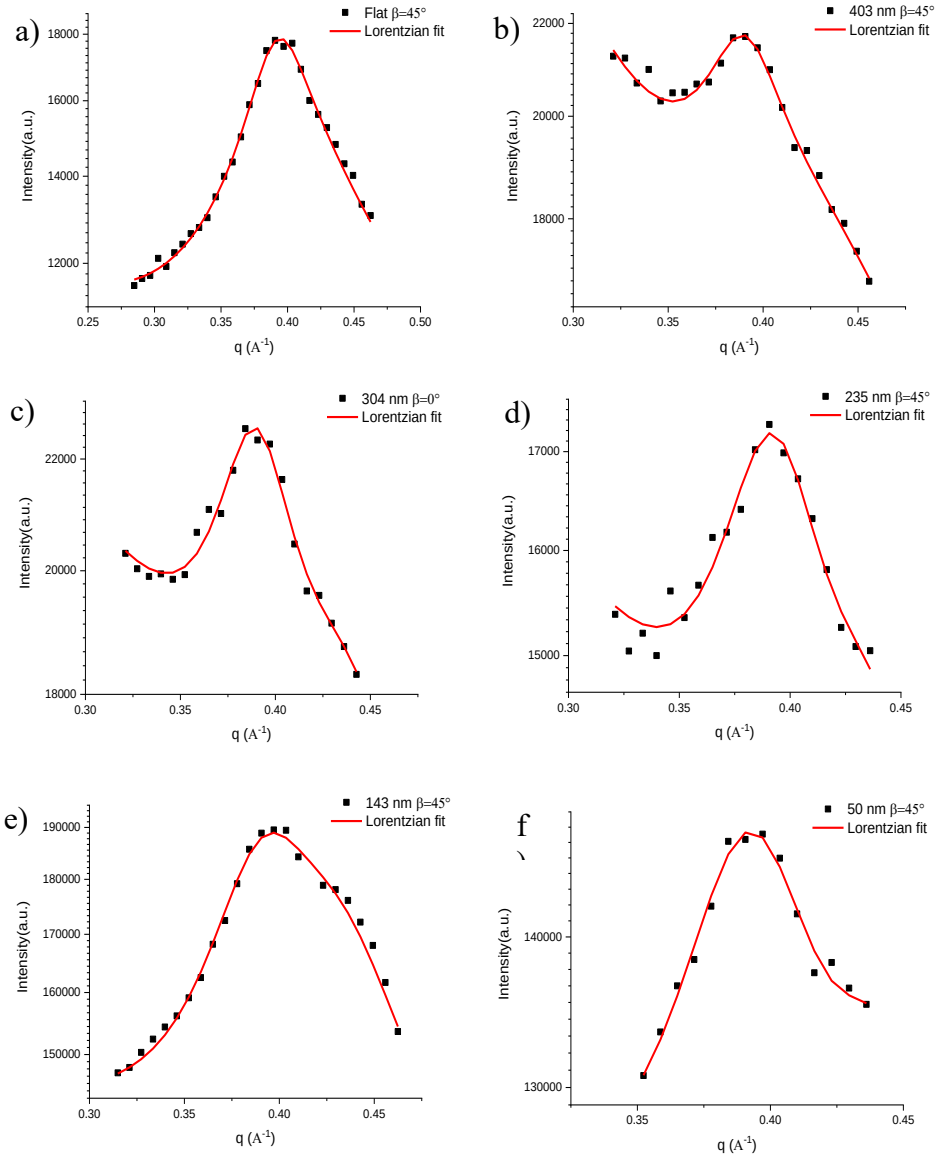

Figure S1.6. Experimental peak of untreated substrates and Lorentzian fit, black symbols and red line respectively, of 1D profiles, extracted from 2D patterns at β=45°.

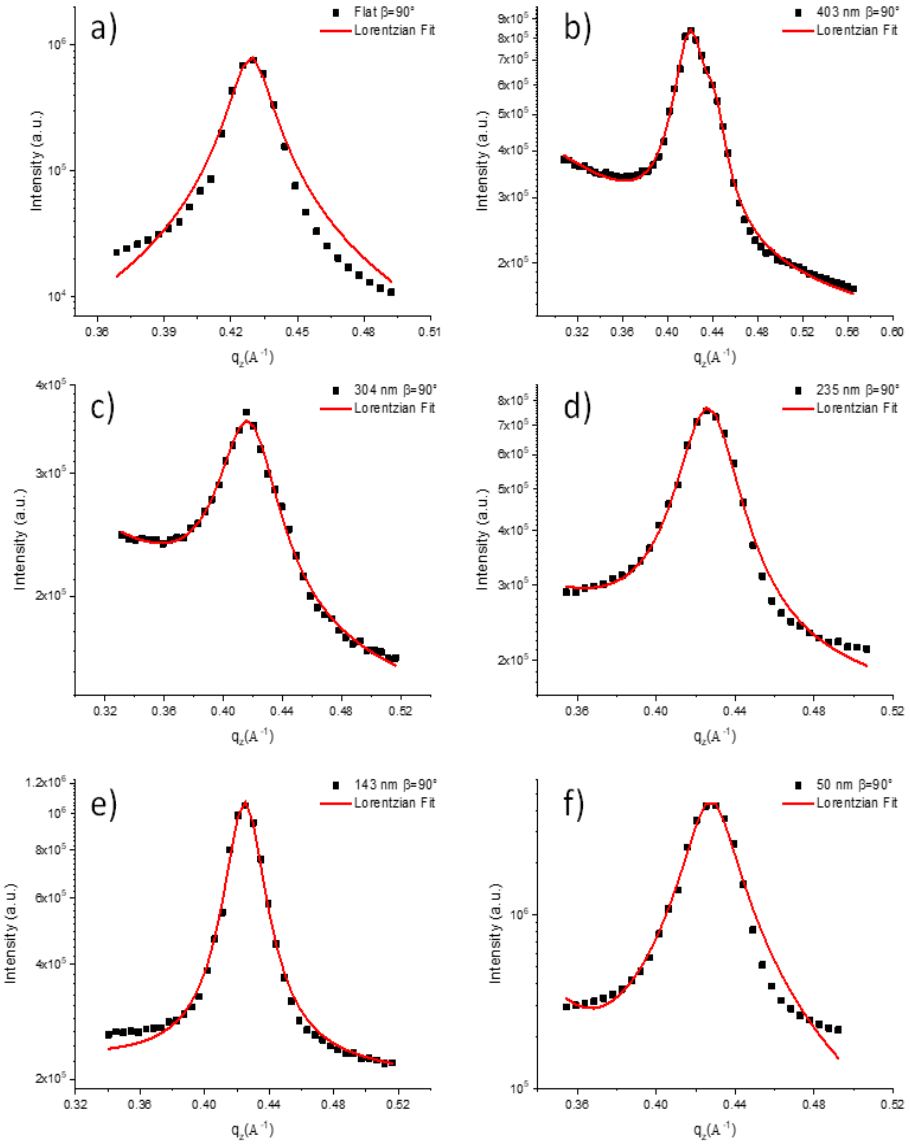

Figure S1.7. Experimental peak of treated substrates and Lorentzian fit, black symbols and red line respectively, of 1D profiles, extracted from 2D patterns along the q_z direction at $\beta \approx 90°$.

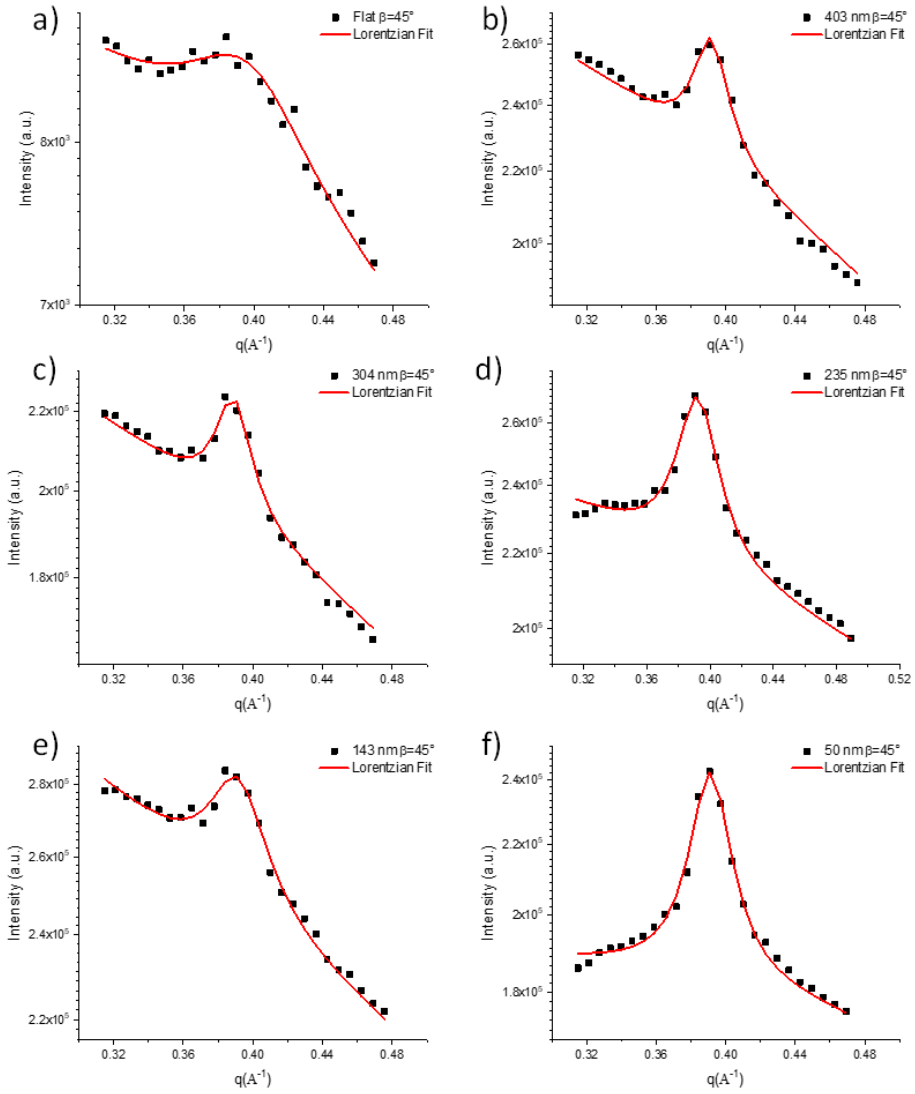

Figure S1.8. Experimental peak of treated substrates and Lorentzian fit, black symbols and red line respectively, of 1D profiles, extracted from 2D patterns along the q_z direction at $\beta = 45°$.

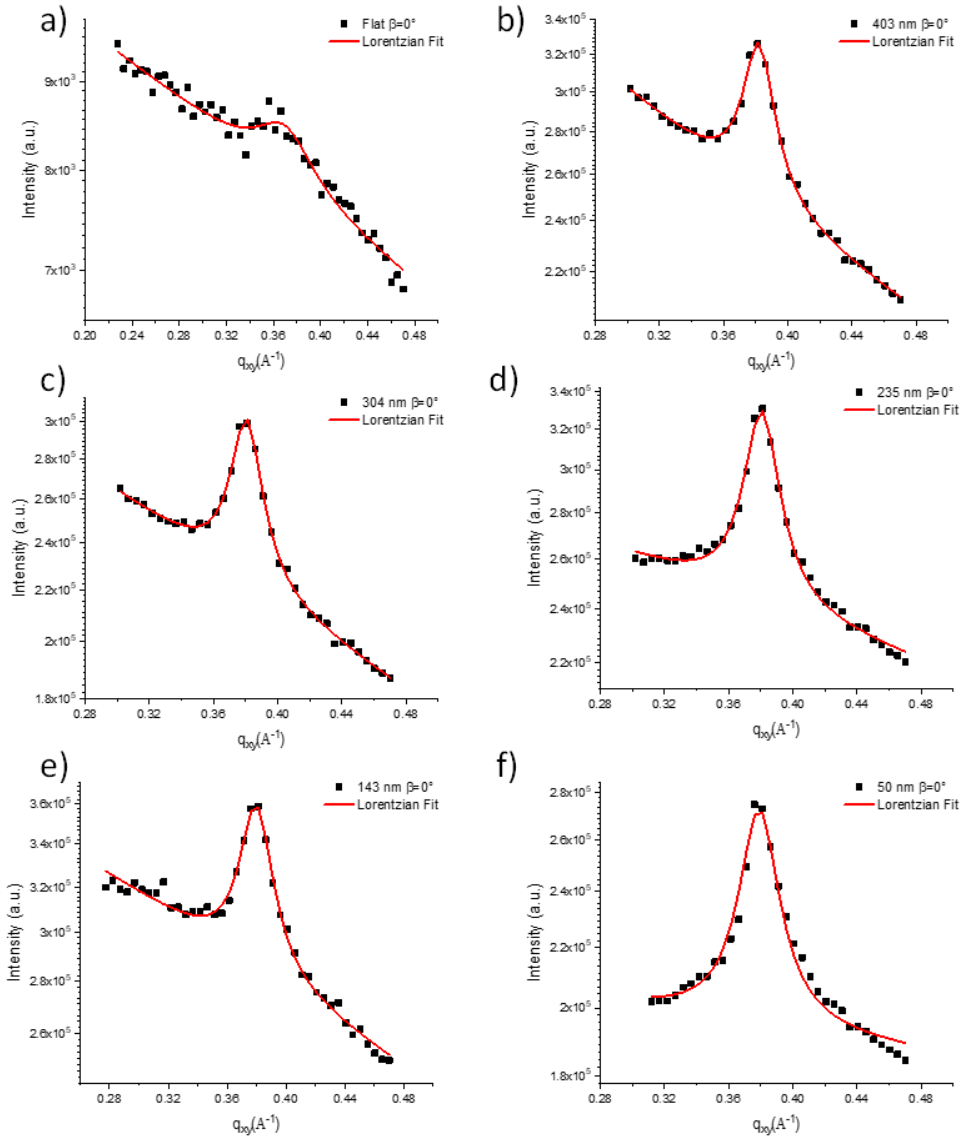

Figure 1.9. Experimental peak of treated substrates and Lorentzian fit, black symbols and red line respectively, of 1D profiles, extracted from 2D patterns along the q_z direction at $\beta = 0°$.

References

(1) Donose, B. C.; Taran, E.; Vakarelski, I. U.; Shinto, H.; Higashitani, K. Effects of Cleaning Procedures of Silica Wafers on Their Friction Characteristics. *J. Colloid Interface Sci.* **2006**, *299* (1), 233–237. https://doi.org/10.1016/j.jcis.2006.01.044.

(2) Messina, G. M. L.; Bocchinfuso, G.; Giamblanco, N.; Mazzuca, C.; Palleschi, A.; Marletta, G. Orienting Proteins by Nanostructured Surfaces: Evidence of a Curvature-Driven Geometrical Resonance. *Nanoscale* **2018**, *10* (16), 7544–7554. https://doi.org/10.1039/c8nr00037a.

(3) Konovalov, O.; Destri, G. L.; Seeck, O. H.; Mezger, M.; Haddad, J.; Deutsch, M.; Checco, A.; Ocko, B. M. Nanoscale Structure of Si / SiO 2 / Organics. *ACS Nano* **2014**, *8* (12), 12676–12681.

(4) Kondo, T.; Watanabe, R.; Shimoyama, Y.; Shinohe, K.; Kulinich, S. A.; Iwamori, S. Effect of Reactive Oxygen Species Generated with Ultraviolet Lamp and Plasma on Polyimide Surface Modification. *Surf. Interface Anal.* **2017**, *49* (11), 1069–1077. https://doi.org/10.1002/sia.6279.

(5) Qu, Y.; Li, L.; Lu, G.; Zhou, X.; Su, Q.; Xu, W.; Li, S.; Zhang, J.; Yang, X. A Novel Melting Behavior of Poly(3-Alkylthiophene) Cocrystals: Premelting and Recrystallization of Component Polymers. *Polym. Chem.* **2012**, *3* (12), 3301–3307. https://doi.org/10.1039/c2py20400b.

(6) van Oss, C. J.; Chaudhury, M. K.; Good, R. J. Interfacial Lifshitz—van Der Waals and Polar Interactions in Macroscopic Systems. *Chem. Rev.* **1988**, *88* (6), 927–941. https://doi.org/10.1021/cr00088a006.

(7) Good, R. J.; Girifalco, L. A. A Theory for Estimation of Surface and Interfacial Energies. III. Estimation of Surface Energies of Solids from Contact Angle Data. *J. Phys. Chem.* **1960**, *64* (5), 561–565. https://doi.org/10.1021/j100834a012.

(8) Usov, I.; Mezzenga, R. FiberApp: An Open-Source Software for Tracking and Analyzing Polymers, Filaments, Biomacromolecules, and Fibrous Objects. *Macromolecules* **2015**, *48* (5), 1269–1280. https://doi.org/10.1021/ma502264c.

(9) Antimonov, M.; Khounsary, A.; Weigand, S.; Rix, J.; Keane, D.; Grudzinski, J. J.; Johnson, A.; Zhou, Z.; Jansma, W. Large-Area Kapton x-Ray Windows. *Adv. X-Ray/EUV Opt. Components X* **2015**, *9588*, 95880F. https://doi.org/10.1117/12.2193680.

Appendix:

Second Section

Materials and Methods

Nanostructuring of the water/air interface. Colloidal aqueous dispersion at 34% wt of negatively charged silica nanoparticles (Ludox), having diameter 24.5 ± 3.9 nm and density 1.23 g/mL was purchased from Sigma Aldrich, Milan (Italy). Before their use, the nanoparticles were dialysed to remove excess ligands and impurities.[1] Negatively charged silica nanoparticles (Sicastar) diameter 19.0 ± 1.4 nm and nominal density 2.1g cm-3 were purchased from Micromod, Rostock (Germany) and used as received. Surfactants having the same polar trimethylammonium and different chain length, such as dodecyltrimethylammonium bromide (C_{12}TAB), myristyltrimethylammonium bromide (C_{14}TAB), hexadecyltrimethylammonium bromide (C_{16}TAB) and octadecyltrimethylammonium bromide (C_{18}TAB) were purchased from Sigma Aldrich, Milan (Italy) and used as received. Mixed C_nTAB/NPs dispersions, where n denotes the different number of C atom in the surfactant hydrophobic chain, were prepared by adding C_nTAB solutions to the silica dispersion. In particular, while the concentration of silica nanoparticles was kept constant, at 0.1% wt, the final concentration of the surfactant was varied. In order to promote the adsorption of the surfactant on the particles, NaCl[2] was added to the C_nTAB/NPs dispersions. The so-prepared dispersions were subsequently sonicated for 30 minutes in an ultrasonic bath, to promote homogenization. Surface tension and compression isotherms measurements were performed with a KSV Minitrough, Helsinki (Finland), equipped with a Wilhelmy paper plate that allows direct measurement of the surface pressure (P) equal to $\Pi = \gamma_0 - \gamma$ where γ_0 is the surface tension of pure water (72.8 mN/m at 20°C) while γ is the surface tension of the adsorbed monolayer. Variations of the surface tension were recorded as a function of the different nature of the surfactant and ionic strength, by monitoring the trend of the surface pressure as a function of time for one hour, in a Petri dish, in order to provide the time to the system to reach the equilibrium. The compression isotherms were conducted in a Langmuir trough, where it is possible to monitor the surface pressure variation during the reduction of the surface area.

Structural characterization. The assembly of surfactant-decorated NPs at the water/air interface was characterized by grazing incidence small angle X-Ray scattering (GISAXS), at the Sirius beamline of the Synchrotron Soleil, Paris (France). An 8 keV X-ray beam, with an angle of incidence of 0.111, e.g. 92% of the critical water/air angle for total external reflection was used. The diffraction patterns were recorded using a Pilatus 1M 2D detector, placed at a distance of 2.740m from the sample. A circular Teflon trough having a diameter of 10 cm was used for the

GISAXS experiments without compression, while a Langmuir trough was used for compression, simultaneously recording the diffraction pattern and the surface

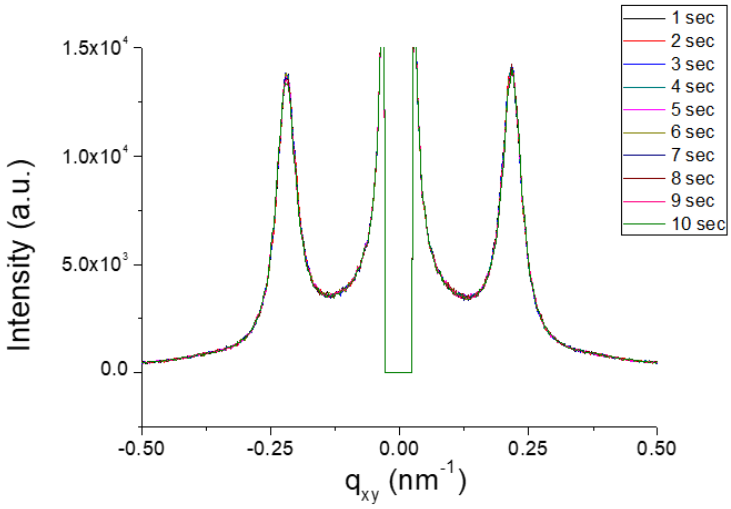

Figure S2.1. Evolution of the GISAXS Bragg rods with X-ray illumination, with ten successive illuminations of 1 second.

pressure. The integration of ten consecutive patterns recorded for one second constitute the diffraction patterns, since, as can be seen in figure S1, no radiation damage is observed. The resulting pattern consists of the intensity of the scattered radiation as a function of the two transfer components of the wave vector q_z and q_{xy}, in which q_z is the transfer component of the wave vector perpendicular to the interface, defined as:[3]

$$q_z = \frac{2\pi}{\lambda}[sin\alpha_d + sin\alpha_i]$$

while q_{xy} is the component parallel to the interface and is defined as: [3]

$$q_{xy} = \frac{2\pi}{\lambda}[\sqrt{cos^2\alpha_d + cos^2\alpha_i - 2cos\alpha_i cos\alpha_d cos\vartheta_d}]$$

where λ is the wavelength of the X-rays, α_i is the angle of the incident beam, α_d is the normal scattering angle and ϑ_d is the scattering angle in the plane. The 1D profiles were obtained from the diffraction patterns by cutting and integrating the GISAXS patterns along q_z in the region between 0.09 and 0.13nm^{-1} (Script 1). Lorentzian fitting of the obtained peaks was performed using the following equation, for both positive and negative q_{xy} peaks:

$$y = y_0 + \frac{B}{q} + \frac{2A}{\pi} * \frac{w}{4(q-q_c)^2+w^2} + \frac{2C}{\pi} * \frac{w_1}{4(q-q_{c_1})^2+{w_1}^2}$$

where the first and the second terms takes into account the background and the third term represent the main Lorentzian peak originated by the integration of the Bragg rod centred at q_c, characterized by an area A and a full width at half maximum (FWHM) w. The fourth term takes into account the possible second weaker peak centred at q_{c1}, between $\sqrt{3}q_c$ and $2q_c$ and characterized by an area C and a FWHM w_1. (Script_2)

Script 1

```
# import libraries

import h5py
import numpy as np
import nexusformat.nexus as nx
import matplotlib.pyplot as plt
from matplotlib.color import LogNorm

## set parameters

Wavelength = 1.55 #A-1
Distance_sample_detector = 2517#mm
pixel_size = 172/1000 #mm
pixels_x = 981
pixels_y = 1043
x = np.arange(0,pixels_x)

zero_x = 489

#conversion from pixel to scattering vector ‘q’
x = np.arange(0,981)
q = np.sin(np.arctan((zero_x -x)* pixel_size /Distance_sample_detector)/2)*
    *4*np.pi/ Wavelength
# load data
fname = nx.nxload(‘file_name.nxs')
scan_name = 'file_name'
scan_data = fname['root.spyc.DiffractoScanConfig/scan_data'] # I indicate the path in
                                                    which the acquired diffractograms are contained
print (scan_data.tree)
```

```
# the tree structure shows that the number data containing the diffraction pattern, with a
dtype int32

line_cut_all= []
for i in scan_data:
   Data = scan_data[i]
   if (Data.dtype)=='int32':
      print(i)

## create a matrix of zeros in order to sum the 'j' acquisitions acquired for the same sample,
selecting the range of cut, in the diffraction pattern, in which the signals are contained.
      data_sum = np.zeros((40,981))
      for j in range (np.shape(Data)[0]):
         image = Data[j,860:900,:]
         print(image.shape)

         Image = np.array(image[:,:])#all_scan
         line_cut_all.append(Image)
         data_sum = data_sum + image #sum_scan
      Image_sum = np.array (data_sum)

plt.imshow(Image_sum, interpolation='nearest',vmin=1, vmax=100000)
plt.savefig(f'director /Cut_{scan_name}.png', dpi = 300)
plt.show()
#Sum_scan and create 1D plot
Image_sum = np.sum(Image_sum, axis=0)
Image_ = (np.vstack((q,Image_sum))).T
plt.plot(q, Image_sum)
plt.yscale('log')
plt.xlabel(r'$q$ ($\mathrm{\AA^{-1}}$)')
plt.savefig(f'director /{scan_name}.png', dpi = 300)
np.savetxt(f'director/{scan_name}.txt', Image_)
plt.show()

##For compression isotherm, the macro used allows to acquire, at each variation of area, the
diffraction pattern, recording at the same time, the values of area and corresponding surface
pressure. Therefore, the script was modified in order to extract the data of our interest,
namely: diffraction patterns and corresponding area and pressure values.

# load data
fname = nx.nxload('file_name.nxs')
```

```
scan_name = 'file_name'
scan_data = fname['root.spyc.DiffractoScanConfig/scan_data'] # I indicate the path in
                                        which the acquired diffractograms are contained
print (scan_data.tree)
# Identify the 'data_number' that contains the value of Surface Pression and Surface area
Surface_Pressure = scan_data['data_n']
Area = scan_data['data_n1']
Area_Surface_Pressure = (np.vstack((Area, Surface_Pressure))).T
np.savetxt(f'director /Area_Surface_Pressure.txt', Area_Surface_Pressure, header= str(f'Area
, Pressure'))
Isotherm = (np.vstack((Area, Surface_Pressure))).T
Image_all = scan_data['data_n2']  # contains 'i' diffraction patterns equal to the ΔA shifts
                                        made during compression
for i in range(np.shape(Image_all)[0]):
    Single_scan = Image_all[i,:,:]
    fig = plt.figure()
    plt.imshow(Single_scan,interpolation='nearest',norm=LogNorm(vmin=0.5, vmax=4000))
    plt.savefig(f'director /Point_{i}_{scan_name}.png', dpi = 300)
    plt.show()
    plt.close(fig)
    Area_value = Area [i]
    Pressure_value = Surface_Pressure[i]
    line_cut = np.array(Single_scan[860:900,:]) #select range in diffraction patter in which
                                        there are the signal
    plt.imshow(line_cut, interpolation='nearest',norm=LogNorm(vmin=0.5,
                        vmax=4000)) #show the range of cut of the diffraction pattern
    plt.savefig(f'director /Point_{i}_{scan_name}.png', dpi = 300)
    plt.show()
    print (line_cut[0])
    for j in range (np.shape(line_cut)[0]):
        plt.yscale('log')
        all_line = line_cut[j,:]
        plt.plot(q, all_line)
    plt.show() # in order to verify that the signals obtained do not change and can be added
    Sum_range = np.sum (line_cut, axis =0)
    Line_cut = (np.vstack((q, Sum_range))).T
    fig1 = plt.figure()
    plt.yscale('log')
    plt.plot(q, Sum_range, label = f'Area ={Area_value}\n Pressure={Pressure_value}')
    plt.xlabel(r'$q$ ($\mathrm{\AA^{-1}}$)')
    plt.legend()
    plt.savefig(f'director/Point_{i}_{scan_name}.png', dpi = 300)
```

```
    np.savetxt(f'director/Point_{i}_{scan_name}.txt', Line_cut , header= str(f'Area
={Area_value}, Pressure={Pressure_value}'))
    plt.show()
    plt.close (fig1)
```

Script 2

```
# import libraries

import os
import numpy as np
import glob
import matplotlib.pyplot as plt
from scipy.optimize import curve_fit

# Define functions for fit
def func_correct (x, A, B, D, w, xc):
    return  A+B/x +(2*D/np.pi)*(w/(4*(x-xc)**2+w**2))

name = []
all_File = []

#Load scan and create matrix
file = sorted([file for file in glob.glob('*_name.txt')], key = lambda filename: int
(filename.split('_')[1]))
for f in file:
    fname = f
    name.append (fname)
    data = np.loadtxt (fname)
    data_1 = data [:,1]
    all_File.append (data_1)
y_data = (np.array (all_File)).T
name = np.array(name)

# select scan and the range in which the are the right and left peak
name = name[:]
y_data = y_data[:,:]

x = data[360:435,0] #right
x_1 = data[550:610,0] #left
```

```
##Fit right and left peaks
for i in range (np.shape (y_data)[1]):
    #right
    y = y_data[360:435,i]
    scan_name = name[i]
    p0= (22080, 3, 100, 0.1, 0.027) #give values to the variables A, B, D, w, xc respectively
    popt, pcov = curve_fit(func_correct, x, y, p0, bounds = ((0.1, -np.inf, 0.1, 0.001, 0.0249),
(np.inf, np.inf, np.inf, 0.9,  0.03)))
    y_opt = func_correct(x, popt[0], popt[1], popt[2], popt[3], popt[4]) # where 'popt'
                                        indicates the values obtained from the fit
    popt = [np.round (popt[i],5) for i in range (np.size (popt))]
    error = np.sqrt(np.diag(pcov))
    error = [np.round (error[i],5) for i in range (np.size (error))]
    value_error = (np.vstack((popt,error))).T
    np.savetxt(f'director/Fit_value_'+scan_name+'_right.par', value_error[2:,:], header =
'Area\nWidth\nPeak_position')
    np.savetxt(f'director/Only_fit_'+scan_name+'_right.par', y_opt)
    fig = plt.figure()
    plt.yscale('log')
    plt.plot(x, y, 'k')
    plt.plot(x, y_opt, label=f'D={popt[2]} ± {error[2]}\nw = {popt[3]} ±
{error[3]}\nxc={popt[4]} ± {error[4]}')
    plt.xlabel(r'$Q$ ($\mathrm{\AA^{-1}}$)')
    plt.ylabel(r'$Intensity (a.u.)$')
    plt.legend()
    plt.savefig(f'director/Fit_'+scan_name+'_right.png')
    np.savetxt(f'director/Fit_'+scan_name+'_right.txt', (np.vstack((x, y, y_opt))).T)
    plt.show()
    plt.close (fig)

    #left
    y_1 = y_data[550:610,i]
    p0= (3500, 3, 100, 0.1, -0.027) ) #give values to the variables A, B, D, w, xc respectively
    popt_1, pcov = curve_fit(func_correct, x_1, y_1, p0, bounds = ((-3000, -np.inf, 0.1,
0.001, -0.04), (np.inf, np.inf, np.inf, 0.5,  -0.026)))
    y1_opt = func_correct(x_1, popt_1[0], popt_1[1], popt_1[2], popt_1[3], popt_1[4]) #
    where 'popt' indicates the values obtained from the fit
    popt = [np.round (popt[i],5) for i in range (np.size (popt))]
    error = np.sqrt(np.diag(pcov))
    error = [np.round (error[i],5) for i in range (np.size (error))]
    value_error = (np.vstack((popt,error))).T
```

```
    np.savetxt(f'director/Fit_value_'+scan_name+'_left.par', value_error[2:,:], header =
'Area\nWidth\nPeak_position')
    np.savetxt(f'director/Only_fit_'+scan_name+'_left.par', y_opt)
    fig1 = plt.figure()
    plt.yscale('log')
    plt.plot(x, y, 'k')
    plt.plot(x, y_opt, label=f'D={popt[2]} ± {error[2]}\nw = {popt[3]} ±
{error[3]}\nxc={popt[4]} ± {error[4]}')
    plt.xlabel(r'$Q$ ($\mathrm{\AA^{-1}}$)')
    plt.ylabel(r'$Intensity (a.u.)$')
    plt.legend()
    plt.savefig(f'director/Fit_'+scan_name+'_left.png')
    np.savetxt(f'director/Fit_'+scan_name+'_left.txt', (np.vstack((x, y, y_opt))).T)
    plt.show()
    plt.close (fig1)
```

Script 3

Interparticle distance and force

```
# import libraries
import numpy as np
import glob

Value_right = []
Error_right = []
Value_left = []
Error_left = []
name_right = []
name_left = []

# load fit value for left and right peak
right = sorted([file for file in glob.glob('director/Fit_value_*name*right.par')], key =
            lambda filename: int (filename.split('_')[3]))
left = sorted([file for file in glob.glob('director/Fit_value_*name*left.par')], key = lambda
            filename: int (filename.split('_')[3]))

#create array  for right and left peak value
for r in right:
    fname = r
    name_right.append(fname)
```

```
    data = np.loadtxt(fname)
    All_file = np.zeros ((6,2))
    All_file[:data.shape[0],:data.shape[1]] = data
    value_right = All_file[:,0]
    error_right = All_file [:,1]
    Value_right.append(np.hstack((value_right)))
    Error_right.append(np.hstack((error_right)))

value_right = (np.array(Value_right))
error_right = np.array(Error_right)
names_right = np.array (name_right)

for l in left:
    fname = l
    name_left.append(fname)
    data = np.loadtxt(fname)
    All_file = np.zeros ((6,2))
    All_file[:data.shape[0],:data.shape[1]] = data
    value_left = All_file[:,0]
    error_left = All_file [:,1]
    Value_left.append(np.hstack((value_left)))
    Error_left.append(np.hstack((error_left)))

value_left = (np.array(Value_left))
error_left = np.array(Error_left)
names_left = np.array (name_left)

xc_value = (np.vstack((value_right[:,2],value_left[:,2])).T)

#Peak_right_left_mean

w_mean = (np.mean((np.vstack((value_right[:,1], value_left[:,1]))).T, axis =1))
xc_mean = (np.mean((np.vstack((value_right[:,2], np.abs(value_left[:,2])))).T, axis =1))

#Distance_length_mean
Interparticles_distance_mean = (4*np.pi/((xc_mean)*np.sqrt(3)))/10 #nm
Error_Interparticles_distance_mean = np.mean((np.vstack(
  (Error_Interparticles_distance_left , Error_Interparticles_distance_right))).T, axis= 1)
Correlation_length_mean = (2*np.pi/w_mean)/10
Error_Correlated_length_mean = np.mean((np.vstack( (Error_Correlated_length_left,
       Error_Correlated_length_right))).T, axis = 1)
Correlated_NPs_mean = Correlation_length_mean/Interparticles_distance_mean
Error_Correlated_NPs_mean = (Error_Correlated_length_mean/
       /Correlation_length_mean+Error_Interparticles_distance_mean/Interparticles_distance
    _mean) *Correlated_NPs_mean
```

```
np.savetxt('Interparticles_distance_Correlation_length_Correlated_NPs_file_name.txt',
(np.vstack((Interparticles_distance_mean,Error_Interparticles_distance_mean,
Correlation_length_mean, Error_Correlated_length_mean, Correlated_NPs_mean,
Error_Correlated_NPs_mean))).T, header= str(f'Interparticles_distance_mean Error,
Correlation_length_mean Error, Correlated_NPs_mean Error '))

#Force
Area_Surface_Pressure = np.loadtxt('Area_Surface_Pressure.txt')
Area = (Area_Surface_Pressure[:,0])/10000 #m
Surface_Pressure = ((Area_Surface_Pressure[:,1])/1000) #N/m
Delta_P = Surface_Pressure[1:] - Surface_Pressure[:450] # N/m
Error_delta_P = 2/1000

#mean
Adsorbed_NPs=  ((Area_Surface_Pressure[:,0])/
                    /(np.pi*((Interparticles_distance_mean/10**7)/2)**2))
Error_Adsorbd_NPs = (3/Area_Surface_Pressure[:,0] +
      +(Error_Interparticles_distance_mean/Interparticles_distance_mean)/10**7)*Adsor
      bed_NPs
Area_molec_mean = (Area / (Adsorbed_NPs [3])) #all_row
Error_Area_molec_mean = ( 3/ Area + (np.full((Surface_Pressure.shape),
                                Error_Adsorbd_NPs[3]))) *Area_molec
Delta_A_mol_mean = Area_molec_mean[1:]- Area_molec_mean[:450] #m2
Error_Delta_A_mol_mean = Error_Area_molec [1:]+ Error_Area_molec [:450]
Lavoro_mean = (Delta_A_mol_mean*Delta_P)/2 #Nm
Error_Lavoro_mean = (Error_Delta_A_mol_mean/Delta_A_mol_mean +
                          Error_delta_P/Delta_P)* Lavoro_mean
Delta_distance_mean = (Interparticles_distance_mean[1:]-
                          Interparticles_distance_mean[:450])/(1*10**9)#m
Error_delta_distance_mean = (Error_Interparticles_distance_mean[1:]+
                            Error_Interparticles_distance_mean[:450])/(1*10**9)
Delta_distance_mean[Delta_distance_mean== 0]= np.inf
Force_mean = Lavoro_mean/(6*Delta_distance_mean)*(1*10**12) #pN
Force_error_mean = (((Error_Lavoro_mean/Lavoro_mean)+
                    (Error_delta_distance_mean/Delta_distance_mean))*(Force_mean/(
                    1*10**12)))*(1*10**12)
Lateral_separation_mean = interparticles_distance_mean[:450] -24.55 #where 24.55 is the
                                                          NPs diameter
np.savetxt('Lateral_separation_Force_Pressure_file_name.txt',
    (np.vstack((Lateral_separation_mean,Surface_Pressure[:450],      Force_mean))).T,
    header= str(f'Lateral_separation_mean  Surface_Pressure Force_mean_pN'))
```

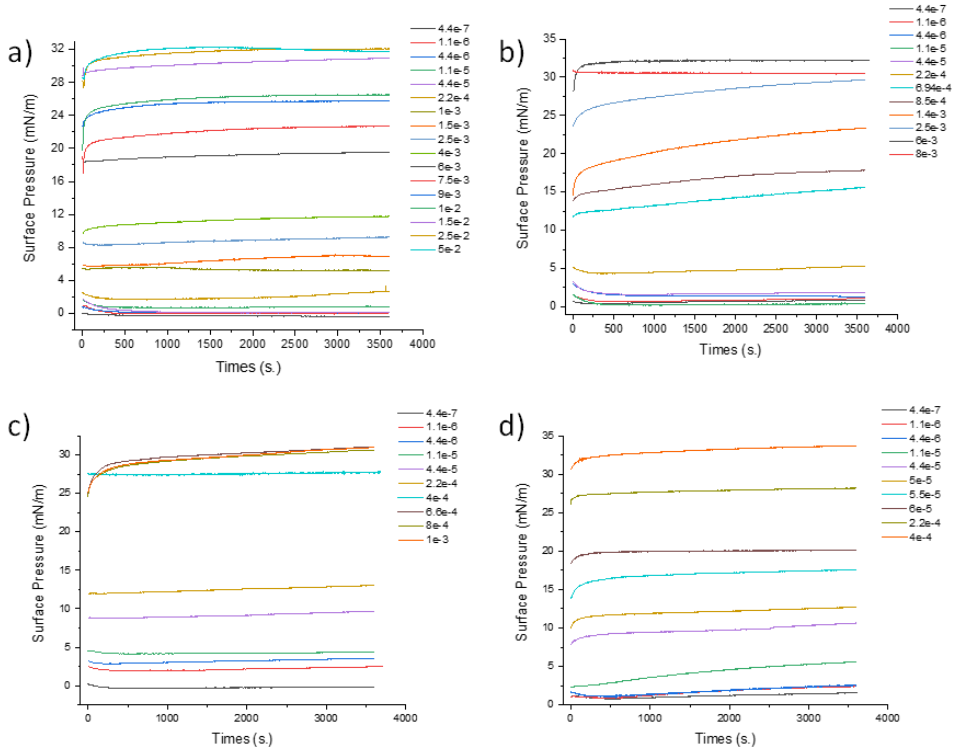

Figure S2.2. Temporal evolution of surface tension for mixed NPs 0.1%wt NaCl 1mM dispersions at the different C_nTAB concentrations (mol/L) reported in the box and for the different surfactant chain length: $C_{12}TAB$ (a), $C_{14}TAB$ (b), $C_{16}TAB$ (c), $C_{18}TAB$ (d).

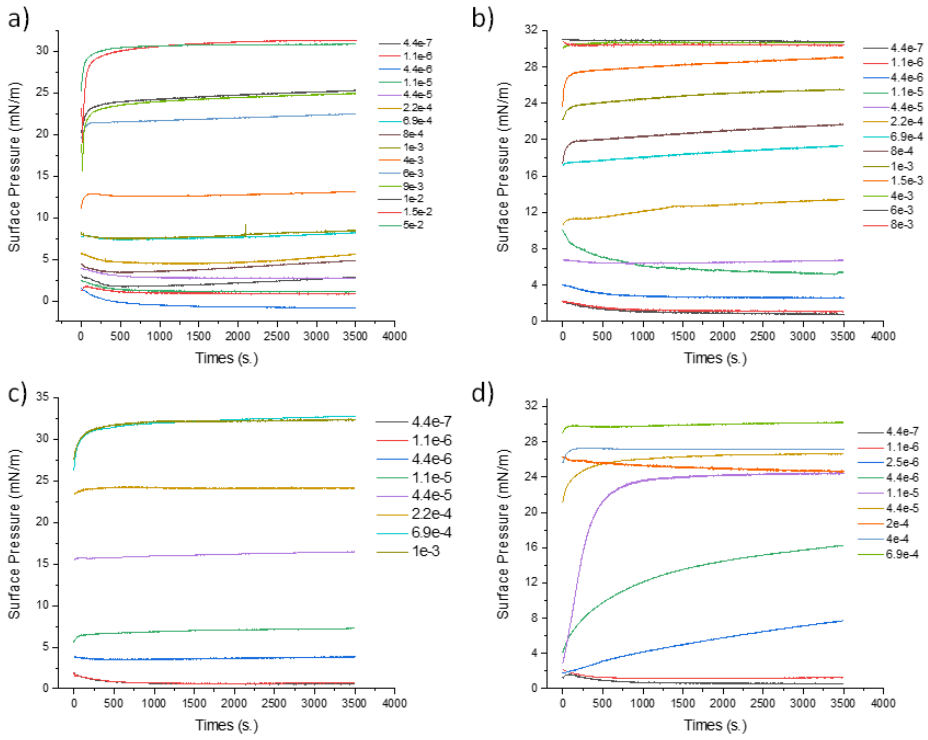

Figure S2.3. Temporal evolution of surface tension for mixed NPs 0.1%wt NaCl 0.1mM dispersions at the different C_nTAB concentrations (mol/L) reported in the box and for the different surfactant chain length: $C_{12}TAB$ (a), $C_{14}TAB$ (b), $C_{16}TAB$ (c), $C_{18}TAB$ (d).

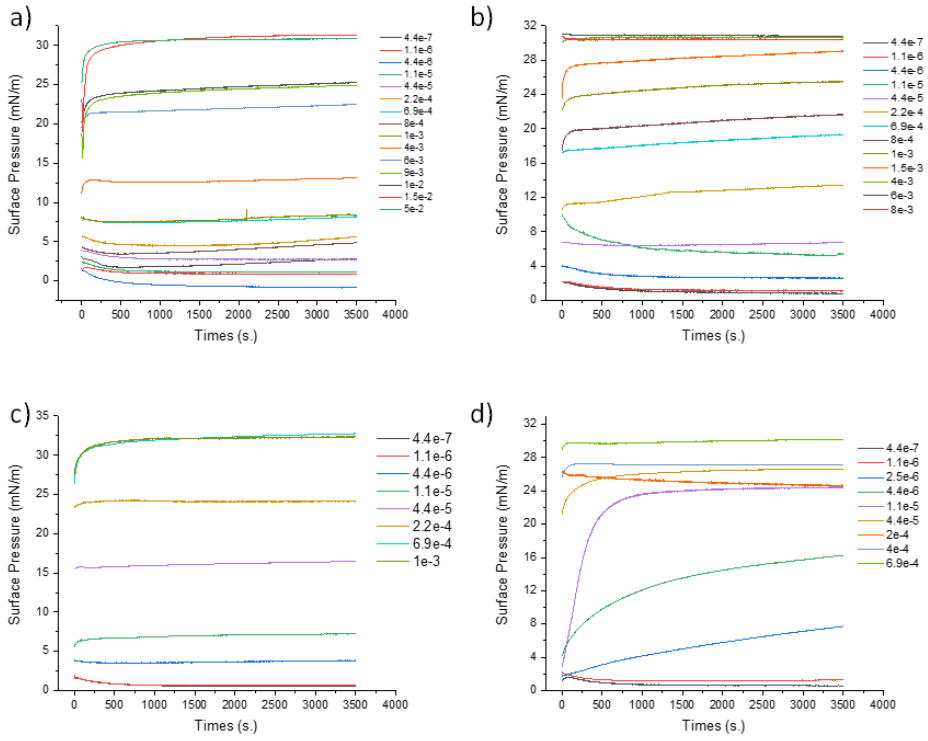

Figure S2.4. Temporal evolution of surface tension for mixed NPs 0.1%wt NaCl 10mM dispersions at the different C_nTAB concentrations (mol/L) reported in the box and for the different surfactant chain length: $C_{12}TAB$ (a), $C_{14}TAB$ (b), $C_{16}TAB$ (c), $C_{18}TAB$ (d).

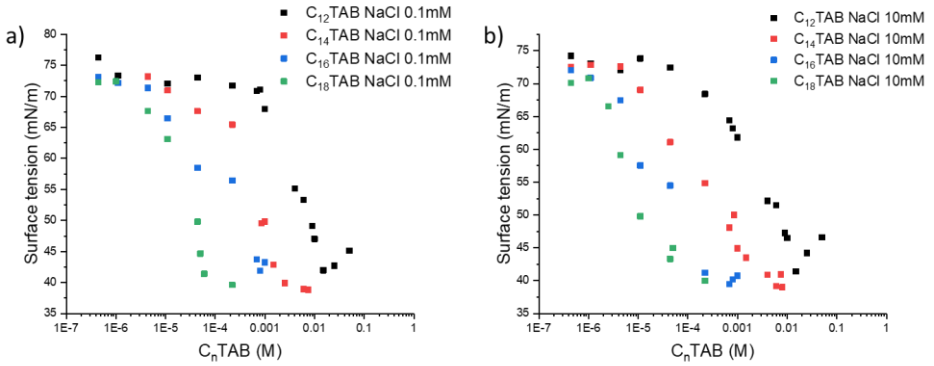

Figure S2.5. Variation of surface tension as a function of the ionic strength depending on the nature and concentration of the surfactant. The trends obtained are like those shown in Figure 12 in the presence of NPs This suggest that the role of NPs on surface tension is negligible.

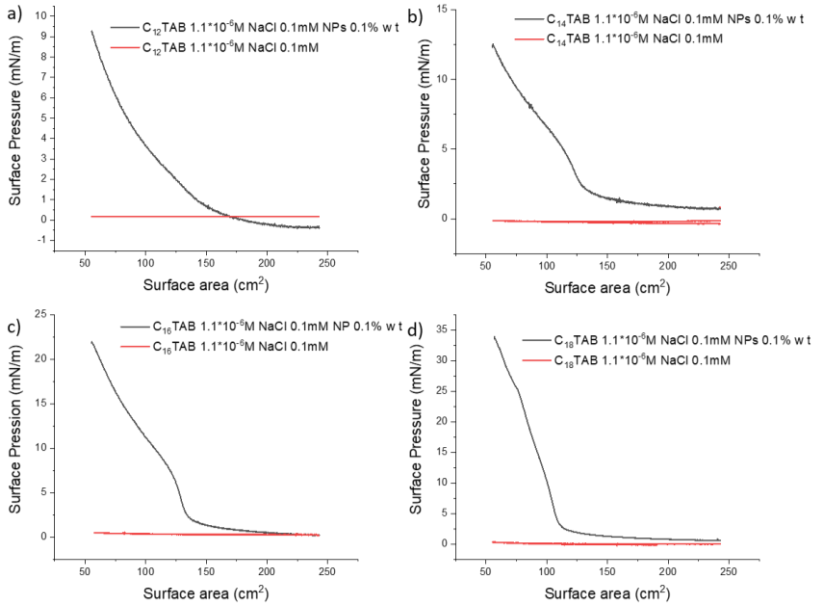

Figure S2.6. Compression isotherms of C_nTAB 1.1*10^{-6} M NaCl 0.1 mM NPs 0.1% wt monolayers (black curves) and of the corresponding surfactant monolayers in the absence of NPs (red curves), for the different chain lengths of surfactants: C_{12}TAB (a), C_{14}TAB (b), C_{16}TAB (c), C_{18}TAB (d). In the absence of NPs, no change of surface pressure is observed with compression.

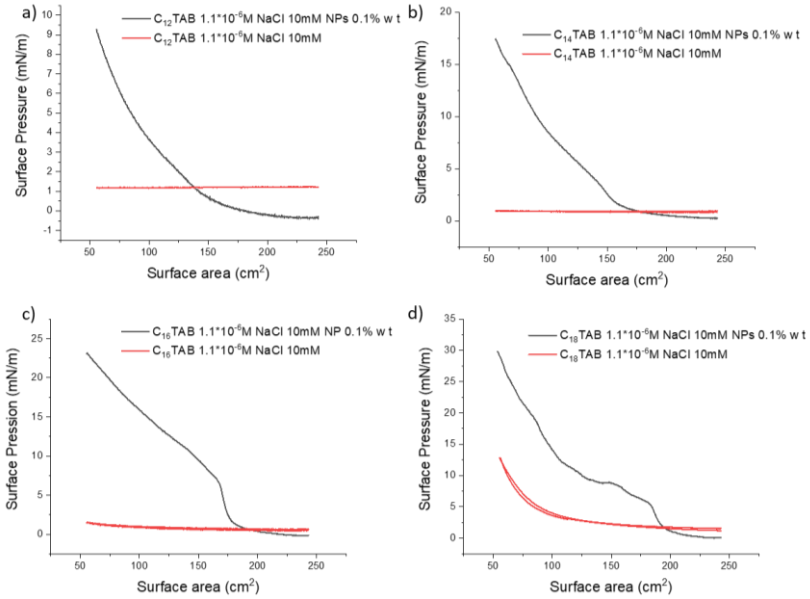

Figure S2.7. Compression isotherms of C_nTAB 1.1*10^{-6} M NaCl 10 mM NPs 0.1% wt monolayers (black curves) and of the corresponding surfactant monolayers in the absence of

NPs (red curves), for the different chain lengths of surfactants: C_{12}TAB (a), C_{14}TAB (b), C_{16}TAB (c), C_{18}TAB (d). While at smaller chain lengths, the presence of the surfactant alone shows no variation of surface pressure with compression, a different behaviour is observed for the higher chain length. However, this variation occurs at low surface areas, which confirms that the trend reported in the presence of complexes C_{18}TAB/NPs, black curve in figure d, is mainly attributed to the presence of NPs.

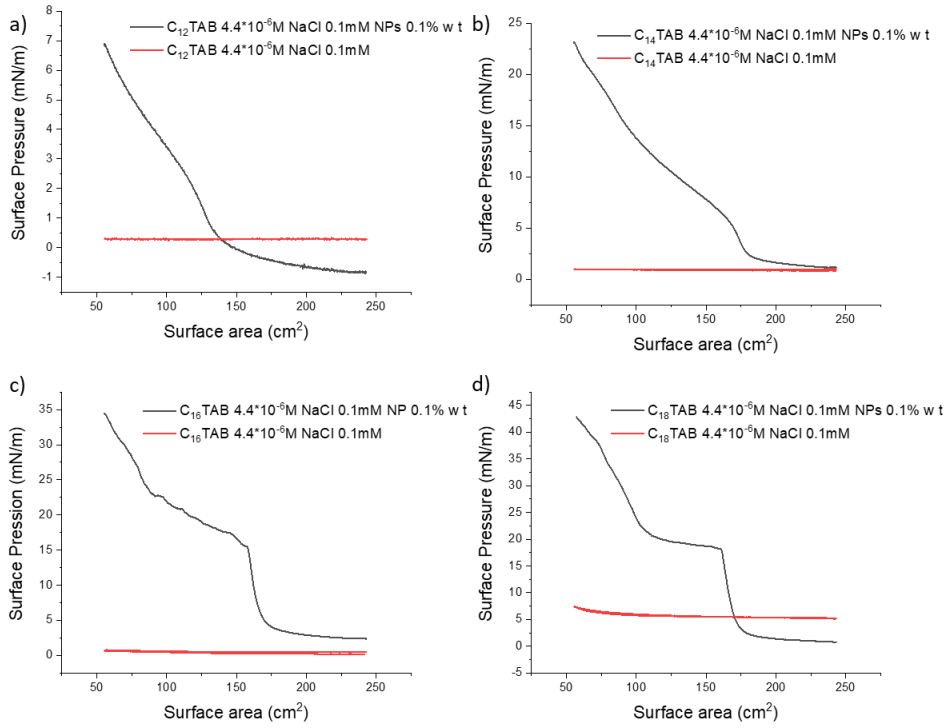

Figure S2.8. Compression isotherms of C_nTAB 4.4*10^{-6} M NaCl 0.1 mM NPs 0.1% wt monolayers (black curves) and of the corresponding surfactant monolayers in the absence of NPs (red curves), for the different chain lengths of surfactants: C_{12}TAB (a), C_{14}TAB (b), C_{16}TAB (c), C_{18}TAB (d). In the absence of NPs, no change of surface pressure is observed with compression.

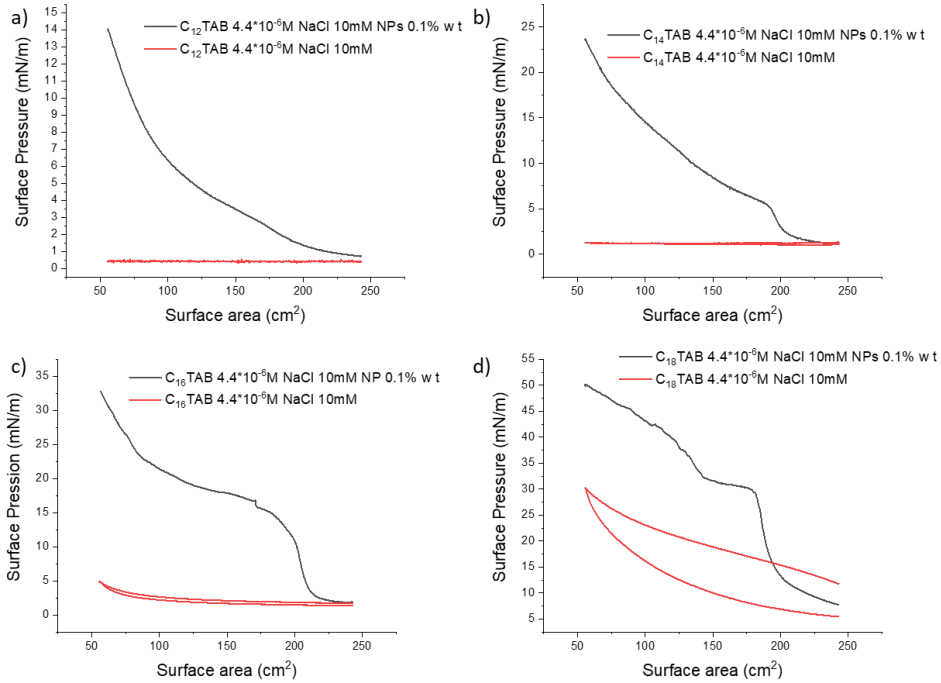

Figure S2.9. Compression isotherms of C_nTAB 4.4*10^{-6} M NaCl 10 mM NPs 0.1% wt monolayers (black curves) and of the corresponding surfactant monolayers in the absence of NPs (red curves), for the different chain lengths of surfactants: C_{12}TAB (a), C_{14}TAB (b), C_{16}TAB (c), C_{18}TAB (d). For the two smaller chain lengths, Figure a and b, in the absence of NPs, even at higher surfactant concentrations, no changes ofn pressure are observed with compression. In the case of C_{16}TAB, of increase in pressure is observed, for very high compressions, which appears more marked for C_{18}TAB. However, even in this case, the variations observed for the black curves, regardless of the surfactant chain length, are attributable to the complexes C_nTAB/NPs adsorbed to the interface.

Nanostructured monolayer in situ characterization

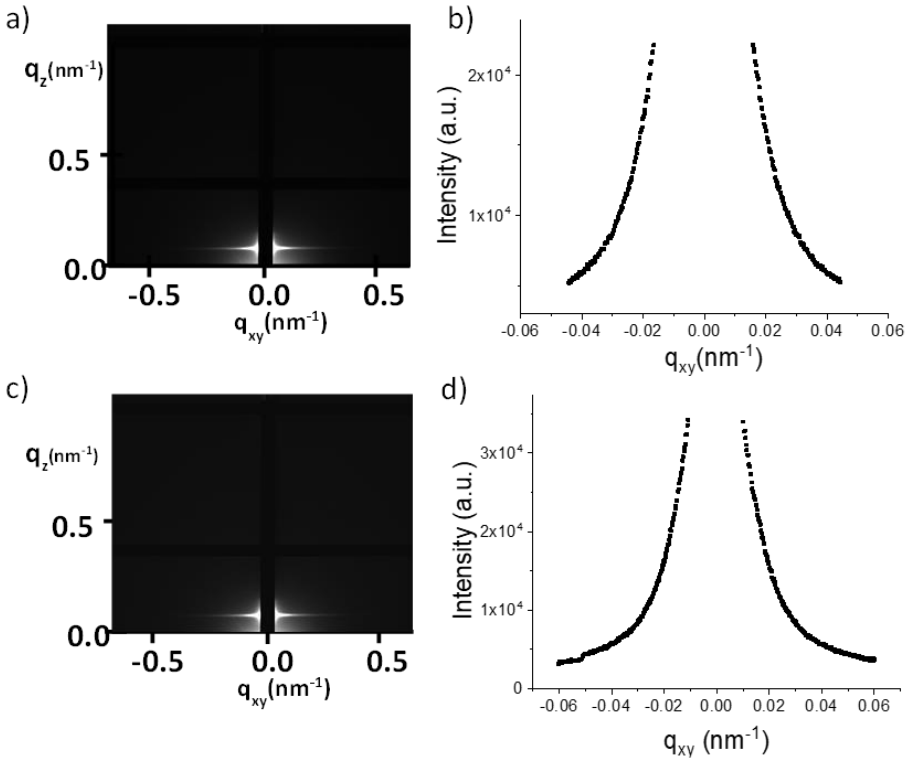

Figure S2.10. GISAXS pattern of NPs 0.1% wt NaCl 1 mM monolayer (a) and the corresponding horizontal cut between q_z 0.09 and 0.13 nm^{-1} (b). GISAXS pattern of C_{16}TAB $1.1 \cdot 10^{-6}$ M NaCl 1 mM monolayer (c) and the corresponding horizontal cut between q_z 0.09 and 0.13 nm^{-1} (d). The clear absence of Bragg rods, in both cases, reveals no NP monolayer formation.

1D Profiles Extracted from the 2D Diffraction Pattern and Lorentzian Fit

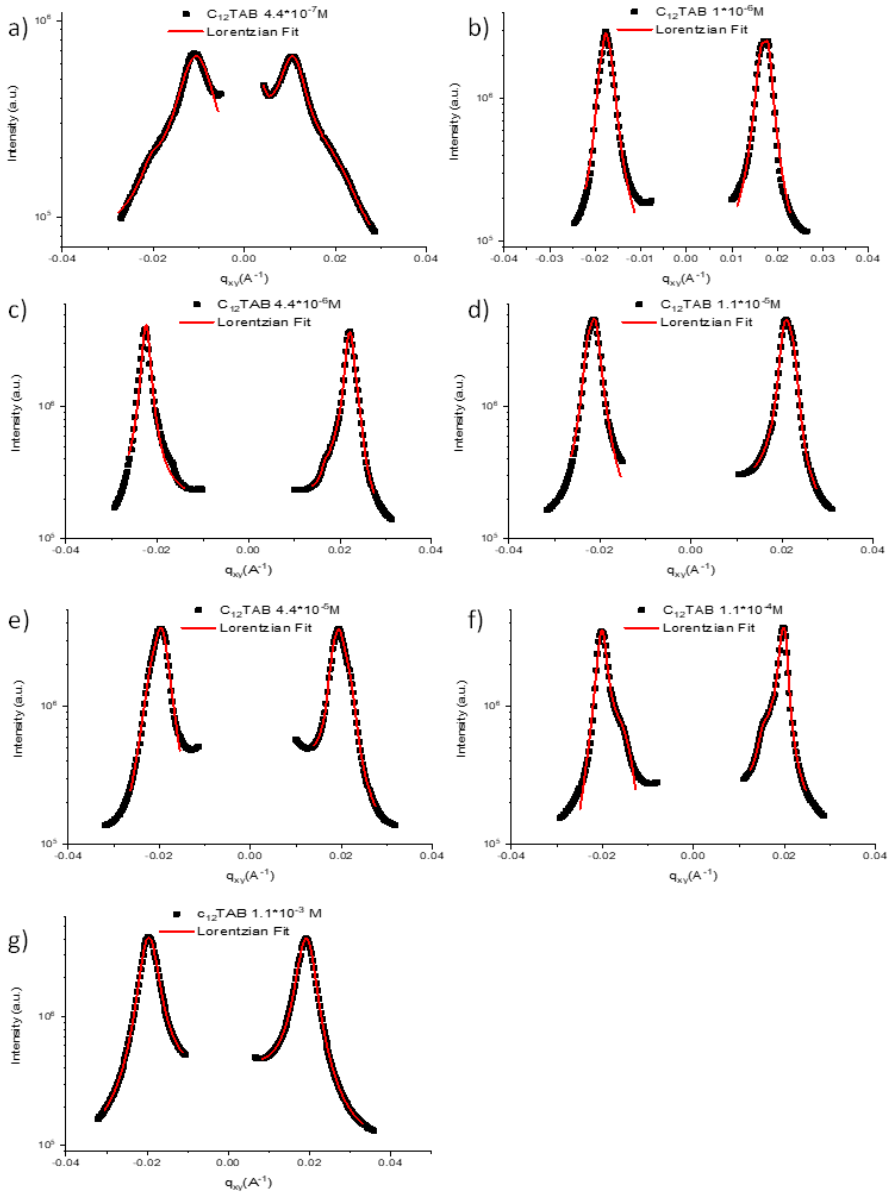

Figure S2.11. GISAXS peak fittings (black symbols: experimental peak, red lines: fitting) of SiO_2 NP monolayers at various C_{12}TAB concentrations.

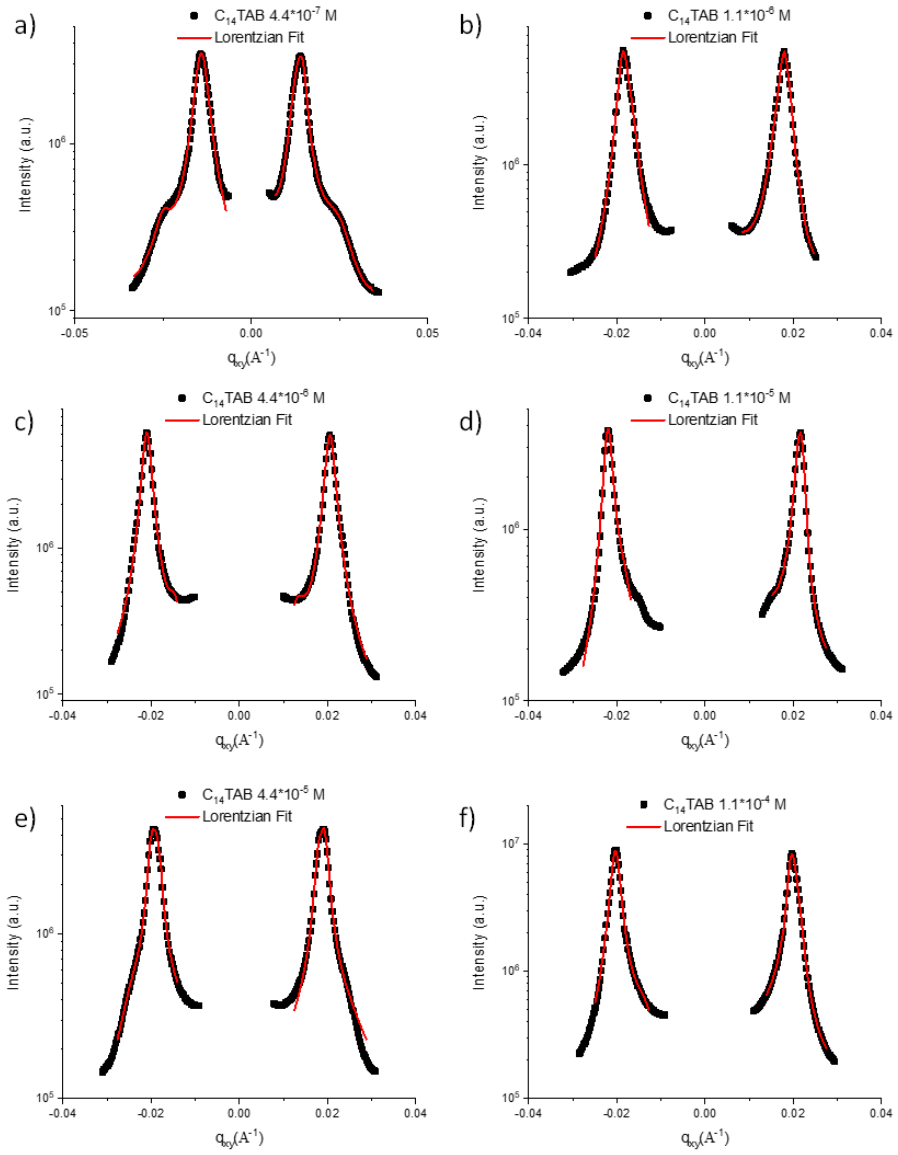

Figure S2.12. GISAXS peak fittings (black symbols: experimental peak, red lines: fitting) of SiO_2 NP monolayers at various $C_{14}TAB$ concentrations.

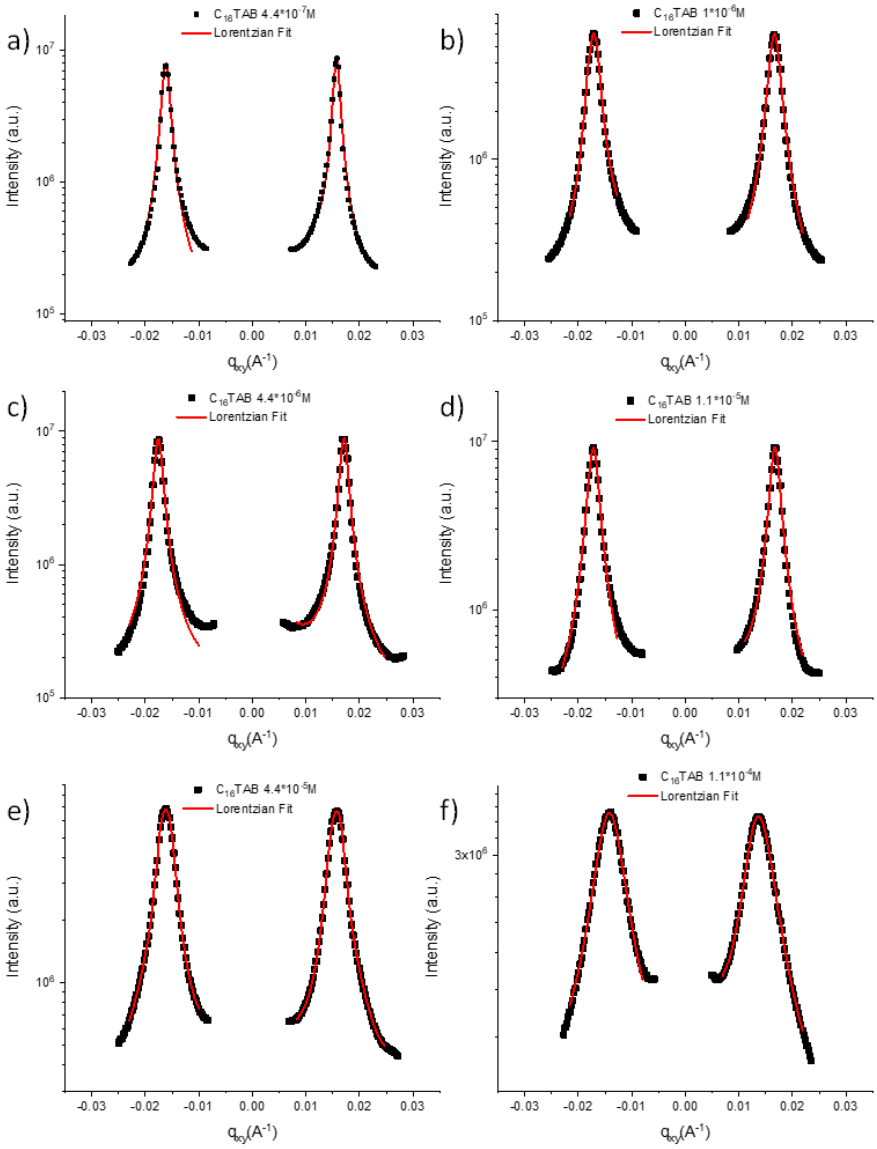

Figure S2.13. GISAXS peak fittings (black symbols: experimental peak, red lines: fitting) of SiO_2 NP monolayers at various C_{16}TAB concentrations.

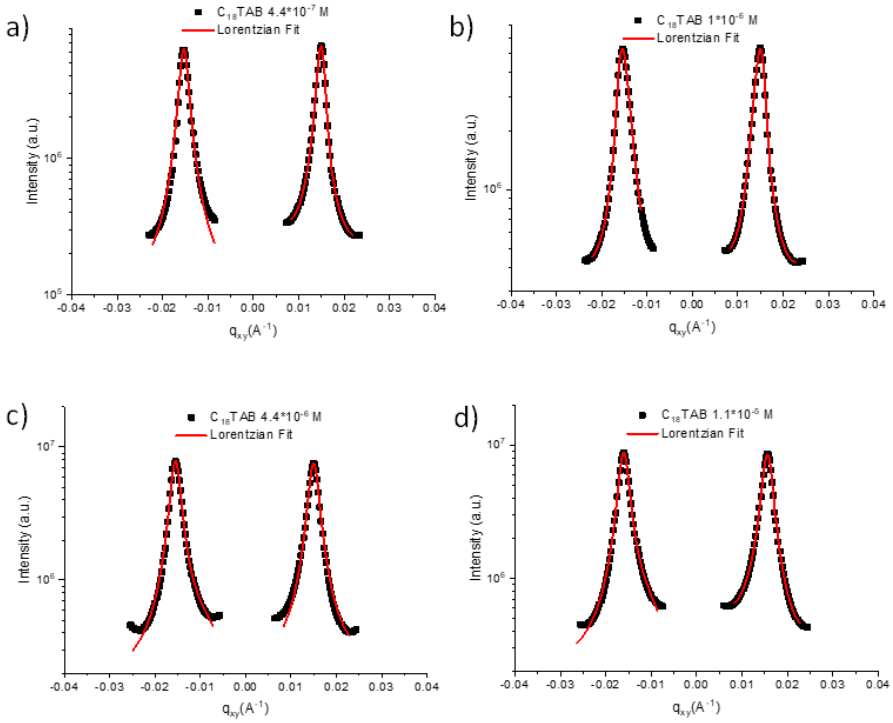

Figure S2.14. GISAXS peak fittings (black symbols: experimental peak, red lines: fitting) of SiO_2 NP monolayers at various C_{18}TAB concentrations.

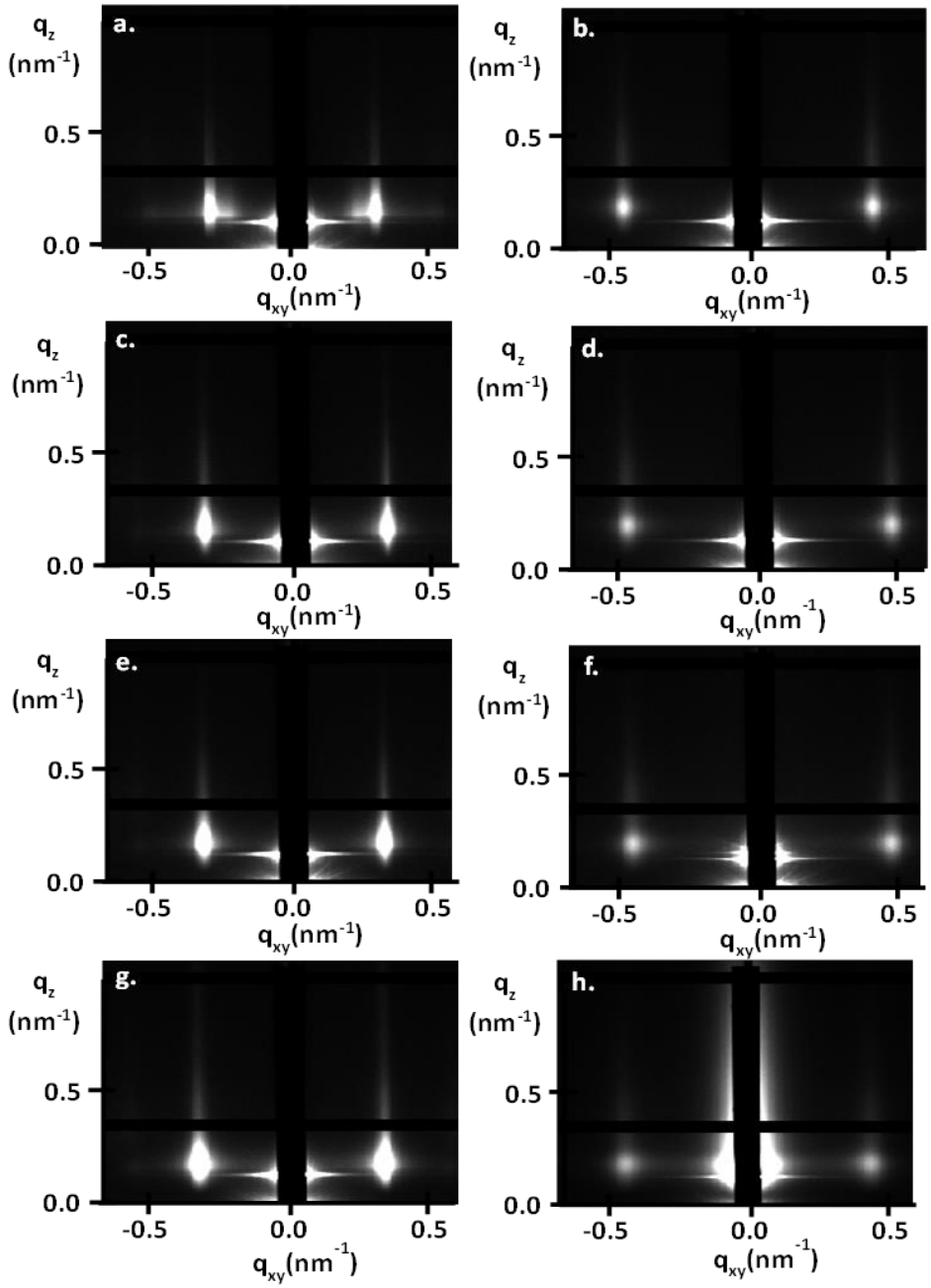

Figure S2.15. GISAXS patterns of the compressed NPs 0.1% wt NaCl 1 mM C_nTAB $1 \cdot 10^{-6}$ M monolayer before (left) and after (right) the collapse for all different chain length: C_{12}TAB (a,b), C_{14}TAB (c,d), C_{16}TAB (e,f), C_{18}TAB (g,h). The presence of diffraction rods rather than rings after the collapse indicates that the system keeps a purely bidimensional structure.

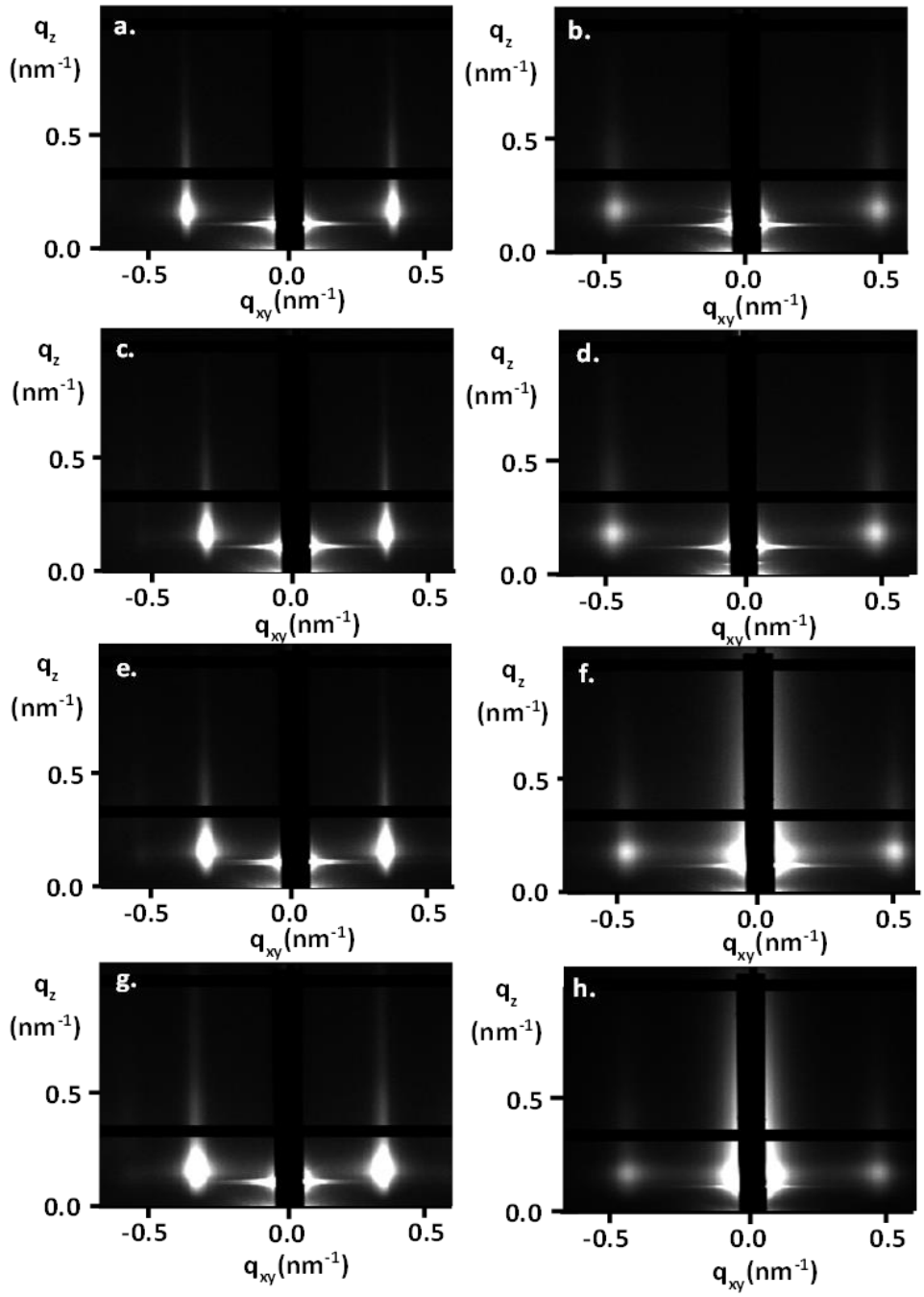

Figure S2.16. GISAXS patterns of the compressed NPs 0.1% wt NaCl 1 mM C_nTAB $4.4 \cdot 10^{-6}$ M monolayer before (left) and after (right) the collapse for all different chain length: C_{12}TAB (a,b), C_{14}TAB (c,d), C_{16}TAB (e,f), C_{18}TAB (g,h). The presence of diffraction rods

rather than rings after the collapse indicates that the system keeps a purely bidimensional structure.

Reference

(1) Shen, Y.; Gee, M. Y.; Greytak, A. B. Purification Technologies for Colloidal Nanocrystals. *Chem. Commun.* **2017**, *53* (5), 827–841. https://doi.org/10.1039/c6cc07998a.
(2) Ravera, F.; Santini, E.; Loglio, G.; Ferrari, M.; Liggieri, L. Effect of Nanoparticles on the Interfacial Properties of Liquid / Liquid and Liquid / Air Surface Layers. **2006**, 19543–19551.
(3) Pershan, P. S.; Schlossman, M. *Liquid Surfaces and Interfaces: Synchrotron X-Ray Methods*; 2012; Vol. 9780521814010. https://doi.org/10.1017/CBO9781139045872.

Appendix:

Instrumentation

Structural Characterization by means not conventional technique: X-Ray with grazing incidence (GI) geometry

It was 1895 when physicist Wilhelm Röntgen discovered, using a discharge tube and a fluorescent plate, mysterious rays capable to passing through the human body. It is from the unknown nature that derived the name X-Ray.[1] From the outset it was felt that X-rays could change the perception of science, with applications in medical diagnosis and physical research. At the beginning of the 20th century, the field of diagnostic radiography began to mature, considering X-rays as visible light, characterized by wavelengths and intensities. The well-known phenomena of light, such as diffraction, refraction and interference, were not observed with X-rays.[2] Wheaton hypothesized the dualistic concept of radiation, particle-wave,[3] but most considered X-rays as another form of electromagnetic waves. In 1912 Max von Laue discovered the first model of crystal diffraction using X-rays. Von Laue explained what he observed considering the dual nature of X-rays and assimilating, at the same time, X-rays to electromagnetic radiation.[4] William Lawrence Bragg and his son William Henry Bragg started to systematically employ X-rays in crystallography and their research enabled an atomic dimension of wavelength to be associated with the X-rays, able to interfere with the lattices and provide information on the crystalline structure that visible light is not able to give.[5,6,7] In particular, they managed to describe the atomic structure of rock-salt (NaCl)[8] and later the one of diamond[9]. Illumination of the crystalline solid with monochromatic X-rays generated an intense reflection visible under a specific angle. In order to describe the diffraction, they modelled the crystal as a set of discrete planes of electronic density, on which the X photons scatter.[5] Only a few years later, more complex structures, such as graphite,[10] were solved; such measurements were carried out on simple and symmetrical cell units, characterized by a low number of atoms. The use of X-rays developed increasingly and in the 1950s, Watson and Crick discovered the double-helix structure of DNA, resulting in modern biological structure and protein crystallography.[11,12] The diffraction patterns of such systems appear very complicated, because the unit cells of these crystals contain hundreds of atoms and a low symmetry, compared to that of the NaCl. The need to use X-rays to characterize the crystalline structure lies in the fact that to obtain constructive interference of electromagnetic waves scattered from a periodic array, the radiation used must have a wavelength comparable to the interatomic distance. X-rays meet this condition, as they have wavelengths in the angstrom range.[13]

The description of the crystalline structure is usually carried out in the reciprocal space; in this way, the periodicity in the structure that occurs for a given crystallographic direction is considered. The Fourier transform is the mathematical

process that allows to go from a real space described by $\boldsymbol{R}_n = n_1\boldsymbol{a_1} + n_2\boldsymbol{a_2} + n_3\boldsymbol{a_3}$ to a reciprocal space described by $\boldsymbol{G} = h\boldsymbol{b_1} + k\boldsymbol{b_2} + l\boldsymbol{b_3}$. In real space the crystal is described by cell units with $\mathbf{a_1}$, $\mathbf{a_2}$, and $\mathbf{a_3}$ and constant lattice vectors n_1, n_2 e n_3; the product of the lattice vectors generates a parallelepiped with volume, V, equal to:

$$V = \boldsymbol{a_1} \cdot (\boldsymbol{a_2 x a_3}) = \boldsymbol{a_2} \cdot (\boldsymbol{a_3 x a_1}) = \boldsymbol{a_3} \cdot (\boldsymbol{a_1 x a_2})$$

Which makes up the unit cell, that is, the smallest volume element that maintains all the symmetry properties of the crystalline lattice.[14,15] In reciprocal space the base vector of the lattice is instead described as:

$$\boldsymbol{b_1} = 2\pi \frac{\boldsymbol{a_2 x a_3}}{V} \; ; \; \boldsymbol{b_2} = 2\pi \frac{\boldsymbol{a_3 x a_1}}{V} \; ; \; \boldsymbol{b_3} = 2\pi \frac{\boldsymbol{a_1 x a_2}}{V}$$

Therefore, by considering the 2D hexagonal lattice of spheres in real space, drawn in Figure S1, the periodicity in the crystal can be identified by the lattice planes which are indicated by the Miller indices h,k,l. These indices are nothing more than the coordinates of the shortest reciprocal lattice vector (**G**), normal to the plane. Because they define a reciprocal lattice vector, they will be integers and will have no common factor, since they represent the smallest vectors. Miller indices thus represent a set of integers proportional to the intercept value on the crystal axes.
Miller's indices are then used to describe reticular planes characterized by a periodicity, in a certain direction, in real space, which will become points in reciprocal space. Their position in reciprocal space will be given by the frequency at which they are in real space, just as the direction in reciprocal space will depend on the direction along which they have periodicity in real space.

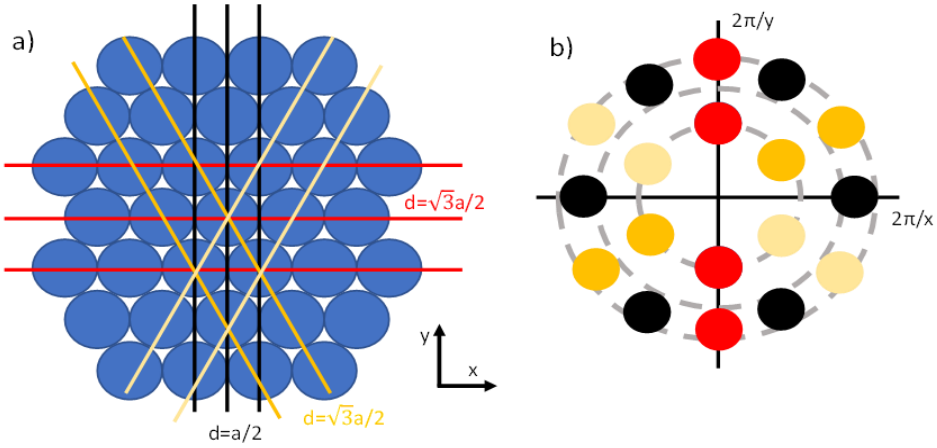

Figure S1. (a) Hexagonal lattice of spheres in real space, with interparticle distance a. The red/yellow/beige/black lines are respectively the {10} and {11} lattice plane. To this series of plane in the real space correspond points into reciprocal lattice space. (b)

During scattering experiments a slice of the reciprocal space is measured, so it is necessary to convert the obtained values in order to obtain the information in real space. Each point of the reciprocal lattice corresponds to a perpendicular plane in the real one. Physically this can be seen as X-rays reflected in the direction perpendicular to the lattice plane. To obtain a diffraction pattern of the crystalline object, the X-ray must be scattered constructively, in the direction governed by the Bragg law.[13,15] This law makes it possible to interpret the phenomenon of diffraction from a crystalline lattice by approximating the event to a simple reflection by the reticular planes of the crystal. The repetitive nature of the crystal causes the distance between the planes to be constant and equal to *d*. When X-rays of wavelength λ arrive in phase, with an angle of incidence ϑ, to observe the diffraction, after reflection the two beams must still be in phase, that is, the wavefront difference (AC and AD) must be an integer number of λ (Figure S2). This means, $AC + AD = n\,\lambda$ but $AC = AD$ and $sin\vartheta = \frac{AC}{d}$ or $AC = d \cdot sin\vartheta$. Bragg's law derives from this, namely:

$$2d \cdot sin\vartheta = n\lambda$$

In addition, in order to have diffraction, the scattering vector resulting from the difference between the incident and reflected beams must be perpendicular to normal planes.

This simple law is used to characterize the crystalline and amorphous phases of all different types of materials. Getting a 2D diffraction pattern is like drawing a line through the reciprocal lattice of the material. Therefore, depending on the orientations of the real lattice and therefore of the reciprocal one, different projections will be obtained.

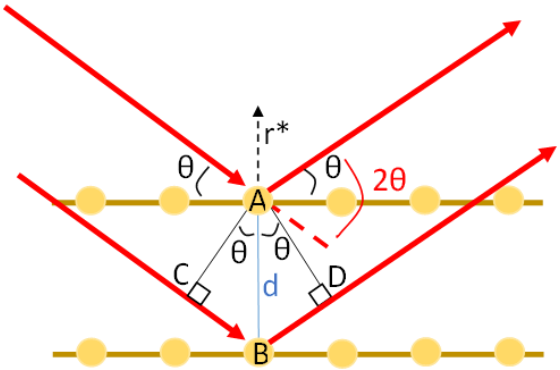

Figure S2. Schematic representation of Bragg law with incidence angle θ and the Bragg angle 2 θ. In order to have diffraction, the scattering vector r* must be perpendicular to the crystalline plane so that incidence and scattering angle are equal, as for reflection.

Moreover, for diffraction phenomena we can consider only the elastic part of the radiation[13], there is no energy loss between the incident and the scattered photon. It follows that the magnitude of wave vectors does not change after scattering with atoms, i.e. $|k_i| = |k_f| = 2\pi/\lambda$ with k_i and k_f wave vectors of incoming and scattered photons. In addition, it is possible to replace the angle 2ϑ with the momentum transfer vector or scattering vector that can be seen as the thrust that the photon receives before scattering, changed in sign, i.e.: $q = k_f - k_i$. The scattering vector and the Bragg angle appear interchangeable, it follows that $|\boldsymbol{q}| = 4\pi sin\vartheta/\lambda$. This results in a plot with a variable independent of energy towards intensity. This is especially useful in synchrotron experiments, as photons with different energy are used. Another consequence of elastic scattering concerns the condition of constructive interference predicted by Laue (reformulation of Bragg's law in reciprocal space, connecting lattice vectors with Miller's indices) that is, in order to have constructive interference, the scattering vector must be equal to that of the reciprocal lattice **q** = **G**. If we project the incident and scattered photon wavevectors on the same basis, they describe a sphere; the Ewald sphere having a radius equal to the wavevector length of the photon entering and scattered. The projections of the scattering vector always follow the sphere surface. Only when the sphere intersects the points of the reciprocal lattice of the material of interest constructive interference will occur.[15] In the case of nanocrystalline lattices, the reciprocal lattice is very small. The points are all close to each other and the curvature of the Ewald sphere can be neglected, obtaining an efficient scattering from many lattice points if there is the presence of a good long-range order. Therefore, referring to Bragg's law, it is evident how small distances, *d*, will generate scattering at high angles while large distances will correspond to small scatter angles. Since the instruments to determine the direction along which the X-rays scatter, it is necessary to describe the intensity of the scattered signal as a function of the output angle. The scattered amplitude contains two terms, deriving from the size and shape of the scattering objects and their spatial organization; we have therefore:

$$S(\boldsymbol{q}) = \sum_j P_j(\boldsymbol{q}) e^{-i\boldsymbol{R}_j\boldsymbol{G}} = \sum_j P_j(\boldsymbol{q}) e^{-i2\pi(x_j h + y_j k + z_j l)}$$

where S(**q**) indicates the structure factor, which depends on the spatial reorganization of the particles within the repeating cell unit, while j indicates all atoms in the cell, with coordinates x_j, y_j and z_j. This explains why, for example in the case of centred-face cubic lattices (FCC), only reflections whose Miller indices are all even or all odd are allowed. The term P(**q**) instead indicates the form factor, which is related to the electronic density of the single elements.[14] It follows that, often, the scattering amplitude A(**q**) is defined as the product of the structure and form factor, i.e. a phase and a amplitude term:

$$A(\boldsymbol{q})\alpha S(\boldsymbol{q})P(\boldsymbol{q})$$

In the case of nanocrystals scattering, P(**q**) is the quadratic module of the Fourier transform of the scattered particles, therefore, it describes the influence of the size and shape of the scattered intensity.[16] In particular, at the atomic scale, it will describe how strong atoms scatter, while the structure factor will give the periodic location of the scattering objects. Experimentally only the intensity of the diffracted signal is measured, not the phase. The intensity alone is connected to the profile of the electronic density but alone it does not allow to go up in univocal way to the structure of the sample in the real space.[17] By modulating the detector-sample distance it is possible to record the scattering of the radiation at low angles (Small Angle X-Ray Scattering, SAXS), originating from the scattering of the nanocrystals' form factor and at high angles (Wide Angle X-Ray Scattering, WAXS) originating from atomic reflections.

Grazing incidence angle

To allow the development of functional materials, powerful systems are needed to quantify the structure of the species involved.[18] X-rays appear promising for both bulk and interface analysis. In the previous paragraph it was already explained how it is possible to structurally characterize samples with periodic assemblies or scattering objects in the range between 1 and 100 nm by means of SAXS Through WAXS it is instead possible to obtain information at smaller scales, with structural elucidations at atomic and molecular intervals eve in systems without a perfect crystalline order.[19] Many modern applications imply the use of thin films of soft matter, whose morphologies may differ from those of the bulk. In the geometry of the film, it is necessary to consider the interactions with both the substrate and the surrounding medium, as well as the energetic factors which affect the resulting morphology. Depending on whether the film support may be impenetrable or not, the density profile and entropy of the film may vary. Additional restrictions may arise from the film thickness, to be added to the interfacial interactions involved.[20,21] These factors are added to the necessity of having to discriminate the signal of relatively weak dispersion of the sample having the thickness of the order of the nanometres from that which comes from the bulk. These problems are overcome by changing the geometry of the system, passing from the transmission geometry used in conventional SAXS and WAXS, with incidence angles of about 90°, to a grazing incidence geometry (GI) with very low incidence angles α_i, generally below 1°.[22] In this way, the beam travels a long way inside the film and get the required scattering interaction. The adoption of this configuration is named as GISAXS and GIWAXS. GIWAXS is also referred to as grazing incidence X-ray diffraction (GIXRD).

Diffraction experiments carried out in this thesis include GISAXS experiments, in order to probe the assembly of particles at the liquid interface and GIXRD to probe polymer crystallization on structured surfaces. In both cases, an X-ray beam with an incident angle α_i <1° is used. This configuration limits the penetration depth of the beam in the sample, with a low dispersion from the bulk. The radiation diffused by the sample is then recorded by an X-ray sensitive 2D detector. The GISAXS detector is usually positioned at large distances, based on the energy of the X-ray photon, since the Bragg reflection must be sufficiently divergent to be separated from the direct beam. At greater scattering angles but at smaller distances, the GIXRD detector is placed, where the atomic planes scatter and the crystallographic orientation can be studied. In particular, it is important to consider that the only scattered planes detectable by GIXRD are tilted with respect to the substrates plane and are characterized by an out of plane direction of periodical repetition (out-of-plane scan).[26] This is related to the geometric asymmetrical condition; therefore, planes with periodical repetition perfectly perpendicular to the substrates will not give scattering events as they do not fulfil, under such conditions, the Bragg Law.

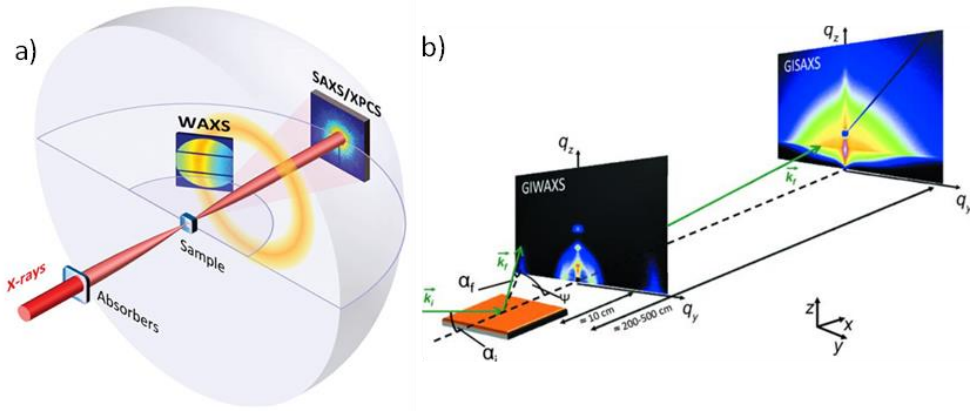

Figure S3. (a) Transmission SAXS/WAXS geometry typically used.[24] (b) GISAXS/GIWAXS geometry. Inclination of the sample relative to the horizon. α_f is the scattered angle while ψ is the in plane angle. In addition, the typical detector sample distances are reported.[25]

Morphological characterization: Atomic Force Microscopy (AFM)

Atomic Force Microscopy (AFM) is a physico-chemical investigation technique that is part of the category of high-resolution microscopes known as "SPM" (Scanning Probe Microscopies). Among these microsopies, it is the most used, as well as the best known. AFM is mainly used to obtain high-resolution topographical images of material surfaces of different nature such as polymers, biomolecules, metals, inorganic functional materials, etc.[27] Other variants of the technique allow, instead, to obtain information about the electrical, magnetic, mechanical properties and the chemical composition of the surface under examination. Thanks to the great resolution of the instrument, in the case of hard and ultra-flat surfaces, it is possible to obtain images with atomic space resolution.

The principle used for the determination of an AFM image is based on the interaction between a tip, held by a flexible lever (cantilever), and the surface atoms of the sample. The tip, usually in silicon nitride, and the cantilever are the probe of the instrument (Figure S5). A crucial factor for resolution is the radius of curvature of the tip (end radius). High resolution AFM images require radii between 4 and 60 nm. One of the main limits for the further development of the technique consists precisely in making tips with a smaller radius.

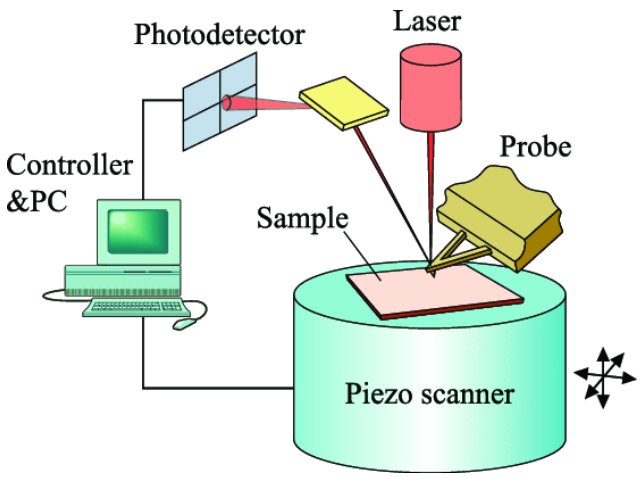

Figure S5. Schematic representation of AFM instrument.[28] The deflections of the cantilever are measured by a photodetector, which collects the reflections of the laser beam focused in the back of the cantilever.

AFM images are recorded by moving the sample along the xy plane, by means of piezoelectric guides, following a lattice pattern with precision in the order of the Angstrom, and by measuring the deflection of the cantilever following the interactions between the tip and the atoms of the surface. The system that detects the movements of the probe consists of a laser beam focused on the upper face of the lever, from which it is reflected towards a two-dimensional photodiode detector. Each cantilever deflection is due to attractive/repulsive interactions between the electron clouds of the tip and those of the surface atomic layers of the material. A mathematical model that well describes such interactions is the Lennard-Jones potential.[29]

$$U(z) = -A \cdot \sum_{i=1}^{n} r_i^{-6} + B \cdot \sum_{i=1}^{n} r_i^{-12}$$

where U(z) is the total interaction potential along the z axis; $-A \cdot \sum_{i=1}^{n} r_i^{-6}$ and $B \cdot \sum_{i=1}^{n} r_i^{-12}$ are the attractive and repulsive contribution respectively; A and B are typical constants of the material atoms.[30] Lennard Jones' function is as follows:

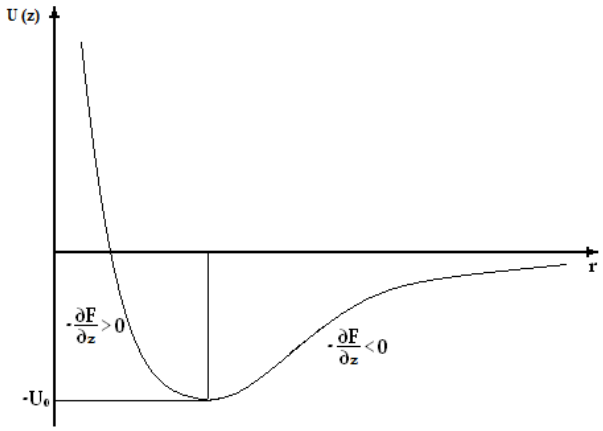

Figure S6. *Evolution of Lennard-Jones' potential*

The potential is governed by the equilibrium between attractive and repulsive forces (minimum curve), which act respectively at distances greater and less than z_0, the equilibrium distance. Therefore, depending on the distance between the probe and the sample, in the order of the interatomic distances, only one of the two terms will prevail. The total interaction force is defined as the opposite of the U derivative to the distance. This force is responsible for the bending of the cantilever on the surface of the sample, detected by the optical system.

At this point, a feedback control system compensates for the probe's path deviations, due to the irregular profile of the surface, by activating a piezoelectric guide along

the z-axis that keeps the peak/sample interaction force constant. The voltage variations, which are applied to the guide to maintain the force constant, are then translated into a topological image of the surface. In a variant of the technique, the feedback system allows the height of the probe to be kept constant. Typical values of interacting forces between probe and sample are between 10^{-11} and 10^{-6} N. The force acting between two atoms joined by a covalent bond at a distance of 1 Å is about 10^{-9} N. By comparing the forces involved in an AFM measurement to the one typical of a chemical bond, it is evident that AFM is, at least for “hard” samples, a non-destructive technique.

Contact Mode

The easiest and most used mode in AFM is the "contact mode". In "contact mode" the probe is placed and kept in contact with the sample: the cantilever is deflected to keep the interaction force constant and its inflections are monitored through the optical system. This mode allows to obtain information about the friction. The friction forces on a rough and homogeneous surface have the same periodicity as the topographic image, but the peaks arising from them and the topographic ones are not located on the same point, because the variation of friction between tip and sample depends on the slope of the surface, rather than on its height. The proposed model foresees a dominant mechanism, called "stop tooth mechanism", according to which there is a direct correspondence between the coefficient of friction and the slope: in the sections with positive slope (ascending) the coefficient of friction increases, while in the sections with negative slope (descending) the coefficient decreases. In addition, it must be considered that, in the ascending sections, there is an additional contribution to the total friction due to the impacts between the tip and the positive gradient zones. In negative gradient regions, however, there are no collisional events, so there will be no other resistant forces contributing to the total effect. These two factors make it possible to justify the difference in friction in the ascending and descending traits and the incorrect correspondence between topographical peaks and friction peaks. During a friction measurement, data on strength forces in a scanning direction and in the opposite direction are useful for the interpretation of the origin of such forces. Indeed, the intensity of the effects induced by the material is independent of the scanning direction, while it will depend on whether the effects are related to the topography. Since the sign of friction forces changes by reversing the scanning direction, adding data from both directions will eliminate the effects induced by the material, while keeping only those induced by the topography. However, the intensities of the signals in the two scanning directions will not be the

same for a given region of the surface. In fact, the increase of the friction force in an ascending stretch of the surface is less than the decrease of the same force when the tip runs along the same stretch in the opposite direction. In addition, surface roughness is generally asymmetrical and this causes a variation in the friction force in the two directions. Because of these differences, subtraction of friction force data in both directions leads to residual peaks. However, this mode is not appropriate for the study of "soft" samples, as their surface structure of the latter may be irreversibly modified by continuous contact between the tip and the sample. As a consequence, "contact mode" is used for the study of "hard" and stable material, the surface of which is not altered by frictional forces.

Tapping Mode

The mode that allows the microscopic investigation of soft samples is the "tapping mode". In this mode, the probe oscillates along the z-axis at a constant frequency (in a range of 50 to 500 KHz via a piezoelectric oscillator) and at an oscillation width ≥ 10 nm. This minimizes the friction effects that, otherwise, would lead to irreversible structural degradation of the "soft" surface. In addition, with "tapping" it is possible to obtain both topographical images and information about the viscoelastic and mechanical properties of the investigated surface layer. The operating principle is the following. At the moment of contact with the surface, the tip loses energy. This loss causes a decrease in the oscillation amplitude. The piezoelectric control system will respond to the variation of the oscillation, moving the sample along the z-axis in order to keep the amplitude constant. As in the case described above, the movements of the cantilever are detected by the optical system and the voltage applied, to move the sample along z, is converted into a topographic image of the surface. The information on the viscosity of the system under investigation is directly related to the phase difference between the frequency imparted by the piezoelectric oscillator (excitation frequency) and the current frequency of the probe: the oscillation change is converted by the instrument into a phase delay. The images that are obtained by exploiting this information are called "phase images".

Other techniques

Contact Angle

The contact angle measurement represents a powerful method to calculate surface free energy of solids. When a liquid does not completely wet the surface, it forms an angle of contact, ϑ, with the surface, with a value related to the interactions that occur along the three-phase contact line, where liquid, gas and solid intersect. The surface free energy can be described by using the Fowkes-van Oss-Chaudry-Good (FOCG)[31] model as a combination of the apolar components (Lifshitz-Van der Waals component γ^{LW}) and two polar one:

$$\gamma = \gamma^{LW} + 2\sqrt{\gamma^{+}\gamma^{-}}$$

The contact angle that the liquid drop forms on the solid can then be expressed in terms of the three components:

$$(1 + cos\vartheta)\gamma_L = 2(\sqrt{\gamma_s^{LW}\gamma_L^{LW}} + \sqrt{\gamma_s^{+}\gamma_L^{-}} + \sqrt{\gamma_s^{-}\gamma_L^{+}})$$

where L refers to the spread liquid while S indicates the solid surface. Thus, it becomes possible to determine the surface free energy of a solid as well as its three components by measuring the contact angle of three different liquids, whose surface tension components are known, spread on the solid of; this results in a system of three equations in three unknowns. The contact angle measurements and subsequent determination of the surface free energy were conducted using an instrument OCA 20, Dataphysics Instruments GmBh, Filderstadt, Germany. The three liquids employed were water, glycerol and tricresyl phosphate whose surface tension components are tabulated in the instrument database.

Wilhelmy plate and Langmuir trough

The surface tension at the liquid/air interface is commonly measured using the Wilhelmy method. A small plate of glass, platinum or filter paper, usually in the order of a few square centimetres, is oriented perpendicularly to the interface and the force exerted on it is measured. (Figure S7).

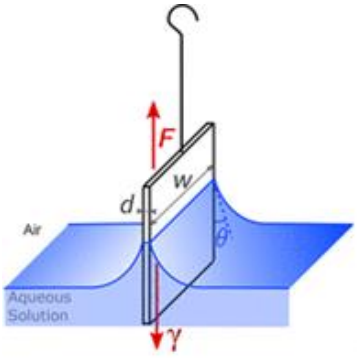

Figure S7. *Schematic representation of Wilhelmy plate method.*[32]

The plate is put in contact with the liquid surface leading to the formation of a meniscus. The plate remains suspended at the interface due to the presence of a force that balances the weight of the plate and the force of the liquid meniscus on the lower edge of the plate. The liquid surface tension acts on the three-phase contact line (solid-liquid-vapour) tangential to the surface of the liquid. The force acting on the plate is measured with a microbalance, to which the Wilhelmy plate is connected, and then the value of the surface tension is determined by the Wilhelmy equation.[33,34,35,36] If the plate has a width equal to l and a weight of W_{plate}, the force necessary for the plate to be detached from the surface is equal to:

$$F = W_{tot} = W_{plate} + 2l\gamma cos\vartheta$$

By considering that the surface tension acts on both sides of the plate, this equation must be multiplied by 2. Moreover, if the liquid completely wets the plate, cosϑ=1, therefore the surface tension becomes equal to:

$$\gamma = \frac{W_{tot} - W_{plate}}{2 \cdot l}$$

In particular, in the present study, the Wilhelmy method was employed to measure the surface pressure $\Pi = \gamma_0 - \gamma$ where γ_0 is the surface tension of pure water (72.8 mn/m at 20°C) and γ is that of the sample. By subtracting the surface tension of water to the measured surface pressure value it was possible to determine the surface tension of the sample. Subsequently, the Wilhelmy plate method was used to monitor the surface tension of the samples during their compression in a Langmuir trough. Langmuir troughs are usually made of Teflon (hydrophobic and chemically inert material) and equipped with two movable barriers, also in Teflon, which run parallel to the walls of the trough, coming into contact only with the upper part of the liquid, allowing the interface monolayer to be compressed. Monolayer formation may occur as a result of the spreading of insoluble molecules at the liquid/air interface or

through spontaneous migration and adsorption of molecules from bulk to interface. The surface compression involves a reduction of the area occupied by the monolayer, while the surface tension is monitored continuously, in order to obtain information characteristic of the monolayer, recording the variation of surface pressure as a function of the molecular area. The compression isotherms obtained are usually characterized by distinct regions, as can be seen in Figure S8.[37] In the case of small amphiphilic molecules spread at the interface, in the absence of applied external forces, the molecules show a gas-like behaviour and follow the equation of state: $\pi A = K_B T$ with π surface pressure, A area per molecule, K_B Boltzmann constant and T temperature. The compression of the monolayer is accompanied by an increase of surface pressure. This leads to the reorganization of the molecules into a liquid-like phase and, with further compression, into a solid monolayer. The three phases are characterized by a sharp change of pressure, in correspondence to the change of state. For additional compressions, the monolayer reaches the collapse, beyond which multilayers are formed. The collapse pressure, π_c, can also be seen as the maximum pressure that a monolayer can sustain before ejecting the molecules. Compression isotherms can provide quantitative information on the size and shape of the molecules under study and they allow the determination of the molecular area under maximum expansion and zero pressure, i.e. hypothetical area occupied by a condensed-phase molecule, in the assumption of a direct correlation to the average physical space occupied by a molecule in the film.

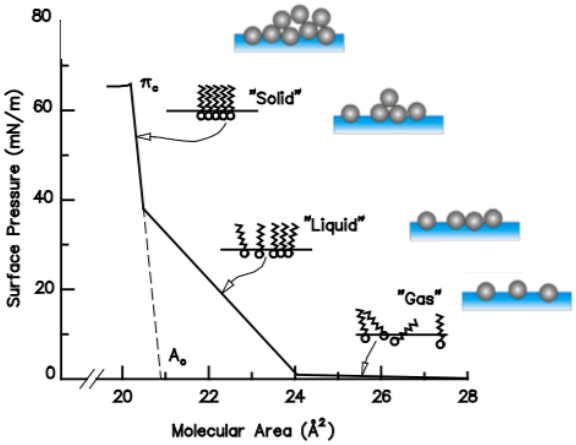

Figure S8. Ideal compression isotherm of monolayer made by amphiphilic molecule. The different region observing can be associated with the different level of ordering of the film, as shown in the cartoons.[37,38]

In the case of the monolayer examined in this thesis, the compression isotherms were made in order to study NPs monolayer coated with amphiphilic molecules, by modifying the interface density following the compressions of the monolayer under examination.

References

(1) Röntgen, W. C. *Aufbruch InsInnere Der Materie*.
(2) Robinson, A. L. History of Synchrotron Radiation. *Synchrotron Radiat. News* **2015**, *28* (4), 4–9. https://doi.org/10.1080/08940886.2015.1059228.
(3) Swenson, L. S.; Wheaton, B. R.; Kuhn, T. S. The Tiger and the Shark: Empirical Roots of Wave-Particle Dualism. *The American Historical Review*. 1985, p 902. https://doi.org/10.2307/1858848.
(4) Eckert, M. Max von Laue and the Discovery of X-Ray Diffraction in 1912. *Ann. Phys.* **2012**, *524* (5), 83–85. https://doi.org/10.1002/andp.201200724.
(5) Bragg, W. H. B. and W. L. The Reflection of X-Rays. *J. Röntgen Soc.* **1913**, *9* (37), 93–98. https://doi.org/10.1259/jrs.1913.0059.
(6) Warren, B. E.; Muldawer, L. *X-Ray Diffraction* ; 1970; Vol. 23. https://doi.org/10.1063/1.3022337.
(7) Arne Hessenbruch. A Brief History of X-Rays. *J. Chem. Inf. Model.* **2019**, *53* (9), 1689–1699.
(8) Bragg, W. L. The Structure of Some Crystals as Indicated by Their Diffraction of X-Rays. **1913**.
(9) Bragg, W. H. B. and W. L. The Structure of the Diamond. **1913**.
(10) Debye, P.; Scherrer, P. Interferenz an Regellos Orientierten Teilchen Im Röntgenlicht I. *Phys. Zeitschrift* **1916**, *17*, 277.
(11) Watson, James D., and F. H. C. Molecular Structure of Nucleic Acids. *Nature* **1953**, 737-738.
(12) Due Credit. *Nature* **2013**, *496* (7445), 270. https://doi.org/10.1038/496270a.
(13) Carmelo Giacovazzo, Carmelo Giacovazzo, Hugo Luis Monaco, Gilberto Artioli, Davide Viterbo, Marco Milanesio, Gastone Gilli, Paola Gilli, Giuseppe Zanotti, Giovanni Ferraris, and M. C. *Fundamentals of Crystallography*.
(14) Kittel, C. *Solid State Physics* -.
(15) Als-nielsen, J.; Mcmorrow, D. *Elements of Modern X-Ray Physics Elements of Modern X-Ray Physics Second Edition*.
(16) Kakudo, N. K. X-Ray Diffraction by Macromolecules. *Springer 2005*.
(17) Miao, J.; Charalambous, P.; Kirz, J.; Sayre, D. Extending the Methodology of X-Ray Crystallography to Non-Crystalline Specimens. *AIP Conf. Proc.* **2000**, *521* (July), 3–6. https://doi.org/10.1063/1.1291749.
(18) Richman, E. K.; Hutchison, J. E. The Nanomaterial Characterization Bottleneck. **2009**, *3* (9), 2441–2446.
(19) Science, E. *Small-Angle Scattering from Con Ned and Interfacial Fluids*.
(20) Zhao, W.; Liu, F.; Wei, X.; Chen, D.; Grason, G. M.; Russell, T. P. Formation of H* Phase in Chiral Block Copolymers: Morphology Evolution as Revealed by Time-Resolved X-Ray Scattering. *Macromolecules* **2013**, *46* (2), 474–483.

https://doi.org/10.1021/ma302139m.
(21) Sunday, D. F.; Hammond, M. R.; Wu, W.; Kline, R. J.; Stein, G. E.; Hammond, M. R. Three-Dimensional x-Ray Metrology for Block Copolymer Lithography Line-Space Patterns Lithography Line-Space Patterns. https://doi.org/10.1117/1.JMM.12.3.031103.
(22) Pershan, P. S.; Schlossman, M. *Liquid Surfaces and Interfaces: Synchrotron X-Ray Methods*; 2012; Vol. 9780521814. https://doi.org/10.1017/CBO9781139045872.
(23) Dosch, H. Critical Phenomena at Surfaces and Interfaces : Evanescent X-Ray and Neutron Scattering Fivefold Symmetry. **1993**, *58*. https://doi.org/10.1063/1.2809011.
(24) Perakis, F.; Amann-winkel, K.; Lehmkühler, F.; Sprung, M.; Mariedahl, D.; Sellberg, J. A. Diffusive Dynamics during the High-to-Low Density Transition in Amorphous Ice. **2017**, 1–6. https://doi.org/10.1073/pnas.1705303114.
(25) Hexemer, A.; Müller-Buschbaum, P. Advanced Grazing-Incidence Techniques for Modern Soft-Matter Materials Analysis. *IUCrJ* **2015**, *2*, 106–125. https://doi.org/10.1107/S2052252514024178.
(26) Birkholz, M.; Fewster, P. F. *Thin Film Analysis by X-Ray Scattering*; 2006.
(27) Microscope, A. F. Atomic Force Microscope. **1986**, *56* (9).
(28) Ishida, N.; Craig, V. S. J. Direct Measurement of Interaction Forces between Surfaces in Liquids Using Atomic Force Microscopy †. **2019**, *36* (36), 187–200. https://doi.org/10.14356/kona.2019013.
(29) O. Wolker, T.H. Bayer, J. G. Journal of Vacuum Science & Technology. **1991**, *9* (1353). https://doi.org/10.1116/1.1532023.
(30) Cappella, B.; Dietler, G. Force-Distance Curves by Atomic Force Microscopy.
(31) Oss, C. J. V. A. N.; Good, R. J. Interfacial Lifshitz-van Der Waals and Polar Interactions in Macroscopic Systems. **1988**, 927–941.
(32) Okur, H. I.; Drexler, C. I.; Tyrode, E.; Cremer, P. S.; Roke, S. The Jones-Ray Effect Is Not Caused by Surface-Active Impurities. *J. Phys. Chem. Lett.* **2018**, *9* (23), 6739–6743. https://doi.org/10.1021/acs.jpclett.8b02957.
(33) Zhang, H. *2 - Surface Characterization Techniques for Polyurethane Biomaterials*; Elsevier Ltd, 2016. https://doi.org/10.1016/B978-0-08-100614-6.00002-0.
(34) Ebnesajjad, S.; Landrock, A. H. Surface Tension and Its Measurement. *Adhes. Technol. Handb.* **2015**, 19–34. https://doi.org/10.1016/b978-0-323-35595-7.00002-4.
(35) Fataraite, E.; Jankauskaite, V.; Marazas, G.; Milašiene, D.; Žukiene, K. Viscosity and Surface Properties of Melamine-Formaldehyde Resin Composition. *Medziagotyra* **2009**, *15* (3), 250–254.
(36) Park, J.; Pasaogullari, U.; Bonville, L. Wettability Measurements of Irregular Shapes with Wilhelmy Plate Method. *Appl. Surf. Sci.* **2018**, *427*, 273–280. https://doi.org/10.1016/j.apsusc.2017.08.186.
(37) Jansen, A. LANGMUIR-BLODGETT FILM EXPERIMENT. *Valid. Graphol. judgments* **2019**, 99–122. https://doi.org/10.1515/9783111556499-007.
(38) Marczak, W.; Rogalski, M.; Modarressi, A.; Rogalska, E. A Model of Compression Isotherms for Analyzing Particle Layers. *Colloids Surfaces A Physicochem. Eng. Asp.* **2016**, *489*, 128–135. https://doi.org/10.1016/j.colsurfa.2015.10.051.